Magnetic separation in microfluidic systems

Smistrup, Kristian

Publication date:
2007

Document Version
Publisher's PDF, also known as Version of record

Ph.D. Thesis, s971611

Magnetic separation in microfluidic systems

Kristian Smistrup

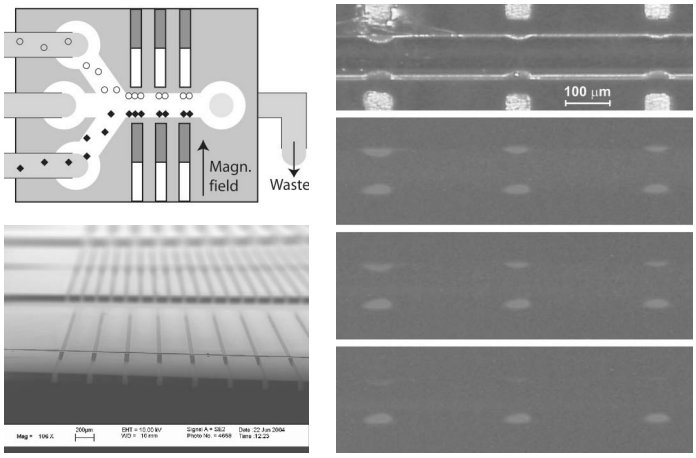

Supervisors: Mikkel F. Hansen, Henrik Bruus, Peter T. Tang, and Ulrich Krühne

MIC – Department of Micro and Nanotechnology
Technical University of Denmark

January 31, 2007

Abstract

This Ph.D. thesis presents theory, modeling, design, fabrication, experiments and results for microfluidic magnetic separators.

A model for magnetic bead movement in a microfluidic channel is presented, and the limits of the model are discussed. The effective magnetic field gradient is defined, and it is argued that it is a good measure, when comparing the performance of magnetic bead separators.

It is described how numeric modeling is used to aid the design of microfluidic magnetic separation systems. An example of a design optimization study is given.

A robust fabrication scheme has been developed for fabrication of silicon based systems. This fabrication scheme is explained, and it is shown how it is applied with variations for several designs of magnetic separators.

An experimental setup for magnetic separation experiments has been developed. It has been coupled with an image analysis program to facilitate real-time monitoring of the experiments. The set-up and experimental protocol are described in detail.

Results are presented for 'active' magnetic bead separators, where on-chip microfabricated electromagnets supply the magnetic field and field gradients necessary for magnetic bead separation. It is shown conceptually how such a system can be applied for parallel biochemical processing in a microfluidic system.

'Passive' magnetic separators are presented, where on-chip soft magnetic elements are magnetized by an external magnetic field and create strong magnetic fields and gradients inside a microfluidic channel. Systems with the elements placed beside the microfluidic channel is combined with hydrodynamic focusing to demonstrate a magnetic bead microarray inside a microfluidic channel. Systems where the on-chip magnetic material is placed underneath the microfluidic channel are also presented. One of these designs feature multiple magnetic length scales, and it is shown that this enhances bead capture ability.

A 'hybrid' magnetic separator design, where the magnetic field from on-chip current lines couples with an externally applied homogenous field to create strong fields and gradients is demonstrated. This gives extra magnetic bead manipulation possibilities compared to the passive designs. It is demonstrated how this can be used for magnetic bead microarrays.

Finally, it is discussed, based on the research presented in this thesis, how to further develop magnetic separation systems in microfluidic systems, and recommendations are given for the choice of magnetic design based on the desired application.

Dansk resumé

Denne Ph.D. afhandling beskriver teori, modellering, design, fremstilling, eksperimenter og resultater opnået med mikrofluide systemer til magnetisk separation.

Der opstilles en model for bevægelsen af magnetiske kugler i et mikrovæskesystem, og modellens begrænsninger diskuteres. Den effektive magnetiske feltgradient introduceres, og der argumenters for, at den er et godt mål, når forskellige magnetiske separatorer sammenlignes.

Det bliver beskrevet, hvordan numeriske beregninger kan være behjælpelige når man designer mikrofluide magnetiske separatorer.

Der er blevet udviklet en robust fremstillingsprocedure til fremstilling af siliciumbaserede systemer. Denne fremstillingsmetode gennemgås, og det vises, hvordan fremstillingsproceduren er blevet tilpasset fremstilling af forskellige systemer.

En forsøgsopstilling til magnetiske separationseksperimenter er udviklet og beskrevet i afhandlingen i detaljer. Den er koblet sammen med et automatiseret billedeanalyseprogram, så der løbende kan følges med i eksperimenternes forløb. En typisk forsøgsprotokol gennemgås.

Der præsenteres resultater for 'aktive' magnetiske separationssystemer, hvor mikrofabrikerede elektromagneter på chippen genererer de nødvendige magnetiske felter og feltgradienter. Det beskrives konceptuelt, hvordan et sådant system kan anvendes til parallel biokemisk processering i et mikrovæskesystem.

I 'passive' magnetiske separatorer bliver bløde magnetiske elementer på chippen magnetiseret af et eksternt magnetfelt og genererer kraftige magnetiske felter og gradienter i væskekanalen. Et system, hvor elementerne er placeret ved siden af væskekanalen demonstreres, og det vises, at det magnetiske system kombineret med hydrodynamisk fokusering, giver mulighed for microarrays med magnetiske kugler i en væskekanal. Andre systemer, hvor de bløde magnetiske elementer er placeret nedenunder væskekanalen demonstreres ligeså. Et af disse designs udnytter to forskellige længdeskalaer i det magnetiske design, og det vises, at dette forøger indfangningseffektiviteten.

Et 'hybrid' magnetisk separator design, hvor magnetfeltet fra strømbaner på chippen kombineres med et eksternt påtrykt homogent magnetfelt demonstreres. Denne type design giver flere muligheder for at manipulere magnetiske kugler i mikrovæskesystemet sammenlignet med passive systemer. Det bliver vist, hvordan denne type system kan bruges til microarrays med magnetiske kugler.

Til sidst diskuteres det, hvordan magnetisk separation i mikrovæskesystemer kan videreudvikles baseret på den forskning, der præsenteres i afhandlingen. Der afsluttes

med nogle anbefalinger i forhold til at vælge magnetisk separationsdesign for en given anvendelse.

Preface

The present thesis is submitted in partial fulfilment of the requirements for the PhD degree at the Technical University of Denmark (DTU). The work has been carried out at MIC – Department of Micro and Nanotechnology in the Magnetic Systems group (MagSys) from February 2004 to January 2007.

The project was funded by Danish Techological Institute (TI), Copenhagen school of Nanotechnology (C:O:N:T), and DTU, who all contributed equally.

The main supervisor for the project was Dr. Mikkel F. Hansen, and co-supervisors were Prof. Henrik Bruus from MIC, Dr. Peter T. Tang from the Department of Manufacturing Engineering and Management at DTU, and Dr. Ulrich Krühne from Danish Technological Institute (TI). I would like to thank my supervisors for good supervision during the project work and also for their good spirits. It has been a pleasure to work with them.

Special mention must be given to Henrik Bruus and Mikkel F. Hansen, with whom I have enjoyed both scientific and not so scientific discussions on an almost daily basis over the last three years.

In the period September 2005 to January 2006 I worked in the group of Howard A. Stone at the Division of Engineering and Applied Sciences at Harvard University. It was a tremendous learning experience for me, and I made some good friends there.

I enjoyed supervising students, Bastian G. Kjeldsen, and Jakob L. Reimers, who worked with me for a total of six months. They worked hard, and never lost their good spirits.

Shortly after starting my Ph.D. work, Torsten Lund-Olesen joined the MagSys group as a master student, and later, he continued as a Ph.D. student in the group. Torsten and I worked together and shared experience. We supplement each other well scientifically and have been able to benefit from that without ever stepping on each others' toes.

The staff at the cleanroom facility at DTU, DANCHIP, are acknowledged for their never ending support during fabrication processes, and the general staff at MIC is acknowledged for making MIC such a nice place to work.

Finally, I wish to thank my family and friends, who stood by me during all parts of this Ph.D. work.

The present version

The text that you read is an edited version of the thesis. A few minor mistakes were discovered after the thesis was handed in. These have been corrected for the printed version. Also, some formatting have been changed.

All changes are listed below

- This section has been added
- Small changes such as misspelled words, missing commas or words are not listed.
- In the introduction, the list of publication has been extended to include the full references. Also, the status of the manuscripts have been updated.
- When using references to specific groups in the Introduction Literature review, the university at which the group reside has been included.
- A few general references were added to the beginning of the Theory chapter in order to discriminate between the author's own work and more common physics knowledge.
- Fig. 4.2(b) had erroneous axis indications - This figure has been corrected.
- A paragraph has been added on oxide removal and the protective function of the oxide in chapter 5
- Some of the discussion in Appendix B has been changed. Discussion of the fundamental version of the Maxwell stress tensor is introduced.
- The bibliography has been updated such that all references have the same form.

Kristian Smistrup
MIC – Department of Micro and Nanotechnology
Technical University of Denmark
January 31, 2007

Contents

List of Figures

List of Tables

List of symbols

Symbol	Description	Unit
$\hat{\mathbf{n}}$	Surface outward normal unit vector	
$\hat{\mathbf{x}}$	unit vector in the x-direction	
$\hat{\mathbf{y}}$	unit vector in the y-direction	
$\hat{\mathbf{z}}$	unit vector in the z-direction	
R	Radius	m
V	Volume	m^3
μ_0	Magnetic permeability of free space	$\mathrm{N\ A^{-2}}$
χ_i	Intrinsic magnetic susceptibility	
χ_m	Measured magnetic susceptibility	
χ_0	Initial magnetic susceptibility	
$\mathbf{B}$	Magnetic field	T
$\mathbf{H}$	Magnetic intensity	A/m
$\mathbf{M}$	Magnetization	A/m
M_s	Saturation magnetization	A/m
$\mathbf{A}$	Magnetic vector potential	T m
φ	Magnetic scalar potential	A
$\mathbf{G}$	Effective magnetic field gradient	T/m
$\mathbf{J}^f$	Free current density	$\mathrm{A\ m^{-2}}$
$\mathbf{F}$	Force	N
$\mathbf{g}$	Gravity	$\mathrm{N\ kg^{-1}}$
p	Pressure	$\mathrm{N\ m^{-2}}$
η	(Dynamic) Viscosity	Pa s
Q	Volumetric flow rate	$\mathrm{m^3\ s^{-1}}$
ρ	Mass density	$\mathrm{kg\ m^{-3}}$
$\mathbf{x}$	Position vector	m
$\mathbf{v}$	Velocity vector	$\mathrm{m\ s^{-1}}$
$\mathbf{u}$	Fluid velocity vector	$\mathrm{m\ s^{-1}}$

Chapter 1

Introduction

The present thesis reports most of the work done by the author, Kristian Smistrup, since starting on the Ph.D. project on February 1st, 2004. The thesis was handed in on January 31st, 2007.

The thesis work has resulted in the publications listed below.

First authored papers

1. K. Smistrup, P.T. Tang, O. Hansen, and M.F. Hansen *Microelectromagnet for magnetic manipulation in Lab-on-a-chip systems* [1], first submitted February 2004, published in J. Magn. Magn. Mater. 300(2), pp. 418–426, 2006 - **Appended as Paper #1**

2. K. Smistrup, O. Hansen, H. Bruus, and M.F. Hansen *Magnetic separation in microfluidic systems using microfabricated electromagnets - Experiments and simulations* [2], first submitted May 2004, published in J. Magn. Magn. Mater. 293(1), pp. 597–604, 2005 - **Appended as Paper #2**

3. K. Smistrup, B.G. Kjeldsen, J.L. Reimers, M. Dufva, J. Petersen, and M.F. Hansen *On-chip magnetic bead microarray using hydrodynamic focusing in a passive magnetic separator* [3], first submitted August 2005, published in Lab Chip 5(11), pp. 1315-1319, 2005 - **Appended as Paper #4**

4. K. Smistrup, T. Lund-Olesen, M.F. Hansen, and P.T. Tang *Microfluidic magnetic separator using an array of soft magnetic elements* [4], first submitted November 2005, published in J. Appl. Phys. 99(8), pp. 8P102, 2006 - **Appended as Paper #3**

5. K. Smistrup, H. Bruus, and M.F. Hansen *Towards a programmable magnetic bead microarray in a microfluidic channel* [5], first submitted May 2006, published in J. Magn. Magn. Mater. 311(1), pp. 409–415, 2007 - **Appended as Paper #6**

6. K. Smistrup, and H.A. Stone *A magnetically actuated ball valve applicable for small-scale fluid flows* [6], first submitted August 2006, published in Phys. Fluids 19(6), pp. 63101/1–9, 2007 - **Appended as Paper #8**

7. K. Smistrup, P.T. Tang, and P. Møller *Pulse reversal plating process for MEMS applications* [7], first submitted November 2006, published in ECS Trans. 3(25), p. 179, 2007 - **Appended as Paper #9**

8. K. Smistrup, M. Bu. A. Wolff, H. Bruus, and M.F. Hansen *Theoretical analysis of a new efficient magnetic bead separator utilizing magnetic structures with multiple length scales* [8], first submitted January 2007, published in Microfluid. Nanofluid. 2007, DOI: 10.1007/s10404-007-0213-0 - **Appended as Paper #7**

Co-authored papers

9. L. Ejsing, K. Smistrup, C.M. Pedersen, N.A. Mortensen, and H. Bruus *Frequency response in surface-potential driven electrohydrodynamics* [9] first submitted September 2005, published in Phys. Rev. E 73(3), pp. 37302, 2006

Co-authored Patents

10. *Pressure Determination in Microfluidic Systems*, patent application filed with the United States Patent and Trademark Office by M. Faivre, M. Abkarian, K. Smistrup, and H. A. Stone. US Patent Application: 60/732,241, International Application No. PCT/US2006/029442

Conference Proceedings

11. K. Smistrup, O. Hansen, P.T. Tang, and M.F. Hansen *Selective magnetic bead capture using an addressable on-chip electromagnet array* [10], Proc. μTAS 2004, pp. 509-511 - **Appended as Paper #5**

First authored Conference Contributions

12. K. Smistrup, O. Hansen, P.T. Tang, and M.F. Hansen *Microelectromagnet for magnetic manipulation in Lab-on-a-chip systems*, IEEE - Nanoscale Devices and Systems Integration, Miami (FL), USA, Oral presentation, February 2004

13. K. Smistrup, O. Hansen, H. Bruus, and M.F. Hansen *Magnetic separation in microfluidic systems using microfabricated electromagnets - Experiments and simulations*, Scientific and Clinical Applications of Magnetic Carriers, Lyon, France, Oral presentation, May 2004

14. K. Smistrup, O. Hansen, P.T. Tang, and M.F. Hansen *Selective magnetic bead capture using and addressable on-chip electromagnet array*, Micro total Analysis Systems, Malmö, Sweden, Poster presentation, September 2004

15. K. Smistrup, T. Lund-Olesen, M.F. Hansen, and P.T. Tang *Microfluidic magnetic separator using an array of soft magnetic elements*, Magnetism and Magnetic Materials, San Jose (CA), USA, Oral presentation, November 2005

16. K. Smistrup, H. Bruus, and M.F. Hansen *Towards a programmable magnetic bead microarray in a microfluidic channel*, Scientific and Clinical Applications of Magnetic Carriers, Krems, Austria, Oral presentation, May 2006

17. K. Smistrup, P.T. Tang, and P. Møller *Pulse reversal permalloy plating process for MEMS applications*, 210th Meeting of the Electrochemical Society, Cancun, Mexico, Oral presentation given by Peter T. Tang, November 2006

Co-authored Conference Contributions

18. M. Faivre, M. Abkarian, K. Smistrup, and Howard Stone *High-speed microfluidic differential manometer for cellular-scale hydrodynamics*, 58th Annual meeting of the Division of Fluid Dynamics of the American Physical Society, Chicago (IL), USA, Oral presentation, November 2005 - I was added as co-author shortly before the meeting, so my name is not featured in the official program

19. M.F. Hansen, T. Lund-Olesen, K. Smistrup, and H. Bruus *Microfabricated Passive Magnetic Bead separators*, Intermag06, San Diego (CA), USA, Invited talk, May 2006

20. M. Bu, K. Smistrup, M.F. Hansen, and A. Wolff *Design and FEM Simulation of a Microfluidic Magnetic Beads Separator*, MNE06, Barcelona, Spain, Poster presentation, September 2006

21. M. Bu, T.B. Christensen, K. Smistrup, A. Wolff, and M.F. Hansen *A high-throughput SU-8 microfluidic magnetic bead separator*, Transducers '07, Lyon, France, June 2007

Papers, [1, 2, 3, 4, 5, 8, 10], present results for magnetic separation in microfluidic systems, and thus represent the most important published results within the subject of the thesis. Paper [6] presents a microfluidic valve design based on magnetic manipulation of a magnetic bead, and although the aim of this work is different from the aim of the rest of the thesis, it is included as part of the thesis for reference and comparison. Paper [7] is included in the thesis and accounts for the work that has been done on further developing the setup for permalloy electroplating. These papers are included at the back of the thesis.

I did my Master's thesis in the magnetic systems (MagSys) group at MIC - Department of Micro and Nanotechnology. Peter T. Tang was co-supervisor, and the main supervisor was Mikkel F. Hansen. The thesis was handed in on December 1st 2003. [11] I chose to continue in the group of Mikkel F. Hansen, since I had enjoyed working in the group immensely, and I found the scientific environment at the department very inspiring.

In the beginning of the Ph.D. studies, I continued working with the systems that were fabricated during my Master's thesis investigating some of the open questions that had arisen during the Master's thesis work.

In the Master's thesis the subject had been active magnetic separators, where on-chip microelectromagnets supply magnetic fields and gradients - An in-depth explanation of active systems is featured in the next section. As mentioned, this study continued through the first few months of the Ph.D. study. Further experimental studies were performed,

and a better theoretical understanding of the movement of magnetic beads in a microflow was developed. This led to publications, [1, 2, 10], of which [1] is mostly covering work from the master thesis, and the two others primarily present results obtained during the Ph.D. project.

Soon, the focus was changed to passive magnetic separators, where on-chip soft magnetic material are magnetized by an external magnetic field and thus create magnetic field gradients (explained in detail below). These are easy to fabricate compared to active systems and have turned out to be more effective for magnetic separation. During this study, I also supervised students. Jakob L. Reimers and Bastian G. Kjeldsen who did their bachelor thesis and two three week project courses with Mikkel F. Hansen and myself as supervisors. This turned out to be a great collaboration. This study of passive magnetic separators lasted for little more than a year and resulted in the publications [3, 4].

During this time, Mikkel F. Hansen and myself also supervised the full-time visiting student, Marc Rüger from the Technical University of Dresden, Germany. He did an obligatory external stay in our group from October 2004 until February 2005. His intention was to apply our passive magnetic separation system for detection of salmonella bacteria in food samples. This turned out to be anything but simple, and some of the problems were definitely rooted in the fact that Marc Rüger was trained as a biotech engineer, whereas Mikkel F. Hansen and myself are physicists/physics engineers. In the end he succeeded in developing and testing a protocol for detection of a model strand E-coli with our systems and compare the results to bench-top experiments.

In January 2005, Mikkel F. Hansen and I supervised students, Edoardo Grazia and Lars Nørgaard during another three week project course. We investigated how to make passive magnetic separators in SU-8. Our results are discussed in section 5.2.1.

A few months into the second year of the Ph.D. study, an investigation of hybrid magnetic separators was started - Here hybrid separators mean microfluidic systems with on-chip current lines that combine with an external magnetic field to make large magnetic fields and gradients. The objective was to make an addressable array of magnetic capture spots such that a dynamic microarray could be constructed inside microfluidic channels using magnetic beads. An extensive design study was made numerically, and the systems were fabricated, but the study was halted, when I had to go on my external stay.

I was given an opportunity to study in the group of Professor Howard A. Stone at the Division of Engineering and Applied Sciences at Harvard University from August 23rd, 2005 till February 2nd, 2006.[1] The external stay was a tremendous personal experience for me, I met some very inspiring and clever people there. Besides the people in the Stone group, whom I now consider friends, I also met people from the George Whitesides group, which is arguably the largest microfluidics group in the world, and also, I met with Robert Westervelt and some of his students, who are doing very inspiring work on magnetic manipulation in microfluidic systems using arrays of microelectromagnets. Armand Ajdari, a professor in Paris, France, working on theoretical aspects of microfluidics, had a position as Visiting Professor at Massachusetts Institute of Technology (MIT), and

[1] At the time of writing this thesis, the division is in the midst of being turned into a school, so the future name will most likely be School of Engineering and Applied Sciences.

in the Stone group during most of my stay, and discussions with him was a great added bonus.

During my time at Harvard University, I worked on aspects of microfluidics and magnetism other than separation. Magalie Faivre and Manouk Abkarian of the Stone group had been studying deformation of red blood cells traveling through narrow channels [12], and they invited me to investigate the microfluidic aspects of their device numerically. This study turned out to be quite comprehensive, but in the end a simple theoretical model for the fluidic behavior of the device was suggested and it was validated numerically. Work is still being done on the experimental side of the project, and hopefully our efforts will turn into a publication at some point.

Before I arrived at Harvard, Howard A. Stone had thought about a concept for a magnetically controlled microfluidic valve using a magnetic bead as the ball in a ball valve design. He suggested this to me, and I investigated both microfluidics and magnetics of the problem analytically and numerically. Our combined efforts turned into paper [6] of this thesis. The Stone group also investigates applications of jammed colloidal shells, where particles cover a fluid-fluid interface and jam the interface [13, 14]. Some experiments were performed with magnetic particles on fluid interfaces, but none of the results were publishable.

Although I did not study magnetic separation during my stay at Harvard, I did pick up some analytic tools that have since then been applied extensively in my analysis of magnetic separation in microfluidic systems.

Upon returning from my external stay, work was continued on the hybrid systems, and it was demonstrated that we could place beads selectively at different addressable capture sites in a microfluidic channel, which resulted in paper [5].

At the time when I started my Ph.D. studies, Anders Heebøll-Nielsen started in a post doc position at Danish Technological Institute (TI) with my supervisor, Ulrich Krühne, as his supervisor. His project was to make magnetic separation systems in polymers. Through the first years of my Ph.D. studies Anders Heebøll-Nielsen and I worked in parallel but separately on our projects. We shared experience, but no real collaborations were done. In the final six months of this project, it was decided to make a collaboration, where we designed systems that could both be fabricated in silicon (by me) and polymer (By TI). At this time Anders Heebøll-Nielsen had ended his post doc position, but his work was continued by Pedro Santos. The design, fabrication, experiments and results of these systems are reported in detail in this thesis.

1.1 Presentation of subject including literature review

Magnetic separation in microfluidic systems is one of many building blocks in Micro Total Analysis Systems (μTAS). We will return to μTAS later, but first magnetic separation and microfluidic systems must be defined.

Magnetic separation is a technique that has been known since the middle of the 19th century. In the beginning, metals were separated from regular dirt in the minerals industry by applying a large magnetic field. In 1974 Oberteuffer reviewed the history of

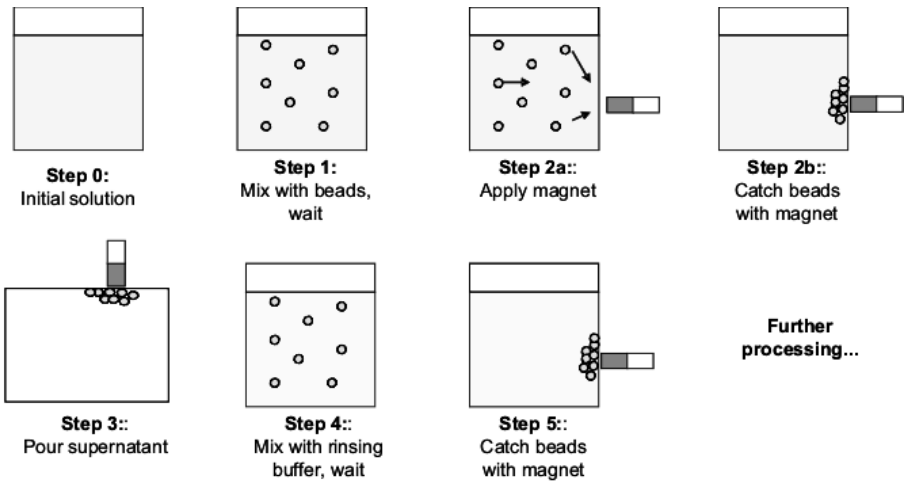

Figure 1.1: Magnetic separation on a test tube level. In step 1 magnetic beads are mixed with a sample and are allowed time for incubation. In step 2 a magnet is applied at the outer wall of the test tube and the magnetic beads are attracted to the sidewalls. Whatever has been bound on the surface of the beads will also be transported to the sidewall. The supernatant is discarded in step 3, and in step 4 a rinsing buffer is applied to the the test tube and the magnet is removed. The magnet is applied once more in step 5 and the rinsing buffer is discarded, such that the beads and whatever has been bound to their surfaces can be used for further processing.

magnetic separators and their uses, [15]. Oberteuffer also mentions the emergence of High Gradient Magnetic Separation (HGMS) systems that were developed around that time. J. H. P. Watson is usually accredited of being the first to describe this phenomenon thoroughly in his 1973-paper, [16]. Whereas regular magnetic separation just utilizes a large magnet to supply the necessary magnetic forces to pull metals out of a slurry, HGMS uses a fine steel wool mesh in a strong magnetic field to make very strong localized magnetic field gradients inside the mesh that create sufficient forces to trap even paramagnetic particles. Since the invention of HGMS, the use of magnetic separation for biotechnology, chemistry and medicine has been growing rapidly as described in reviews, [17, 18, 19, 20].

Some chemical and biological species have their own magnetic moment, and in those cases the species can be separated by their internal moment. In most cases, however, chemical and biological species are almost non-magnetic and will not react to a magnetic field gradient. Today, superparamagnetic beads and particles are commercially available with numerous surface coatings that will bind with high specificity to certain chemical or biological species. Binding the desired species to the surface coating of a magnetic bead thus puts a magnetic handle onto this species of a sample.

The uses of magnetic beads and particles in chemistry, biology, and medicine are numerous. Some of these applications are reviewed by Pankhurst *et al.* in their 2003 paper, [21], and the semi-annual conference "Scientific and Clinical Applications of Magnetic Carriers" that was held for the first time in Germany in 1996 [22] encompasses every aspect of magnetic bead and particle technology. Technical papers from the conference in 2004 in Lyon, France, can be found in volume 293 of J. Magn. Magn. Mat. and another

special volume of this journal is scheduled to appear in the Spring of 2007 containing technical papers from the 2006 conference in Krems, Austria.

Magnetic separation using magnetic beads on a bench-top level is illustrated in Fig. 1.1. Assume as an example that the beads are coated with a specific antigen for an antibody that is known to be in the sample. When the beads are mixed with the sample, only the specific antibodies will bind to the beads, and the rest of the sample is discarded. Further rinsing steps can be performed before further processing.

A microfluidic system is, as the name suggests, a system of one or more fluid channels, where the smallest characteristic length scale for the fluid flow is on micron scale, i.e. less than a millimeter. For most microfluidic systems the smallest characteristic length scale is the height of a rectangular fluid channel, and the height is most-often in the range of 50 to 300 μm. In such fluid channels fluid flow is dominated by viscous forces rather than inertia, which is reflected in the fact that the flow is almost always laminar in microfluidic systems. The physics of fluids on that length scale is thoroughly reviewed by Squires and Quake, [23].

Two schools of utilizing microfluidic systems exist. One school uses the facts that mixing is strictly diffusive in microfluidic systems and that experimental parameters are can be controlled with high precision to study subjects within analytical chemistry (usually related to reaction kinetics) that could otherwise not be studied or to significantly speed up processing times. See for example section 4.1 in the review by Weigl and co-workers [24].

The other school aims to miniaturize and integrate the functionalities of chemical, biochemical, and medical laboratories. The idea is that several laboratory functionalities should be miniaturized and integrated onto a single chip such that the chip is able to perform a test that would otherwise have required an entire laboratory. This idea has been given the name, Lab-on-a-chip.

One of the earliest examples and certainly the most well-known of an automated portable total analysis system is the home pregnancy test. A drop of urine is applied to the device, and a few minutes later a well-defined answer is provided for the user. It is debatable whether this is in fact a microsystem, but it is certainly a total analysis system, and it is small and portable.

Several good reviews of μTAS exist. Knight wrote a Nature News feature, [25], that explains the concept of μTAS in layman's terms. Reyes *et al.* wrote a review paper, [26], that tells the chronological story of μTAS from the early studies in microfluidic systems in 1975 and onwards. Manz *et al.* coined the term μTAS in 1990 [27] (although his version was "miniaturized total ..."), and that year also marked the time of take-off for the μTAS field. It has since then been growing rapidly, and by now there is an annual conference called "Micro Total Analysis Systems" and the journal, Lab on a chip was first issued in 2002 and in 2005, it had an impact factor of 5.3.

The advantages of μTAS are many, but usually the following are mentioned as the most general [24, 28]

- Minute sample consumption. Microfluidic systems are inherently small, and thus only small samples are needed. Typically in the range of pico to micro liters.

- Fast diffusion times. The distances inside a microfluidic system are small, and thus fast operation of diffusion limited processes is possible.
- Large surface to volume ratio makes surface-based assays more feasible.
- Laminar flows supply new means of studying chemical reactions at interfaces.
- Possibility of integrating several functionalities into hand-held portable devices resulting in lab-on-a-chip systems.

Many of today's applications and possibilities of microfluidic lab-on-a-chip systems have been reviewed by Weigl and co-workers [24] and more recently by Dittrich *et al.* [29].

In 2003, Elizabeth Verpoorte reviewed the many applications of beads in microfluidic total analysis systems [30], and the combination of of magnetic beads and microfluidic systems was reviewed by Martin A. M. Gijs in 2003, [28], and Nicole Pamme in 2006 [31]. Introduction of magnetic beads into a microfluidic system further reduces the required diffusion time when chemical species have to diffuse to the surface of randomly distributed beads rather than channel walls.

1.1.1 Magnetic separation in microfluidic systems

This section reviews the development of magnetic separation and to some extent manipulation in microfluidic systems.

Some of the very early work was simply done by holding a strong magnet next to a microfluidic channel trapping the beads on a wall. While this is sufficient for some applications, this section will focus on systems with micron scale magnetic structures or where microfluidic properties are used in the application.

Papers in this review will be categorized based on their working principle. Systems for magnetic bead capture with on-chip electromagnets will be called active systems, systems for bead capture with on-chip magnetic material that are magnetized by an external magnetic field will be called passive systems, and systems for bead capture or bead manipulation with on-chip current lines coupled to an external magnetic field will be called hybrid systems. Furthermore, a category of systems that form plugs and chains of magnetic beads have been developed over the last few years to form dynamic filters inside fluid channels constituted by magnetic beads. In the end, a few papers that could not be categorized will be reviewed.

Fig. 1.2 illustrates how magnetic separation can be applied in a microfluidic system. The figure illustrates a simple antibody-antigen assay where beads are coated with a specific antibody and brought in contact with a sample that contains the specific antigen. The specific antigen bind to the antibody, and are thus separated from the sample.

Active systems

The first microfluidic system with integrated micron sized magnetic structures was presented by Chong H. Ahn and Mark G. Allen in 1994 [33, 34]. Two meander type copper

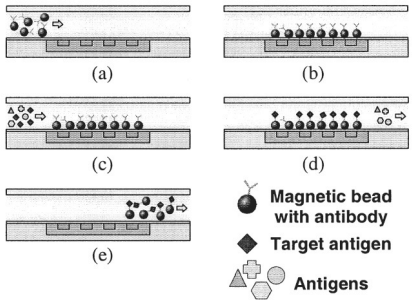

Figure 1.2: Magnetic separation in a microfluidic system. The figure is taken from ref. [32]. In (a) magnetic beads with a specific antibody surface coating is loaded into the channel and captured on the magnetic elements in (b). A sample containing many different antigens are flown into the channel in (c). The antigens are allowed time to react with the antibodies on the captured beads. Buffer is flown through the channel in (d) and unbound antigens flow out of the channel. In (e) the beads are released from the microfluidic channel, and the beads with bound antibody and antigen can be collected for further processing or analysis.

coils with permalloy magnetic cores supplied a magnetic field across a microfluidic channel in a quadrupole configuration. A field of 0.03 T could be generated in the microfluidic channel, and from the geometry, it is estimated that the characteristic length scale is 100 μm. This yields a magnetic field gradient of order 10^2 T/m.

The group of Chong H. Ahn at University of Cincinnati has continued to publish several different designs of microfluidic magnetic separators. Some are based on a serpentine shaped current line, which is semi-encapsulated by permalloy beneath the microfluidic channel, [32, 35, 36, 37]. These were even integrated with an electrochemical sensor with electrical read-out to form a true lab-on-a-chip system. These systems run with a current on the order of 30 mA, and the characteristic magnetic length scale is 20 μm, such that the field can be estimated to 2 mT and a magnetic field gradient of approximately 10^2 T/m. A further developed version of this design was presented by Jaephil Do of the Ahn group in 2004 [38], where the electromagnets have been moved off-chip, which reduces fabrication cost and allows for larger magnetic fields.

Semi-encapsulated spiral electromagnets constitute a third class of publications from the Ahn group [39, 40]. This design was the basis for the work done in my Master's thesis [11], and the early papers [1, 2, 10]. The performance of such a system is analyzed in paper [1] of this thesis.

Rong Rong of the Ahn group developed a fourth class of magnetic separators with electromagnets both on and off-chip [41, 42]. These systems have flux guides close to the channel that are magnetized by either external or on-chip electromagnets. From the information in the papers it is hard to deduce, what the magnetic fields and gradients might be, but one might guess that the characteristic field is the saturation field of permalloy, and the characteristic distance is roughly 200 μm. This gives a gradient of $\approx 10^4$ T/m, but this may be a vast over-estimate.

Qasem Ramadan from the Institute of Microelectronics, Singapore and co-workers

presented several different designs of microfabricated electromagnets with and without magnetic cores. These are characterized by being quite close to the channel and small compared to the spiral designs of the Ahn group. They were able to demonstrate both capture and controlled movement of magnetic beads. [43, 44, 45, 46]. The systems are quite well-characterized in terms of magnetic bead capture ability. With their most efficient system, 84.3 % bead capture efficiency is achieved at a flow rate of 20 μl/min, which corresponds to a linear flow velocity of 0.7 mm/s. It should be noted that these systems have magnetic material inside the microfluidic channel, which may inhibit biological reactions.

Hakho Lee of the Westervelt group at Harvard University has presented arrays of very small magnetic bead traps composed of planar on-chip microelectromagnets with an outer diameter of 30 μm that can be individually addressed and thus used to transport beads inside a microfluidic system [47, 48, 49, 50]. They even present the ability to move cells bound to magnetic particles around inside a microfluidic system using magnetic actuation.

Roel Wirix-Speetjens from the Interuniversity Microelectronics Center (IMEC) has also investigated capture and transport of magnetic beads using tapered conductors inside microfluidic channels [51, 52, 53] and shown that magnetic beads can be effectively transported along the conductors. They are able to transport beads with speeds up to 60 μm/s.

The active systems above all include some form of silicon microfabrication, and in general they are expensive to fabricate. Adam C. Siegel of the Whitesides group at Harvard University recently demonstrated that on-chip electromagnets and microfluidic channels could be fabricated in PDMS using solder as the current line in a two-step process. By applying a current of 1 A through the current line, he is able to move 90 % of the magnetic beads to one side of the 100 μm wide microfluidic channel within one second. [54]

In general active magnetic systems generate small magnetic fields in the microfluidic channel, $\lesssim$ 30 mT, they are difficult and expensive to fabricate, and also they generate heat very close to the microfluidic channel, which may interfere with biological entities in the channel. The main advantage of active systems is that coils and current lines can be individually addressed such that advanced manipulation of magnetic beads are possible. Such systems were only pursued at the very beginning of this thesis work.

Passive systems

In this section, passive magnetic systems are reviewed. Such systems are characterized by having on-chip soft magnetic material, which is magnetized by external magnetic fields.

While these are less common in literature compared to active systems, they have the potential of being much more effective than their active counterparts, they are easier to fabricate, and no heat is generated on-chip. If the external field is large enough to magnetically saturate the magnetic beads, then the job of maximizing the force is equal to maximizing the magnetic field gradient. Soft magnetic materials generally have saturation fields on the order of one Tesla, and if the geometry can be designed such that the characteristic length scale for the magnetic field is on the order of a 100 μm or less, then magnetic field gradients in the range of 10^4 T/m are within reach.

The first passive system that the author is aware of is one by Deng from the Whitesides group published in 2002. 7 μm high cylindrical nickel posts with a diameter of 15 μm were fabricated and placed inside a microfluidic channel, where they were magnetized by a neodymium iron boron (NdFeB) permanent magnet [55].The system is reminiscent of the HGMS system devised by Watson in 1973 [16], since the magnetic posts constitutes a microscale magnetic mesh inside the microfluidic channel. The arrangement is like likely to produce magnetic field gradients close to 10^4 T/m. There are, however, two problems with this design. The sample is in direct contact with the nickel posts, which may inhibit biology and the nickel has substantial hysteresis which is problematic, when one wants to release the beads, as it is shown in the paper.

In 2004, Ichikawa from Toyo University and co-workers demonstrated a system with patterned sputtered permalloy film beneath a microfluidic channel. [56] The film had a thickness of only 500 nm, which means that forces from the film are short-ranged, but retention of a plug of beads was successfully demonstrated.

Mirowski and Moreland from the Russek group at NIST have demonstrated systems where a 30 nm thick permalloy film is patterned into 1.2×3.6 μm^2 squares on a 0.2-1.0 μm thick nitride membrane that separates the permalloy squares from the microfluidic channel [57]. Such a system creates large but very localized gradients, and it is thus mostly applicable for single bead manipulation. Single bead manipulation was demonstrated using a magnetic force microscope in combination with the system in their 2005 paper [58]. Moreland used the same basic idea, but the permalloy pads were replaced with spin-valves that could be actuated by current pulses, such that the spin-valves function as addressable permanent magnets that could be turned on and off. This allows for controlled movement of single beads inside the microfluidic channel with small current consumption [59].

In 2004 and 2006, Han and Frazier from Georgia Institute of Technology demonstrated a system for continuous separation of red and white blood cells based on their intrinsic magnetic properties (red blood cells are paramagnetic and white blood cells are diamagnetic). The system consists of a nickel wire placed in the middle of a microfluidic channel, and this wire either repels or attracts paramagnetic cells depending on the direction of the applied magnetic field. [60, 61]

Inglis *et al.* from Princeton University presented a system with nickel stripes at the bottom of a microfluidic channel. The nickel stripes were placed at an angle to the fluid flow, and magnetic particles would tend to follow the direction of the magnetic stripes, and would thus be deflected and separated from the rest of the sample [62]. Inglis and co-workers did a review on microfluidic systems for magnetic cell separation in 2006. [63]

A second class of microfluidic passive magnetic separators exists. These, all use external permanent magnets, and depend on the fact that in microfluidic systems fluid flow is laminar, and thus co-flowing fluids do not readily mix. The principle is that of magnetic field flow fractionation, which was described in 1999 by Zborowski *et al.* in ref. [64] from Lerner Research Institute.

Gert Blankenstein and Ulrik Darling Larsen From the Technical University of Denmark demonstrated this principle in a microfluidic system in 1998 [65]. In a channel with two inlets, sample was infused at one inlet, and buffer was infused at the other. The two streams do not mix due to the laminar flow, but by application of a magnetic field, mag-

netic particles were pulled from the sample stream into the buffer stream. The two fluids were split into two outlets downstream. Steen Østergaard of the same group demonstrated a slightly more advanced system based on the same approach in 1999 [66].

Fuh and co-workers from Chaoyang University of Technology have published several experimental studies using a system similar to ref. [65] in refs. [67, 68, 69, 70]. Kim and Park from Korea Advanced Institute of Science and Technology applied the same principle for a multiplexed immuno-assay in 2005 [71].

Pamme and co-workers from University of Hull published several experimental studies of a system similar to ref. [65]. However, their system had the advantage of multiple outlets. The systems above usually only have two outlets, which means that particles are either measured as magnetic or non-magnetic. With multiple outlets, Pamme and co-workers were able to separate several kinds of particles based on the induced magnetic moment of the particles, i.e. particles with higher susceptibility are separated from particles with lower susceptibility, and smaller particles can be separated from larger particles. [72, 73, 74]

Nan Xia of the Ingber group at Harvard University presented a system in 2006 for continuous separation of magnetic beads from non-magnetic beads and E-coli bacteria bound to magnetic beads from a sample using a magnetic structure similar to paper [3] of this thesis. [75]

Passive systems have been investigated extensively in this project. Papers [3, 4, 6, 8] of this thesis can all be classified as passive systems. Torsten Lund-Olesen from my own group demonstrated how the efficiency of passive magnetic separators could be enhanced by the addition of herringbone mixer structures in the bottom of the microfluidic channel [76, 77].

Hybrid systems

Hybrid systems have on-chip current lines or coils. At the same time a homogenous magnetic field is applied. The on-chip current lines supply magnetic field gradients, and the applied field magnetizes the magnetic beads.

We have chosen to call this type of systems 'hybrid systems' since they have the best of both active systems and passive systems. They have the addressability of the active systems and the strong magnetic fields of the passive systems. However, it is usually difficult to achieve the magnetic field gradients available in passive systems, but still hybrid systems generate more force than active systems. Another important feature of hybrid systems is that the force in a certain position can be switched from attractive to repulsive. This stems from the fact that when the current is turned on, the field from the conductor will couple constructively with the external field in some positions and destructively in other positions. When the current in the conductor is reversed, these positions are switched such that in places where the fields coupled constructively before, they now couple destructively. Neither passive nor active systems can do that.

Tao Deng of the Whitesides group published a system in 2001 with two serpentine conductors next to each other. By switching the current in the two conductors they could make magnetic beads move along the conductors [78]. Rida of the Gijs group at Swiss Federal Institute of Technology (EPFL) presented a system capable of doing the same thing, but where the Deng system would move beads at speeds ≈ 100 μm/s, the Rida

system is capable of a speed of ≈ 400 μm/s. The Rida system uses overlapping coils on a printed circuit board to supply the moving force [79].

Marc Tondra, Nikola Pekas, and co-workers from NVE Corporation have presented systems, where current lines are buried beneath the bottom of a microfluidic channel. The magnetic field from the buried current lines coupled with an external field and would divert magnetic beads in the flow to either of two channel outlets.[80, 81]

The systems above (except the Rida system) are made using sputtered thin ($\lesssim 1$ μm) metal films for the conductors. Such systems supply strong but localized field gradients. The author have presented a system, where thick (175 μm) current lines are buried in the backside of a silicon wafer. Such current wires can carry much more current at the same power limit, and the magnetic field gradients are of a longer range. The separation between current lines and channel is larger, so the forces at the very bottom of the channel are reduced compared to systems with thin current lines. [5]

Dynamic plugs and chains of magnetic beads

Recently, more advanced applications of magnetic beads in microchannels have emerged. The systems, discussed so far either trap magnetic beads on channel walls or divert the bead flow into one or more fluid outlets. Immunoassays with functionalized beads on the sidewalls have been demonstrated, but in such systems it is necessary to allow time for the sample to diffuse to the channel walls. This time can be reduced and assay sensitive increased, if the beads are not at the walls but held across the fluid, such that the beads form a porous filter. In 2004 Nicolas Minc of the Viovy group at Curie Institute and Amar Rida from the Gijs group both published results where arrays of magnetic bead columns were formed reaching across the entire microfluidic channel in the direction of an applied magnetic field. [82, 83]

Rida and co-workers moved on to demonstrate an efficient mixing method using an AC version of the setup demonstrated earlier [84]. The group of Viovy, on the other hand, continued biological experiments with the type of system presented earlier, [85], and also a system, where they used a dense plug of bead as a filter [86].

Suzuki of University of Tokyo and co-workers presented a chaotic microfluidic mixer based on manipulation of magnetic beads in 2004 [87]. Thick copper lines (40×40 μm^2) were formed with their top sides at the bottom of the microfluidic channel (in contact with the fluid), and the fluid channel was designed in a serpentine structure such that fluid flow combined with switching of the magnetic forces gave chaotic mixing.

Mixing was also achieved by Biswal and Gast from Massachusetts Institute of Technology using chemically linked chains of magnetic beads in a rotating magnetic field. The chains of beads function almost as stir bars. [88]

The systems that did not fit into the other categories

Two systems, the author is aware of, use magnetic fields and magnetic beads or particles in combination with surfaces with engineered wetting properties to perform interesting functionalities. The first of these systems was presented by Gary Zabow and co-workers

from Harvard University in 2002 [89]. They were able to demonstrate focusing of beads in the vertical and horizontal center of a microfluidic channel using a combination of surface tension and magnetic force, such that problems like beads sticking to surface were eliminated.

The second of these systems were presented by Lehmann and co-workers of the Gijs group [90]. Using On-chip electromagnets combined with an external field they could move a droplet containing magnetic particles on a hydrophobic surface. The droplet could be moved to regions with hydrophilic surfaces and mix with stationary droplets in these regions (one droplet per region). The droplets would be allowed to mix, but the droplets could be separated by application of the magnetic forces. In this way a sequential experiment could be performed on the particles inside the 'magnetic' droplet.

Finally, it should be mentioned that at least one Micro Total Analysis System has been presented by Liu of Arizona State University *et al.* in 2004, where magnetic separation of magnetic beads are combined with on-chip pumps, valves, sensors, magnets, and fluid channels to perform DNA microarrays on whole blood. The system is self-contained and needs only the addition of sample. [91]

1.2 Scope and outline of the thesis

The work in this thesis has been focused on the capture of magnetic beads on the walls of microfluidic channels. It has been investigated how this could be done most efficiently, and if the functionality of such a system could be enhanced beyond the simple assay. This lead to the investigation of array systems, where sets of beads with different surface functionalizations are placed at individual capture sites in a microfluidic channels such that programmable (by the bead surface functionalizations) parallel assays could be performed inside microfluidic channels.

The structure of the thesis is that of a paper or book. The Ph.D. has covered many different subjects and projects, so instead of a thorough account of every sub-project (which to some extent is given in the included papers), the author has chosen to give a general view of the subject as it is viewed by the author at this stage.

1. **Introduction** The present chapter. The reader is almost already at the end and is expected to decide for him or herself what the contents of the chapter were.

2. **Materials** Magnetic Materials have been an integral part of this work. This chapter discusses ferromagnetic materials, with the focus on soft ferromagnetic materials and superparamagnetic beads and particles. The chapter also discusses some of the other materials used during the project.

3. **Theory** In this chapter, the theory of magnetic separation in microfluidic channels is developed. It is shown how to calculate magnetic field gradients and forces, and how to determine magnetic bead movement in microfluidic channels.

4. **Numerics and design** This chapter describes how numerics have been applied in the design phases of this project. An example of such application is presented.

5. **Fabrication** A fabrication scheme for silicon systems was developed at an early stage of the project. This scheme is described, and the critical steps are discussed. It is shown how the same fabrication scheme has been adapted to the different chip designs.

6. **Experimental methods** This chapter describes the experimental setup and experimental methods that have been used for bead capture experiments.

7. **Results** This chapter summarizes and discusses the results of the work. The papers of this thesis are discussed in the context of the general aims of the thesis.

8. **Discussion and outlook** Discussion and outlook

9. **Conclusion** Conclusion

At the end of the main thesis, the reader will find three appendices. These appendices are notes that have been written at different times during the Ph.D. project. They should be viewed as in-depth investigations of specialized topics - Too specialized to be part of the main thesis, but sufficiently relevant to be publicly available with this thesis. They may even be useful for future researchers who wish to study magnetic separation in microfluidic systems. The appendices are

A Magnetic force on a magnetic bead in an arbitrary magnetic field

B Variations of the electromagnetic stress tensor

C Magnetic separation with constant force

1.2.1 Mathematical notation

The mathematical notation in this thesis is quite standard. Scalar variables are noted in italic. For example, this v is a scalar.

Vectors and vector fields are written as non-italic bold-face. $\mathbf{B}$ is a vector field. A component of a vector field along a direction is written as a scalar with a direction indicator as subscript. H_y is the y-component of the $\mathbf{H}$-field. The magnitude of a vector is written as the scalar value of the vector. For example, $H \equiv |\mathbf{H}|$.

Tensors are rarely used in this thesis, but we denote a tensor as non-italic bold-face with a double arrow above. $\overleftrightarrow{\mathbf{T}}$ is a tensor. The components of a tensor are written as a scalar with two direction subscripts. T_{xy} is the xy-component of $\overleftrightarrow{\mathbf{T}}$. All tensor equations are written in full, index tensor notation with Einstein summation convention is not used in this thesis.

As we will see, it is often useful to introduce dimensionless variables and parameters. Dimensionless variables will be marked with a tilde. For instance, $\widetilde{x}$ is a dimensionless variable.

Chapter 2

Materials

2.1 Magnetic materials

Several different magnetic materials have been used throughout this project. In this section, a short description is given of their physical properties. Only ferromagnetic materials are discussed; diamagnetic and paramagnetic materials are not relevant for this thesis, and such materials will be assumed to have no magnetic moment throughout.

In a ferromagnetic material the individual magnetic moments are aligned with their neighbors. The quantum mechanical exchange coupling makes it energetically favorable for the magnetic moments to be aligned. However, if all the magnetic moments in a block of magnetic material are aligned, there must be a large magnetic field outside the material, and it costs an energy proportional to the volume of the block to sustain this field. This means that there is an energy competition between having fully aligned atomic moments and minimizing the field outside the material. This causes the magnetic material to form domains, where the magnetization is parallel inside each domain, and these domains are separated by domain walls. A domain wall is a region of the material, where the moments are misaligned to accommodate the change in magnetization between the domains. The energy cost of a domain wall is proportional to its area. Inside magnetic domains the magnetization is equal to the saturation magnetization of the magnetic material, M_s. Fig. 2.1(a) shows an example of a magnetic material with domains.

When one applies a magnetic field to a piece of magnetic material, it becomes energetically favorable for the atomic moments to be aligned with the applied field. When this happens the domain walls start to move such that the domains with parallel magnetization grow, and other domains shrink. When the domains with parallel magnetic moments have grown to fill the entire block of material, the magnetization of the material cannot grow anymore, and the whole piece of material has attained its saturation magnetization. Fig. 2.1(a) illustrates this process. The figure also introduces the concepts of remanent magnetization, M_r, and coercive field, H_c. The treatment of magnetic hysteresis loops is often imprecise (as shown by Rudowicz and Sung [94, 95]), so here we specify that when we mention the remanent magnetization of a material, M_r we mean the magnetization inside the material, when H inside the material is zero, and when we mention the coercive

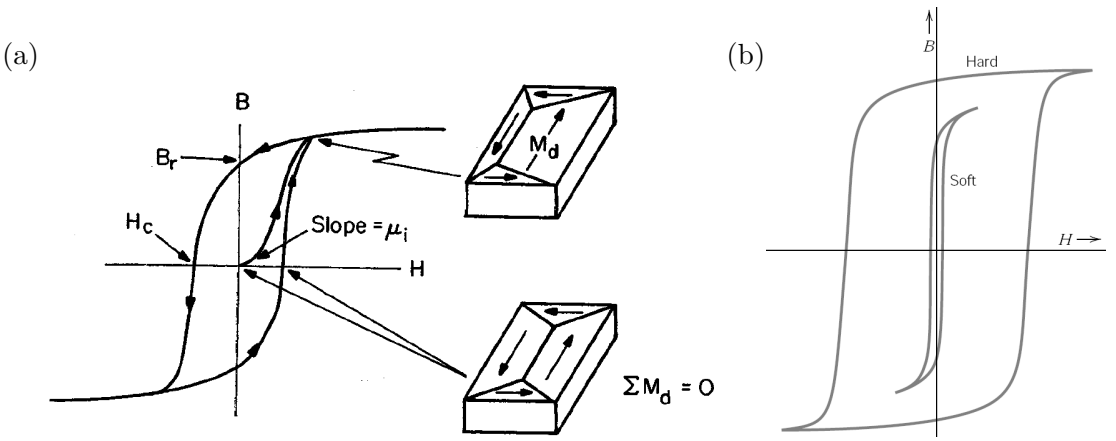

Figure 2.1: (a) The magnetization process for a block of ferromagnetic material. Initially the material is not magnetized; that is the magnetization in the magnetic domains sum up to zero such that the net magnetization is zero. When a magnetic field is applied the domain walls move, and a net magnetization results. When the applied field is removed, the domain walls move again, but they will not move far enough to make the net magnetization go back to zero. There will be a remanent magnetization, $M_r \approx B_r/\mu_0$ as shown on the figure. In order to return the net magnetization to zero, it is necessary to apply a field in the opposite direction. The field that will reduce the net magnetization to zero is known as the coercive field, H_c. The figure is taken from [92, p. 20]. (b) Hysteresis loops for soft and hard magnetic materials, taken from [93, p. 280]. The figure is somewhat misleading; soft magnetic materials usually have larger saturation magnetizations than hard magnetic materials, and the coercive fields of hard magnetic materials is usually several orders of magnitude larger than that of soft magnetic materials.

field, H_c, we mean the intrinsic coercive field, i.e. the H-field inside the material, when the magnetization of the material is zero.

Ferromagnetic materials are often divided into (at least) two classes; soft and hard magnetic materials, where the soft magnetic materials have a small hysteresis loop, i.e., H_c is small, and they are easy to magnetize. Hard magnetic materials have a large hysteresis loop with large H_c. Fig. 2.1(b) shows hysteresis loops for soft and hard magnetic materials. Permanent magnets are made of hard magnetic materials. The difference between hard and soft magnetic materials on a microscopic level is the ease with which domain walls move inside the material. In soft materials domain walls move easily, and such materials are thus easily magnetized and demagnetized and has little or no hysteresis. In hard materials it takes a lot of energy to move the domain walls, and it is therefore hard to change the magnetization of a hard magnetic material.

2.1.1 Magnetic susceptibility and the demagnetization field

Magnetic susceptibility, χ, is the ratio between $\mathbf{H}$ and $\mathbf{M}$, such that $\mathbf{M} = \chi\mathbf{H}$. However, as we have seen in Fig. 2.1 the relation between $\mathbf{H}$ and $\mathbf{M}$ is certainly not linear. In fact χ is in general a hysteretic tensor that depends on $\mathbf{H}$ and the history of $\mathbf{H}$, and $\mathbf{M}$ can also be non-zero in the absence of $\mathbf{H}$. Clearly, $\mathbf{M}(\mathbf{H})$ is a complicated function, and the

meaning of the term, magnetic susceptibility, can be unclear if not properly specified.

In this project, we are mainly working with soft magnetic materials and superparamagnetic materials, and for such materials, it is a reasonable approximation to say that they are hysteresis free, and that the magnetization is always parallel to $\mathbf{H}$. This means that we can write $\mathbf{M} = \chi(\mathbf{H})\mathbf{H}$, where $\chi(\mathbf{H})$ is now a non-hysteretic scalar function. In this case χ is relatively well-defined, but still further clarifications are needed.

The χ mentioned above is the 'intrinsic magnetic susceptibility', χ_i. This is the ratio of the local magnetization and the local magnetic field inside the magnetic material. However, this is not what is usually measured. It is common to measure χ by applying a homogenous magnetic field, H_a, on a piece of magnetic material, and then measure the dipole field that is generated around the material, which is a direct measure of the magnetization of the material. This means that one measures the magnetization as a function of the applied field, and one thus defines the 'measured magnetic susceptibility' as $\chi_m = M/H_a$.

The intrinsic and measured susceptibilities are connected through the demagnetization factor and the demagnetization field. When a piece of magnetic material is magnetized, a demagnetization field, $\mathbf{H}_d$, arises. This field is $\mathbf{H}_d = -\overleftrightarrow{\mathbf{N}} \cdot \mathbf{M}$, where $\overleftrightarrow{\mathbf{N}}$ is the demagnetization factor, which is in general a tensor field that depends on the geometry. $\overleftrightarrow{\mathbf{N}}$ is required to have $\mathrm{Tr}\big(\overleftrightarrow{\mathbf{N}}\big) = N_{xx} + N_{yy} + N_{zz} = 1$. In many geometries, it is a good approximation to say that $\overleftrightarrow{\mathbf{N}}$ has non-zero elements only on the diagonal, and that these are constant [92, Chap. 2.3].

The $\mathbf{H}$-field inside a piece of magnetic material, $\mathbf{H}_i$ is the sum of the applied field, and the demagnetization field, $\mathbf{H}_i = \mathbf{H}_a + \mathbf{H}_d$, and $\chi_i = M/H_i$ whereas $\chi_m = M/H_a$. From this, we find (we have switched to scalar quantities for simplicity, and N represents the appropriate component of $\overleftrightarrow{\mathbf{N}}$)

$$\chi_m = \frac{M}{H_a} = \frac{\chi_i H_i}{H_a} = \frac{\chi_i(H_a - N\chi_m H_a)}{H_a} \Leftrightarrow \chi_m = \frac{\chi_i}{1 + N\chi_i}. \tag{2.1}$$

It is important to notice that $\chi_m < 1/N$. This is especially noticeable for a sphere that has $N_{xx} = N_{yy} = N_{zz} = 1/3$, such that a spherical magnetic bead will always have $\chi_m < 3$ regardless of the intrinsic susceptibility of the material.

Furthermore, the initial susceptibility, χ_0, is defined as

$$\chi_0 \equiv \frac{\partial M}{\partial H}\,|_{H=0}\,. \tag{2.2}$$

Notice that the initial magnetization can be both intrinsic and measured.

2.1.2 Soft magnetic materials

In this project, soft magnetic materials have been used extensively. In my master's thesis and the early Ph.D. work, soft magnetic material was used as magnetic yokes on the on-chip electromagnets [1, 2, 10], but the primary use of soft magnetic materials has been as on-chip magnetic flux guides that create strong magnetic field gradients, when an external magnetic field is applied. For this we need a material that is easy to magnetize, i.e. that has a high χ_0, has a high saturation magnetization and a small hysteresis loop with

a low coercive field and remanent magnetization. Low mechanical stress is also a key requirement.

Three types of low-stress electroplated soft magnetic thin films are available in our electroplating facility: nickel (Ni), the nickel-iron alloy permalloy ($Ni_{80}Fe_{20}$, Py), and the cobalt-nickel-iron alloy (CoNiFe). Some of the properties of the available baths are described by F.E. Rasmussen *et al.* [96] and by P.T. Tang [97]. More recently Korsbæk and Rubæk made a thorough characterization of the Py and CoNiFe baths [98]. The different studies do not agree completely on the magnetic properties of the electroplated materials, but they do agree that CoNiFe has a higher saturation magnetization than permalloy ($M_{s,\mathrm{CoNiFe}} \approx 1.8$ T and $M_{s,\mathrm{Py}} \approx 1.2$ T), where it should be mentioned that the plating baths are not identical in the two studies. The two studies do not agree on the coercive field, but they do agree that the coercive field of Py is lower than that of CoNiFe. The coercive fields are in the range of a few hundreds A/m. The electroplated nickel has low mechanical stress, and thus it is practical for mechanically fragile structures such as the microfabricated electromagnets. For this reason, we have used nickel for some of the early work, but as shown in [2, Fig. 3], the saturation magnetization is only approximately 0.6 T and the coercive field is as much as 3 kA/m.

Although CoNiFe is clearly the best material in terms of saturation magnetization, we have chosen to work with permalloy in this work. Permalloy has lower coercivity, lower stress, and most importantly it is easier to work with. We have demonstrated the long term stability of the permalloy bath [7], and it is easy to get reproducible results with a two-component alloy plating bath compared to a three-component alloy plating bath. As we will see in chapter 3, the effect of increasing the saturation magnetization from 1.2 T to 1.8 T is an increase in the magnetic force by the opposite ratio, $1.8/1.2 = 1.5$, but we expect the increase in fabrication problems to be more than 50 %, if we try to use the CoNiFe electrolyte, which is why, it was ultimately chosen to work with permalloy.

2.1.3 Magnetic beads

When the size of a particle of ferromagnetic material is reduced to approximately 50-20 nm in diameter, the particle diameter becomes comparable to typical domain wall thicknesses [28], and furthermore, it is no longer energetically favorable to sustain a domain wall, and the particles become single domain particles, that is, all atomic moments in the particle are aligned. The magnetic material will usually have an easy axis of magnetization, and it is energetically favorable that the magnetization is parallel to this axis. There is an energy barrier for switching between the two directions that are parallel. This barrier depends on particle size, so if the particle diameter is further reduced to approximately 10-20 nm; this energy barrier becomes comparable to the thermal energy, kT, where k is the Boltzmann constant, and T is the absolute temperature, and the magnetization switches randomly inside the particle - such particles are called superparamagnetic particles.

If one averages over an ensemble of superparamagnetic particles in the absence of a magnetic field, zero net magnetization is obtained. However, if a magnetic field is applied, it becomes energetically favorable for the magnetic moments of the particles to align with the field, and the average magnetization rises in the direction of the field.

It can be shown that the average magnetization of a volume, V, that contains an ensemble of N_p non-interacting superparamagnetic particles in thermodynamic equilibrium is

$$\mathbf{M}(\mathbf{H}) = M_{s,\mathrm{p}} \frac{N_\mathrm{p} V_\mathrm{p}}{V} \mathcal{L}\left(\frac{V_\mathrm{p} M_{s,\mathrm{p}}\, \mu_0 H}{kT}\right) \frac{\mathbf{H}}{H}, \tag{2.3}$$
$$\mathcal{L}(x) = \coth(x) - \frac{1}{x},$$

where V_p is the volume of an individual particle, $M_{s,\mathrm{p}}$ is the (saturation) magnetization of an individual particle, and $\mathcal{L}(x)$ is the Langevin function. Fig. 2.3 shows the functional form Langevin function.

Magnetic beads are superparamagnetic particles enclosed in a polymer matrix of spherical shape, which means that magnetic beads can be described as ensembles of superparamagnetic particles. In order to use Eq. (2.3), all we need to do is put in that the ensemble volume, V, is the volume of a magnetic bead.

Now that we know the theory behind magnetic beads, we can discuss the beads that have actually been used for this project. A great variety of different magnetic beads are commercially available (cf. [22]), but for this project, two types of magnetic beads were the primary choices, although others have been used also.

MyOne beads from Invitrogen

The properties of the MyOne magnetic bead from Invitrogen is well-documented, and in our group it has more or less been viewed as the industry standard, and it is the benchmark bead in this project.

The MyOne magnetic beads exist with many different surface coatings. We have mainly used the cheapest ones that have a carboxylic acid coating, but for experiments involving biology, we have used the ones with streptavidin coating.

Geir Fonnum *et al.* made a very thorough characterization of the MyOne, M-280, and M-450 beads [99], and since the data from this paper will be used extensively, the most important data are re-stated in Table 2.1 for the MyOne beads.

Table 2.1: Physical properties of the MyOne magnetic bead from Invitrogen [99, Table 1]

Diameter	Standard deviation on diameter	Mass density	χ_m	M_s
1.05 μm	0.02 μm	$1.7 \cdot 10^3 \mathrm{kg/m^3}$	1.4	40.0 kA/m

We have also measured the magnetization curve for MyOne magnetic beads. Fig. 2.2 shows the result of this measurement.

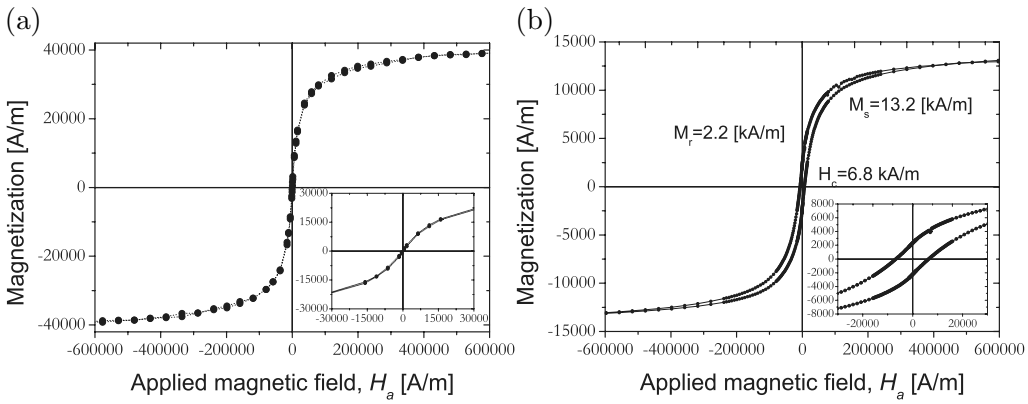

Figure 2.2: (a) The magnetization curve for Dynabead MyOne beads. The curve produced by taking a measuring the magnetic moment of a small but unknown bead volume, and fitting the saturation magnetization to the one given in Table 2.1. (b) The Magnetization curve for Spherotech FCM1052-2. The beads have a diameter of 1.0-1.4 μm. This curve was produced by measuring the magnetic moment of a known bead volume.

Beads from Spherotech

The magnetic beads from Invitrogen have worked very well for the purposes of this project, but they are not available as fluorescent beads. It is possible to bind a fluorochrome to the surface of the beads such that they will show fluorescence. However, this fluorescence have proven to be insufficient for the fluorescence experiments in this project.

Therefore, we have chosen to work with Spherotech fluorescent magnetic beads. Fig. 2.2 shows the magnetization curve for Spherotech FCM1052-2 beads[1] that have a diameter of 1.0-1.4 μm according to the manufacturer. The fluorescence of the beads clearly comes at a price; the saturation magnetization is only one third of the saturation magnetization of MyOne beads, and the Spherotech beads also exhibit a substantial hysteresis. The lower saturation magnetization translates directly into lower force applied in the same magnetic gradient field, as we will see in Chap. 3.

Since the Spherotech FCM1052-2 beads have been used extensively, their data is collected in Table 2.2.

Table 2.2: Physical properties of the Spherotech FCM1052-2 magnetic bead. The magnetic data was extracted from Fig. 2.2, the other data was taken from the Spherotech data sheet.

Diameter	Mass density	χ_m	M_s
1.0-1.4 μm	$1.58 \cdot 10^3$kg/m^3	0.4	13.2 kA/m

[1]This graph was also featured in [4]

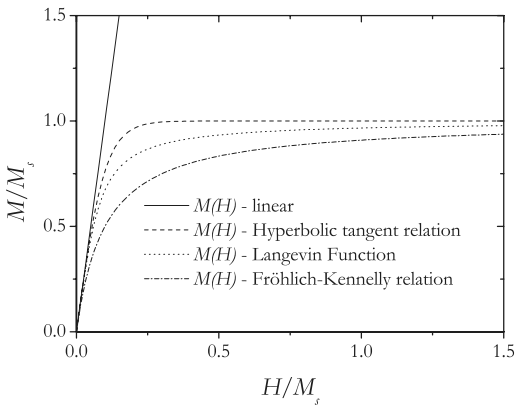

Figure 2.3: M vs H for different approximations to the magnetic susceptibility. $\chi_0 = 10$ in all functions. All functions for $\chi(H)$ are even functions of H such that $\chi(H)H$ is an odd function of H.

2.1.4 Mathematical description of magnetic materials

We have seen that in general, $\chi(\mathbf{H})$ of a magnetic material is a complicated non-single-valued tensor-function, so for simulations, we have to make some approximations. We stated earlier that it is reasonable to assume that for most of the materials in this thesis χ is a single-valued scalar function, and we simply choose a function that emulates the real magnetization curve.

There are two requirements that such a function must fulfill.

1. $\frac{\partial \chi(H)}{\partial H}\Big|_{H=0} = \chi_0$
2. $\chi(H)H \to M_s$ as $H \to \infty$

Magnetic bead suppliers rarely supply full magnetization curves, but sometimes χ_0 and M_s are available.

Below we state three functions that all fulfill the requirements, and they are preceded by the simple 'χ is constant' approximation.

$$\chi(H) = \chi_0, \tag{2.4a}$$

$$\chi(H) = \frac{M_s}{|H|} \tanh\left(\frac{\chi_0 |H|}{M_s}\right), \tag{2.4b}$$

$$\chi(H) = \frac{M_s}{|H|} \mathcal{L}\left(\frac{3\chi_0 |H|}{M_s}\right), \tag{2.4c}$$

$$\chi(H) = \frac{\chi_0 M_s}{M_s + \chi_0 |H|}. \tag{2.4d}$$

Fig. 2.3 shows M vs H for these different equations.

Eqs. (2.4) may seem a bit coincidental, but they each have a place in literature of magnetic materials. Eq. (2.4a) is just a very simple but bad approximation that is featured in many textbooks, Eq. (2.4b) is the magnetization for a paramagnetic spin $\frac{1}{2}$ system[2] [100, p. 25], Eq. (2.4c) is the Langevin function that are relevant for superparamagnetic materials, and Eq. (2.4d) is the empirical Fröhlich-Kennelly relation [101, pp. 115-117].

It is not certain that any measured magnetization curve will actually fit any of these functions, so if one wants to make very good approximation to actual magnetization curves, then it may be useful to make a linear combination of Eqs. (2.4b), (2.4c), (2.4d) to best fit the data. Eq. (2.4d) seems to be the one of the three that best fit the data in Fig. 2.2(a) and (b).

It has only been necessary to describe hard magnetic materials on very few occasions, and it has been found that it is sufficient just to set a constant remanent magnetization, and then define a χ, usually from Eq. (2.4a) that describes the small change in magnetization, when $H \neq 0$.

2.2 Substrate materials

Most of the systems in this thesis have been fabricated on silicon substrates. This was chosen, since very good silicon microfabrication facilities and experience are available at MIC - Department of Micro and Nanotechnology and DANCHIP at the Technical University of Denmark. Microsystems fabricated in silicon has the advantage that they can be fabricated with minute tolerances (compared to the typical size of a microsystem used in this project), so we can compare the performances of different designs with little uncertainty in the fabrication process.

At the Technological Institute of Denmark, they are experts on polymer micromachining, and since polymer fabrication is both cheaper and faster than silicon fabrication, it was the intention also to fabricate polymer microsystems. It is, however, not straightforward to deposit metallic films on polymers, so in the end, it was chosen to limit this to fabrication of fluid channels in polymers and then integrate these with magnetic structures fabricated in other materials.

2.3 Other materials

It has been chosen to seal the silicon microfluidic systems with borofloat glass (pyrex) lids. This is due to the very good anodic bonding mechanism that is available with pyrex and silicon.

Electroplated copper has been used for making on-chip current wires for generating magnetic fields on chip without magnetic structures.

[2] Admittedly this is not a strong argument to feature the function here, but it is useful nonetheless.

Chapter 3

Theory

In this chapter a model is developed for the movement of magnetic beads in a microfluidic channel flow under the influence of a magnetic field.

3.1 Governing equations

In the present thesis magnetostatics only are considered, such that the Maxwell equations reduce to [102, 103],

$$\boldsymbol{\nabla} \cdot \mathbf{B} = 0, \tag{3.1a}$$

$$\boldsymbol{\nabla} \times \mathbf{H} = \mathbf{J}^f. \tag{3.1b}$$

In addition, the material constitutive relation that relates $\mathbf{B}$, $\mathbf{H}$ and $\mathbf{M}$ is [102, 103]

$$\mathbf{B} = \mu_0 \left(\mathbf{H} + \mathbf{M}(\mathbf{H}) \right). \tag{3.2}$$

The relations between $\mathbf{H}$, and $\mathbf{M}$ were discussed in Chapter 2.

In this project it has often been the case that $\mathbf{J}^f = \mathbf{0}$. In this case Eq. (3.1b) shows that $\mathbf{H}$ is curl-free and thus can be written as the gradient of a magnetic scalar potential, $\mathbf{H} = -\boldsymbol{\nabla}\varphi$. Inserting this into Eqs. (3.1a) and (3.2) yields

$$\mu_0 \boldsymbol{\nabla} \cdot \Big(-\boldsymbol{\nabla}\varphi + \mathbf{M}\big(-\boldsymbol{\nabla}\varphi \big) \Big) = 0, \tag{3.3}$$

which is a non-linear partial differential equation for the magnetic scalar potential, φ. [102, 103] Eq. (3.3) is a great simplification for numerical calculations, since we only need to solve for a scalar potential and not for all the three components of the magnetic vector potential or the magnetic field itself. [104]

If $\mathbf{J}^f \neq \mathbf{0}$, we need to solve for the magnetic vector potential, $\mathbf{A}$, defined such that $\mathbf{B} = \boldsymbol{\nabla} \times \mathbf{A}$ and $\boldsymbol{\nabla} \cdot \mathbf{A} = 0$, and it can be shown that $\nabla^2 \mathbf{A} = -\mu_0 \big(\mathbf{J}^f + \boldsymbol{\nabla} \times \mathbf{M} \big)$ [102]. In three dimensions this is computationally memory and time demanding, since all three components of the vector potential must be found. However, the symmetry of a problem

sometimes allows for a simplification of the problem and a reduction of the number of components of $\mathbf{A}$ that need to be found numerically. [104] This was the case in papers [2, 5] of this thesis.

The governing equations for the steady fluid flow in the microfluidic systems is the time-independent Navier-Stokes equations with no body forces and the continuity equation for an incompressible fluid in dimensionless form [105, p. 46],

$$\mathcal{R}(\widetilde{\mathbf{u}} \cdot \widetilde{\boldsymbol{\nabla}})\widetilde{\mathbf{u}} = -\widetilde{\boldsymbol{\nabla}}\widetilde{p} + \widetilde{\nabla}^2\widetilde{\mathbf{u}}, \tag{3.4a}$$

$$\widetilde{\boldsymbol{\nabla}} \cdot \widetilde{\mathbf{u}} = 0, \tag{3.4b}$$

where the Reynolds number, $\mathcal{R}$, is defined as, $\mathcal{R} = \rho u L \eta^{-1}$, where L is the characteristic length scale for the variation in the fluid velocity - usually the channel height. For microfluidic systems $\mathcal{R}$ is usually low. Characteristic numbers might be (water) $\rho = 10^3$ kg m^{-3}, $u = 10^{-2}$ m s^{-1}, $L = 10^{-4}$ m, and $\eta = 10^{-3}$ Pa s, which yields $\mathcal{R} = 1$. A Reynolds number of order 1 ensures that the flow will be laminar everywhere in microfluidic channels, but it is not low enough that we can completely discard the non-linear term in Eq. (3.4a). However, we study steady flow in straight rectangular channels with no body forces almost exclusively, such that $(\widetilde{\mathbf{u}} \cdot \widetilde{\boldsymbol{\nabla}})\widetilde{\mathbf{u}} = 0$, so in most cases Eqs. (3.4) reduce to

$$\mathbf{0} = -\widetilde{\boldsymbol{\nabla}}\widetilde{p} + \widetilde{\nabla}^2\widetilde{\mathbf{u}}, \tag{3.5a}$$

$$\widetilde{\boldsymbol{\nabla}} \cdot \widetilde{\mathbf{u}} = 0. \tag{3.5b}$$

In this case it is possible to calculate the flow field analytically, as shown in paper [2] of this thesis. This fluid flow field has been used for all simulations of bead trajectories in the present thesis.

3.2 Forces on a magnetic bead

In this section we study the most important forces on a magnetic bead moving in a microfluidic channel. This includes gravity, magnetic force and fluid drag. The magnitudes of these forces will be estimated using a MyOne magnetic bead as example.

3.2.1 Gravity

The simplest force on a magnetic bead is the gravity or buoyancy force.

$$\mathbf{F}_{\text{buoyancy}} = V_{\text{bead}}(\rho_{\text{bead}} - \rho_{\text{fluid}})\mathbf{g}, \tag{3.6}$$

where $V_{\text{bead}} = \frac{4}{3}\pi R_{\text{bead}}^3$ is the volume of the magnetic bead, R_{bead} is the radius of the bead, ρ_{bead} is the mass density of the bead, and ρ_{fluid} is the mass density of the surrounding fluid. For future reference, we note that for a MyOne magnetic bead in water this force is 4.2 fN.

3.2.2 Magnetic force

Despite the fact that all the basic expressions for calculation of magnetic fields and magnetic forces on magnetizable objects have been available for centuries, there is still surprisingly large confusion about these subjects in literature (see for example refs. [106, 107, 108]).

Engel and Friedrichs set the record straight in ref. [109], where the electromagnetic force on polarizable and magnetizable objects in analytically solvable situations is calculated, showing that one obtains the same result using several different force expressions, if they are applied correctly.

For most of the calculations in this thesis we adopt Eq. (3) in [109] which also agrees with Landau, Lifshitz, and Pitaevskii [110].

$$\mathbf{F}_{\text{mag}} = \mu_0 \int_{V_{\text{bead}}} (\mathbf{M} \cdot \boldsymbol{\nabla}) \mathbf{H}_0 dv, \tag{3.7}$$

where the integral is taken over the volume of the magnetic bead, and $\mathbf{H}_0$ denotes the field that would be present in the absence of the bead.

In this thesis, it is almost always used that the length scale of the magnetic field gradient is much larger than the diameter of the magnetic bead, such that the integrand can be considered constant over the volume of the bead. We get

$$\mathbf{F}_{\text{mag}} \approx \mu_0 V_{\text{bead}} (\mathbf{M} \cdot \boldsymbol{\nabla}) \mathbf{H}_0 = V_{\text{bead}} M(H_0) \mathbf{G}, \tag{3.8}$$

where we see that the magnetic force is the magnitude of the magnetic moment of a magnetic bead times the effective magnetic field gradient, $\mathbf{G}$, defined as

$$\mathbf{G} \equiv \mu_0 \left(\frac{\mathbf{H}_0}{H_0} \cdot \boldsymbol{\nabla} \right) \mathbf{H}_0. \tag{3.9}$$

$\mathbf{G}$ has the unit T/m, and is independent of the specific bead type. $\mathbf{G}$ is thus a good measure for comparing different systems.

There are two important limits of Eq. (3.8). The first limit is the low-field limit, where the magnetic susceptibility can be considered constant, such that $\mathbf{M} = \chi_m \mathbf{H}_0$. In this limit, we get

$$\mathbf{F}_{\text{mag}} \approx V_{\text{bead}} \chi_m H_0 \mathbf{G} = \frac{1}{2} \mu_0 V_{\text{bead}} \chi_m \boldsymbol{\nabla} H_0^2, \tag{3.10}$$

where it has been used that $\mathbf{H}$ is curl-free inside the bead. This limit is not relevant for most of the work in this thesis, but it is relevant for some of the early work including papers [1, 2, 10] and my master's thesis [11], where on-chip electromagnets supplied the magnetic field, and as we saw in Chap. 1 such fields are small compared to the fields necessary for magnetic bead saturation.

The other limit is the high-field limit, where the magnetization of the magnetic bead has attained its saturation value, $M(H_0) = M_{s,\text{bead}}$,

$$\mathbf{F}_{\text{mag}} \approx V_{\text{bead}} M_{s,\text{bead}} \mathbf{G}, \tag{3.11}$$

where it is seen that the magnetic force on a magnetic bead is the saturation magnetic moment of the bead times the magnetic field gradient. Most of the systems in the present thesis have forces at or close to the high-field limit.

Eq. (3.8) is useful for numerical calculations since it only requires calculation of the magnetic field in the absence of the bead. With that, it is easy to calculate the average magnetization of the bead.

Before moving on, it is useful to estimate the magnetic force on a MyOne magnetic bead using Eq. (3.11). If it is assumed that magnetically saturated permalloy $M_{s,\mathrm{Py}}$ structures generate magnetic field gradients that have a characteristic length scale (set by the gap between the elements) of $L = 100$ μm, the force is estimated as $F \approx \mu_0 V_{\mathrm{bead}} M_{s,\mathrm{bead}} M_{s,\mathrm{Py}} L^{-1} \approx 0.3$ nN, which is approximately five orders of magnitude more than gravity on the same bead. This crude estimate shows that magnetic beads may be very efficiently separated from non-magnetic beads with the same density.

Since the beginning of the Ph.D. work, it has been a nuisance to the author that we assume that the integrand in Eq. (3.7) is constant, since this requires that the magnetization is constant, but still a field gradient needs to be present. These two requirements seem to exclude each other. In Appendix A I calculate analytically the field around a magnetic bead and the force on a magnetic bead in an applied gradient field. It is shown that to first order only the average magnetization of the bead enters the force calculation. It is also shown how to move to higher orders.

If the structures that generate the magnetic field are small enough that they are comparable in size to the magnetic bead, Eq. (3.8) is still valid to first order, but higher orders may be needed, and then the full calculation of Eq. (3.7) is impractical, since it requires calculation of the field both when the bead is present, and when it is not present. This was the case in the magnetic valve paper [6], where the magnetic field gradient was created by a gap that had a size comparable to the diameter of a magnetic bead. In such cases other strategies are needed for calculation of the magnetic forces. One good strategy is the use of the Maxwell stress tensor or the more general electromagnetic stress tensor. Several versions of this stress tensor exist in literature. In Appendix B the different versions of the tensor and their applicability are discussed.

3.2.3 Fluid drag

The magnetic beads are moving in a fluid flow, and thus the fluid exerts a force on the beads. Throughout this thesis, it will be assumed that this force is the stokes drag

$$\mathbf{F}_{\mathrm{drag}} = 6\pi R_{\mathrm{bead}} \eta (\mathbf{u} - \mathbf{v}). \tag{3.12}$$

The drag force on a MyOne magnetic bead held still in water flowing at 1 cm/s is 0.1 nN which is comparable to the magnetic force estimate, but fortunately we do not attempt to stop the beads in the middle of the fluid flow, but rather near the walls, where fluid flow is slower. Still, this shows that the magnetic forces do not completely dominate the movement of magnetic beads, fluid drag cannot be discarded, whereas gravity is rarely important.

3.2.4 Newton's 2nd law

At this point, the equation of motion for a single bead can be written using Newton's 2nd law

$$\rho_{\text{bead}} V_{\text{bead}} \partial_t \mathbf{v} = 6\pi R_{\text{bead}} \eta(\mathbf{u} - \mathbf{v}) + \mathbf{F}_{\text{mag}} + (\rho_{\text{bead}} - \rho_{\text{fluid}}) V_{\text{bead}} \boldsymbol{g}. \tag{3.13}$$

If we assume for a moment that the magnetic force, $\mathbf{F}_{\text{mag}}$ is constant, then this differential equation for $\mathbf{v}$ has the solution

$$\mathbf{v}(t) = \mathbf{v}_{\text{t}} + (\mathbf{v}_0 - \mathbf{v}_{\text{t}}) \exp\left(-\frac{t}{\tau}\right), \tag{3.14a}$$

$$\mathbf{v}_{\text{t}} = \frac{\mathbf{F}_{\text{mag}} + (\rho_{\text{bead}} - \rho_{\text{fluid}}) V_{\text{bead}} \mathbf{g}}{6\pi\eta R_{\text{bead}}} + \mathbf{u}, \tag{3.14b}$$

$$\tau = \frac{2\rho_{\text{bead}} R_{\text{bead}}^2}{9\eta}, \tag{3.14c}$$

where $\mathbf{v}_{\text{t}}$ is the terminal velocity that the velocity, $\mathbf{v}(t)$, will tend to on the timescale τ, and $\mathbf{v}_0$ is the initial velocity vector, $\mathbf{v}_0 = \mathbf{v}(t = 0)$. Inserting the data for a MyOne magnetic bead and water yields that $\tau \approx 0.1\,\mu$s, which means that even if a bead is moving with 1 m/s, it will not move a full bead diameter before reaching the terminal velocity. Since the magnetic force field is constant in time, and does not change much on the scale of single microns, it is safe to assume that the bead is always moving with the terminal velocity.

Finally, we can write the relevant equation of motion for a magnetic bead moving in a fluid flow,

$$\partial_t \mathbf{x} = \mathbf{u} + \frac{2R_{\text{bead}}^2 M(H_0)}{9\eta} \mathbf{G} + \left(\frac{2R_{\text{bead}}^2 (\rho_{\text{bead}} - \rho_{\text{fluid}})}{9\eta} \mathbf{g}\right), \tag{3.15}$$

where it is seen that the relevant measure for comparing the ease of capturing different types of magnetic beads is $R_{\text{bead}}^2 M(H_0)$, and it has been indicated that in many situations, gravity can be neglected.

In Appendix C I have included some useful calculations of separation dynamics of single beads affected by a constant force flowing in a parabolic fluid flow. This is useful, because microfluidics will often feature wide channels with near-parabolic flow and even if magnetic forces are almost never constant - estimates made with the lower limit or the average force in some domain may still be very useful and certainly faster than the full numeric calculations.

In the treatment so far, the random thermal motion of particles has been neglected. Friedman and Yellen give an elaborate discussion of the validity of this assumption [111]. A simple criterion is the comparison of the magnetic work required to move a magnetic bead or particle one diameter and the thermal energy. The buoyancy force on a MyOne magnetic bead is ≈ 4.2 fN, and as it turns out the work done by gravity to move a MyOne bead one bead diameter is 4.2×10^{-21} J, whereas thermal energy at room temperature is

4.1×10^{-21} J, so only if magnetic force is much larger than gravity, it is safe to assume that random motion can be completely neglected. However, since gravity is on the same scale as random motion, it is reasonable to believe that movement of magnetic beads will on average be dominated by gravity, when no magnetic forces are present. Most forces in this project has been orders of magnitude larger than gravity, and in these cases it is completely valid to neglect thermal motion. In case thermal motion is dominating, one needs to use a different approach to calculate bead motion. This approach is based on the convection-diffusion equation coupled with the navier-stokes equations, such as it is described in the paper by Friedman and Yellen [111].

3.3 Scaling laws for the magnetic equations

It is sometimes useful to make the equations non-dimensional, especially for optimization studies. Early in the 20th century Buckingham [112] and Rayleigh [113] stressed the importance of dimensional analysis in engineering problems. They showed how to determine the minimum number of independent non-dimensional parameters for a given problem, and also how this could in some cases be used to determine the functional relations between parameters.

In the case of magnetic beads moving in fluid flow in magnetic fields, all that is needed is the magnetic field in the absence of magnetic beads, $\mathbf{H}_0$ and in turn the magnetic field gradient, $\mathbf{G}$. In such a calculation there are only two characteristic magnetic measures; the saturation magnetization of the magnetic structures, M_s, and the applied magnetic field, H_a, that magnetizes the structures. The non-dimensional magnetic field is introduced as $\widetilde{\mathbf{H}} \equiv \mathbf{H}/M_s$, and this leaves only one non-dimensional parameter for the calculations, $\xi = H_a/M_s$.

Furthermore, a characteristic length scale, ℓ, must be introduced. This yields a new coordinate system, where the new coordinates are are related to the old by $\widetilde{\mathbf{x}} = \ell^{-1}\mathbf{x}$, and $\widetilde{\boldsymbol{\nabla}} = \ell\boldsymbol{\nabla}$. It is required that $\widetilde{\mathbf{H}}(\widetilde{\mathbf{x}}) = M_s^{-1}\mathbf{H}(\mathbf{x})$, and thus the scalar potential must be chosen as $\widetilde{\varphi}(\widetilde{\mathbf{x}}) = \ell^{-1}M_s^{-1}\varphi(\mathbf{x})$. It is easily seen that Eq. (3.3) becomes

$$\widetilde{\boldsymbol{\nabla}} \cdot \big(-\widetilde{\boldsymbol{\nabla}}\widetilde{\varphi} + \widetilde{\mathbf{M}}(-\widetilde{\boldsymbol{\nabla}}\widetilde{\varphi})\big) = 0, \tag{3.16}$$

where $\widetilde{\mathbf{M}} = \mathbf{M}/M_s$, and it is seen that the differential equation does not change its form.

Finally, the dimensionless effective field gradient is introduced as

$$\widetilde{\mathbf{G}} \equiv \frac{\ell}{\mu_0 M_s}\mathbf{G}. \tag{3.17}$$

There are two important features of Eq. (3.17); $\mathbf{G}$ scales linearly with M_s (if ξ is kept constant), and $\mathbf{G}$ is inversely proportional to ℓ, such that the smaller structures that generate the gradients, the larger forces are obtained, and this is just another good reason to do magnetic separation in microsystems. So far, the nature of ℓ has not been discussed, but in most microfabrication there will be one length scale that is limited by the fabrication process, and it would be natural to choose this length scale as ℓ. For example

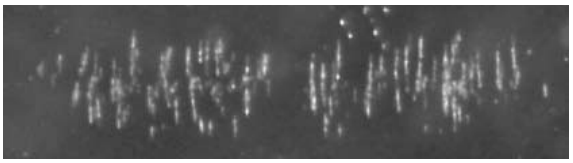

Figure 3.1: Collection of captured magnetic beads (Yellowish) on the bottom of a microfluidic channel (Dark blue). The beads are clearly captured in lines that are aligned with the magnetic field that is applied in the plane of the picture from the top to the bottom. The image has an approximate height of 0.19 mm.

the distance between magnetic structures and the microfluidic channel should always be as small as possible but is limited by the fabrication process.

The advantage of using this scaling is getting one less magnetic parameter and one less geometric parameter to optimize, when optimizing the geometry of magnetic structures, and also, it is possible to compare different fabrication methods that will often have different limiting length scales without making new calculations - simply change the prefactor in Eq. (3.17). This will be utilized in Chap. 4.

3.4 Discussion

In this chapter, the theory for a magnetic bead moving in a microfluidic channel under the influence of a magnetic field has been developed.

During such a theory discussion some effects are always neglected, and it is important to keep these effects in mind. Many effects have been neglected in this treatment of separation of magnetic beads in a microflow, but most of these do not apply to this situation; for instance quantum mechanical and relativistic effects do not apply. However, there are still effects that have been omitted from this treatment that would be important, if one were to make a complete description of magnetic separation in microfluidic channels.

The most important neglected features are bead-bead and bead-wall interactions. The calculations of bead trajectories in the present thesis are all made using the assumption that the fluid force on the beads is Stoke's drag, and that the fluid velocity field is completely unchanged by the flow of beads. Also, the magnetic force is calculated for one bead and the disturbance of the magnetic field due to the presence of other beads is completely neglected. This is a major simplification for the calculation, but it is also invalid at least when the concentration of beads in the fluid is large. When magnetic beads are in a magnetic field each bead generates a dipole field, and when the beads get close they feel the dipole field of each other, and they are therefore attracted to each other and align their dipole moments, and thus they will start to move as small chains of beads aligned with the magnetic field. Fig. 3.1 shows beads captured on a channel bottom, and how they are aligned in chains directed by the magnetic field.

Christian Mikkelsen showed how to treat these magnetic and fluidic interactions in his Ph.D. work [114], and he showed that fluidic interactions (arising from the disturbance of the flow field, when a bead is dragged through a fluid) are more important for capture

dynamics than magnetic interactions.

When a sphere is pulled by a force towards a wall Stoke's drag no longer applies as the fluid force. The assumption of Stoke's drag requires that the fluid extends infinitely on all sides of the bead, and also that the Reynolds number is much smaller than 1. The latter requirement is usually fulfilled, since the length scale in the Reynolds number is now the bead diameter, and thus we get a Reynolds number of order 10^{-2} using the same numbers as before. However, as the beads approach the channel walls the first assumption is clearly invalidated[1]. This was described by H. Brenner [115] in 1961 (and possibly earlier by others), and it is still an active topic of research, see for example Lecoq *et al.* [116] from 2004, but not the topic of this thesis, so we choose to use the simple approximation of Stoke's drag.

Furthermore, any forces related to the bead surfaces and their chemistry are neglected. For instance, when a bead is suspended in a fluid, it is expected to attain a surface charge, and thus an electrostatic repulsion force between beads must be expected, and also there may be electrostatic repulsion or attraction between beads and the channel walls. This is also neglected.

When calculating single bead trajectories it is assumed that the beads stick as soon as they hit the surface. This neglects any effects related to pile-up of beads including magnetic screening and changes in the fluid flow, and also rolling of beads at the channel walls.

Finally, some effects related to the magnetization of the magnetic materials are neglected. The small but finite superparamagnetic relaxation time is ignored, so it is assumed that the magnetization of the magnetic beads is always parallel to the applied field. It is also assumed that both soft magnetic materials and superparamagnetic beads are both hysteresis free.

With all these assumptions and omissions one might wonder, if there is any chance of describing the flow of magnetic beads in a microfluidic channel, and the answer is: Yes, it seems that the descriptions given by Eqs. (3.1) through (3.15) yield a good description of most of the phenomena seen in experimental magnetic separation in microfluidic channels. At least, we found good agreement between experiments and theory in paper [2] of this thesis, and Lund-Olesen *et al.* finds good agreement between experiments and simulations using the same equations [77].

[1] In the magnetic valve paper [6] the bead was furthermore in a narrow gap, and Stoke's drag clearly did not apply in that case.

Chapter 4

Numerics and Design

Numerical analysis has been used extensively for the work in this thesis. Magnetic fields and field gradients have been calculated using the finite element method in Comsol Multiphysics [104], and designs have been optimized using that same program in combination with Matlab [117]. Bead trajectories have been evaluated numerically using Mathematica [118]. Comsol Multiphysics and Mathematica were used for paper [2] of this thesis, and Comsol Multiphysics with Matlab was used for the calculations in papers [6, 8] of this thesis. Furthermore Comsol multiphysics has been used in the design phases for papers [3, 4, 5].

This chapter discusses how the finite element method has been applied for optimization of geometric structures for generation of magnetic field gradients.

Whenever one makes numerical calculation one should always have a desired accuracy in mind on beforehand. Numerical calculations are never exact, and increasing accuracy equals increasing memory consumption, and increasing calculation times.

4.1 The Finite Element Method in Comsol Multiphysics

The Finite Element Method (FEM), sometimes also known as Finite Element Analysis (FEA), has been used extensively in the course of this project. All designs, except the first ones, have been optimized using this type of analysis.

It is not the purpose of this section to give a full account of FEA and FEM, so for further details, the reader is referred to the thorough and accessible explanation given by Laurits Højgaard Olesen [119].

FEM solver programs exist, but most of these are optimized for one specific field of engineering. For instance, AnSys and Coventor were originally optimized for solving problems within mechanical and electrical engineering, respectively, although now they both have made add-ons that facilitate broader use.

Comsol Multiphysics is one of only few (if not the only) software packages on the market that was originally made just for solving partial differential equations (PDEs) without being specialized for some purpose. Many of differential equations relevant for engineering and physics have since then been written into the program, but also generic

forms of PDEs are available, and the user can even write his own systems of PDEs. It is also possible to couple the pre-written equations to each other or to user-defined equations. This makes Comsol Multiphysics a very powerful and versatile tool for research - especially within μTAS, where several branches of physics are often coupled. In μTAS it would often be relevant to couple mechanical, electrical, thermal, fluidic, magnetic or even optical equations. The possibility of combining many branches of engineering and physics combined with the ease of use is the reason that Comsol Multiphysics has become the software package of choice at MIC.

At the beginning of this Ph.D. work Comsol Multiphysics was named FEMLAB, and it was available in version 2.3. At that time, it was less powerful, but many calculations could be performed. At the stage of writing the thesis version 3.3 has just become available, but the author has only little experience with that version. In version 3.2, Comsol Multiphysics is a very strong software package. It is available in a 64-bit version, and with the computing power available at The Technical University of Denmark, calculations with several millions of degrees of freedom can be performed, although the time consumption grows rapidly with the number of degrees of freedom. At this point, time is a more limiting factor than memory.

4.2 Setting up calculations in Comsol Multiphysics

Setting up calculations in Comsol multiphysics is easy to get started with, but it takes skill to do it right. This section is meant as a short step-by-step guide to setting up Comsol calculations illustrating the most common choices for the work done for the present thesis.

First, one needs to choose which equations to solve and how many spatial dimensions that will be necessary. Comsol Multiphysics has many different modules and pre-programmed equations and physics-couplings. For some applications it may be useful to use one of the modules, but for most applications, it is preferable to use the generic forms of a partial differential equation. The modules have a lot of well-suited pre-made choices and built-in functionalities, and although this is practical - for instance the Maxwell Stress Tensor is integrated into the electromagnetics module - it sometimes makes it difficult to figure out, what is actually going on. While most problems are in reality 3D problems, symmetry should be used to reduce the number of spatial dimensions in the problems as much as possible. 3D calculations are numerically memory demanding and time consuming, so if a 2D approximation suffices greater speed and/or precision can be achieved.

We have used the 'PDE Modes - PDE Coefficient form - Stationary Analysis' form extensively in this project. It has the form

$$\boldsymbol{\nabla} \cdot (-c\boldsymbol{\nabla} u - \boldsymbol{\alpha} u + \boldsymbol{\gamma}) + au + \boldsymbol{\beta} \cdot \boldsymbol{\nabla} u = f, \tag{4.1}$$

where u is the dependent variable, and c, $\boldsymbol{\alpha}$, $\boldsymbol{\gamma}$, a, $\boldsymbol{\beta}$, and f are parameters of the model that may depend on u and its derivatives.

If we make the substitutions $u \to \varphi$, $c \to \mu_0$, $\boldsymbol{\alpha} \to \mathbf{0}$, $\boldsymbol{\gamma} \to \mu_0 \mathbf{M}$, $a \to 0$, $\boldsymbol{\beta} \to \mathbf{0}$, and $f \to 0$, we get Eq. (3.3). If $\mathbf{M}$ can be expressed as $\mathbf{M} = \chi \mathbf{H}$, then $c \to \mu_0(1 + \chi)$ and

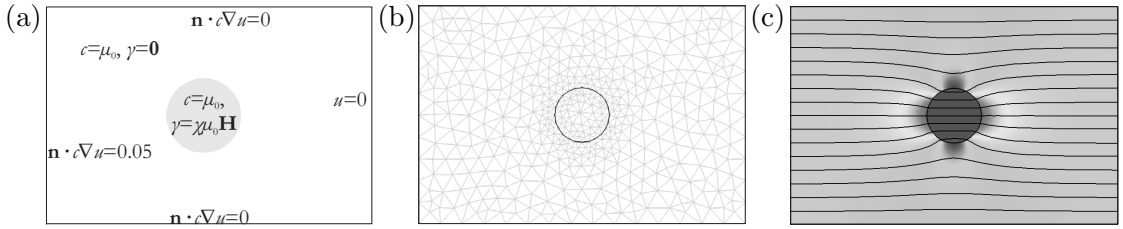

Figure 4.1: Simple numerical example: Magnetization of a magnetic cylinder with susceptibility, χ, in a homogenous magnetic field. For pedagogical reasons symmetry has not been applied here. (a) The calculation geometry showing the subdomain settings and the boundary settings. (b) The calculation mesh. (c) Result of the calculation featuring field lines of the magnetic field, and a surface plot showing the magnitude of the magnetic field. As expected the field is large (red) at the front and back of the cylinder, and small (blue) on the top and the bottom of the cylinder. The applied field shows up as a green color.

$\boldsymbol{\gamma} \to \mathbf{0}$ can be useful alternative substitutions. Remember that both $\mathbf{M}$ and χ may depend on φ and its derivatives.

The next essential choice is the element order, which is the order of the polynomials in the basis functions (sometimes called shape functions in FEM literature).

For the magnetic calculations, it is almost always the goal to find the magnetic force field, i.e., the field gradient, $\mathbf{G}$, and since $\mathbf{G}$ contains the derivative of $\mathbf{H}$, which is itself the derivative of φ, we need a well-defined second derivative of φ. If we use second order basis functions, we have second order polynomials on each element, such that the second derivative is constant on each element. This means that the calculated field gradient will be a piece-wise constant function. This gives insufficient precision on $\mathbf{G}$, and even worse, if $\mathbf{G}$ should be used as input for a numerical calculation of a bead trajectory, the calculation is unlikely to converge or due to the discontinuous magnetic force. Therefore, we need to use at least third order elements, such that the second derivative becomes a piece-wise linear and continuous function. This gives reasonable precision and allows numerical calculation of bead trajectories.

In Comsol Multiphysics one can also choose the shape of the mesh elements. The standard is triangular elements (2D) or tetrahedral elements (3D), but several other element shapes, such as rectangular or hexagonal, are available. Choosing the right element shape for the problem is a science on its own. Only standard mesh element shapes have been used in this project.

When it comes to defining the calculation geometry of the system under consideration, it is important to consider, if the geometry can be reduced by use of symmetry. Any symmetry plane or line within the drawn structure should ideally be replaced by a boundary with the appropriate boundary condition.

Having drawn the structures, the next task is to set the physical properties of the different subdomains (In Comsol Multiphysics, the geometric/physical structures within the calculation domain are called subdomains), and this is done simply by setting the values and/or formulas for c, $\boldsymbol{\alpha}$, $\boldsymbol{\gamma}$, a, $\boldsymbol{\beta}$, and f on each domain.

If one is doing non-linear calculations the solver needs an initial guess for φ. The

default guess is $\varphi = 0$ everywhere. This is bad for magnetic calculations, since that means that $\mathbf{H} = -\boldsymbol{\nabla}\varphi = 0$ everywhere, and when setting the magnetic properties ($\mathbf{M}(\mathbf{H})$ or $\chi(H)$), it is often necessary at some point to divide by H. If $H = 0$ the calculation will fail. Therefore it is practical to set another initial guess for φ, which is also done on a subdomain level. $\varphi = x$ is a good initial guess that will ensure that the calculation can start and hopefully it will converge. If it is expected that the magnetic materials are magnetically saturated, $\varphi = \zeta x$, where ζ is a large number is a good alternative initial guess.

In this mode of Comsol Multiphysics two different boundary conditions are available:

$$\hat{\mathbf{n}} \cdot (c\boldsymbol{\nabla}u + \boldsymbol{\alpha}u + \boldsymbol{\gamma}) + qu = g, \quad \text{(Neumann)} \tag{4.2a}$$

$$u = r, \quad \text{(Dirichlet)} \tag{4.2b}$$

where q, g, and r are the boundary parameters. The two kinds of boundary conditions can also be mixed.

Using the Neumann type boundary condition, Eq. (4.2a), two important magnetic boundary conditions can be set:

1. Applied magnetic field: Setting $q = 0$ and $g = \mu_0 H_a$, will apply a magnetic field that has a component, H_a normal to the boundary and an unknown component parallel to the boundary. This is how most fields have been applied in this work.

2. Mirror symmetry boundary: Setting $q = 0$ and $g = 0$ ensures that there can be no flux of magnetic field across this boundary. This makes the boundary an axis or plane of a mirror-image symmetry. Mathematically, it can be stated $\varphi(s\hat{\mathbf{s}}+p\hat{\mathbf{p}}+t\hat{\mathbf{t}}) = \varphi(-s\hat{\mathbf{s}}+p\hat{\mathbf{p}}+t\hat{\mathbf{t}})$, where $\hat{\mathbf{s}}$ is a unit vector perpendicular the boundary plane (in 3D), and $\hat{\mathbf{p}}$ and $\hat{\mathbf{t}}$ are linearly independent unit vectors in the plane of the boundary.

The dirichlet boundary condition (Eq. (4.2b)) can be used to set two other important types of boundary conditions.

1. Applied magnetic field: Setting $r = H_a s$, where H_a is the applied field, and s is a coordinate with a coordinate axis that lies parallel to the applied field. The applied field is parallel to the boundary, and the component normal to the boundary is undetermined.

2. Anti-symmetry boundary: Setting $r = \text{const}$ specifies that all magnetic field lines are perpendicular to the boundary, which is equivalent of having an anti-symmetry plane. Mathematically this is stated as $\varphi(s\hat{\mathbf{s}} + p\hat{\mathbf{p}} + t\hat{\mathbf{t}}) = -\varphi(-s\hat{\mathbf{s}} + p\hat{\mathbf{p}} + t\hat{\mathbf{t}})$, where the unit vectors are specified as before.

Care should be taken never to over-specify φ. It is recommended only to use Dirichlet conditions at one boundary of a calculation domain. Therefore it is also customary to use $r = 0$ at anti-symmetry boundaries. Notice the similarity to an electric ground plane. For non-linear calculations, it is best to specify the potential, φ, in at least one point.

In most applications, we would like to apply the magnetic field at infinity, and we would normally also want the field disturbance of our magnetic structures to vanish at infinity. Exact calculations in this situation require infinite calculation domains, which is of course impossible without mapping the coordinates into a finite domain. In the AC/DC module of Comsol Multiphysics 3.3 infinite elements are available, with such a mapping [104, AC/DC module, vers. 3.3]. This kind of method is treated in [120, Chap 16.4].

Comsol Multiphysics 3.3 was not released until just before the end of the project, so the infinite elements method has never been tested in this project, and it has not been attempted to implement such a method. Therefore, the poor-mans infinite domains have been used instead. The calculation domains have simply been made sufficiently large that the magnetic field in the area of interest is unaffected by the boundary. This is checked by moving the boundary further away and monitoring the change in the area of interest. If the change is within the desired precision, the boundary is sufficiently far away.

Fig. 4.1(a) shows a calculation domain for the calculation of the magnetic field around a magnetic cylinder in a homogenous applied field. The field is applied on the left-hand boundary, symmetry conditions are applied on the top and bottom boundaries, and an anti-symmetry condition is used on the right-hand boundary. The magnetic cylinder has $\chi = 10$, and the surrounding medium has $\chi = 0$. For pedagogical reasons it has been chosen not to utilize the obvious symmetries in this example.

At this point it is necessary to generate a mesh, and in Comsol Multiphysics a multitude of possibilities for defining a mesh exists; one can set how fast the mesh elements can grow compared to its neighbor, and the maximum sizes of mesh elements. In general constructing a good mesh is tedious work, and for the author it has been based mostly on trial and error. The parameters 'Resolution of narrow regions' and the 'Element growth rate' have proven to be powerful tools for setting up good quality meshes that are independent of the specific geometries. A 'Resolution of narrow regions' setting of 3, and a 'Element growth rate' between 1.05 and 1.2 have proven to give good quality meshes in many situations. The only way to test the quality of a mesh is to redo the calculation having refined the mesh using the built-in Comsol method and see if the change is within the desired precision. Since calculation times and memory requirements grow rapidly with the number of mesh elements (and the element order), the goal should be to have the coarsest possible mesh that is fine enough to give the desired precision.

Fig. 4.1(b) shows an example of a very simple mesh for the calculation of the magnetic field around a magnetizable cylinder in an applied magnetic field.

At this point, we are ready to solve the model, and again Comsol Multiphysics has many options for this. For non-linear problems one should choose the non-linear solver and solution form should be set to 'weak' or 'General' (in 3.2 and later versions this can also be set to 'automatic'). The standard settings for the non-linear solver are sufficient for most problems, and the only thing left is to choose the linear solver that inverts the matrix produced by the finite element method. In version 3.2 the direct solver 'Umfpack' is the fastest, and should always be the first try. Umfpack calculations are fast, but are memory intensive; if Umfpack fails due to lack of memory, one may try the other direct solver 'Spooles'. If Spooles fails also due to lack of memory, one needs to choose one of the iterative solvers. In this project the most successful iterative solver has been 'GMRES'

with the 'Algebraic Multigrid' pre-conditioner.

There are many possibilities of how to visualize the results, which I will not go into. Fig. 4.1(c) shows the result of the calculation of a magnetizable cylinder in an applied field displaying some (very few) of the visualization possibilities.

The last thing to do is to extract the data for further data analysis. Comsol Multiphysics has (at least) two functions for this. From the Graphical User Interface, one can just choose export data, or if one is using the program with Matlab, one can use the command 'postinterp' to get results in an array of points.

At this stage, setup, calculation and data analysis are complete. This brings us to a very important and often underestimated part of numerical analysis, which is model validation. Although the Comsol calculations converge, and some pretty graphs appear on the screen, the data may still be rubbish. In order to trust the data that Comsol calculates, data should be tested against some sort of benchmark - This may be experimental data, or it may be a simplified model, where a solution can be found analytically, or it may be data calculated using a different method (maybe a different FEM package). In this project, convergence of the model has also been used often as a criterium for model validation. This means that we have made a calculation with the best possible numerical resolution (using university super computers). Using this result as a benchmark, the calculation is redone with lower resolutions. If the model is sound then the results must converge towards the benchmark as resolution is increased. In this project a combination of the above possibilities has been used in most cases.

Finally, it must be mentioned that using Comsol Multiphysics with Matlab, it is possible to run automated calculations. The model is saved as an m-file, and then this can be edited and run from Matlab just like regular Matlab m-files. The parameters in the m-file, for example a number for a side length can be changed to a variable name, such that the side length in the simulation can be changed by changing the value of the variable. This allows for automated optimizations controlled by Matlab, which has been used frequently.

4.3 Numerical optimization of a periodic structure using Comsol Multiphysics

In this section, I present an example of an optimization process that was performed using Comsol Multiphysics and Matlab.

Fig. 4.2(a) shows an overview of the system in mind. The basic idea is that an external magnetic field magnetizes the magnetic elements under the microfluidic channel, and in the gaps between the magnetic elements there will be large magnetic field gradients that attract magnetic beads. The structure is periodic, and if we ignore end effects it can be thought to extend to infinity in both sides.

Fig. 4.2(b) shows the unit cell of the periodic array, which is half the period of the structure. This is also the calculation domain. p, t, w, h and a coordinate system are defined on the figure. The calculation domain extends to $y = 15p$ in the vertical direction.

At the vertical boundaries of the domain, symmetry requires that the magnetic field is perpendicular to the boundary, such that the boundaries are in fact anti-symmetry

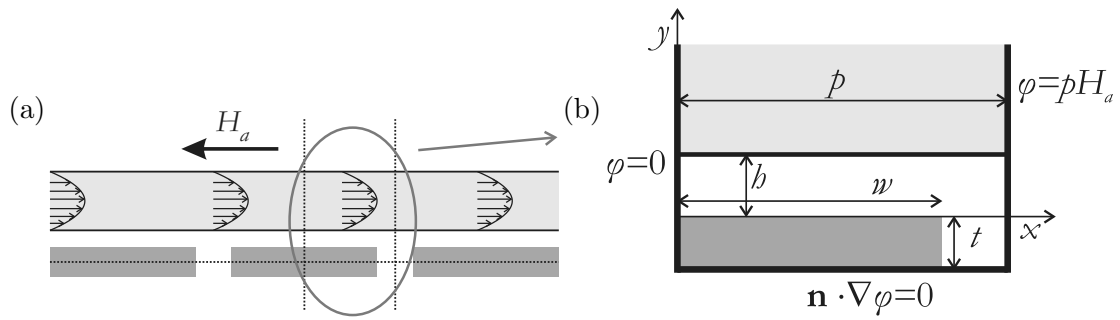

Figure 4.2: (a) Cross-section of a system with soft magnetic elements (dark gray) underneath a microfluidic channel (light gray). The arrows indicate a Poiseuille flow profile. The dotted lines indicate three of the symmetry axes in the magnetic part of the geometry. (b) The calculation domain, where the symmetries have been utilized. Here p is half the period of the structure, w is the width of the magnetic element, h is the distance from the magnetic element to the fluid channel, and t is half the thickness of the magnetic element. The boundary conditions are also indicated. A coordinate system has been indicated, but notice that $x = 0$ at the left boundary, and $y = 0$ at the top of the magnetic material.

boundaries, and φ is constant on these boundaries. We have set $\varphi = 0$ on the left-hand boundary, and in order to have the applied field at $y = \infty$, we must require that $\varphi = pH_a$ on the right-hand boundary. At the lower horizontal boundary, symmetry requires that the field is parallel to the boundary, such that $\hat{\mathbf{n}} \cdot \boldsymbol{\nabla}\varphi = 0$. At the upper horizontal boundary (not shown on figure) we have the same boundary condition.

Inside the magnetic material, we have $\mathbf{M} = M_s \tanh\left(\frac{\chi_0 H}{M_s}\right)\frac{\mathbf{H}}{H}$ with $M_s = 10^6$ A/m and $\chi_0 = 10^3$, which are approximately the properties of permalloy, and outside the magnetic material, we have $\mathbf{M} = \mathbf{0}$. In the lab, we can apply a magnetic field of $H_a = 50$ kA/m.

The goal of the optimization is to maximize the average downwards magnetic force at $y = h$. Mathematically stated, we wish to optimize

$$G_{y,\mathrm{av}}(h) = \frac{1}{p}\int_0^p -\hat{\mathbf{y}} \cdot \mathbf{G}(x,h)\,\mathrm{d}x, \tag{4.3}$$

where we have used the directional magnetic field gradient instead of the force to eliminate bead dependence.

As mentioned in Chap. 3 numerical optimizations can often be simplified by using scalings. One of the ideas in this part of the project is to fabricate the systems both in silicon using cleanroom technology but also as a hybrid system, where the fluid structures are fabricated using polymer micromachining, and the magnetic structures are fabricated using old-fashioned milling and gluing (more on that later). It is important to remember that these two fabrication methods are both limited in how close the magnetic structures can be placed to the microfluidic channel. With cleanroom fabrication, we can get $h = 50\,\mu$m, and with the polymer fabrication $h = 200\,\mu$m. Therefore, we introduce a scaled coordinate system where all length scales are scaled by h, and all measures in this new coordinate system are marked with a tilde. For instance $\widetilde{h} = h/h = 1$ and $\widetilde{x} = x/h$. All

magnetic fields are scaled with M_s, such that for instance $\widetilde{\mathbf{H}} = \mathbf{H}/M_s$.

The coordinate system that we introduced above is the most sensible coordinate system to get the results in, but actually, it is not the one that will reduce the amount of calculations the most. The calculation of $\widetilde{G}_{y,\mathrm{av}}(h)$ requires a FEM calculation of the magnetic field of the geometric structure and an integration of $-\hat{\mathbf{y}} \cdot \mathbf{G}$ along $y = h$. Of these two tasks the FEM calculations is by far the most time consuming, and therefore we can reduce the calculation time further by scaling the coordinate system by p instead of h. This coordinate is marked with a breve such that for instance $\breve{x} = x/p$. In that way, we only need to do FEM calculations for different combinations of $\breve{w}$ and $\breve{t}$, we can just integrate $-\hat{\mathbf{y}} \cdot \breve{\mathbf{G}}$ at different values of $\breve{h}$. Using these scalings, we have reduced the amount of necessary FEM calculations from 2×10^3 to 10^2 assuming that we need w, t, and p on ten levels each and h on two levels. Note that

$$\widetilde{G}_{y,\mathrm{av}}(\widetilde{1}) = \breve{h}^{-1}\breve{G}_{y,\mathrm{av}}(\breve{h}) = \frac{p}{\mu_0 M_s} G_{y,\mathrm{av}}(h). \tag{4.4}$$

The following parameters have been used

$$\begin{aligned}
\breve{t} &= \{0.1, 0.3, 1, 3\}, \\
\breve{w} &= \{0.5, 0.6, 0.7, 0.8, 0.9, 0.92, 0.94, 0.96, 0.98\}, \\
\breve{h} &= \{0.1, 0.4, 0.8, 1, 1.5, 2, 2.5, \cdots, 8.5, 9, 9.5, 10, 13, 16, 20\}^{-1},
\end{aligned}$$

where the $\{\}^{-1}$ in $\breve{h}$ applies to each individual element of the list, and the $\cdots$ mean that the list continues in increments of 0.5.

FEM calculations have been carried out for every possible combination of $\breve{t}$ and $\breve{w}$, and for each FEM calculation $\breve{G}_{y,\mathrm{av}}(\breve{h})$ has been evaluated at each value of $\breve{h}$.

These results have then been re-scaled into the coordinate system with one tilde.

Remember that $G_{y,\mathrm{av}} = \frac{\mu_0 M_s}{h}\widetilde{G}_{y,\mathrm{av}}$, so it may be useful to know that $\frac{\mu_0 M_s}{h} = 2.5 \times 10^4$ T/m for $h = 50\,\mu$m and 6.3×10^3 T/m for $h = 200\,\mu$m.

It is observed in Fig. 4.3(a) that $\widetilde{G}_{y,\mathrm{av}}$ grows with the length of the half-period, $\widetilde{p}$. Clearly, the upper limit of the gradient has not been achieved in the simulations, but the

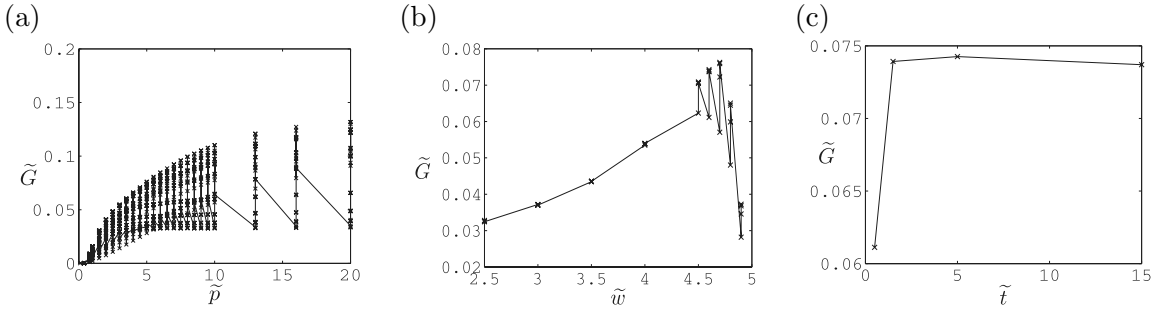

Figure 4.3: (a) $\widetilde{G}_{y,\mathrm{av}}$ as a function of $\widetilde{p}$. Both $\widetilde{w}$ and $\widetilde{t}$ are also varied, which is why there are so many points for every value of $\widetilde{p}$. (b) $\widetilde{G}_{y,\mathrm{av}}$ as a function of $\widetilde{w}$ for $\widetilde{p} = 5$. $\widetilde{t}$ is still varied within each value of $\widetilde{w}$. (c) $\widetilde{G}_{y,\mathrm{av}}$ as a function of $\widetilde{t}$ for $\widetilde{p} = 5$, $\widetilde{w} = 4.6$.

Table 4.1: Characteristics of the different TI-system designs F_{av} is the average downwards force that a saturated MyOne bead will experience as it is moving through the channel.

$h = 50\,\mu$m	(silicon, bottom of channel)	$F_{\mathrm{av}} = 4.5$ pN
$h = 100\,\mu$m	(silicon, middle of channel)	$F_{\mathrm{av}} = 2.3$ pN
$h = 150\,\mu$m	(silicon, top of channel)	$F_{\mathrm{av}} = 1.5$ pN
$h = 200\,\mu$m	(polymer, bottom of channel)	$F_{\mathrm{av}} = 1.1$ pN
$h = 250\,\mu$m	(polymer, middle of channel)	$F_{\mathrm{av}} = 0.9$ pN

growth is slow as we move to higher values of $\widetilde{p}$. There is an upper limit to the size of $\widetilde{p}$. Remember that for the polymer systems $h = 200\,\mu$m, such that if $\widetilde{p} = 5$ the full period will be 2 mm in the real system. Therefore, it was chosen to limit the design to $\widetilde{p} = 5$. Fig. 4.3(b) shows how $\widetilde{G}_{y,\mathrm{av}}$ varies with $\widetilde{w}$ for $\widetilde{p} = 5$. It is seen that the gradient grows steadily for $\widetilde{w} \lessapprox 4.7$ after which it drops rapidly. To be on the safe side, it was chosen to have $\widetilde{w} = 4.6$. The variation of $\widetilde{G}_{y,\mathrm{av}}$ with $\widetilde{t}$ is illustrated in Fig. 4.3(c). The change is actually small enough that it may be within the uncertainty of the model, but it seems that it is preferable to have $\widetilde{t} \gtrsim 1.5$.

Until now, it has been assumed that h is the distance between the top of the soft magnetic elements and the bottom of the microfluidic channel, but this does not have to be the case. In fact, it would not make the most sense to optimize the average magnetic force at the bottom of the channel, at the bottom of the channel the magnitude of the local forces at the bead capture sites is more important. A large average force is more important in the middle or top of the channel. It was decided to make 5 designs characterized by the value of h that all have $\widetilde{p} = 5$, $\widetilde{w} = 4.6$, $\widetilde{t} > 1.5$ and a microfluidic channel that is $100\,\mu$m high. The designs are characterized in Table 4.1. The magnetic forces are approximately three orders of magnitude larger than gravity.

The design and fabrication of these systems were done as a collaboration with Danish

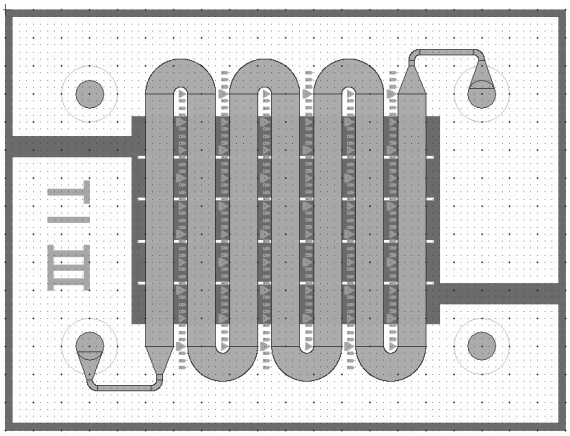

Figure 4.4: The chip design for the TI-systems. The green represent the serpentine shaped fluid channel, and the blue is the magnetic structure, which is under the channel. The shown design is the one with $h = 150$ μm.

Technological Institute (TI), and the systems shall henceforth be known as the TI-systems. We will return to the fabrication of and experiments with these systems in subsequent chapters. Fig. 4.4 shows the total design of the chips. It was chosen to use a serpentine shaped microfluidic channel, this allowed for the magnetic field to be applied across the narrow side of the chip, and the long channel give many magnetic capture points, i.e., many periods in the design. The microfluidic channel is 1 mm wide, 100 μm deep, and a total of ≈ 77 mm long. This gives a total channel volume of ≈ 8 μl.

4.4 Discussion

This chapter has carried the discussion of application of FEM as a design tool magnetic separation systems. Specifically, it has been shown how to set up magnetostatic calculations in Comsol Multiphysics.

Finally, it was shown how to make a parametric study of a specific microsystem design, and it was illustrated how scalings helped the analysis of the problem. In the end five different geometries were chosen for fabrication and experiments.

Chapter 5

Fabrication

This chapter describes the fabrication processes of this project. The fabrication of on-chip microelectromagnets was covered extensively in my master's thesis [11], so it will not be treated here.

5.1 Silicon process

At an early stage of this project a fabrication process was developed that has worked well giving a good yield without major problems. This process has been re-used with small modifications for every silicon based chip design presented in this thesis.

As an example of the basic fabrication process, the fabrication process for the first generation of the chips with soft magnetic elements besides a microfluidic channel is presented here. Later generations of this design were used for papers [4] and [3] of this thesis. The fabrication process was first developed as part of a three weeks project, where the author supervised students, B.G. Kjeldsen and J.L. Reimers, who are acknowledged for their work in the project. T. Lund-Olesen continued work on the fabrication process optimizing some of the fabrication parameters. Some of his work with this fabrication process

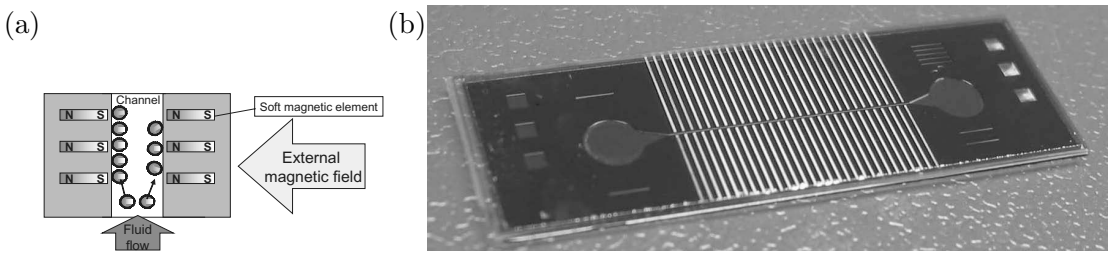

Figure 5.1: (a) The conceptual design of the passive magnetic separators. An external magnetic field magnetizes the long soft magnetic elements that in turn create large magnetic fields and field gradients in the microfluidic channel. Magnetic beads flowing in the channel are attracted to the side walls and the ends of the magnetic elements. (b) Picture of the finalized chip. The magnetic elements show up in yellow, and the inlet and outlet of the microfluidic channel are easily seen.

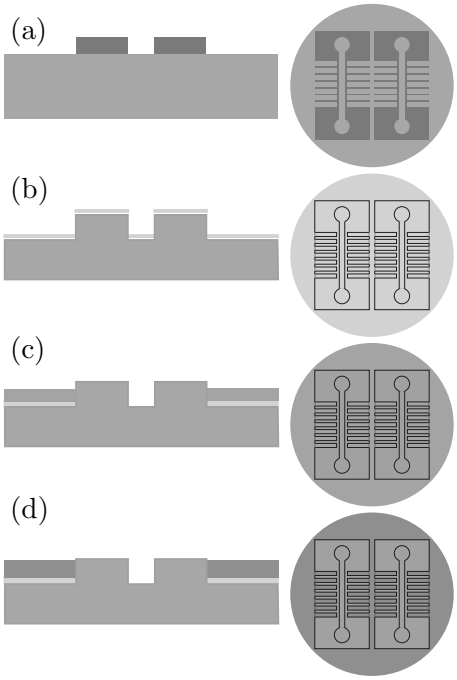

Figure 5.2: The basic silicon fabrication process. Cross-sections of the structure are shown on the left. Top-views of the structure/wafer are shown on the right. (a) 9.5 μm AZ4562 photo resist is spun on to a silicon wafer, and patterned using UV-lithography. Both microfluidic channels and magnetic structures are defined in this mask. (b) 50–200 μm Deep Reactive Ion Etching (DRIE) of the structures, resist strip, RCA clean, growth of a 1 μm wet silicon oxide, and E-beam evaporation of 5 nm Ti and 200 nm Au. (c) Electroplating of 2.5 μm copper in the bottom of the trenches designated for magnetic structures. Only the trenches that are connected to the rim of the wafer are electroplated. The uncovered gold is etched in entreat. (d) The copper is removed using nitric acid and 40–200 μm permalloy is electroplated in the bottom of the magnet trenches.

is presented in ref. [77] and his Master's thesis [121].

Fig. 5.1(a) shows the working principle of these chips. An external magnetic field magnetizes the long magnetic elements that create strong magnetic fields and gradients inside the microfluidic channel, such that beads are attracted to the ends of the magnetic elements on the side walls.

Fig. 5.1(b) shows a photograph of the entire chip. The microfluidic channel measures $l \times h \times w = 20000 \times 100 \times 100$ μm^3 ($\approx 0.2\,\mu$L), and each of the permalloy magnetic elements measures $l \times h \times w = 5900 \times 50 \times 150$ μm^3. The elements are placed with a periodicity of 450 μm and a spacing to the channel of 50 μm. The long thin shape of the magnetic elements is chosen to minimize demagnetization effects and thus maximize fields and gradients.

Fig. 5.2 summarizes the fabrication procedure. As Wu *et al.* [122], Deep Reactive Ion Etched (DRIE) structures are used as electroplating moulds, but the process have been developed substantially for this project. In Fig. 5.2(a) a 9.5 μm thick layer of AZ4562 photoresist (Hoechst, NJ, USA) is patterned using UV-lithography on a single polished Si (100) wafer. The photoresist pattern is used as an etch mask for a DRIE in (b) to create trenches for the electroplating mould as well as the microfluidic channels. The wafer is RCA-cleaned, a 1 μm thick SiO_2 is grown on the wafer, and finally a seed layer of 5 nm Ti and 200 nm Au is E-beam evaporated onto the wafer giving the structure shown in (b).

The trenches designated for electroplated magnetic elements are all connected to the outer rim of the wafer by a network of conducting streets. The poor step-coverage obtained by the metal E-beam evaporation ensures that little or no contact exists between the metal in the conducting network and the metal on top of the wafer. This is illustrated by the

(a) (b)

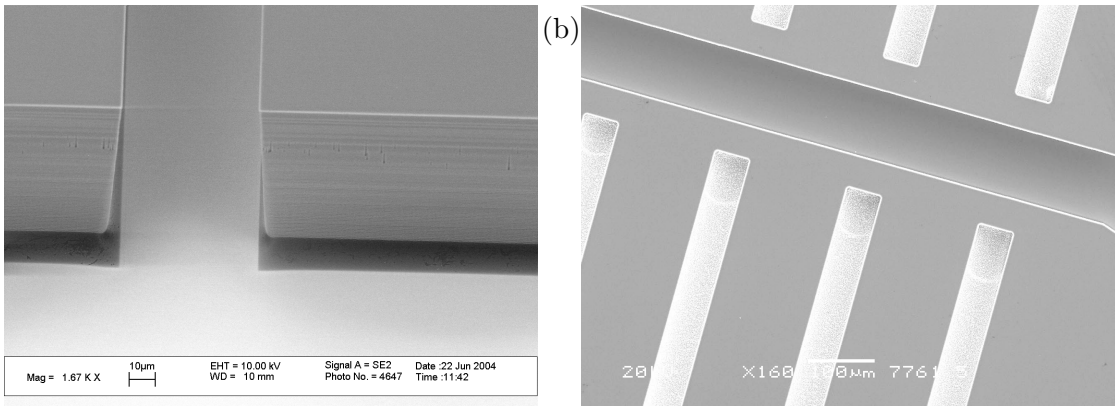

Figure 5.3: Scanning Electron Microscope (SEM) images from different stages of the fabrication process. (a) Picture of a T-crossing between a the end of a trench designated for a magnetic element (away from the microfluidic channel) and the conducting network corresponding to the stage of the fabrication process shown in Fig. 5.2(b). The trademark scallops of the DRIE process are clearly seen, and it is also seen how DRIE causes some under-etch. A shadow effect from the under-etch is seen in the pattern of the evaporated gold. (b) The structure after permalloy electroplating (Fig. 5.2(d)). Both permalloy elements (here 50 μm wide) and microfluidic channel are well-defined.

SEM-image in Fig. 5.3(a) that shows how the DRIE under-etches, and the gold in the bottom of the fluid channel does not reach the channel side wall.

Before electroplating, short etches of Au are performed in Entreat 100 (Engelhard, NJ, USA) until no contact persists between the top and the bottom.[1] The resistance is measured after each etch using a hand-held multi-meter. If the resistance between the top of any chip and the conducting network is less than 2.5 kΩ, the etch is repeated. In Fig. 5.2(c) a 2.5 μm thick protective Cu layer is electroplated in the bottom of the conducting network using the commercially available CuproStar LP-1 electrolyte (Enthone, CT, USA) with a current density of 25 mA/cm^2. Subsequently, the unprotected Au and Ti is etched away in Entreat 100 and 5 % hydrofluoric acid, respectively. Finally, the Cu layer is removed in nitric acid.

At this point the wafer features the microfluidic channels and the conducting network. Permalloy is electroplated into the network, including the trenches for magnetic elements using a pulse-reversal plating electrolyte as described in [123] and also in [7] of this thesis. The average current density was 10 mA/cm^2. The resulting structure is shown in Fig. 5.2(d). Fig. 5.3(b) shows a SEM-image of the structures at this state for a chip design where the width of the permalloy elements is 50 μm. Both the microfluidic channel and the permalloy elements are seen to be sharply defined as expected from silicon microfabrication.

The silicon oxide is removed using buffered hydrofluoric acid, in order to make the surface suitable for anodic bonding. Also, removing the oxide at this late stage of the

[1] Usually the etches was one or two minutes each, but our Entreat 100 is very old, so etch times will be different, if a new one is mixed.

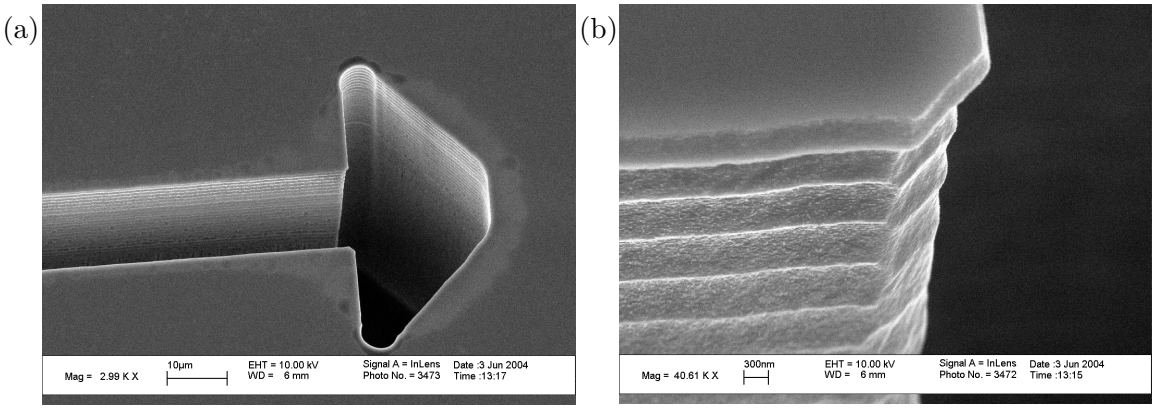

Figure 5.4: Scanning Electron Microscope (SEM) images of signatur scallops of DRIE. (a) Picture of an arrow test structure. (b) Close-up of the corner of the arrow. The scallops from the DRIE process are clearly seen, and it is also seen that they have a size of approximately 300 nm.

fabrication lifts off any dirt that has settled on the wafer surface during fabrication, and hence the oxide functions as a protection layer for the silicon surface.

Subsequently, a pyrex lid is bonded anodically to the top of the wafer sealing the microfluidic channel. When the wafer is diced into chips, the conducting streets are cut away leaving only the soft magnetic elements on the chip, such that we obtain the structure in Fig. 5.1(b). Access to the microfluidic channel is achieved by drilling holes in the pyrex wafer.

5.1.1 Deep Reactive Ion Etching

Deep reactive ion etching has been used extensively for the microfabrication in this project. Therefore, a more in-depth discussion of this process is appropriate.

The DRIE machine available at MIC is an "Advanced Silicon Etcher or ASE (STS MESC Multiplex ICP serial no. 30343)". The machine performs anisotropic silicon etch using the Bosch process [124]. The standard deep-etch recipe has been used without modifications, and this will not be discussed. However, there are issues with the use of this process that must be observed during fabrication.

From the manual (only available internally at the department), we expect that the etch rate is $\approx 5\,\mu$m/min, but this is heavily dependent on the etching area. Therefore, the etch rate has always been measured for every mask design. An etching process aiming at etching approximately one quarter of the total desired etch depth has been run first, and then the etch depth was measured using a Dektak 8 profiler. Etch rates between 4.5 and 7.5 μm/min have been experienced. After the etch rate measurement the wafer can be etched to the desired depth.

The signature of the DRIE process are the scallops that are caused by the repeated almost isotropic etch and subsequent passivation. An example of these are shown in the SEM-image in Fig. 5.4. These scallops may have an effect on the fluid flow near the fluid channel side walls, but this has not been investigated.

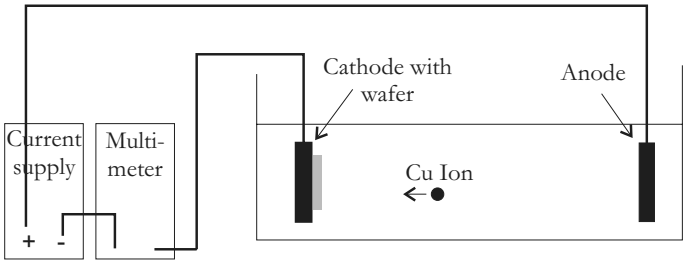

Figure 5.5: Electroplating process. Basic principle of copper electroplating. The current drives Cu-ions towards the cathode where they deposit.

The standard DRIE deep etch process causes some under etch of structures, and this under etch is also very dependent on the etching area. Fig. 5.3(a) shows this under etch, and in some cases it has been much more severe. For instance; fabrication of the systems that were designed in Chap. 4 with $h = 50\,\mu$m required an etch where walls that were 60 μm wide and 200 μm high were left standing. The under etch was severe enough to completely under etch these structures, and they fell off. The under etch can be tailored by adjusting the passivation step of the DRIE process, but there was no time to optimize this, and thus the structures with $h = 50$ μm were never realized.

5.1.2 Electroplating

Electroplating is the other key step in the fabrication processes mentioned above. All silicon micro fabrication in this project has involved electroplating on one or more stages.

The electroplating process is illustrated in Fig. 5.5 for a simple copper plating process. When a current is driven through the electrolyte, positive ions flow towards the cathode and deposit on the cathode. A short account of electroplating of single metals and binary alloys are given in the following based loosely on the work of Abner Brenner, [125, 126] and Schlesinger and Paunovic, [127].

Electroplating processes can be described as redox processes where electrons are exchanged between metals and ions due to the processes

$$\mathrm{Me} \leftrightarrow \mathrm{Me}^{z+} + z\,e^{-}, \tag{5.1}$$

where Me represents any metallic species, z is the number of exchanged electrons, and e is an electron.

The reaction in Eq. (5.1) goes both ways. Whether the reaction occurs primarily to the left or right is determined by the Nernst equation

$$E_{\mathrm{eq}} = E^0 + \frac{RT}{zF} \ln \frac{a[\mathrm{Me}^{z+}]}{a[\mathrm{Me}]}, \tag{5.2}$$

where E_{eq} is the activity-dependent potential of the Me^{z+}/Me electrode, E^0 is the relative standard electrode potential of the electrode, R is the gas constant, T is the absolute

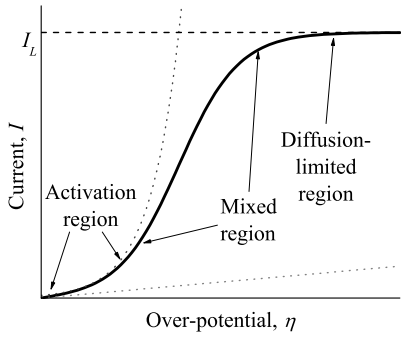

Figure 5.6: Current as a function of over-potential for a typical electrolyte. The blue line denotes the situation, if the relation was purely exponential. The red lines denotes the situation, if the relation was linear. I_L denotes the limiting current density.

temperature, F is the Faraday constant[2], $a[\mathrm{Me}^z]$ is the activity[3] of the ion, and $a[\mathrm{Me}]$ is the activity of the metal, which by definition is $a[\mathrm{Me}] = 1$.

If $E_{\mathrm{eq}} > 0$ the reaction primarily goes to the left until it reaches an equilibrium where $E_{\mathrm{eq}} = 0$.

The Nernst equation determines whether a reaction will primarily go to left or right, but not whether the reaction will occur at all. When an ion is transferred from solution to solid it costs energy and this energy barrier must be overcome. In electroplating the primary concern is the number of charges transferred onto the solid, and thus this energy barrier is viewed as an energy per charge i.e. a voltage. When electroplating at a given current, I, the voltage, $E(I)$, across the electrolyte will be given as

$$E(I) = E_{\mathrm{eq}} + \eta_a + \eta_c + \eta_D + \eta_r + \eta_\Omega \tag{5.3}$$

where the over-voltages, η_x, can be divided into the following contributions

1. Activation over-voltage, η_a: Energy cost of electron transfer.

2. Crystallization over-voltage, η_c: Incorporation of the metal atom into the crystal structure.

3. Diffusion over-voltage, η_D: When the metal ions near the surface solidifies, a deficit of ions is created in a layer (the Nernst layer) near the surface. If there is a complete depletion of ions at the surface a surface charge will build up, corresponding to a voltage.

4. Reaction over-voltage, η_r: An electrolyte will often contain one or more complexing agents. An energy cost is associated with the dissociation of the metal complex.

[2]The Faraday constant is the number of charges per mole $F = 96487 \frac{\mathrm{C}}{\mathrm{mol}}$

[3]The activity of any ion in a solution is proportional to and can in most cases be approximated by the concentration of the ion in the solution.

(a) 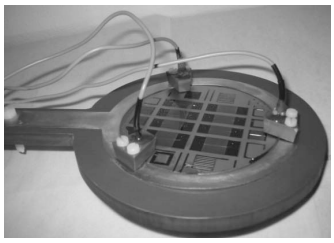 (b) 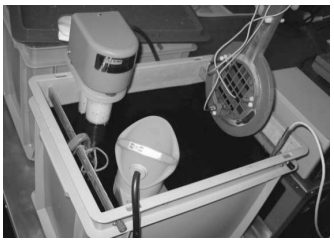

Figure 5.7: (a) The wafer holder used in our plating lab. A wafer is mounted, and a permalloy electroplating has just finished. (b) The 25 l plating bath with tank and holder. The pump for agitation (blue) and the heater (green) are also seen. (Both pictures are courtesy of T. Lund-Olesen. [121])

5. Ohmic over-voltage, η_Ω: IR-loss in the electrolyte.

Depending on the applied current different contributions to the over-voltage dominate. At low currents the activation energy dominates. In this case the current grows exponentially with the over-voltage[4]. At higher currents the Nernst layer is depleted of free ions, such that the diffusion and/or reaction energy dominate, which means that the current is limited by the ion transport through the Nernst Layer, and thus the over-potential grows rapidly for small increases in the current. This is illustrated in Fig. 5.6.

In order to calculate the speed of these reactions, a relation is needed between the amount of deposited metal and the applied current. The number of deposited moles per time is simply the current divided by the number of charges per mole. $\partial_t n = \frac{I}{zF}$, where n is the number of deposited moles.

Fig. 5.6 illustrates many of the problems one faces, when one wants to deposit a metal alloy with a given composition. Different metals have different relative standard electrode potentials , E^0, and thus their activity-dependent electrode potentials, E_{eq}, will also be different. This means that different metals in a given electrolyte will experience different over-potentials, and thus they will deposit with different rates. This can be controlled by adjusting the ion concentrations of the alloy metals in the electrolyte, but often unrealistic ratios between the concentrations are necessary to get useful alloy compositions. Another remedy is the addition of complexing agents to the electrolyte. If the complexing agent forms complexes with one metal preferably over the other, this shifts the alloy composition. The presence of one metal species can affect the deposition of the other in other ways than predicted by Nernst equation and the over-voltages. This sometimes leads to abnormal deposition, and nickel-iron electrodeposition is an example of abnormal deposition. It is usually difficult if not impossible to predict the behavior of abnormal deposition when plating parameters are changed, so experimental studies are necessary. Such studies have been performed for our permalloy plating bath (cf. Rasmussen [96], Korsbæk and Rubæk [98], Tang [123], and my own work in paper [7] of this thesis).

Fig. 5.7 shows the setup used in our plating facility. It is seen on the figure how contact is established to the wafer, and one also sees the pump supplying agitation and the heater

[4]At very low currents the current actually grows linearly with the over-voltage due to competing exponentials.

used for the permalloy plating bath. The plating process itself is well-documented in paper [7] of this thesis.

The result of an electroplating process depends on many things. The hardest thing to control is the uniformity of the deposition across the wafer. Ions follow the electric field lines, so if the electric field is stronger in one region than another, the local current density will be higher, and more material will be deposited. Also, the composition of permalloy depends on the local current density and bath agitation during the deposit, so the compositions will vary between positions.

The only way to get uniform deposits is to have a uniform plating area, but of course this is not possible if one needs a specific structure. Therefore many tricks are performed to even out the non-uniformities of the plating area. Fig. 5.7 shows that a current thief (Stainless steel structure around the wafer) is sometimes used and also, in our wafer designs, there is always allowed room for an on-wafer current thief as ring close to or at the edge of the wafer, and the conducting network on the chips also functions as current thieves around the single chips. All this helps, but still there are issues; plating will always be faster near edges and corners of a structure, and this may result in over-plating. For the systems with magnetic elements next to the channel, this is a major concern, since it is impossible to bond a pyrex wafer to the surface, if there is overplated permalloy on the surface of the wafer. The only way to solve this is to avoid plating all the way to the top of the wafer. This is one of the motivations for shifting towards systems where the magnetic elements are buried in the side of the wafer opposite from the fluid channels.

5.1.3 Variations of the silicon fabrication scheme

As mentioned, the basic fabrication scheme has been used with small modifications throughout this project.

Papers [1, 2, 10] of this thesis used the on-chip electromagnets, so they are outside this treatment.

The paper on magnetic separation using an array of soft magnetic elements [4] used a fabrication process identical to the one described above. Paper [3] used the same fabrication process except that another DRIE step was added to allow for a fluid outlet through the bottom of the chip.

The systems, described in [5], with microfluidic channels on one side of a wafer and copper current lines buried deep into the other side of a wafer were fabricated using a similar fabrication method, only this time three DRIE steps are needed on each wafer, so the fabrication is slightly more complicated. First a 2.5 μm thick silicon oxide was grown on the wafer. The pattern for the fluid channels was applied to the front side using UV-lithography. The pattern for the current wires and the outlet hole were applied to the oxide on the back side using UV-lithography. A third photo resist layer was applied to the front side and patterned with a mask containing only the outlet hole. The photo resist was used as etch mask for DRIE, the resist was stripped, and then the two oxide patterns were used as etch masks in turn for two further DRIE processes. The oxide was stripped, the wafer was RCA cleaned, and a new 100 nm thick silicon oxide was grown on the wafer. A pyrex wafer was anodically bonded to the front side of the silicon wafer,

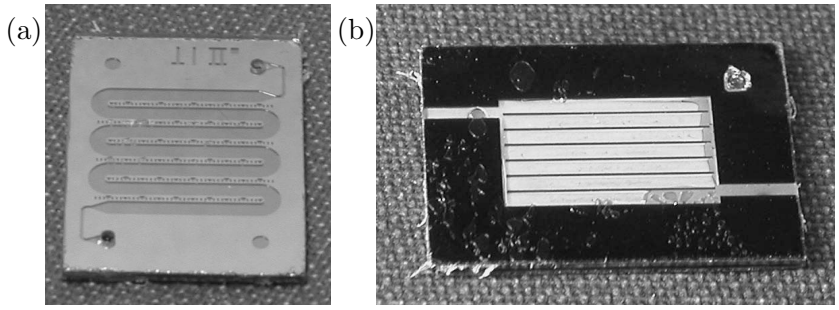

Figure 5.8: Chip with magnetic elements under the channel, i.e. a TI-system. (a) The frontside of the chip with the serpentine shaped fluid channel. It is seen how holes have been drilled to access the fluid channel. The width of the fluid channel is 1 mm. (b) The backside of the chip showing the magnetic elements. The free standing silicon walls that separate the magnetic elements are also shown. The two lines of electroplated permalloy on the sides of the chip are connections to the conducting network.

and a seed layer of 5 nm Ti and 200 nm Au was E-beam evaporated onto the back side of the wafer. At this point the backside of the wafer looked just like Fig. 5.2(b), and the fabrication continued as described from that point except that copper was electroplated as the final step instead of permalloy.

The chips for the TI-systems were fabricated in the same way as described in the previous paragraph except that permalloy was electroplated as the final step, and there was no outlet hole through the bottom of the wafer, such that only two DRIE processes were needed. A final chip is shown in Fig. 5.8.

5.2 Polymer fabrication

Since the beginning of the project, it has been the intention to fabricate magnetic separators in polymers - It is cheaper and fabrication can be much faster.

Two different approaches have been attempted for cleanroom SU-8 fabrication, and also a third approach where the fluid channels are fabricated in PDMS and the magnetic structures are made in metal structures.

5.2.1 SU-8 fabrication

Following the success of the basic silicon fabrication process, a similar SU-8 fabrication process was tested. SU-8 is a photo-definable epoxy resin.[5]

These tests were performed during a project with the students, Lars Nørgaard and Edoardo Grazia supervised by the author. It was attempted to make chips similar to the ones in Fig. 5.4 only using pyrex and SU-8 instead of silicon.

For this process, we spin an 80 micron thick SU-8 layer onto a pyrex wafer, pattern the SU-8 using UV-lithography, and develop the SU-8. A seed layer of 50 nm Ti and 200 nm

[5]See for example www.microchem.com/products/su_eight.htm

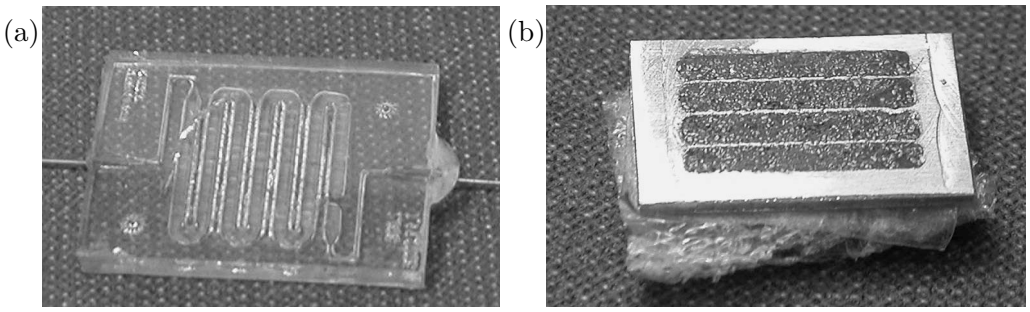

Figure 5.9: The hybrid chip fabricated in collaboration with Danish Technological Institute. (a) The polymer part fabricated by Pedro Santos. The width of the microfluidic channel is 1 mm. (b) The magnetic part containing the free standing aluminium walls and the fixated iron filings. The metallic part is mounted on a piece of elastic foam material for even pressure distribution when the metallic part is pressed against the polymer part. The width of the free standing walls should be 120 μm. The entire metallic part measures $1.0 \times 1.5 \times 0.1$ cm^3.

Au is E-beam evaporated onto the wafer. At this point the wafers look like Fig. 5.2, and everything proceeds as in the basic fabrication process.

This fabrication method proved to be much faster than the silicon process, but new difficulties arose. The SU-8 between trenches designated for the magnetic elements and the trench designated for a fluid channel cracked, and there would be electrical contact to the gold in the fluid channel from the outer rim of the wafer. Electroplating inside the fluid channel was thus unavoidable. This problem could most likely be solved just by changing the design of the magnetic structures a little bit, but this fabrication method has not been pursued further.

The author has been involved in a project lead by Minqiang Bu, which used a slightly different SU-8 fabrication scheme. A patterned seed layer is laid onto a pyrex wafer using lift-off of the seed layer with UV-lithography. Then SU-8 is spun onto the wafer, the wafer is turned upside down, and the patterned seed layer is used as photo mask for the patterning of the SU-8. After SU-8 development a plating mould with perfectly aligned patterned seed layer have been produced, and permalloy can be electroplated in the bottom of the trenches. This project has lead to two conference contributions with Minqiang Bu as first author.[128, 129]

5.2.2 Laser ablation and mechanical milling

From the beginning of the project, it has been the intention to fabricate microfluidic magnetic separators using polymer microfabrication.

Anders Heebøll-Nielsen from Danish Technological Institute made some nice systems, but the author was not really involved with this except for discussions on design and exchange of experience.

In the end, it was decided to try to make a hybrid system, where the microfluidic part would be fabricated by Pedro Santos from Danish Technological institute using CO_2 laser ablation of PDMS. The magnetic part was fabricated at MIC, and the two parts would

be integrated to form a hybrid system. These were the polymer systems of the TI-design of Table 4.1, and they should be directly comparable to the silicon systems that were fabricated at MIC.

The magnetic part was fabricated at MIC. Trenches were milled in a piece of aluminium by Stig Ahrent Pedersen (MIC, Mechanical Workshop). Very thin walls between the trenches were needed, so it was decided to use a thicker block of aluminium, and not mill all the way through. The trenches were filled with iron filings, and the filings were fixated with a low-viscosity glue that were applied into the space between the iron filings. When the glue had dried, the backside of the aluminium block were milled until the trenches with metal filings were uncovered. Fig. 5.9 shows the final chip. In the end, the width of the free standing wall was not well-defined, so only one magnetic part was fabricated, with a design corresponding to $h = 200$ μm, but as mentioned the width of the wall may not correspond exactly to the design.

5.3 Discussion

The basic fabrication process used in this project has been presented in this chapter, and it has been show how this process has been modified to fabricate the different designs featured in this thesis.

The basic fabrication process did have some yield problems due to overplating. This problem is eliminated by burying the magnetic elements into the opposite side of the wafer.

The systems with elements or current wires under the channel has one problem, though. Since the elements need to get close to the channel, the membrane between channel and elements becomes quite thin, and thus these systems are mechanically fragile.

The SU-8 fabrication processes have proven to be much faster than the silicon fabrication process. However, bonding of a lid to the SU-8 structures proved to be a major problem. Some solutions have been found, but none are as effective as anodic bonding between silicon and pyrex.

Both polymer fabrication methods have the disadvantage that the beads stick to the polymer, and it can be problematic to clear the system of beads after experiments. It has been necessary to use high pressures, which has caused the lids to delaminate.

The silicon fabrications is the most stable, and the silicon systems are more durable than the polymer systems, but if it is accepted that the polymer systems are for single use, then this fabrication method is both fast and cheap. In case of the polymer TI-system, only the polymer fluid part needs to be single use.

Chapter 6

Experimental methods

This chapter demonstrates the experimental techniques that have been used during this project. Most of the chapter concerns the experimental procedure for the microfluidic experiments, but at the end of the chapter, some techniques for data analysis are discussed.

6.1 Fluid connections to the chips

Fluid connections to the chip are made using a number of fluid connectors, syringes, filters, tubes and valves. Fig. 6.1 shows the most important ones. Fluid connectors, luer locks, and switch valves all come from Upchurch Scientific (www.upchurch.com). The filter is from Whatman (www.Whatman.com), and the tubing is from Bohlender GMBH (www.bola.de). The tubing in the picture has an inner diameter of 0.8 mm, which means it holds 5 μl/cm. This tubing is well-suited for most applications. If very low flow rates are used, e.g. 0.5 μl/min, the linear flow rate inside the tubing will be very small, and beads (that are usually heavier than water) will tend to settle on the tube wall. For such flow rates, it may be useful to use tubing with a smaller inner diameter, and for this purpose,

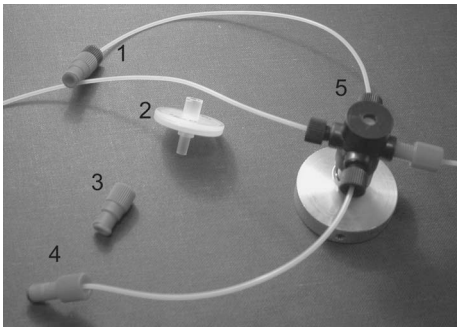

Figure 6.1: Parts for the microfluidic setup. All parts except 2 are from Upchurch Scientific. 1 is a (black) P-347 fluidic connector with a P-678 Luer lock (red). 2 is a 0.2 μm filter from Whatman. 3 is a P-678 Luer lock. 4 is a P-202 fluid connector (red). 5 is a V-101D switch valve with fluid connectors. The tubing is S1810-10 from Bohlender and has an inner diameter of 0.8 mm.

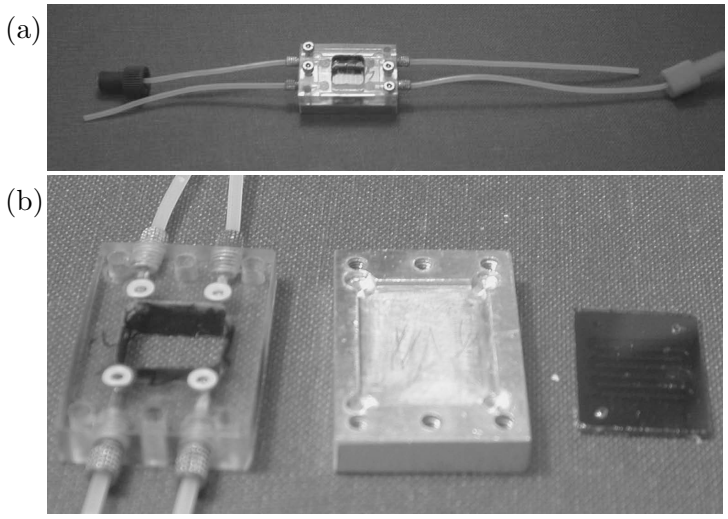

Figure 6.2: Example of a chip holder. (a) The assembled chip holder complete with tubing and chip. (b) The disassembled chip holder. To the left is shown the top made in polycarbonate. Four white O-rings are inserted into their recesses that are milled such that they will fit perfectly onto the drilled holes on the chip. Also seen is the four Lee fittings that connect to the fluid tubing. The connections from the Lee fittings to the center of the O-rings are just drilled pipes in the polycarbonate. The aluminium bottom is shown in the middle. A recess has been cut out for the chip, such that all chips will be placed exactly the same, and the O-rings will fit. The chip is shown on the right (the chip has a width of 15 mm. It is the same chip that was also shown in Fig. 5.8. The chip and chip holder are assembled by placing the chip in its recess, putting the top onto the aluminium bottom, and tightening the screws.

we have sometimes used tubing with an inner diameter of 0.25 mm from Mikrolab, Aarhus, Denmark (www.mikrolab.dk), which only holds 0.5 μl/cm. The drawback of using such tubing is that is has a large hydraulic resistance, and also microfluidic dispersion is large.

We use standard syringes with luer locks, and usually syringes with volumes of 1, 5, 10, and 20 ml are used. The luer locks on the syringes attaches to the luer lock (3 in Fig. 6.1), which in turn fits into a fluid connector that fits on the tubing. The fluid connectors also fit directly onto the switch valves.

For connections between the tubing and and the chips, we use Lee fittings (Minstac 062 fittings, www.theleeco.com) and O-rings put together with in-house built chip holders.

Fig. 6.2 shows an example of one of the chip holders used in this project. All chip holders have shared the same basic design; a recess is cut in the bottom part, in which the chip is placed, and O-rings in the top part are pressed against the chip to make sealed fluidic connections.

6.2 Samples and buffers

For most of this thesis, the samples have been solutions containing Milli-Q water and magnetic beads, and the buffer has also been Milli-Q water.

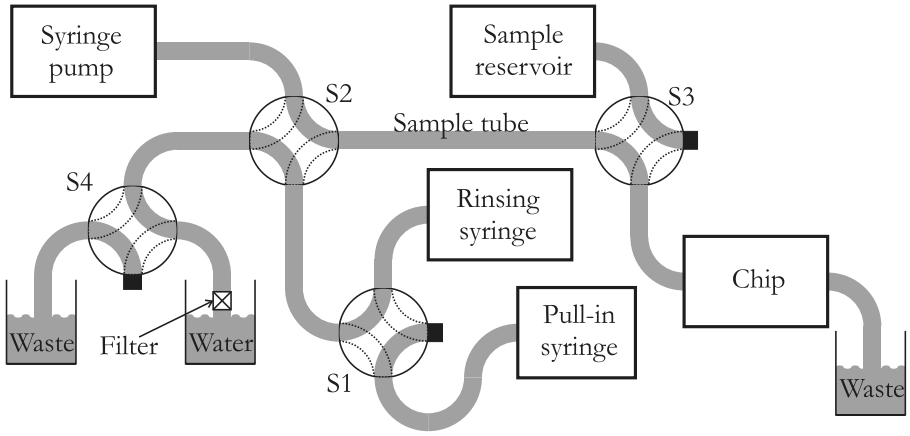

Figure 6.3: Microfluidic setup. The setup has four switch valves, S1, S2, S3, and S4, that control the fluid flow. Valves S1, S3, and S4 have one of their outlets blocked. All switch valves shown in position A, and can be switched to position B by rotating the valves a quarter turn, such that the flow will follow the dashed lines instead. To the left is shown a water reservoir with a filter just after the reservoir. All buffer fluid is pulled into the system from this reservoir through the filter. With all switch valves in position A, fluid is flowing from the syringe pump through the sample tube and into the chip, and finally ends up in the righthand side waste tank. At the same time, water can be pulled into the rinsing syringe from the water reservoir.

The beads are taken from their flask using a pipette, and suspended in Milli-Q water to give the desired bead concentration. The flask is given a good shake before the bead solution is taken from it. Beads are heavier than water, and if the solutions are left to themselves the beads will settle at the bottom. Most experiments have been done with mixtures of 1:100 down to 1:500 parts bead solution : Milli-Q.

Before using diluted bead solutions for experiments the solution container must be given a good shake. The solutions must also be given a good shake before use in order to re-suspend the beads.

Before using Milli-Q water as buffer, it must be left standing still for a day or so. This is in order to let air bubbles out of the water.

Milli-Q has been used as the buffer for all experiments presented in this thesis except for the biological experiments in paper [3] of this thesis, where the beads were suspended in a TE-buffer solution (10 mM TRIS·HCl, 1 mM EDTA, 2.0 M NaCl).

After experiments, some beads are often stuck inside the microfluidic channel. Most often these can be flushed by applying a high flow rate obtained by applying maximum thumb pressure to the syringe. If this does not suffice, we usually flush the channel at a large flow rate with 0.1×SSC, 0.5% SDS solution. If further cleaning is needed a 1 M NaOH solution is sent into the system, and allowed to be there for a while. Subsequently, the channel can be flushed with Milli-Q water, and most beads will be removed.

6.3 Experimental setup

The setup in Fig. 6.3 may look complicated, as it has been developed over several years. The best way to explain the setup is to illustrate how experiments are performed with it.

Assume that all fluid tubes are initially filled with water, but all syringes are empty. Then the procedure goes as follows

1. With all valves in position A (as shown in Fig. 6.3), the rinsing syringe is filled pulling water from the water reservoir. (S1=A,S2=A,S3=A,S4=A)

2. S2 is shifted to position B, and the syringe in the syringe pump is filled pulling water from the water reservoir. (S1=A,S2=B,S3=A,S4=A)

3. S1 and S3 are then set to position B, and the sample is pulled from the sample reservoir using the Pull-in syringe. Enough sample is pulled from the reservoir to fill the sample tube completely, and some sample will flow into the valve and the tubing on the other side of the valve. Before pulling sample from the reservoir, the reservoir should be give a little shake to redistribute the sample in the reservoir. (S1=B,S2=B,S3=B,S4=A)

4. S2 and S3 are set back to position A, and the syringe pump is started. The sample in the sample tube is now being pushed through the chip and into the waste reservoir by the syringe pump. (S1=B,S2=A,S3=A,S4=A)

5. While the syringe pump is pumping, S4 is set to position B, and with S1 still in position B, the Pull-in syringe is emptied. (S1=B,S2=A,S3=A,S4=B)

6. Then S1 is shifted to position A, and a few milliliters are pushed out of the rinsing tube such that the tubes between the rinsing syringe and the righthand side waste are all emptied of sample. (S1=A,S2=A,S3=A,S4=B)

7. S4 is shifted back to position A, and the rinsing syringe is filled with water from the water reservoir. (S1=A,S2=A,S3=A,S4=A)

8. Once the syringe pump is finished S2 is set position B, and the whole system is flushed using water from the rinsing syringe with a high pressure. (S1=A,S2=B,S3=A,S4=A)

9. When the rinsing syringe is emptied, S2 can be set back to position A, and we are back, where we started and ready for a new experiment. (S1=A,S2=A,S3=A,S4=A)

The advantages of the setup are numerous, but its major strongpoint is that air bubble problems are greatly reduced. When the systems has been initially filled with water (this can be troublesome) there is no way that air bubbles can be introduced to the system, since the ends of the tubes going into the water and sample reservoirs can be submerged at all times, and there is never any need to disassemble any part of the system. The filter (2 in Fig. 6.3) on the tube for the water reservoir removes small air bubbles in the fluid and also dust particles from the water reservoir. All water going into the system is going

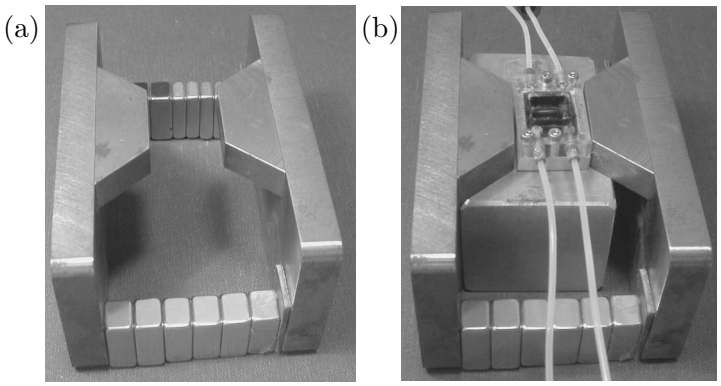

Figure 6.4: Magnetic circuit that supplies an almost homogenous magnetic field between the pole pieces. (a) The magnetic circuit consists of a number of permanent NdFeB magnets at each end. The magnetization of all permanent magnets point in the same direction. On the sides are thick iron plates that guide the magnetic flux to the pole pieces and across the gap. The magnetic field between the pole pieces are 50-70 mT. (b) The magnetic circuit with a chip holder and chip mounted between the pole pieces. The chip holder has a width of 20 mm.

through this filter. Unfortunately, no filter can be applied to the sample reservoir tube. That would remove the beads, but only small amounts of fluids are introduced this way. Another important feature of the setup is the sample tube, which is similar to an injection valve that allows us to introduce the same sample volume every time experiments are run. Using a length of tubing instead of a commercially available injection valve allows us to change the sample volume just by changing the length and/or inner diameter of the sample tube.

As mentioned this setup has been developed over the entire run of the Ph.D. work, and the one presented here is the latest version. In paper [3] an earlier and simpler version is used, but in order to control two sample streams two setups are needed. Three independent fluid streams were needed, and an integrated system was built where two independent fluid systems supplied the sample flows, and a simple fluid flow directly from a syringe pump (with filter) supplied the third flow stream - The barrier flow.

For the experiments in paper [5] one of the systems above was used to supply the sample flow, and a simple tube with fluid flow directly from a syringe pump (with filter) supplied the buffer stream.

6.3.1 Application of homogenous magnetic field

Fig. 6.4 shows the magnetic setup that is used to supply the magnetic field. The permanent NdFeB magnets magnetizes the plates on the sides that in turn magnetizes the pole pieces that supply an almost homogenous field between the pole pieces. This setup supplies 50-70 mT. One would think that so many permanent magnets would give a more powerful field, but unfortunately the NdFeB magnets are not very good flux guides themselves, so much of the magnetomotive force is lost by the field lines from the permanent magnets closing through air without ever going through the pole pieces.

At an early stage of this project, almost the same magnetic circuit was used. The only difference was that the permanent magnets were replaced by coils with soft magnetic cores. This setup would supply almost the same field or maybe even a little bit more, but the setup would also generate a lot of heat, and large power supplies were necessary. The author thinks that the simple setup with permanent magnets is preferable, although it is not as powerful or versatile as the setup with electromagnetic coils. When it was needed to flush beads from the system, and thus, zero field was needed, the chip and chip holder would simply be removed from between the pole pieces.

6.4 Data collection and characterization methods

All data for bead experiments in this project has been in the form of pictures taken using a Leica MZ FL III top-view stereo microscope equipped with a Sony DFW-X710 CCD camera or sometimes a BFI Optilas Serenity 2 camera and fluorescence filters and fluorescence lamp. The microscope is a stereo microscope with the option of going to small magnifications, such that entire chips can be seen in the microscope.

Analysis of experiments involves different forms of image analysis. Usually, the amount of captured magnetic beads are related to the amount of red, green, or blue within a picture or part of the picture, and the time-lapsed capture of magnetic beads can therefore be related to the amount of for example green content in an area of a picture. Picture analysis has mostly been performed using Mathematica, but also sometimes using Matlab.

This is illustrated in Fig. 6.5, where we measure the green content of the pictures as a function of time (measured as the picture number - pictures were taken with a set time interval). The figure also illustrates the importance of making real time picture analysis. A close inspection and comparison of Figs. 6.5(d) and (h) show that in (d) the green content grows steadily until no more beads enter the channel and the graph reaches a plateau. (h) on the other hand shows a much more ragged graph with several plateaus. The raggedness of (h) is a fingerprint of a small air bubble being stuck somewhere in the system. The bubble blocks the flow until the pressure on the bubble is large enough that the bubble is compressed so much that fluid is allowed to pass. Therefore, the fluid enters the channel as high flow rate bursts instead of as a steady flow, and the series of pictures taken in the experiment shown in (e-f) can thus not be used to assess the capture efficiency at the given flow rate. This also explains why capture seemingly has been much more effective for 80 μl/min than for 20 μl/min (for 20 μl/min the beads are spread all over the channel, for 80 μl/min the beads have all been captured in the left-hand side of the chip) - The flow rate in the bursts is simply much higher than both 20 and 80 μl/min.

The robustness of the fluidic setup against outside disturbances, and the real-time monitoring of capture dynamics give grounds to believe that experiments performed with the setup and the image analysis are reproducible.

Besides bead capture experiments, the fabricated chips have also been characterized after fabrication. This has been done using a Vibrating Sample Magnetometer (VSM), Scanning Electron Microscope (SEM), and Energy Dispersive X-ray analysis (EDX) inside the SEM. VSM was used to determine the magnetic properties of the chips; SEM and EDX

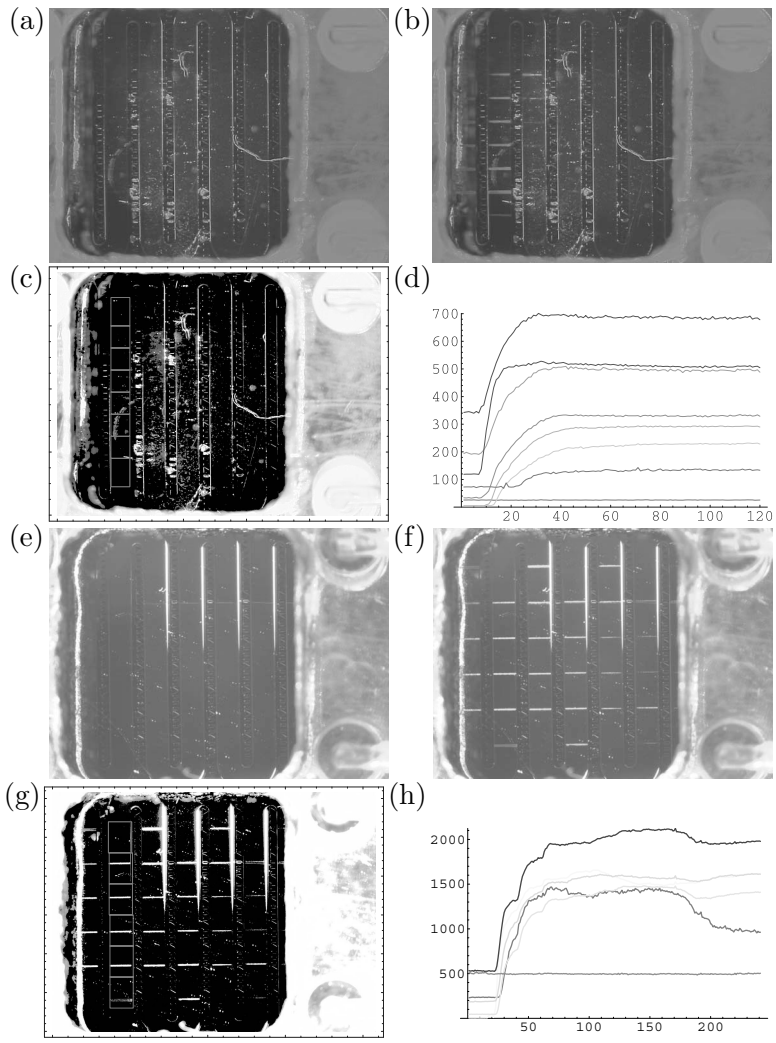

Figure 6.5: An example of image analysis. The channel width is 1 mm in every picture. (a)-(d) show data for an experiments performed with a flow rate of 80 μl/min. (a) shows the channel before beads start flowing. (b) shows the channel after beads have stopped flowing. (c) is the green content of (a) but with a threshold below which all greyscale pixel values are set to zero. Also defined on (c) is the analysis areas shown as square red overlays. (d) shows the development over time of the green content of the six analysis areas. A picture was taken every 2.5 s, and a total of 120 pictures were taken and analyzed. (e-h) show the same for an experiment with a flow rate of 20 μl/min. Here, however, (g) is the green content of (f). In (h) a picture was taken every 5 s, and a total of 240 pictures were taken and analyzed.

were used to characterize the electroplated materials, mostly permalloy. VSM, SEM, and EDX are all standard methods, so the specifics of the methods will not be discussed here.

Magnetic beads have also been characterized using the VSM. Most often the bead suppliers do not supply sufficient magnetic data, so sometimes it has been necessary to measure this data ourselves. A known amount of stock bead sample was taken from the

flask and transferred to a PCR tube using a pipette. The sample was left to dry with a magnet under the PCR tube such that the beads would go to the bottom of the tube. After the drying process the beads were fixated with glue. When the glue had dried, the PCR tube was placed in the VSM, and the magnetic properties were measured. Background measurements with PCR tube and glue were performed without beads and subtracted from the bead measurements. This method was developed by T. Lund-Olesen [121].

6.5 Experiments with the TI-systems

Three of the TI-system designs (refer to Table 4.1) were successfully fabricated, the designs with $h = 100$ μm, $h = 150$ μm, and one, that was designed with $h = 200$ μm, but as mentioned in Chapter 5, the width of the free-standing wall was not well-defined.

In order to compare these three designs, a series of experiments were conducted with the systems. A stock Invitrogen MyOne bead solution with carboxylic acid surface coating was diluted 500 times such that the bead concentration in the sample was 0.02 mg/ml. The magnet frame (Fig. 6.4(a))was set up such that a magnetic field of 50 mT was measured close to the pole piece, and 38 mT was measured at the center. This was measured without a chip holder in place with a hand held Gauss/Tesla meter (F.W. Bell model 4048).

The microscope camera settings were chosen such that for the experiments with the silicon systems the green color was enhanced, and blue and red were suppressed. This gave the kind of pictures shown in Fig. 6.5(a), (b), (e), and (f).

A setup similar to the one shown in Fig. 6.3 was used for the experiments. The sample tube was cut to a length of 18 cm, such that the sample volume including the sample in the switch valves would be approximately 100 μl. Experiments were performed with a number of flow rates for each of three systems. The experimental procedure was exactly as described above. The flow rates were set by the syringe pump, and the pumping time was chosen such that a total volume of 400 μl sample and buffer was pumped through the system. For most flow rates pictures of the chip were taken every 5 s, but for the flow rates above 75 μl pictures were taken every 2.5 s. Image analysis were not applied until after the experiments had finished for the first couple of experiments. After that, real-time image analysis was developed and was used for the rest of the experiments. Image analysis has been performed on all measurement series that we report in the Results chapter, and measurement series that showed irregularities such as the one shown in Fig. 6.5(h) have been discarded.

6.6 Discussion

In this chapter, the experimental method for bead experiments has been presented. The method has been developed over time, so not all experiments have been performed in this way, but the final version of the method seems to work very well.

Chapter 7

Results

This chapter sums up the results that have been obtained throughout this thesis. To some extent it will be a run-through of papers, but the chapter will also feature comparisons between the different systems, and the different systems will be be put into a more general context.

Only the results for magnetic separation are discussed in this chapter, so there will be no discussion of the Magnetic valve paper (Paper #8) and the paper on permalloy plating (Paper #9)

At the end of the chapter, the unpublished results on the TI-systems will be presented.

7.1 Systems with on-chip electromagnets

Microfluidic magnetic separators using on-chip electromagnets were fabricated during the author's master's thesis work [11]. Paper [1] was published based on these results, but some of the work following the recommendations of the paper referees was done during the Ph.D.

7.1.1 Paper #1: Microelectromagnet for magnetic manipulation in Lab-on-a-chip systems

This paper, [1], presented the fabrication and characterization of on-chip electromagnets. The paper also demonstrated the use of these electromagnets for capturing magnetic beads in a microfluidic system. Compared to earlier work on similar systems by others [130, 131, 40], this paper featured a microfluidic channel that was closer to the electromagnets, and both electromagnets and magnetic separation system were in the author's opinion characterized more thoroughly. Also, this paper presented separation of magnetic beads from a flow, whereas Choi *et al.*, [40], presented separation of beads from a non-moving fluid.

In order to compare these systems with some of the later systems, some data must be extracted from this paper. Most importantly the maximum field gradient in the channel was 13 T/m for the large systems, and 42 T/m for the smaller systems. A magnetic field of a maximum of 5.3 mT for the larger systems and 10 mT for the smaller systems were

achieved. This means that the beads were magnetically unsaturated, which means that $m = V\chi_0 H$, so for MyOne beads this gives force estimates of 0.05 pN and 0.3 pN for the large and small systems, respectively. Bead capture was demonstrated at a flow rate of 2 μl/min, which in a 1.5 mm wide and 100 μm high channel corresponds to an average linear flow rate of 0.2 mm/s.

7.1.2 Paper #2: Magnetic separation in microfluidic systems using microfabricated electromagnets – experiments and simulations

This paper, [2], featured a quite thorough discussion of the theory behind magnetic beads moving in a straight microfluidic channel similar to the discussion presented in Chap. 3. The authors felt that such a discussion was missing from literature.

The paper demonstrated good qualitative agreement between theory and experiments. Simulations for a cylindrical electromagnet showed that the magnetic field from the on-chip electromagnets would be largest near the edge of the inner part of the magnetic yoke. Experimentally, it was found that the beads near the corners of the inner part of the square magnetic yoke. Since these corners are two-fold edges, it seems reasonable that the corners are even more attractive than pure edges for magnetic beads.

It is interesting to note that the bead capture patterns of papers, [1] and [2] are different. In [1] the beads are captured in lines going across the channel, whereas in [2] they are captured in spots near the corners. The only notable difference between the two experiments is that the flow rates are 2 and 1 μl/min, respectively. It has not been attempted to find the reason for this discrepancy.

7.2 Systems with magnetic elements next to the channel

Shortly after the beginning of the Ph.D. the author started looking into designs where soft magnetic elements were placed next to a microfluidic channel. It had been attempted to fabricate such systems in SU-8 in a bachelor project within the group. Unfortunately, this attempt failed.

At the IEEE Nanoscale systems and Systems Integration conference in February 2004, I met Dr. Gary H. Bernstein, who directed my attention to the work of his Ph.D. student, Jie Wu, and himself fabricating electroplated structures using silicon as plating mould [122]. This seemed to be a possible path for fabricating structures with soft magnetic elements next to a microfluidic channel, so work was initiated on developing our own fabrication process based on this idea. At the end of the Summer 2004, this work was finished and the result was the basic silicon fabrication scheme presented in Chap. 5.

7.2.1 Paper #3: Microfluidic magnetic separator using an array of soft magnetic elements

The first design of this type of magnetic separator was the simple design presented in paper [4]. In this paper bead capture is measured using fluorescence microscopy. Fig. 7.1 shows Figs. 1 and 5 of the paper, and it illustrates the chip design and the fluorescence

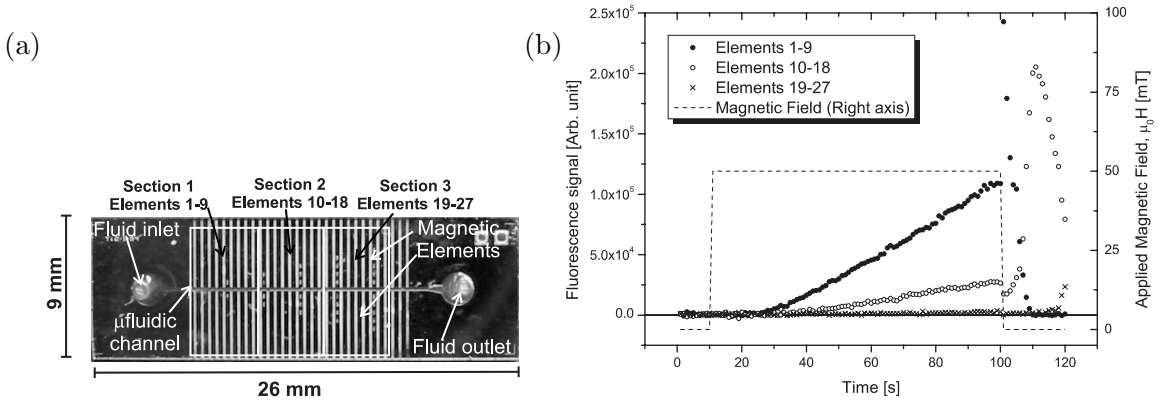

Figure 7.1: (a) Picture of the magnetic separation chip showing the position of the microfluidic channel and the passive soft magnetic elements. The external homogenous magnetic field is applied vertically in the plane of the paper. Also, it is shown how the chip is divided into sections. (b) This figure shows the development of the fluorescence signal from the three sections as well as the applied magnetic field as a function of time.

measurements. The main conclusion of the paper is that since there is no measurable fluorescence signal from beads in section 3, all beads must have been captured in sections 1 and 2.

The magnetic field gradient in the middle (horizontally) of the microfluidic channel is zero due to symmetry. However, it is estimated from Comsol Multiphysics calculations that 10 μm from the channel wall magnetic fields of $\approx 1.5 \times 10^5$A/m and magnetic field gradients of ≈ 3 kT/m exist. For a saturated MyOne bead this corresponds to a force of 0.1 nN, which is 3-4 orders of magnitude better than what was obtained with the on-chip electromagnets.

In the experiment all beads are separated from the flow at a flow rate of 5 μl/min, and the average linear flow velocity is 5 mm/s.

7.2.2 Paper #4: On-chip magnetic bead microarray using hydrodynamic focusing in a passive magnetic separator

The microsystem in this paper, [3], has the same magnetic design as the previous paper, but the microfluidic system has been made with three inlets to allow for hydrodynamic focusing. This has two advantages over the simpler microfluidic system. Having two sample streams separated by a barrier stream in the middle allows us to place different sets of magnetic beads on either side of the channel without cross-contamination. Also, the magnetic force is zero in the middle of the channel, so having the beads in sample streams closer to the channel walls, and thus the magnetic elements, facilitates more efficient bead capture.

With this system, we were able to demonstrate a magnetic bead microarray, where two sets of magnetic beads functionalized with wild type (WT) and mutant type (MT) DNA capture probes, respectively, are placed on either side of a microfluidic channel.

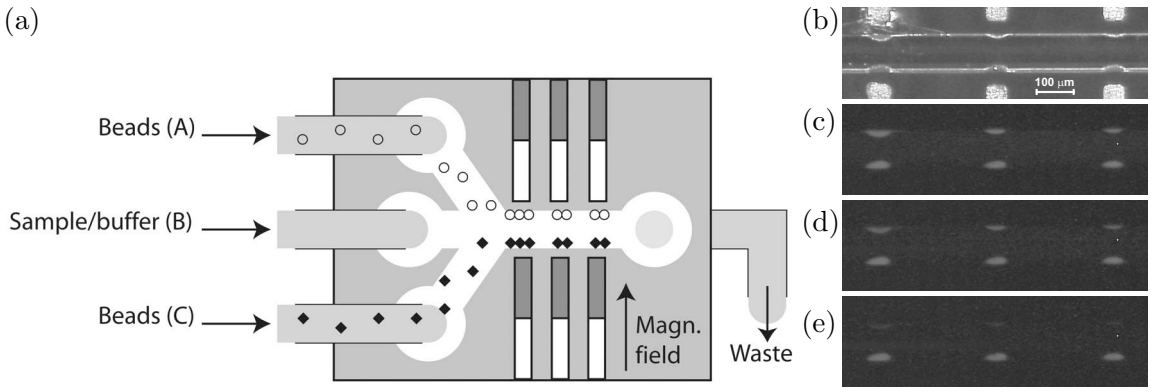

Figure 7.2: (a) The working principle of the magnetic bead microarray. The three inlets, the soft magnetic elements and the direction of the applied field are indicated. Two sample streams, (A) and (C) are separated by a barrier flow, (B), such that the wild type (WT) DNA coated beads from inlet (A) are placed on one side of the channel, and the beads with mutant (MT) type DNA from inlet (C) are placed on the opposite side of the channel. (b) Normal micrograph showing that beads are captured on both sides of the channel. (c) Cy5 micrograph of the same channel section after hybridization with CY5-labeled WT target. (d) Same channel section after washing with 0.1 6 SSC,0.5% SDS for approximately 2 min, (e) Same section after further washing for 2 min.

Subsequently, Cy5-labeled WT-target is sent in through inlet (B) with no flows in (A) and (C), and when the target has entered the channel, the flow is stopped and the target is left to hybridize for an hour. After a stringency wash, it is clearly seen that the wild type DNA has bound to the WT-DNA on the beads, but not to the MT-DNA on the bottom side wall. This demonstrates the microarray capability, and that a Single Nucleotide polymorphism/point mutation detection can be performed. In the paper, it was also demonstrated that the systems could be cleaned, and subsequently new experiments could be performed without experiment to experiment cross-talk. Furthermore, the microarray is generic and any two surface functionalizations that work with magnetic beads can be applied to the sides of the microfluidic channel.

A Comsol Multiphysics calculation shows that the magnetic field gradient 5 μm from the wall is approximately 0.8 kT/m. Magnetic beads were separated from the flow in sufficient amounts at a total flow rate of 30 μl/min, which in this system corresponds to an average linear velocity of 4 cm/s.

7.3 Towards a programmable magnetic bead micro array

At an early stage of the project my supervisor, Ulrich Krühne from Danish Technological Institute, suggested that we thought about making a programmable magnetic bead microarray.

The idea of a magnetic bead microarray was also used in paper [3], which was discussed above. Below are two more publications that pursue that general idea.

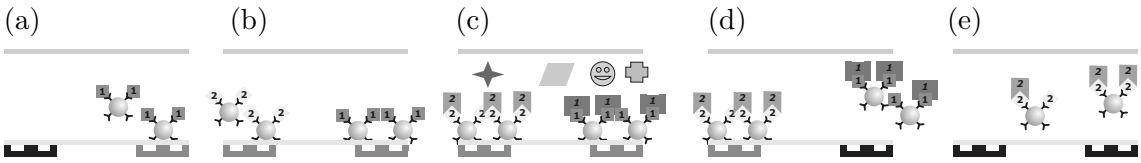

Figure 7.3: The schematic demonstrates how an addressable array can be applied to achieve a magnetic bead microarray in a microfluidic channel. In (a), magnetic beads functionalized with antibody 1 are captured on the rightmost electromagnet (Blue indicates that the electromagnet is turned on). In (b), beads with antibody 2 are captured on the leftmost electromagnet. A suspension containing many different species of antigens are flown through the channel in (c). The target antigens of antibody 1 and 2 (if present in the suspension) will bind to their antibodies. Upon rinsing with buffer the magnetic beads on the rightmost electromagnet are released and antibody 1 is collected along with its antigen in (d). In (e) the magnetic beads on the leftmost electromagnet are released and antibody 2 along with its antigen is collected.

7.3.1 Paper #5: Selective magnetic bead capture using an addressable on-chip electromagnet array

The idea of a magnetic bead microarray was first demonstrated at the MicroTAS conference in Malmö Sweden [10]. The systems with on-chip electromagnets were used for selective bead capture.

Proof of concept was demonstrated that one set of beads could be captured on one electromagnet, then another set of beads on another electromagnet. Subsequently, the two sets of beads could be independently released. There was no investigation of cross-talk between the two sets of beads. Fig. 7.3 demonstrates the working principle of a magnetic bead microarray and/or parallel assays with this design.

7.3.2 Paper #6: Towards a programmable magnetic bead microarray in a microfluidic channel

The pursuit of a programmable magnetic bead array inside a microfluidic channel raised the need for addressability. In Fig. 7.2 the ability to place two sets of differently functionalized beads on either side of a microfluidic channel is demonstrated. However, it is desirable to have more than two independent capture sites such that beads with more than two different surface functionalizations can be placed at different spots in a microfluidic channel. Therefore, the idea with on-chip electromagnets was revived. Electromagnets have the advantage that they can be switched on and off independently, whereas the capture sites in Fig. 7.2 are all on or off at the same time, since they are controlled by an external magnetic field common to all the elements.

On-chip electromagnets would not give sufficient forces, so instead a hybrid system was designed, where an external magnetic field magnetizes the magnetic beads and couples with the field from current lines buried in the backside of a silicon wafer below a microfluidic channel. The magnetic field gradients in this system is only up to 60 T/m at the bottom of the microfluidic channel, but since an external magnetic field saturates the magnetic beads this system still generate magnetic forces on MyOne beads that are ≈30 times larger

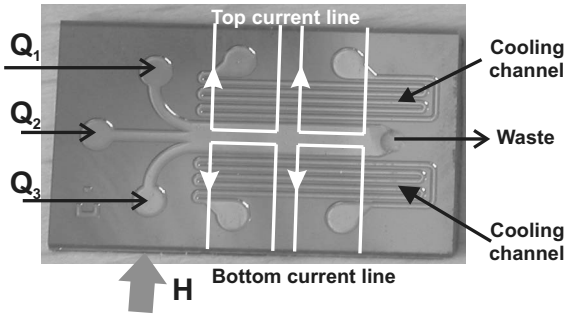

Figure 7.4: Chip for making magnetic bead microarrays. Four current lines are buried in the back side of the chip (indicated in white). A homogenous magnetic field is applied across the chip in the plane of the chip and couples with the field from the current lines. There are three fluid inlets to allow for hydrodynamic focusing, such that different bead streams can be guided to each side of the channel for parallel loading of the magnetic capture sites (on top of the current lines). Cooling channels are included on the chip for temperature control and to counteract the joule heating from the current lines.

than the ones generated by the large on-chip electromagnets.

In the paper, [5], we presented a system, where current wires are buried beneath a microfluidic channel. See Fig. 7.4. In the paper, it is demonstrated that this systems is capable of capturing magnetic beads, and that fluorescent and non-fluorescent magnetic beads can be placed selectively at the top and bottom side of the channel (refer to Fig. 7.4).

One disadvantage of the design presented in Fig. 7.4 is that the magnetic force is perpendicular to the fluid flow, and thus no force opposes the fluid force. This means that the beads roll along the channel and the length of the current line without resistance. Originally, the idea was that four individual sets of beads should be placed in the channel. Unfortunately, the rolling of the beads meant that downstream cross-talk was unavoidable. This meant that this system could not deliver the multiple capture site functionality, it was designed for. Chips of different designs were fabricated, but unfortunately the chips have never been tested. Some of these designs did have magnetic forces that opposed fluid flow, such that rolling problems would most likely have been eliminated.

7.4 Systems with multiple length scales

It should be apparent from the previous discussion that the magnetic field gradients is the most important characteristic feature of magnetic separation systems. Larger gradients give higher bead capture efficiency. At this stage it is thus natural to think that large magnetic bead gradients is the only important feature of magnetic separation systems. However, if the magnetic field gradient is large, the range of the gradient and force is short. For instance, in the magnetic valve paper, [6], the maximum field gradient is $\approx 10^5$ T/m, and A.R. Urbach of the Whitesides group even presented a field gradient of $10^6 - 10^7$ T/m [**?**], but the problem with such gradients is that a field of one Tesla reduces to zero over a distance of a few hundred nanometers, and this makes such a

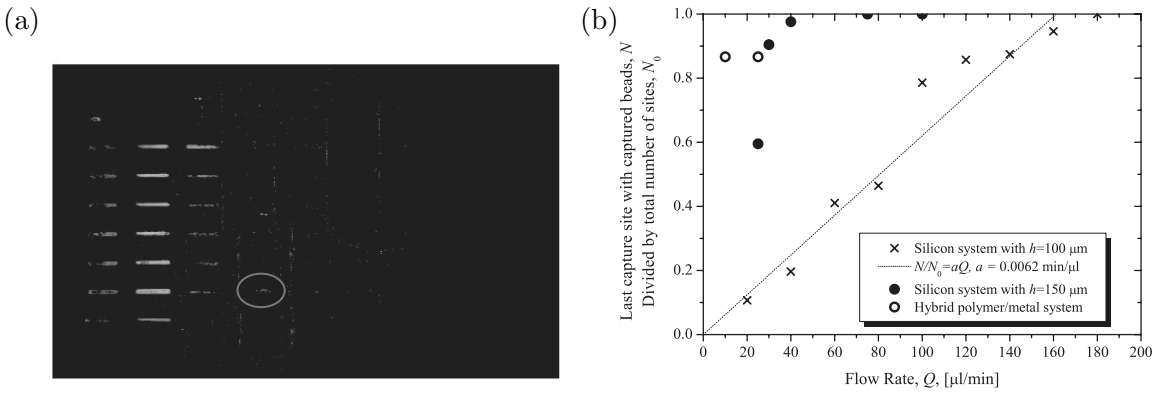

Figure 7.5: (a) Picture of captured beads after image analysis (Described in the text) for a bead capture experiment with a silicon system with $h = 100$ μm and a flow rate of 80 μl/min. The red circle indicates the last line of captured beads. (b) The graph shows the capture site at which the last beads were captured as a function of flow rate. A straight line fit has been included for the capture of beads with the silicon systems with $h = 100$ μm.

gradient irrelevant for separation of magnetic beads in microfluidic systems, where the characteristic length scale for the fluid channel is usually hundreds of μm.

Large magnetic forces and and short range are inseparable, and we have seen that it is the characteristic length scale of the structures that create the magnetic field gradients that determine the order of magnitude of the gradients and the range of the force.

7.4.1 Paper #7: Theoretical analysis of a new efficient magnetic bead separator utilizing magnetic structures with multiple length scales

Combination of magnetic structures with different length scales can overcome this problem. In paper [8] of this thesis, a system was designed, where millimeter sized permanent magnets create long-range magnetic gradients ($\approx$ 450 T/m), and thin ($\approx$ 5 μm) soft magnetic elements placed very close to the channel bottom ($\approx$ 5 μm below) create strong but short-range magnetic gradients ($\approx$ 15 kT/m). In this system, magnetic beads are drawn towards the bottom of the microfluidic channel by the gradients from the permanent magnets, and they are ultimately captured and held by the gradients from the soft magnetic elements. The holding force opposing the fluid drag on the beads, is very small in the absence of the soft magnetic element, but the addition of the soft magnetic elements increases this holding force by a factor of approximately 400.

7.5 Systems with magnetic elements under the channel (TI-systems)

Magnetic separation experiments have been performed with the TI-systems of the three different designs that were successfully fabricated. The experiment method was described in the previous chapter.

The picture analysis method was not developed until midway through this run of experiments, so some series of pictures have been discarded after completion of the experiments. This applies to many of the experiments with $h = 150$ μm, so only a few data points are available from these experiments. Unfortunately, the chips had a tendency to break, so it was not possible to redo the experiments. Also, there was problems with the permalloy plating bath during fabrication, so the thickness of the permalloy layer is unknown.

The hybrid polymer/metal systems have only been tested at two flow rates. It took very large pressures to rid these systems of captured beads after experiments, and the large pressures caused the microfluidic (polymer) part to delaminate, so further experiments have not been possible.

The experiments with the chip with $h = 100$ μm have been quite successful, and a number of good data sets have been obtained.

Fig. 7.5 shows the results of the experiments. When an experiment has been 'approved' by the image analysis method described in Chap. 6, the green content of every pixel in the first image in the series was subtracted from the green content in the last image and the result was divided by the sum of the green contents of the two images. Then, a threshold was applied, such that all pixel values below 0.1 were set to zero. This yields a greyscale image like Fig. 7.5(a). From this picture, it was determined where the last visible line of captured beads was (marked with a red circle on the figure, and this was noted as the result of the experiment with that flow rate. Fig. 7.5(b) shows the results for all the different successful experiments.

It is seen from the figure that the system designs with $h = 100$ μm captures beads more efficiently than the two other types of systems. Also, there seems to be a linear relation between the element number, where the last beads are captured and the the flow rate. This corresponds well with the result given in Eq. (C.9b) of Appendix C, where it is assumed that the force is constant. In these experiments the force field is not constant, but if the force field is primarily in the y-direction or averages to zero in the x-direction, then the effect of the force field will be to pull the bead towards the bottom with a speed that depends on position, but not on flow rate. In this case, the time before the bead hits the bottom is independent of the flow rate, and thus increasing the flow rate, which is proportional to the fluid velocity everywhere in the fluid channel, will just increase the length that a bead is carried by the fluid flow before reaching the bottom of the microfluidic channel. Therefore, it seems reasonable to expect a linear relation between the element number and the flow rate.

Insertion of the slope found in Fig. 7.5(b), and replacing N/N_0 on the y-axis with x_0/L, where x_0 is the traveled length before capture, refer to Eq. (C.9b), and L is the length of the channel without the turns ($L = 63$ mm), then an average force can be calculated using Appendix C, and one gets a force of 0.4 pN, which is within a factor of 6 of the number, given in Table 4.1 as the average force in the middle of the channel. Considering the simplicity of the models in Appendix C, the agreement between the model and these experiments is impressive.

A peculiar fact of these experiments is that it seems that the two outer capture sites, i.e. the ones at the top and bottom of Fig. 7.5(a) are not efficient at bead capture. Eight capture lines should be seen in the vertical direction, but only six are present. This is an

effect that is not clearly understood, but as it is seen on Fig. 5.1 on page 43 the serpentine fluid channel extends further out on the chip than the magnetic elements, and thus the outer capture sites are at the outside edge of the periodic structure, and it is obvious that the properties of such a capture site are different from the properties of a capture site that lies in the midst of the periodic structure. In the experiments with the systems with $h = 150$ μm the first capture site that a bead encounters in a vertical channel captures many beads, whereas the last capture site still captures no beads. This is shown in Fig. 7.6.

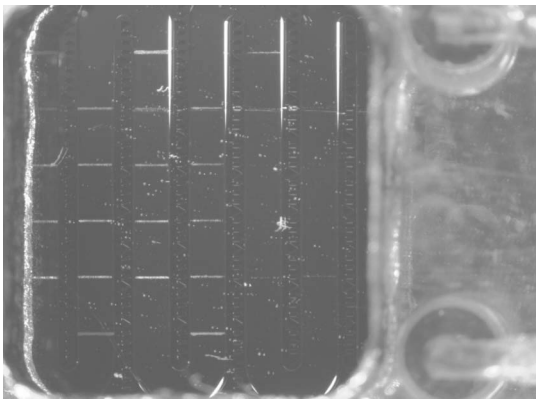

Figure 7.6: Micrograph of captured beads in a system with $h = 150$ μm. The beads enters the chip in from the top left. It is seen that beads are captured on the first capture site that a bead encounters in a vertical fluid channel, but not on the last.

The silicon TI-systems with $h = 100$ μm have proven to be effective for bead capture even at relatively high flow rates. Fig. 7.5 shows that the system with $h = 100$ μm has a 100 % capture efficiency for flow rates below 100 μl/min and maybe even higher. The two other systems are not as effective, but still have 100 % capture efficiency at flow rates ≈ 20 μl/min.

These systems have the advantage over the systems of papers, [3] and [4] that the captured bead collections are available for visible inspection in a microscope at the channel bottom. Also, it is possible to drive a bead solution into the channel at a very high flow rate (≈ 100 μl/s), and when the beads have entered the channel, the flow can be stopped, and the beads in the channel will quickly settle in almost even amounts at all the capture sites in the channel. This allows for quick preparation of a system with functionalized beads at the bottom, where 100 % capture is irrelevant. A sample can then be applied to the channel and bind to the captured beads. Subsequently, the bound sample can be studied with appropriate optical techniques.

The system with $h = 100$ μm has a calculated average field gradient in the middle of the fluid channel of 95 T/m, and a maximum downwards field gradient at the bottom of the channel of 1.6 kT/m.

7.6 Discussion

In this chapter the different magnetic separation systems that have been investigated during this Ph.D. project have been investigated and compared.

The systems with on-chip electromagnets were quite inefficient for bead capture, but they do have the advantage of addressability.

The systems with long soft magnetic elements next to the microfluidic channel have large magnetic field gradients compared to the on-chip electromagnets, and are much more efficient at bead capture. They have the disadvantages that the microfluidic channel must be narrow, since the range of the magnetic field gradient is limited, and that the bead collections at the channel side walls are not readily available for optical inspection.

The TI-systems have the advantage that the soft magnetic elements are below the channel, so the beads are captured at the channel bottom and are available for optical inspection. Also, the channel can have any width, but the channel height is limited. This design makes it possible to have a serpentine channel such that a longer capture length can be achieved.

It has been attempted to fabricate systems for programmable magnetic bead arrays. Although promising results have been obtained, this goal has not quite been reached.

Chapter 8

Discussion and Outlook

In this chapter, the author will give his view on the further development of magnetic separation in microfluidic systems, and how the results of this thesis can be utilized. Recommendations are given for the choice of magnetic design based on the desired application.

8.1 Choice of system type

When designing a microfluidic magnetic separation system, the first thing the designer needs to consider is, which type of system to use, i.e., if the system should be active, passive, a magnetic bead plug, or a hybrid system.

The author recommends that it is never considered to make an active system with on-chip electromagnets as the only source of magnetic fields and gradients. Active systems are difficult and expensive to fabricate, they generate heat on-chip, and most importantly, they generate small magnetic fields compared to saturation magnetizations of both magnetic beads and soft magnetic materials, and thus the available magnetic forces are small. The addressability is an advantage of active systems, but this is also available in hybrid systems.

8.1.1 Passive systems

If it is needed to capture and hold many magnetic beads in a microfluidic channel, where the beads flow through the channel at a high velocity, passive systems should be chosen.

Several passive systems have been designed and tested in this thesis. The systems with long soft magnetic elements next to the microfluidic channel with three inlets [3] capture beads at relatively high flow rates, and it is possible to capture two differently functionalized sets of beads on the side walls. This makes it possible to make two parallel assays in the same channel. This is useful if, for instance, a positive test is needed.

The systems with soft magnetic elements adjacent to the microfluidic channel have the disadvantages that the the beads are captured on the side walls, and thus, they can be difficult to inspect optically. Also, there is an upper limit to the width of the microfluidic channel, since the magnetic force decays rapidly away from the channel side walls. The upper limit of the width of the channel, and the finite thickness of a silicon wafer set an

upper limit for the channel cross-section, and thus it may be difficult to achieve separation with high volumetric flow rates in such systems.

The two disadvantages of the systems with soft magnetic elements next to the microfluidic channels are eliminated with the TI systems. The capture sites in these systems are at the bottom of the microfluidic channel, and thus they are readily available for optical inspection, and the microfluidic channel can be as wide as needed. In these systems on the other hand, it is not possible to place differently functionalized sets of beads without cross-talk.

Following the lines of Lund-Olesen *et al.*, [77], the capture efficiency of the TI systems may be further enhanced by the addition of microfluidic passive mixer structures, e.g. diagonal or herringbone mixers, in the bottom of the microfluidic channel in the turns of the serpentine channel.

The TI systems capture beads efficiently, and it is possible to fill all capture sites within seconds if 100 % bead capture is not necessary. Subsequently, sample can be loaded at a flow rate of 100 μl/min without tearing loose the captured beads. The entire channel volume is approximately seven microliters, so this operation can also be completed within a few seconds. While the sample reacts with the bead collections, and the flow is stopped, it may be advantageous to turn off the external magnetic field. This will allow beads to diffuse into the sample, while the sample also diffuses towards the bead collections. Upon turning the field back on, the beads will quickly return to the capture sites. When the sample has been allowed to react long enough (depending on the given chemistry or biology) the field is turned back on, and after a few seconds, the channel can be flushed with buffer and the result of the assay can be detected via fluorescence or other methods. This protocol constitutes a fast and efficient way to perform assays using magnetic beads in a microfluidic channel, and it would have been interesting to test this method.

For very sensitive assays, where very low concentrations should be detected in a sample, the strictly diffusion based mixing described above may be insufficient, but assay sensitivity can be enhanced by allowing a flow going back and forth in the microfluidic channel with zero net flow. The addition of the passive magnetic structures in the turns of the microfluidic channel will enhance this effect. Another route to sensitive assays is mixing of the beads and sample in a channel with passive mixers before the beads and sample enter the magnetic capture area.

Recently presented papers with plugs or chains of magnetic beads, mentioned in the introduction, describe another route towards very sensitive assays. Whether such systems are more or less sensitive than systems with integrated mixers remains to be determined.

The systems with several magnetic length scales that were proposed in paper [8] of this thesis offer rapid capture of large amounts of beads. Dr. Minqiang Bu and Troels B. Christensen have started making experiments with systems of this kind, and the first results indicate that it is possible to obtain close to 100 % bead capture in a 200 μm high and 5 mm wide channel at a volumetric flow rate of 1000 μl/min. However, since the permanent magnets are integrated in to the chip holder captured beads cannot be released without disassembly of the chip and holder. These systems are well-suited for applications, where a large number of beads needs to be separated from a large sample volume in a short time. In this application, the beads and sample are mixed before entering the microfluidic

separation chamber.

8.1.2 Hybrid systems and programmable arrays

Compared to the passive systems, the hybrid systems have the advantage that the capture sites can be turned on and off individually, and capture sites that normally attracts magnetic beads can be made repelling by reversing the current.

Hybrid systems are thus the ideal choice for applications were more advanced magnetic bead manipulation is needed. As a simple example, the procedure shown in Fig. 7.3 cannot be performed in a passive system, but it is possible in a hybrid system.

Compared to active systems, hybrid systems have more functionalities, larger forces can be applied, they can be simpler to fabricate. This is why, active systems should never be used.

The array functionality that was our original motivation for investigating hybrid systems was never quite achieved. Systems were fabricated that had multiple individually addressable capture sites, and these were able to attract magnetic beads. Unfortunately, the capture sites were not capable of holding on to captured beads in a flow. It should, however, be possible to solve this problem in a future design.

We have presented a functional programmable array with two capture sites and two sets of differently functionalized magnetic beads using the passive system discussed above. Such systems create stronger magnetic field gradients than is readily available with the hybrid systems, and maybe fluidics in the passive systems can be designed such that more than two individually addressable capture sites become available.

It is unclear which of the two paths towards a programmable array is best, hybrid systems or passive systems with advanced fluidic designs. It has been discussed, however, if the capture sites need to be in the same channel; maybe it is sufficient, if the different sets of beads can be captured in different but parallel channels, and the sample can be applied to all channels simultaneously. In this case passive systems are definitely the better choice.

8.2 System fabrication

In this work, most systems have been fabricated using silicon micromachining, where the microfluidic channels have been defined in silicon using Deep Reactive Ion Etching. This is an expensive fabrication procedure at least for fabricating small numbers of chips, especially if the chips are intended for single-use.

Polymer fabrication in the form of SU-8 fabrication was tested with success for some designs. This is a faster and cheaper fabrication method, but as mentioned it may be difficult to seal the channel properly, since no bonding method for SU-8 is available that is as effective as anodic bonding for silicon and pyrex. Also, the surface chemistry is different from silicon systems, so technology is not immediately transferrable.

Polymer fabrication of fluidic systems and metallic magnetic parts were also successfully demonstrated. Fabrication of the metal part could not be completed within the desired tolerances, but still an operational magnetic bead capture system was fabricated.

The polymer parts are fast and cheap to fabricate, but also here, sealing of the microfluidic channels proved to be problematic.

The Whitesides group has demonstrated polymer fabrication based on soft lithography for many applications [132], and it is certainly also be a possible route for fast and cheap polymer fabrication of microfluidic systems for magnetic separation. In ref. [75] a fabrication scheme is demonstrated using soft lithography that is capable of creating comb permalloy structures similar to the ones we have used for the systems with magnetic elements next to the channel, [3, 4].

Polymer fabrication is most likely necessary for commercial single-use systems, so these fabrication methods should be further developed and tested. However, we have shown in ref. [3] that it is possible to clean and re-use the silicon systems, so for laboratory applications, where the systems can be cleaned and re-used, silicon fabrication may be the best choice.

8.3 Outlook

If time had allowed for further studies, it would have been my number one priority to make a more thorough comparison of the three different realized versions of the TI systems. The design with $h = 100$ μm has been properly characterized, but it would have been very interesting to have more good data points for the two other systems.

As mentioned above, several tests could have been performed with the TI systems, and it would have been interesting to test the described assay protocols.

The systems with multiple magnetic length scales is a promising idea for enhanced bead capture using a combination of long-range forces for beads attraction and short ranged forces for bead holding. It would have been interesting to study such systems in more depth both numerically and experimentally.

The goal of a programmable magnetic bead microarray with more than two capture sites in a microfluidic channel was not achieved, but some of the fabricated hybrid systems were never tested, and it would have been interesting to make experiments with these, and also to make a second generation of the designs, where the problems of the first generation had been addressed. I believe that it is possible to make such a system.

Chapter 9

Conclusions

In the present Ph.D. thesis, a model for magnetic bead movement in a microfluidic channel has been presented, and the limits of the model have been discussed. It was also shown that the best measure when different magnetic separators are compared is the effective magnetic field gradient, **G**.

It was described how numerics have been used to aid the design of microfluidic magnetic separation systems. As an example, the optimization of the TI systems was shown. It was demonstrated how scaling of the geometric parameters could speed up calculations and increase the general applicability of the optimization. In the end, five different designs of the TI systems were chosen to be fabricated.

A robust fabrication scheme has been developed, and it has been applied with different variations for most of the systems fabricated during this thesis work. Other fabrication methods have been tested with moderate success.

An experimental setup for magnetic separation experiments has been developed. It has been coupled with an image analysis program to facilitate real-time monitoring of the experiments. The set-up and experimental protocol have been described in detail, and it has been illustrated how image analysis was used to monitor the progress of experiments.

Active magnetic separators with on-chip electromagnets have been successfully demonstrated [1], the flow of magnetic beads inside such a device has been calculated and compared to experiments [2]. A conceptual idea of using active systems for parallel assays in a microfluidic channel has been demonstrated [10].

Passive magnetic separators with on-chip soft magnetic elements next to a microfluidic channel have been demonstrated, and the capture efficiency has been measured [4]. Using such systems combined with hydrodynamic focusing, it was demonstrated that beads with different surface functionalizations can be selectively placed on either side of a microfluidic channel. Finally, it has been demonstrated that the constructed microarray can be used for 'single nucleotide polymorphism' / 'point mutation detection' with selectivity comparable to regular spotted DNA microarrays [3].

A hybrid design, where the magnetic field from on-chip current lines couples with an external homogenous magnetic field has been demonstrated. The external field magnetizes magnetic beads, and the on-chip current lines create magnetic field gradients that facilitate

bead manipulation. It was demonstrated that this system was also capable of selective capture of two different sets of magnetic beads. [5]

Another type of passive magnetic separator where the soft magnetic elements are placed beneath the microfluidic channel was demonstrated, and it was shown that it had a bead capture efficiency of 100 % for flow rates up to 100 μl/min, which corresponds to a linear velocity of approximately 1.7 cm/s.

A new design of passive magnetic separators was demonstrated, where two different length scales for the magnetic structures were utilized. Permanent magnets with a side length of 2 mm create long range forces, and 5 μm thick permalloy elements very close to the microfluidic channel create strong field gradients near the bottom of the channel. [8]

Finally, it was discussed how to further develop magnetic separation systems in microfluidic systems based on the research presented in this thesis, and recommendations were given for the choice of magnetic design based on the desired application.

Appendix A

Magnetic force on a magnetic bead in an arbitrary magnetic field

When discussing magnetic force on a magnetic bead, one often starts out by assuming that the magnetic field is constant across the magnetic bead, calculate the magnetization, and finally one multiplies with the magnetic field gradient to obtain the force. It has always been a nuisance to the author that on one hand you assume that the field is constant, but on the other hand a gradient in the field is necessary for a finite force to be present. In this appendix the validity of this assumption is investigated by the calculation of the total magnetic field around a bead in an applied linear gradient magnetic field and a discussion of the force calculation. In the end the applicability of the assumption above is discussed, and it is shown that this assumption is perfectly valid to first order.

We wish to calculate the magnetic force on a magnetic bead in a general linear gradient magnetic field. We require that no free currents are presents such that the magnetic field can be written as the gradient of a magnetic scalar potential $\mathbf{H} = -\boldsymbol{\nabla}\varphi$. Also, we require the magnetic bead to consist of a linear material, such that the susceptibility is a constant scalar, χ_0, and thus $\boldsymbol{\nabla} \cdot \mathbf{B} = 0$ reduces to

$$\nabla^2 \varphi = 0, \tag{A.1}$$

which is just the Laplace equation.

We choose our coordinate system such that the bead is centered at the origin, and thus the system is rotationally symmetric.

First we need to introduce a bit of mathematics. Given one solution, ϕ_0, to the Laplace equation, more solutions can be generated by taking the gradient of the solution

$$\begin{aligned} &\boldsymbol{\nabla}(\nabla^2 \phi_0) = \boldsymbol{\nabla} 0 \Rightarrow \\ &\nabla^2(\boldsymbol{\nabla}\phi_0) = \mathbf{0}, \end{aligned} \tag{A.2}$$

where it is seen that all three components of the gradient of ϕ_0 are also solutions to the Laplace equation, and thus any linear combination of the components will also be a solution. It has been used that $\boldsymbol{\nabla}$ and ∇^2 are commutative operators.

Following these lines, it can be shown that given one scalar solution, ϕ_0, then an infinite number of solutions can be generated by the following formulas:

$$\boldsymbol{\phi}_{n,a} = \underbrace{\boldsymbol{\nabla}\boldsymbol{\nabla}\ldots\boldsymbol{\nabla}}_{n}\phi_0, \tag{A.3a}$$

$$\boldsymbol{\phi}_{n,b} = r^{2n+1}\underbrace{\boldsymbol{\nabla}\boldsymbol{\nabla}\ldots\boldsymbol{\nabla}}_{n}\phi_0, \tag{A.3b}$$

where $\boldsymbol{\phi}_{n,a}$ and $\boldsymbol{\phi}_{n,b}$ are n'th order tensors, where every element of the tensor is a solution.[1]

Now, we take one scalar solution to Eq. (A.1)

$$\phi_0 = \frac{1}{r}, \tag{A.4}$$

and generate multiple solutions by using Eq. (A.3)

$$n = 0, \quad \phi_{0,a} = \phi_0 = \frac{1}{r}, \tag{A.5a}$$

$$\phi_{0,b} = r^1\phi_0 = 1, \tag{A.5b}$$

$$n = 1, \quad \boldsymbol{\phi}_{1,a} = \boldsymbol{\nabla}\phi_0 = \frac{\mathbf{r}}{r^3}, \tag{A.5c}$$

$$\boldsymbol{\phi}_{1,b} = r^3\boldsymbol{\nabla}\phi_0 = \mathbf{r} \tag{A.5d}$$

$$n = 2, \quad \overleftrightarrow{\boldsymbol{\phi}}_{2,a} = \boldsymbol{\nabla}\boldsymbol{\nabla}\phi_0 = \frac{\mathbf{rr}}{r^5} - \frac{\overleftrightarrow{\mathbf{I}}}{3r^3}, \tag{A.5e}$$

$$\overleftrightarrow{\boldsymbol{\phi}}_{2,b} = r^5\boldsymbol{\nabla}\boldsymbol{\nabla}\phi_0 = \mathbf{rr} - \frac{r^2}{3}\overleftrightarrow{\mathbf{I}}. \tag{A.5f}$$

We now construct the most general linear gradient magnetic field

$$\mathbf{H}_a = \mathbf{H}_0 + \overleftrightarrow{\mathbf{G}} \cdot \mathbf{r}, \tag{A.6}$$

where the applied field at infinity, $\mathbf{H}_a$, is a sum of a constant field, $\mathbf{H}_0$, and the inner product of the position vector and the gradient tensor, $\overleftrightarrow{\mathbf{G}}$. $\overleftrightarrow{\mathbf{G}}$ has constant components

$$G_{ij} = \partial_j H_i. \tag{A.7}$$

Due to the Maxwell equations and the requirement that $\mathbf{H}$ should be curl-free, we must require that $G_{ij} = G_{ji}$, and that $\boldsymbol{\nabla}\cdot\mathbf{B} = \overleftrightarrow{\mathbf{G}} : \overleftrightarrow{\mathbf{I}} = \text{Trace}\overleftrightarrow{\mathbf{G}} = 0$.[2]

Since Eq. (A.1) is a linear differential equation, we can solve with the boundary condition at infinity, Eq. (A.6), in two parts. First we solve for the scalar potential φ_A that corresponds to having $\mathbf{H} = \mathbf{H}_0$ at infinity. Any solution must include $\mathbf{H}_0$ in some form,

[1] Actually, I have not been able to find a general proof of Eq. (A.3b), but one can easily convince oneself that all elements of the tensors in Eq. (A.5) are indeed solutions to the Laplace equation

[2] For completeness, we note that the double dot product ':' is defined as $\overleftrightarrow{\mathbf{A}} : \overleftrightarrow{\mathbf{B}} = \sum_i\sum_j A_{ij}B_{ij}$ and $\overleftrightarrow{\mathbf{A}} : \mathbf{ba} = \sum_i\sum_j T_{ij}b_ja_i$

and the only way we can form a scalar from $\mathbf{H}_0$ and Eq. (A.5) is with the following linear combination

$$\begin{aligned}\varphi_A =& A_a \mathbf{H}_0 \cdot \boldsymbol{\phi}_{1,a} + A_b \mathbf{H}_0 \cdot \boldsymbol{\phi}_{1,b} \\ =& A_a \frac{\mathbf{H}_0 \cdot \mathbf{r}}{r^3} + A_b \mathbf{H}_0 \cdot \mathbf{r}\end{aligned} \tag{A.8}$$

which we immediately recognize as the solution for a magnetic bead in a homogenous applied field (cf. [103]), and we just write that

$$A_a = \frac{3\chi}{\chi + 3}, \tag{A.9a}$$

$$A_b = -1, \tag{A.9b}$$

outside the bead. The coordinate system has been normalized such that the bead has radius 1. We notice that the first term in Eq. (A.8) is the disturbance due to the bead, and the second term is just the applied field.

Next we solve for the scalar potential, φ_B, that has $\mathbf{H} = \overleftrightarrow{\mathbf{G}} \cdot \mathbf{r}$ at infinity. Again, any such solution must include $\overleftrightarrow{\mathbf{G}}$, and therefore the only way, we can form a scalar using Eq. (A.5) is the following linear combination[3]

$$\begin{aligned}\varphi_B &= B_a \overleftrightarrow{\mathbf{G}} : \overleftrightarrow{\boldsymbol{\phi}}_{2,a} + B_b \overleftrightarrow{\mathbf{G}} : \overleftrightarrow{\boldsymbol{\phi}}_{2,b} \\ &= B_a \frac{\overleftrightarrow{\mathbf{G}} : \mathbf{rr}}{r^5} + B_b \overleftrightarrow{\mathbf{G}} : \mathbf{rr}.\end{aligned} \tag{A.10}$$

Applying the boundary at infinity quickly shows that

$$B_b = -1/2, \tag{A.11}$$

and as we shall see, there is no need to calculate B_a. Again, the first term in Eq. (A.10) is due to the presence of the bead, and the second term is just the applied field gradient.

The full solution is the sum of the two partial solutions

$$\varphi = \varphi_A + \varphi_B, \tag{A.12}$$

and from that, we can write the magnetic field, $\mathbf{H}$ as

$$\begin{aligned}\mathbf{H} &= -\boldsymbol{\nabla}\varphi \\ &= -\boldsymbol{\nabla}\left(\mathbf{H}_0 \cdot \mathbf{r}\Big(\underbrace{\frac{A_a}{r^3}}_{\propto r^{-3}} - \underbrace{1}_{\propto r^0} \Big) + \overleftrightarrow{\mathbf{G}} : \mathbf{rr}\Big(\underbrace{\frac{B_a}{r^5}}_{\propto r^{-4}} - \underbrace{1/2}_{\propto r^1} \Big) \right).\end{aligned} \tag{A.13}$$

[3] See footnote 2 on page 80

Below the terms in the expression for the **H**-field, it has been indicated how they scale with distance after the gradient operator has been applied.

Now that we have found the magnetic field outside the bead, we wish to calculate the force on the bead. We do this by applying Maxwell's stress tensor [103, 102]

$$\mathbf{F} = \mu_0 \oint_{\partial\Omega} (\mathbf{HH} - \frac{1}{2}\overleftrightarrow{\mathbf{I}} H^2) \cdot d\mathbf{a}, \tag{A.14}$$

where $\partial\Omega$ is any closed surface that encloses the entire magnetic bead. We choose a spherical surface centered at the origin. Since we are free to choose the radius, ρ, of the sphere, and the area of the surface grows as ρ^2, then the integrand must scale as ρ^{-2} in order for the integral to be independent of ρ.

When we form the product of **H** with itself, only one term of the product will scale as r^{-2}, all other terms must integrate to zero. The non-zero term is

$$\begin{aligned}\mathbf{HH}_{\text{non-zero}} &= \Big(-\boldsymbol{\nabla}\frac{A_a \mathbf{H}_0 \cdot \mathbf{r}}{r^3}\Big)\Big(-\boldsymbol{\nabla}\big(-\frac{1}{2}\overleftrightarrow{\mathbf{G}} : \mathbf{rr}\big)\Big) \\ &= \frac{3\chi}{\chi+3}\Big(\frac{(3\mathbf{H}_0 \cdot \mathbf{r})\mathbf{r}}{r^5} - \frac{\mathbf{H}_0}{r^3}\Big)\big(\overleftrightarrow{\mathbf{G}} \cdot \mathbf{r}\big).\end{aligned} \tag{A.15}$$

We will stop the analysis here. The calculation of the integral in Eq. (A.14) is complicated and slightly meaningless without making statements about the form of $\mathbf{H}_0$ and $\overleftrightarrow{\mathbf{G}}$. However, all the relevant information has already been revealed to us. From Eq. (A.15) we see that only the dipole field due to the magnetization of the bead by the constant part of the applied field, and the gradient part of the applied field enter the integrand. This means that for a linear gradient field, it is only necessary to include the average magnetization and the applied gradient the other terms do not contribute to the force.

Magnetic fields in general are not linear gradient fields, they will often have parabolic and cubic as well as higher order terms. In most cases, it is possible to describe the field as a Taylor series that includes a linear gradient field, a second order term described by a third order tensor, a third order term described by a fourth order tensor etc. The second order term will contribute with two terms to **H** that will be proportional to r^{-5} and r^2, and then it is possible to form one extra non-zero term in the integrand combining the term proportional to r^{-4} with the term that is proportional to r^2. The third order term in the Tayloy series will contribute with one more non-zero term, and so will all the higher order terms.

We have found that the integrand in the force calculation has more non-zero terms than the one generated by the linear gradient field. Is this bad news? No, since the magnetic structures that generate the magnetic field will most often have much larger length scales than the length scale of a magnetic bead, the generated magnetic fields will be slowly varying compared to the size of the bead, and therefore a first order approximation including only the linear gradient field is sufficient in most cases. It is only if the structures that create the magnetic field gradients have the same length scale as the beads that we need to include higher order terms and do more elaborate calculations. In the Magnetic Valve

paper [6] a more thorough calculation of the magnetic force was needed since magnetic structures scale with the magnetic bead or particle, but in all other aspects of this project a first order calculation has been sufficient.

Appendix B

Variations of the electromagnetic stress tensor

When searching through literature on electromagnetic forces one eventually meets several different versions of the Maxwell Stress Tensor (MST). Lately (This appendix was written during my external stay in the Autumn of 2005), this has been grounds for an extended debate around the office (Harvard, Pierce Hall 402). This apparent discrepancy in literature baffled me, and I set out to re-discover the hidden nuances between the formulae. The present document reviews three different expressions for the Maxwell Stress Tensor and emphasizes their physical differences and interpretations.

The three different versions of MST, $\overleftrightarrow{\mathbf{T}}$, that one will (most likely) find in literature are.

$$T_{ij} = \varepsilon_0\big[E_iE_j - \frac{1}{2}\delta_{ij}E^2\big] + \frac{1}{\mu_0}\big[B_iB_j - \frac{1}{2}\delta_{ij}B^2\big] \tag{B.1a}$$

$$T_{ij} = \big[D_iE_j - \frac{1}{2}\varepsilon_0\delta_{ij}E^2\big] + \big[B_iH_j - \frac{1}{2}\mu_0\delta_{ij}H^2\big] \tag{B.1b}$$

$$T_{ij} = \big[D_iE_j - \frac{1}{2}\varepsilon_0\varepsilon_r\delta_{ij}E^2\big] + \big[B_iH_j - \frac{1}{2}\mu_0\mu_r\delta_{ij}H^2\big] \tag{B.1c}$$

Eq. (B.1a) is the microscopic version of MST that will be found in almost all books on electrodynamics such as 'Griffiths: Introduction to Electrodynamics' [103] and 'Jackson: Classical Electrodynamics' [102].

Eq. (B.1b) can be found in many papers including a the very instructional paper by Andreas Engel,[1], where several different expressions for the electromagnetic force are applied to several analytically solvable problems. It is of course shown that all expressions lead to the same force. (He only demonstrates it for this one version of MST)

Eq. (B.1c) is the one you find in Landau and Lifschitz and also in Saville's book on colloidal dispersions. (Actually, you also find Eq. (B.1b) in Saville's book, but more on that later)

[1]Engel, Am. J. Phys **70** (4) pp. 428-432, April 2002

So, why do different expressions exist? Are one or more of these expressions wrong? First of all, we see that the three expressions are equivalent in vacuum. This means that if we calculate the total force on a magnetic object by calculating the surface integral around the object (in vacuum), we get the same the result regardless of the specific choice of MST.

The reason for the discrepancies between the MST's is that they relate to different electromagnetic force densities. It is customary in continuum mechanics to write body forces as $\mathbf{f} = \boldsymbol{\nabla} \cdot \overleftrightarrow{\mathbf{Y}}$ and surface forces as $\mathbf{f} = \hat{\mathbf{n}} \cdot \overleftrightarrow{\mathbf{Y}}$, where $\overleftrightarrow{\mathbf{Y}}$ is a stress tensor. This is also true for the MST expressions, and it is a fact that they are different, because they describe different volumetric force densities on charges and currents as well as magnetic or dielectric materials.

The first of these force densities is

$$\mathbf{f}_v = \rho\mathbf{E} + \mathbf{J} \times \mathbf{B}, \tag{B.2}$$

where ρ is the total charge, and $\mathbf{J}$ is the total current density. Although this expression seems very appealing, since this is the fundamental Lorentz force, on which all of electrodynamics is based, it fails to accurately describe the force distribution inside a polarizable or magnetizable material.

This is easily seen if one calculates the electric volume force $\mathbf{f}_v = (\varepsilon_0 \boldsymbol{\nabla} \cdot \mathbf{E})\mathbf{E} = (\boldsymbol{\nabla} \cdot (\varepsilon_r^{-1}\mathbf{D})\mathbf{E} = (\varepsilon_r^{-1}\boldsymbol{\nabla} \cdot \mathbf{D} + \mathbf{D} \cdot \boldsymbol{\nabla}\varepsilon_r^{-1})\mathbf{E}$, where $\boldsymbol{\nabla} \cdot \mathbf{D} = \rho^f$ is the free charge. Inside a linear dielectric $\rho^f = 0$, and the permittivity is constant, so this expression for the electromagnetic force density leads to $\mathbf{f}_v = 0$ everywhere inside any linear dielectric regardless of the external field and the shape of the dielectric. This is clearly not true since we know that a gradient field will exert a force on the dipoles as $\mathbf{f}_v = (\mathbf{P} \cdot \boldsymbol{\nabla})\mathbf{E}$. The same type of argument can be made for the magnetic force.

The Lorentz force density describes the forces on dielectrics and magnetic materials as the electric and magnetic fields working on bound charges and bound currents. Although this will give the correct total force, we have seen that this does not give the correct local volume/body force.

Both Griffiths and Jackson derive Eq. (B.1a) from Eq. (B.2).

It is often not written explicitly in electromagnetics texts, but the Lorentz force density should actually not be expected to work in a polarized material. This force density describes the microscopic (single particle) picture, where as polarization and magnetization are terms we use to describe the macroscopic state of a material.

The force density corresponding to Eq. (B.1b) is known as the Lorentz-Kelvin force density and it is given as

$$\mathbf{f}_v = \rho^f\mathbf{E} + (\mathbf{P} \cdot \boldsymbol{\nabla})\mathbf{E} + \mu_0\mathbf{J}^f \times \mathbf{H} + \mu_0(\mathbf{M} \cdot \boldsymbol{\nabla})\mathbf{H} \tag{B.3}$$

It is not entirely clear to me (from a physical stand point), why it is $\mu_0\mathbf{H}$ and not $\mathbf{B}$ that enters the force expression in the magnetic part, but as it turns out this expression is in fact consistent with all the notions we have of magnetic and electric body forces.

In this description, only the free charges and currents are affected by the Lorentz force. The bound charges and currents feel only dipolar forces.

Eq. (B.1b) is easily derived from Eq. (B.3). For simplicity I will consider quasi-statics only. The derivation of the electric part goes as

$$\mathbf{f}_v = \rho^f \mathbf{E} + (\mathbf{P}\cdot\boldsymbol{\nabla})\mathbf{E} = (\boldsymbol{\nabla}\cdot\mathbf{D})\mathbf{E} + (\mathbf{P}\cdot\boldsymbol{\nabla})\mathbf{E} \tag{B.4a}$$

$$= \boldsymbol{\nabla}\cdot(\mathbf{DE}) - (\mathbf{D}\cdot\boldsymbol{\nabla})\mathbf{E} + (\mathbf{P}\cdot\boldsymbol{\nabla})\mathbf{E} = \boldsymbol{\nabla}\cdot(\mathbf{DE}) - \varepsilon_0(\mathbf{E}\cdot\boldsymbol{\nabla})\mathbf{E} \tag{B.4b}$$

$$= \boldsymbol{\nabla}\cdot(\mathbf{DE}) - \frac{1}{2}\varepsilon_0\boldsymbol{\nabla}(\mathbf{E}\cdot\mathbf{E}) = \boldsymbol{\nabla}\cdot\Big[\mathbf{DE} - \frac{1}{2}\varepsilon_0 E^2\mathbf{I}\Big], \tag{B.4c}$$

where $\mathbf{I}$ is the unit tensor.

The magnetic part follows along the same lines as the electric, and here goes.

$$\mathbf{f}_v = \mu_0\mathbf{J}^f\times\mathbf{H} + \mu_0(\mathbf{M}\cdot\boldsymbol{\nabla})\mathbf{H} = \mu_0(\boldsymbol{\nabla}\times\mathbf{H})\times\mathbf{H} + \mu_0(\mathbf{M}\cdot\boldsymbol{\nabla})\mathbf{H} \tag{B.5a}$$

$$= -\frac{1}{2}\mu_0\boldsymbol{\nabla}(H^2) + \mu_0(\mathbf{H}\cdot\boldsymbol{\nabla})\mathbf{H} + \mu_0(\mathbf{M}\cdot\boldsymbol{\nabla})\mathbf{H} \tag{B.5b}$$

$$= -\frac{1}{2}\mu_0\boldsymbol{\nabla}(H^2) + (\mathbf{B}\cdot\boldsymbol{\nabla})\mathbf{H} + (\boldsymbol{\nabla}\cdot\mathbf{B})\mathbf{H} \tag{B.5c}$$

$$= \boldsymbol{\nabla}\cdot(\mathbf{BH}) - \frac{1}{2}\mu_0\boldsymbol{\nabla}(H^2) = \boldsymbol{\nabla}\cdot\Big[\mathbf{BH} - \frac{1}{2}\mu_0 H^2\mathbf{I}\Big] \tag{B.5d}$$

In going from Eq. (B.5b) to Eq. (B.5c) it has been used that $\mathbf{B} = \mu_0(\mathbf{H}+\mathbf{M})$ and that $\boldsymbol{\nabla}\cdot\mathbf{B} = 0$, so that it is 'free' to add the term $(\boldsymbol{\nabla}\cdot\mathbf{B})\mathbf{H}$.

Looking at the end results (Eqs. (B.4c) and (B.5d)), it is clear that the sum of the tensors in the square brackets match Eq. (B.1b).

The final force density is known as the Korteweg-Helmholtz force density. I managed to find a web-site, where Prof. Michael Brenner[2] shows how Eq. (B.1c) is derived from

$$\mathbf{f}_v = \rho^f\mathbf{E} - \frac{1}{2}\varepsilon_0\mathbf{E}\cdot\mathbf{E}\boldsymbol{\nabla}\varepsilon_r + \mu_0\mathbf{J}^f\times\mathbf{H} - \frac{1}{2}\mu_0\mathbf{H}\cdot\mathbf{H}\boldsymbol{\nabla}\mu_r. \tag{B.6}$$

This force density is the same as Eq. (B.3) for the free charges and currents, but it handles the dipolar contribution differently. Actually, Eq. (B.6) does not handle the dipolar forces at all in an electromagnetic sense. This force density will not give a body force on a linear dielectric in a gradient field (the same holds for the magnetic field), so it does not describe the electromagnetic body force precisely.

If the above statement is true, why does the Korteweg-Helmholtz force density exist, and why is Eq. (B.1c) the version of MST that Landau and Lifschitz derived - they rarely make mistakes. In fact they did not make a mistake. Both the Korteweg-Helmholtz electromagnetic force density and Eq. (B.1c) were derived from thermodynamic principles rather than an exact evaluation of electromagnetic force. It is seen that Eqs. (B.1b) and (B.1c) are only different by a diagonal term i.e. a pressure. It should be remembered that in any continuum, finite stress leads to movement, and therefore any electromagnetic body force must be countered by a pressure gradient at equilibrium. It is this fact that

[2]Michael Brenner is professor at DEAS at Harvard University, and he published this note on the web for one of his courses. http://www.deas.harvard.edu/brenner/taylor/handouts/ehd/node1.html

Eqs. (B.1c) and (B.6) take into account. In other words, we get that the total body force on a volume of fluid or solid is

$$\mathbf{f}_v = \boldsymbol{\nabla} p_0 + \boldsymbol{\nabla} p^* + \boldsymbol{\nabla} \cdot \overleftrightarrow{\mathbf{T}}_2 = \boldsymbol{\nabla} p_0 + \boldsymbol{\nabla} \cdot \overleftrightarrow{\mathbf{T}}_3, \tag{B.7}$$

where $\overleftrightarrow{\mathbf{T}}_2$ is MST given by Eq. (B.1b), and $\overleftrightarrow{\mathbf{T}}_3$ is the MST given by Eq. (B.1c), p_0 is the pressure in the absence of the electromagnetic field, and p^* is the pressure added by the electromagnetic field.[3]

This means that the Korteweg-Helmholtz force density does not consider the local forces that electromagnetic forces exert. It does, however, account for the pressure build-up in a continuous medium due to these forces, and thus the Eq. (B.1c) form of the MST is well-suited for calculations where one wishes to calculate the deformation of a fluid or the movement of interfaces between fluids.

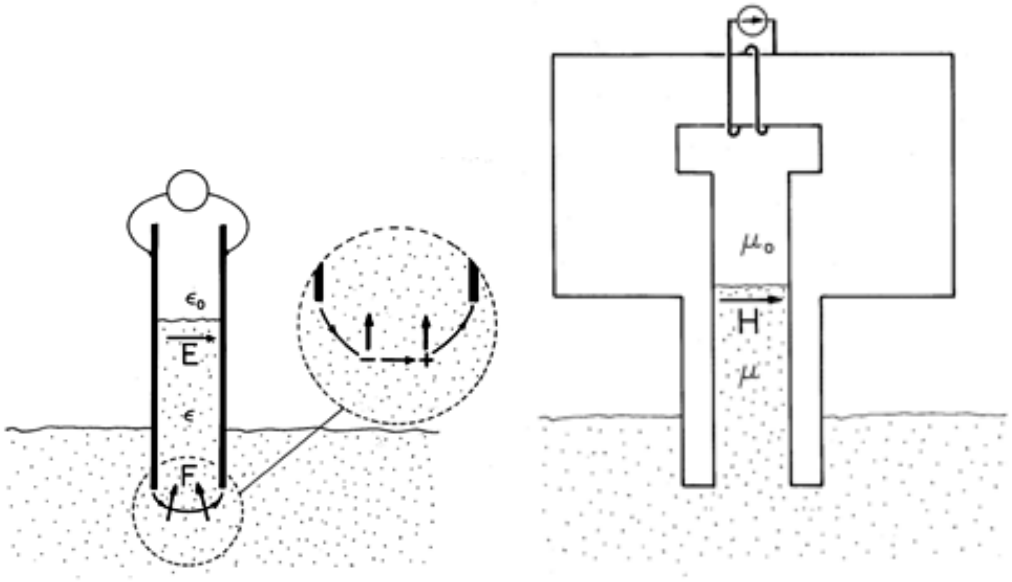

Figure B.1: Two equivalent situations. The right picture shows a situation, where a fluid dielectric is pulled into the gap between two vertical electrodes. The right picture shows the equivalent situation for a ferrofluid.

At this point an example must be in order [4]. Fig. B.1 shows two equivalent situations for a dielectric fluid and a ferrofluid. In both situations, the fluid will be sucked into the gap between the metal plates when the electric or magnetic field is turned on.

If we turn our attention to the (linear) dielectric case, then Eqs. (B.1b) and (B.3) correctly show that the electric force works in the fringing field just outside the electrodes (the inserted blow-up). In this region $(\mathbf{P} \cdot \boldsymbol{\nabla})\mathbf{E} \neq 0$, and thus there is a dipole force, the

[3] According to Saville's book this has been shown by Landau and Lifschitz, but I haven't really found that proof (I haven't been looking too hard for it though).

[4] The figures for the example is taken from this web-site http://web.mit.edu/6.013_book/www/chapter11/11.9.html that also discusses parts of the issues that are discussed in this note.

body force is integrated over the whole fluid, the result is that there is an upwards force on the fluid, and thus the fluid will rise between the plates, until the upwards force is balanced by gravity.

If we now try to use Eqs. (B.1c) and (B.6), we find that $-\frac{1}{2}\varepsilon_0 \mathbf{E}\cdot\mathbf{E}\boldsymbol{\nabla}\varepsilon_r = 0$ throughout the fluid. However, if we turn our intention to the interface (the fluid surface between the plates), it is clear that there is an upwards force at the interface, so again it is found that the fluid will rise between the plates until the force is balanced by gravity. This force distribution is not in agreement with normal theory for forces on dielectrics, however, we were able to calculate the force correctly, and we only had to consider the interface, we didn't have to calculate the electric field throughout the fluid, and we didn't have to integrate the force density throughout the fluid.[5]

Eqs. (B.1a) and (B.2) fail to evaluate the force in this situation.

Finally, in this note we have seen that in situations where one considers fluid interfaces, Eqs. (B.1c) and (B.6) is the easiest expression to use, but there is more physical insight and a more 'correct' distribution of electromagnetic body forces is gained by the use of Eqs. (B.1b) and (B.3).

[5]Strictly speaking, we could also have calculated the forces by a surface integral in the previous case, but then we would have to integrate over a surface that included the entire force carrying region.

Appendix C

Magnetic separation with constant force

It is investigated how a magnetic bead moving in a horizontally moving fluid behaves under the influence of a constant vertical force, F, which could be magnetic, gravitational or any other force. This sketched in Fig. C.1

It is assumed that the fluid profile is parabolic, such that the velocity of the fluid is given by

$$u_x(y) = 4u_0 \frac{y}{h}(1 - \frac{y}{h}), \tag{C.1}$$

where u_0 is the maximum fluid velocity, and h is the height of the microfluidic channel. This gives a volumetric flow rate

$$Q = w \int_0^h u_x(y)dy = \frac{2}{3}u_0 hw \tag{C.2}$$

If fluid drag is the only force that affects the magnetic bead in the horizontal direction, magnetic beads will move with the fluid velocity in the horizontal direction. In the vertical direction the bead will be affected by F and the fluid drag. Newton's second law yields

$$\rho \frac{4}{3}\pi R_{\text{bead}}^3 \, \partial_t v_y = -6\pi\eta R_{\text{bead}} \, v_y - F, \tag{C.3}$$

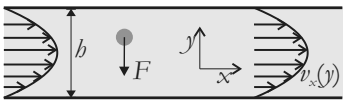

Figure C.1: . Sketch of the calculation geometry showing the fluid flow, u_x, the constant downwards force, F, h, and the coordinate system.

which has the solution

$$v_y = c\exp\Big(-\frac{t}{\tau}\Big) - v_t,, \tag{C.4a}$$

$$v_t = (6\pi\eta R_{\text{bead}})^{-1}F, \tag{C.4b}$$

$$\tau = \frac{2\rho R_{\text{bead}}^2}{9\eta} \approx 10^{-7}\text{s}, \tag{C.4c}$$

where ρ is the density of the magnetic bead, R_{bead} is the radius of the magnetic bead v_y is the instantaneous velocity of the magnetic bead, η is the viscosity of the fluid, c is some constant, τ is the time constant of the exponential function, and v_t is the terminal velocity of the bead.

Since τ of Eq. (C.4c) is much shorter than any other time scale relevant to this problem, the exponential part of Eq. (C.4a) can be discarded, and the velocity of the magnetic bead can be assumed to be the terminal velocity v_t, given by Eq. (C.4b), always.

The time t_0 that a bead will take before it hits the bottom of the channel, if it starts at y_0 is $t_0 = \frac{y_0}{v_t}$. This means that we can calculate the horizontal distance x_0 that the magnetic bead travels before it hits the bottom of the microfluidic channel.

$$x_0 = \int_0^{t_0} u_x(y_0 - v_t t)dt = 4v_0\left(\Big(\frac{y_0}{h} - \frac{y_0^2}{h^2}\Big)t_0 + \Big(\frac{y_0 v_t}{h^2} - \frac{v_t}{2h}\Big)t_0^2 - \frac{v_t^2}{3h^2}t_0^3\right), \tag{C.5}$$

and inserting t_0 gives

$$x_0 = 4u_0\frac{y_0^2}{v_t h}\left(\frac{1}{2} - \frac{y_0}{3h}\right). \tag{C.6}$$

This result allows us to get some other interesting and useful results. First of all it is often such that x_0 is given and one wishes to calculate the maximum y_0 that results in bead capture

$$y_0 = \frac{h}{2} + \frac{\sqrt[3]{\Psi}}{2u_0} + \frac{h^2 u_0}{2\sqrt[3]{\Psi}}, \tag{C.7a}$$

$$\Psi = -h^2 u_0^2\Big(3\,v_t\,x_0 - u_0\,h - \sqrt{3v_t\,x_0\,(3\,v_t\,x_0 - 2\,u_0\,h)}\Big). \tag{C.7b}$$

From this we can calculate the bead capture efficiency α

$$\alpha = \frac{\int_0^{y_0} v_x(y)dy}{\int_0^h v_x(y)dy} = \frac{y_0^2\,(3h - 2y_0)}{h^3}. \tag{C.8}$$

Given v_t, h, and x_0, what v_0 will give us 100% capture efficiency. By setting $y_0 = h$ in Eq. (C.6) we get

$$v_0 = v_t\frac{3x_0}{2h}, \tag{C.9a}$$

$$Q = v_t x_0 w. \tag{C.9b}$$

This appendix has shown how to estimate if beads will be captured if an estimate of the magnetic force, the flow rate, and the bead starting height is given. It is also shown how to estimate the flow rate that will give 100 % capture efficiency given the length of the capturing device, an estimate of the applied force, and the width of the microfluidic channel.

Bibliography

[1] K. Smistrup, P.T. Tang, O. Hansen, and M.F. Hansen. Microelectromagnet for magnetic manipulation in lab-on-a-chip systems. *J. Magn. Magn. Mater.*, 300(2):418–426, 2006.

[2] K. Smistrup, O. Hansen, H. Bruus, and M.F. Hansen. Magnetic separation in microfluidic systems using microfabricated electromagnets - experiments and simulations. *J. Magn. Magn. Mater.*, 293(1):597–604, 2005.

[3] K. Smistrup, B.G. Kjeldsen, J.L. Reimers, M. Dufva, J. Petersen, and M.F. Hansen. On-chip magnetic bead microarray using hydrodynamic focusing in a passive magnetic separator. *Lab Chip*, 5(11):1315–1319, 2005.

[4] K. Smistrup, T Lund-Olesen, M.F. Hansen, and P.T. Tang. Microfluidic magnetic separator using an array of soft magnetic elements. *J. Appl. Phys.*, 99(8):8P102, 2006.

[5] K. Smistrup, H. Bruus, and M.F. Hansen. Towards a programmable magnetic bead microarray in a microfluidic channel. *J. Magn. Magn. Mater.*, 311(1):409–415, 2007.

[6] K. Smistrup and H.A. Stone. A magnetically actuated ball valve applicable for small-scale fluid flows. *Phys. Fluids*, 19(6), pp. 63101/1 9, 2007.

[7] K. Smistrup, P.T. Tang, and P. Møller. Pulse reversal plating process for mems applications. *ECS Trans*, 3(25), p. 179, 2007.

[8] K. Smistrup, M. Bu, A. Wolff, H. Bruus, and M.F. Hansen. Theoretical analysis of a new efficient magnetic bead separator utilizing magnetic structures with multiple length scales. *Microfluid. Nanofluid.*, 4:565–573, 2008.

[9] L. Ejsing, K. Smistrup, C.M. Pedersen, N.A. Mortensen, and H. Bruus. Frequency response in surface-potential driven electrohydrodynamics. *Phys. Rev. E*, 73(3):37302, 2006.

[10] K. Smistrup, O. Hansen, P.T. Tang, and M.F. Hansen. Selective magnetic bead capture using an adressable on-chip electromagnet array. In Thomas Laurell, Johan Nilsson, Klavs Jensen, D. Jed Harrison, and Jörg P. Kutter, editors, *Micro Total Analysis Systems 2004*, pages 509–511. The Royal Society of Chemistry, 2004. September 26-30, Malmö, Sweden.

[11] K. Smistrup. Integrated micromachined magnetic bead separator. Master's thesis, MIC – Department of Micro and Nanotechnology, Technical University of Denmark, 2003.

[12] M. Abkarian, M. Faivre, and H.A. Stone. High-speed microfluidic differential manometer for cellular-scale hydrodynamics. *Proceedings of the National Academy of Sciences of the United States of America*, 103(3):538–542, 2006.

[13] A.B. Subramaniam, M. Abkarian, L. Mahadevan, and H.A. Stone. Colloid science: Non-spherical bubbles. *Nature : UK Edition*, 438(7070):930, 2005.

[14] A.B. Subramaniam, M. Abkarian, and H.A. Stone. Controlled assembly of jammed colloidal shells on fluid droplets. *Nat. Mater.*, 4(7):553–556, 2005.

[15] J.A. Oberteuffer. Magnetic separation: a review of principles, devices, and applications. *IEEE Trans. Magn.*, Mag-10(2):223–238, 1974.

[16] J.H.P. Watson. Magnetic filtration. *J. Appl. Phys.*, 44(9):4209–4213, 1973.

[17] M. Zborowski, G.R. Ostera, L.R. Moore, S. Milliron, J.J. Chalmers, and A.N. Schechter. Red blood cell magnetophoresis. *Biophys. J.*, 84(4):2638–2645, 2003.

[18] C.H. Setchell. Magnetic separations in biotechnology - a review. *J. Chem. Technol. Biotechnol.*, 35B(3):175–182, 1985.

[19] I. Safarik. Use of magnetic techniques for the isolation of cells. *J. Chromatogr. B*, 722(1-2):33–53, 1999.

[20] I. Safarik and M. Safarikova. Magnetic techniques for the isolation and purification of proteins and peptides. *Biomagn. Res. and Technol.*, 2:7, 2004.

[21] Q.A. Pankhurst, J. Connolly, S.K. Jones, and J. Dobson. Applications of magnetic nanoparticles in biomedicine. *J. Phys. D: Appl. Phys.*, 36:R167–R181, 2003.

[22] See www.magneticmicrosphere.com for suppliers of magnetic beads and particles.

[23] T.M. Squires and S.R. Quake. Microfluidics: Fluid physics at the nanoliter scale. *Rev. Mod. Phys*, 77(3):977–1026, 2005.

[24] B.H. Weigl, R.L. Bardell, and C.R. Cabrera. Lab-on-a-chip for drug development. *Adv. Drug Del. Rev.*, 55(3):349–377, 2003.

[25] J. Knight. Honey, i shrunk the lab. *Nature*, 418:474–475, 2005.

[26] D.R. Reyes, D. Iossifidis, P.-A. Auroux, and A. Manz. Micro total analysis systems. 1. introduction, theory, and technology. *Anal. Chem.*, 74(12):2623–2636, 2002.

[27] A. Manz, N. Graber, and H.M. Widmer. Miniaturized total chemical analysis systems. a novel concept for chemical sensing. *Sens. Actuators B Chem.*, B1(1):244–248, 1990.

[28] M.A.M. Gijs. Magnetic bead handling on-chip: new opportunities for analytical applications. *Microfluid. Nanofluid.*, 1:22–40, 2004.

[29] P.S. Dittrich, K. Tachikawa, and A. Manz. Micro total analysis systems. latest advancements and trends. *Anal. Chem.*, 78(12):3887–3908, 2006.

[30] E. Verpoorte. Beads and chips: new recipes for analysis. *Lab Chip*, 3:60N–68N, 2003.

[31] N. Pamme. Magnetism and microfluidics. *Lab Chip*, 6:24–38, 2006.

[32] J.-W. Choi, C.H. Ahn, S. Bhansali, and H.T. Henderson. A new magnetic bead-based, filterless bio-separator with planar electromagnet surfaces for integrated bio-detection systems. *Sens. Actuators B Chem.*, 68:34–39, 2000.

[33] C.H. Ahn and M.G. Allen. A fully integrated micromachined magnetic particle manipulator and separator. In *Proceedings IEEE Micro Electro Mechanical Systems An Investigation of Micro Structures, Sensors, Actuators, Machines and Robotic Systems*, pages 91–96. IEEE, 1994.

[34] C.H. Ahn, M.G. Allen, W. Trimmer, Y.-N. Jun, and S. Erramilli. A fully integrated micromachined magnetic particle separator. *J. Microelectromech. Syst.*, 5:151–158, 1996.

[35] J.-W. Choi, K.W. Oh, A. Han, C.A. Wijayawardhana, C. Lannes, S. Bhansali, K.T. Schlueter, W.R. Heineman, H.B. Halsall, J.H. Nevin, A.J. Helmicki, H.T. Henderson, and C.H. Ahn. Development and characterization of microfluidic devices and systems for magnetic bead-based biochemical detection. *Biomed. Microdevices*, 3:191–200, 2001.

[36] J.-W. Choi, K.W. Oh, J.H. Thomas, W.R. Heineman, H.B. Halsall, J.H. Nevin, A.J. Helmicki, H. Thurman-Henderson, and C.H. Ahn. An integrated microfluidic biochemical detection system with magnetic bead-based sampling and analysis capabilities. pages 447–450. IEEE, 2001.

[37] J.-W. Choi, K.W. Oh, J.H. Thomas, W.R. Heineman, H.B. Halsall, J.H.Nevin, A.J. Helmicki, H.T. Henderson, and C.H. Ahn. An integrated microfluidic biochemical detection system for protein analysis with magnetic bead-based sampling capabilities. *Lab Chip*, 2:27–30, 2002.

[38] J. Do, J.-W. Choi, and C.H. Ahn. Low-cost magnetic interdigitated array on a plastic wafer. *IEEE Trans. Magn.*, 40:3009–3011, 2004.

[39] T.M. Liakopoulos, J.-W. Choi, and C.H. Ahn. A bio-magnetic bead separator on glass chips using semi-encapsulated spiral electromagnets. volume 1, pages 485–488. IEEE, 1997.

[40] J.-W. Choi, T.M. Liakopoulos, and C.H. Ahn. An on-chip magnetic bead separator using spiral electromagnets with semi-encapsulated permalloy. *Biosens. Bioelec.*, 16:409–416, 2001.

[41] R. Rong, J.-W. Choi, and C.H. Ahn. A functional magnetic bead/biocell sorter using fully integrated magnetic micro/nano tips. In *Proceedings IEEE Sixteenth Annual International Conference on Micro Electro Mechani....*, pages 530–533. IEEE, 2003.

[42] R. Rong, J.W. Choi, and C.H. Ahn. A novel magnetic chaotic mixer for in-flow mixing of magnetic beads. In *7th lnternational Conference on Miniaturized Chemical and Biochemlcal Analysts Systems*, pages 335–338. IEEE, 2003.

[43] Q. Ramadan, V. Samperb, D. Poenara, and C. Yub. On-chip micro-electromagnets for magnetic-based bio-molecules separation. *J. Magn. Magn. Mater.*, 281:150–172, 2004.

[44] Q. Ramadan, D. Poenar, V. Samper, and C. Yu. Magnetic-based microfluidic platform for biomolecular separation. *Biomed. Microdevices*, 8(2):151–158, 2006.

[45] Q. Ramadan, C. Yu, V. Samper, and D.P. Poenar. Microcoils for transport of magnetic beads. *Appl. Phys. Lett.*, 88(3):32501, 2006.

[46] Q. Ramadan, V. Samper, D.P. Poenar, and C. Yu. An integrated microfluidic platform for magnetic microbeads separation and confinement. *Biosens. Bioelec.*, 21(9):1693–1702, 2006.

[47] C.S. Lee, H. Lee, and R.M. Westervelt. Microelectromagnets for the control of magnetic nanoparticles. *Appl. Phys. Lett.*, 79(20):3308–3310, 2001.

[48] H. Lee, A.M. Purdon, and R.M. Westervelt. Manipulation of biological cells using a microelectromagnet matrix. *Appl. Phys. Lett.*, 85(6):1063–1065, 2004.

[49] H. Lee, A.M. Purdon, and R.M. Westervelt. Micromanipulation of biological systems with microelectromagnets. *IEEE Trans. Magn.*, 40(4):2991–2993, 2004.

[50] H. Lee, Y. Liu, E. Alsberg, D.E. Ingber, R.M. Westervelt, and D. Ham. An ic/microfluidic hybrid microsystem for 2d magnetic manipulation of individual biological cells. *Solid-State Circuits Conference, 2005. Digest of Technical Papers. ISSCC. 2005 IEEE International*, pages 80–586, 2005.

[51] R. Wirix-Speetjens and J.D. Boeck. On-chip magnetic particle transport by alternating magnetic field gradients. *IEEE Trans. Magn.*, 40(4):1944–1946, 2004.

[52] R. Wirix-Speetjens, W. Fyen, K. Xu, J.D. Boeck, and G. Borghs. A force study of on-chip magnetic particle transport based on tapered conductors. *IEEE Trans. Magn.*, 41(10):4128–4133, 2005.

[53] R. Wirix-Speetjens, W. Fyen, J.D. Boeck, and G. Borghs. Enhanced magnetic particle transport by integration of a magnetic flux guide: Experimental verification of simulated behavior. *J. Appl. Phys.*, 99(8), 2006.

[54] A.C. Siegel, S.S. Shevkoplyas, D.B. Weibel, D.A. Bruzewicz, A.W. Martinez, and G.M. Whitesides. Cofabrication of electromagnets and microfluidic systems in poly(dimethylsiloxane). *Angew. Chem.*, 45(41):6877–6882, 2006.

[55] T. Deng, M. Prentiss, and G.M. Whitesides. Fabrication of magnetic microfiltration systems using soft lithography. *Appl. Phys. Lett.*, 80:461–463, 2002.

[56] N. Ichikawa, Y. Katsuyama, Y. Nagasaki, and T. Ichiki. Microfluidic devices integrated with permalloy micropatterns for bead-based assay. In *Proceedings of the 8th International conference on Miniaturized Systems in Chemistry and Life Sciences (μTAS)*, pages 384–386, 2004.

[57] E. Mirowski, J. Moreland, S.E. Russek, and M.J. Donahue. Integrated microfluidic isolation platform for magnetic particle manipulation in biological systems. *Appl. Phys. Lett.*, 84(10):1786–1788, 2004.

[58] E. Mirowski, J. Moreland, A. Zhang, S.E. Russek, and M.J. Donahue. Manipulation and sorting of magnetic particles by a magnetic force microscope on a microfluidic magnetic trap platform. *Appl. Phys. Lett.*, 86(24):243901, 2005.

[59] J. Moreland, E. Mirowski, and S.E. Russek. Microfabrictaed spin-valve traps for manipulation of individual magnetic beads in a microfluidic environment. *Nanomedicine*, 1(3):280, 2005.

[60] K.-H. Han and A.B. Frazier. Continuous magnetophoretic separation of blood cells in microdevice format. *J. Appl. Phys.*, 96(10):5797–5802, 2004.

[61] K.-H. Han and A.B. Frazier. Paramagnetic capture mode magnetophoretic microseparator for high efficiency blood cell separations. *Lab Chip*, 6(2):265–273, 2006.

[62] D.W. Inglis, R. Riehn, R.H. Austin, and J.C. Sturm. Continuous microfluidic immunomagnetic cell separation. *Appl. Phys. Lett.*, 85(21):5093–5095, 2004.

[63] D.W. Inglis, R. Riehn, J.C. Sturm, and R.H. Austin. Microfluidic high gradient magnetic cell separation. *J. Appl. Phys.*, 99(8):8K101, 2006.

[64] M. Zborowski, L. Sun, L.R. Moore, P.S. Williams, and J.J. Chalmers. Continuous cell separation using novel magnetic quadrupole flow sorter. *J. Magn. Magn. Mater.*, 194(1-3):224–230, 1999.

[65] G. Blankenstein and U.D. Larsen. Modular concept of a laboratory on a chip for chemical and biochemical analysis. *Biosens. Bioelec.*, 13(3-4):427–438, 1998.

[66] S. Oestergaard, G. Blankenstein, H. Dirac, and O. Leistiko. A novel approach to the automation of clinical chemistry by controlled manipulation of magnetic particles. *J. Magn. Magn. Mater.*, 194(1-3):156–162, 1999.

[67] C.B. Fuh and S.Y. Chen. Magnetic split-flow thin fractionation: new technique for separation of magnetically susceptible particles. *J. Chromatogr. A*, 813(2):313–324, 1998.

[68] C.B. Fuh and S.Y. Chen. Magnetic split-flow thin fractionation of magnetically susceptible particles. *J. Chromatogr. A*, 857(1-2):193–204, 1999.

[69] C.B. Fuh, J.Z. Lai, and C.M. Chang. Particle magnetic susceptibility determination using analytical split-flow thin fractionation. *J. Chromatogr. A*, 923:263–270, 2001.

[70] C.B. Fuh, H.Y. Tsai, and J.Z. Lai. Development of magnetic split-flow thin fractionation for continuous particle separation. *Anal. Chim. Acta*, 497(1-2):115–122, 2003.

[71] K.S. Kim and J.-K. Park. Magnetic force-based multiplexed immunoassay using superparamagnetic nanoparticles in microfluidic channel. *Lab Chip*, 5(6):657–664, 2005.

[72] N. Pamme and A. Manz. On-chip free-flow magnetophoresis: Continuous flow separation of magnetic particles and agglomerates. *Anal. Chem.*, 76(24):7250–7256, 2004.

[73] N. Pamme, J.C.T. Eijkel, and A. Manz. On-chip free-flow magnetophoresis: Separation and detection of mixtures of magnetic particles in continuous flow. *J. Magn. Magn. Mater.*, 307(2):237–244, 2006.

[74] N. Pamme and C. Wilhelm. Continuous sorting of magnetic cells via on-chip free-flow magnetophoresis. *Lab Chip*, 6(8):974–980, 2006.

[75] D.E. Ingber, R.M. Westervelt, G.M. Whitesides, E. Alsberg, B.T. Mayers, T.P. Hunt, and N. Xia. Combined microfluidic-micromagnetic separation of living cells in continuous flow. *Biomed. Microdevices*, 8(4):299–308, 2006.

[76] T. Lund-Olesen, H. Bruus, and M.F. Hansen. Passive magnetic separator integrated with microfluidic mixer: Demonstration of enhanced capture efficiency. In *Micro Electro Mechanical Systems, 2006. MEMS 2006 Istanbul. 19th IEEE International Conference on*, pages 386–389. IEEE, 2006.

[77] T. Lund-Olesen, H Bruus, and M.F. Hansen. Quantitative characterization of magnetic separators: Comparison of systems with and without integrated microfluidic mixers. *Biomed. Microdevices*, 9:195–205, 2007.

[78] T. Deng, G.M. Whitesides, M. Radhakrishnan, G. Zabow, and M. Prentiss. Manipulation of magnetic microbeads in suspension using micromagnetic systems fabricated with soft lithography. *Appl. Phys. Lett.*, 78(12):1775–1777, 2001.

[79] A. Rida, V. Fernandez, and M.A.M. Gijs Long-range transport of magnetic microbeads using simple planar coils placed in a uniform magnetostatic field. *Appl. Phys. Lett.*, 83(12):2396–2398, 2003.

[80] M. Tondra, M. Granger, R. Fuerst, M. Porter, C. Nordman, J. Taylor, and S. Akou. Design of integrated microfluidic device for sorting magnetic beads in biological assays. *IEEE Trans. Magn.*, 37:2621–2623, 2001.

[81] N. Pekas, M. Granger, M. Tondra, A. Popple, and M.D. Porter. Magnetic particle diverter in an integrated microfluidic format. *J. Magn. Magn. Mater.*, 293(1):584–588, 2005.

[82] A. Rida and M.A.M. Gijs. Dynamics of magnetically retained supraparticle structures in a liquid flow. *Appl. Phys. Lett.*, 85(21):4986–4988, 2004.

[83] N. Minc, C. Futterer, K.D. Dorfman, A. Bancaud, C. Gosse, C. Goubault, and J.-L. Viovy. Quantitative microfluidic separation of dna in self-assembled magnetic matrixes. *Anal. Chem.*, 76(13):3770–3776, 2004.

[84] A. Rida and M.A.M. Gijs. Manipulation of self-assembled structures of magnetic beads for microfluidic mixing and assaying. *Anal. Chem.*, 76(21):6239–6246, 2004.

[85] N. Minc, P. Bokov, K.B. Zeldovich, C. Futterer, J.-L. Viovy, and K.D. Dorfman. Motion of single long dna molecules through arrays of magnetic columns. *Electrophoresis*, 26(2):362–375, 2005.

[86] M. Slovakova, N. Minc, Z. Bilkova, C. Smadja, W. Faigle, C. Futterer, M. Taverna, and J.-L. Viovy. Use of self assembled magnetic beads for on-chip protein digestion. *Lab Chip*, 5(9):935–942, 2005.

[87] H. Suzuki, C.-M. Ho, and N. Kasagi. A chaotic mixer for magnetic bead-based micro cell sorter. *J. MEMS*, 13(5):779–790, 2004.

[88] S.L. Biswal and A.P. Gast. Micromixing with linked chains of paramagnetic particles. *Anal. Chem.*, 76(21):6448–6455, 2004.

[89] G. Zabow, F. Assi, R. Jenks, and M. Prentiss. Guided microfluidics by electromagnetic capillary focusing. *Appl. Phys. Lett.*, 80(8):1483–1485, 2002.

[90] U. Lehmann, S. Hadjidj, V.K. Parashar, C. Vandevyver, A. Rida, and M.A.M. Gijs. Two-dimensional magnetic manipulation of microdroplets on a chip as a platform for bioanalytical applications. *Sens. Actuators B Chem.*, 117(2):457–463, 2006.

[91] R.H. Liu, J. Yang, R. Lenigk, J. Bonanno, and P. Grodzinski. Self-contained, fully integrated biochip for sample preparation, polymerase chain reaction amplification, and dna microarray detection. *Anal. Chem.*, 76(7):1824–1831, 2004.

[92] R.C. O'Handley. *Modern Magnetic Materials*. John Wiley & Sons, Inc., New York, 2000.

[93] W.D. Callister Jr. *Fundamentals of Materials Science and Engineering*. John Wiley and Sons Inc., 5th edition, 2001.

[94] C. Rudowicz and H.W.F. Sung. Textbook treatments of the hysteresis loop for ferromagnets-survey of misconceptions and misinterpretations. *Am. J. Phys.*, 71(10):1080–1083, 2003.

[95] H.W.F. Sung and C. Rudowicz. Physics behind the magnetic hysteresis loop-a survey of misconceptions in magnetism literature. *J. Magn. Magn. Mater.*, 260(1-2):250–260, 2003.

[96] F.E. Rasmussen, J.T. Ravnkilde, P.T. Tang, O. Hansen, and S. Bouwstra. Electroplating and characterization of cobalt-nickel-iron and nickel-iron for magnetic microsystems applications. *Sens. Acuators A*, 92:242–248, 2001.

[97] P.T. Tang. Pulse reversal plating of nickel and nickel alloys for mems. In *Proceedings of the sur/fin, Nashville 2001*, 2001.

[98] K. Korsbæk and R. Rubæk. Udvikling og karakterisering af magnetiske legeringer til mikromekaniske komponenter. Bachelor of engineering, final report, Technical University of Denmark, January 2004.

[99] G. Fonnum, C. Johansson, A. Molteberg, S. Mørup, and E. Aksnes. Characterization of dynabeads by magnetization measurements and mössbauer spectroscopy. *J. Magn. Magn. Mater.*, 293:41–47, 2005.

[100] S. Blundell. *Magnetism in Condensed Matter*. Oxford University Press, 1st edition, 2001.

[101] D. Jiles. *Introduction to magnetism and Magnetic Materials*. Chapman & Hall, 2nd edition, 1998.

[102] J.D. Jackson. *Classical Electrodynamics*. John Wiley and & Sons. Inc., Hoboken, 3rd edition, 1999.

[103] D.J. Griffiths. *Introduction to electrodynamics*. Prentice-Hall, Inc., New Jersey, 2nd edition, 1989.

[104] Comsol support and Comsol Multiphysics documentation, www.comsol.com.

[105] H. Bruus. *Theoretical Microfluidics - Lecture Notes*. MIC - Department of Micro and Nanotechnology, Technical University of Denmark, 2nd edition, 2005.

[106] S. Odenbach and M. Liu. Invalidation of the kelvin force in ferrofluids. *Phys. Rev. Lett.*, 86:328–331, 2001.

[107] A. Engel. Comment on invalidation of the kelvin force in ferrofluids. *Phys. Rev. Lett.*, 86:4978, 2001.

[108] M. Liu. Reply on the comment on invalidation of the kelvin force in ferrofluids. *Phys. Rev. Lett.*, 86:4979, 2001.

[109] A. Engel and R. Friedrichs. On the electromagnetic force on a polarizable body. *Am. J. Phys.*, 70:428, 2002.

[110] L.D. Landau, E.M. Lifshitz, and L.P. Pitaevskii. *Electrodynamics of Continuous Media*, volume 8 of *Landau and Lifshitz, Course of Theoretical Physics*. Butterworth-Heinemann, Oxford, 2nd edition, 1984.

[111] G. Friedman and B. Yellen. Magnetic separation, manipulation and assembly of solid phase in fluids. *Current Opinion in Colloid and Interface Science*, 10(3-4):158–166, 2005.

[112] E. Buckingham. On physically similar systems; illustrations of the use of dimensional equations. *Phys. Rev.*, 4(4):345–376, 1914.

[113] Rayleigh. The principle of similitude. *Nature*, 95:66–68, 1915.

[114] C.I. Mikkelsen. *Magnetic Separation and Hydrodynamic Interactions in Microfluidic Systems*. PhD thesis, MIC - Department of Micro and Nanotechnology, Technical University of Denmark, 2006.

[115] H. Brenner. The slow motion of a sphere through a viscous fluid towards a plane surface. *Chem. Eng. Sci.* , 16(3-4):242–251, 1961.

[116] N. Lecoq, R. Anthore, B. Cichocki, P. Szymczak, and F. Feuillebois. Drag force on a sphere moving towards a corrugated wall. *J. Fluid Mech.* , 513:247–264, 2004.

[117] Matlab including help pages by Mathworks, www.mathworks.com.

[118] Mathematica including help pages by Wolfram Research, www.wolfram.com.

[119] L.H. Olesen. Computational fluid dynamics in microfluidic systems. Master's thesis, MIC — Department of Micro and Nanotechnology, Technical University of Denmark, 2003. Available through http://www.mic.dtu.dk/mifts at the time of writing.

[120] J.P. Boyd. *Chebyshev and Fourier Spectral Methods*. Dover Publications Inc., 31 East 2nd Street, Minneola, New York 11501, 2nd edition, 2000.

[121] T. Lund-Olesen. Integrated microfluidic mixer and magnetic bead trap. Master's thesis, MIC – Department of Micro and Nanotechnology, Technical University of Denmark, 2005.

[122] J. Wu, V. Quinn, and G.H. Bernstein. Powering efficiency of inductive links with inlaid electroplated microcoils. *J. Micromech. Microeng.*, 14:576–586, February 2004.

[123] P.T. Tang. *Fabrication of Micro components by Electrochemical Deposition - Part A*. PhD thesis, Department of Manufacturing Engineering – Technical University of Denmark, 1998.

[124] R.B. Bosch GMBH. 'time multiplexed deep etching' (tmde), 1994. US Patent Specification 4855017 and German Patent Specification 4241045CI.

[125] A. Brenner. *Electrodeposition of Alloys - Principles and practice*, volume 1. Academic Press, 111 Fifth Avenie, New York 3, New York, 1st edition, 1963.

[126] A. Brenner. *Electrodeposition of Alloys - Practical and specific information*, volume 2. Academic Press, 111 Fifth Avenie, New York 3, New York, 1st edition, 1963.

[127] M. Schlesinger and M. Paunovic. *Modern Electroplating*. Electrochemical society series. John Wiley & Sons, Inc., 605 Third Avenue, New York, N.Y., 4th edition, 2000.

[128] M. Bu, K. Smistrup, M.F. Hansen, and A. Wolff. Design and fem simulation of a microfluidic magnetic bead separator. In *32nd international conference on Micro- and Nano-Engineering (MNE06)*, 2006.

[129] M. Bu, T.B. Christensen, K. Smistrup, A. Wolff, and M.F. Hansen. A high-throughput su-8microfluidic magnetic bead separator. In *Solid State Sensors and Actuators, 2007. TRANSDUCERS '07. International Conference on*, pages 1773–1776. IEEE, 2007.

[130] D.J. Sadler, W. Zhang, C.H. Ahn, H.J. Kim, and S.H. Han. Micromachined semi-encapsulated spiral inductors for micro electro mechanical systems (mems) applications. *IEEE Trans. Magn.*, 33(5):3319–3321, 1997.

[131] D.J. Sadler, S. Gupta, and C.H. Ahn. Micromachined spiral inductors using uv-liga techniques. *IEEE Trans. Magn.*, 37(4):2897–2899, 2001.

[132] Y. Xia and G.M. Whitesides. Soft lithography. *Annu. Rev. Mater. Sci.*, 28:153–184, 1998.

Available online at www.sciencedirect.com
SCIENCE DIRECT®
ELSEVIER
Journal of Magnetism and Magnetic Materials 300 (2006) 418–426
Journal of magnetism and magnetic materials
www.elsevier.com/locate/jmmm

Microelectromagnet for magnetic manipulation in lab-on-a-chip systems

Kristian Smistrup[a,*], Peter T. Tang[b], Ole Hansen[a], Mikkel F. Hansen[a]

[a] *MIC– Department of Micro and Nanotechnology, Technical University of Denmark, DTU—Building 345 East, DK-2800 Kgs, Lyngby, Denmark*
[b] *Department of Manufacturing Engineering and Management, Technical University of Denmark, DK-2800 Kgs, Lyngby, Denmark*

Received 8 February 2005; received in revised form 19 May 2005
Available online 21 June 2005

Abstract

We demonstrate a simple scheme for fabrication of microelectromagnets consisting of planar spiral coils semi-encapsulated in soft magnetic yokes using conventional microfabrication techniques. The microelectromagnets are suitable for applications operating at frequencies below 250 kHz. Conventional fabrication schemes for planar microelectromagnets typically rely on five mask steps. We allow the current to flow in the soft magnetic yoke and thereby two mask steps are eliminated. We have characterized the electromagnets electrically, the results agree well with theory, and the implications arising from current flowing in the magnetic yoke are discussed. We have integrated the microelectromagnets with microfluidic channels, and demonstrated separation of commercially available magnetic beads from a fluid in a microfluidic system, i.e. a lab-on-a-chip system.

PACS: 85.70.Ay; 85.90.ph; 85.80.Jm; 85.85.+j

Keywords: Magnetic microsystems; Separation; Microelectromagnets; Magnetophoresis

1. Introduction

Microelectromagnets have several low-frequency applications in lab-on-a-chip systems. These include magnetically induced motion [1,2], magnetic mixing [3,4], and magnetic separation [5–11].

Conventional fabrication schemes for planar spiral coil microelectromagnets typically rely on five mask steps for defining the spiral coil, electrical connector to the coil center, insulation layers and soft magnetic core [12]. In 1997 Sadler et al. [13] reported a three-mask process for fabrication of microelectromagnets on a Pyrex

*Corresponding author. Tel.: +45 4525 5753, fax: +45 4588 7762.
E-mail address: krs@mic.dtu.dk (K. Smistrup).

0304-8853/$ - see front matter © 2005 Elsevier B.V. All rights reserved.
doi:10.1016/j.jmmm.2005.05.031

substrate. This process was further refined and extended to silicon substrates in 2001 [14].

We demonstrate a simple fabrication scheme requiring only three mask steps. In this design the soft magnetic yoke of the microelectromagnet is also used as a return path for the electrical current. This eliminates the need for additional mask steps necessary to define the electrical connector to the coil center as well as an insulation layer between the electrical connector and the coil. The fabricated microelectromagnets are suitable for DC and low-frequency applications. The larger cross-sectional area of the soft magnetic material compensates for its lower electrical conductivity. Furthermore, we have integrated microfluidic channels into the same silicon wafer, and thus the microfluidic channel is brought into a region with larger magnetic fields and forces.

Manipulation of superparamagnetic nanoparticles encapsulated in polymer beads (magnetic beads) is a well-known technique in biochemical analysis and processing [15]. Recently microsystems offering the same functionality have been reported [5–11]. Since the magnetic force on a magnetic bead is related to the gradient of the magnetic field energy density, it is crucial in magnetic bead separation systems to create large magnetic fields with large local field gradients.

We have chosen to fabricate microsystems where three microelectromagnets fabricated on one side of a silicon wafer create magnetic field gradients in a microfluidic channel etched into the other side the wafer. Finally we demonstrate magnetic bead separation in such a system.

Compared to a similar design by Choi et al. [5], where the microelectromagnets and microfluidic channels were defined on separate wafers, our integrated fabrication scheme brings the microelectromagnets closer to the microfluidic channel enhancing the magnetic field in the channel and thus the bead capture efficiency in the system. Also, we have restricted the channel to the area above the centers of the electromagnets, which further enhances the magnetic forces within the fluid channel.

2. Fabrication of microelectromagnets integrated with microfluidic channels

The fabrication process for the microelectromagnet integrated with a microfluidic channel is summarized in Fig. 1. Micrographs of the fabricated structures at different process steps are shown in Fig. 2.

Three of the fabrication steps involve the patterning of thick photoresist. Hoechst AZ4562 is used throughout. The thick photoresist moulds used require aspect ratios on the order of two. Several recipes capable of meeting these requirements as well as higher aspect ratios are reported in literature [16–20]. We have chosen to adopt a recipe developed in-house by Rehder [21] and

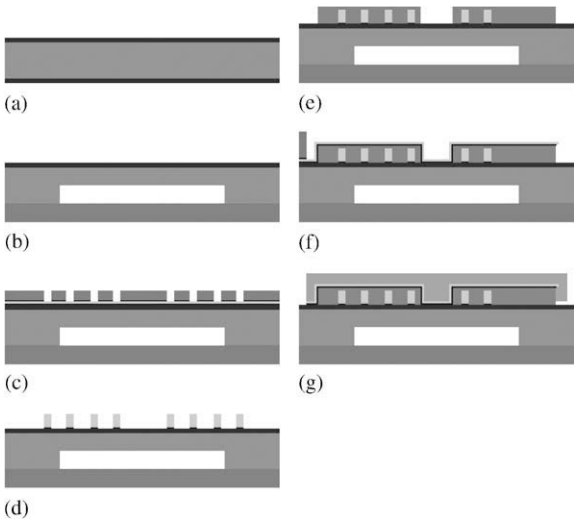

Fig. 1. The major steps in the fabrication process of a microelectromagnet integrated with a microfluidic channel. (a) 50 nm of SiO_2 and 100 nm of Si_3N_4 are grown on an Si (1 0 0) wafer. (b) Si_3N_4 and SiO_2 are removed using RIE and HF on the bottom side. Using UV-lithography and DRIE microfluidic channels are etched into the wafer. A Pyrex wafer is anodically bonded to the bottom side of the silicon wafer. (c) A seed layer is deposited on the wafer and a photo resist mould, 25 μm in thickness is deposited on the wafer. (d) The copper coil is defined by electroplating. The resist and seed layer is removed. (e) The copper coil is encapsulated in a dielectric hard baked layer of photoresist. (f) Another seed layer is deposited on the wafer and another resist mould 25 μm in thickness is deposited on the wafer. (g) The magnetic yoke is defined by electroplating. Finally the resist mould and the seed layer are removed.

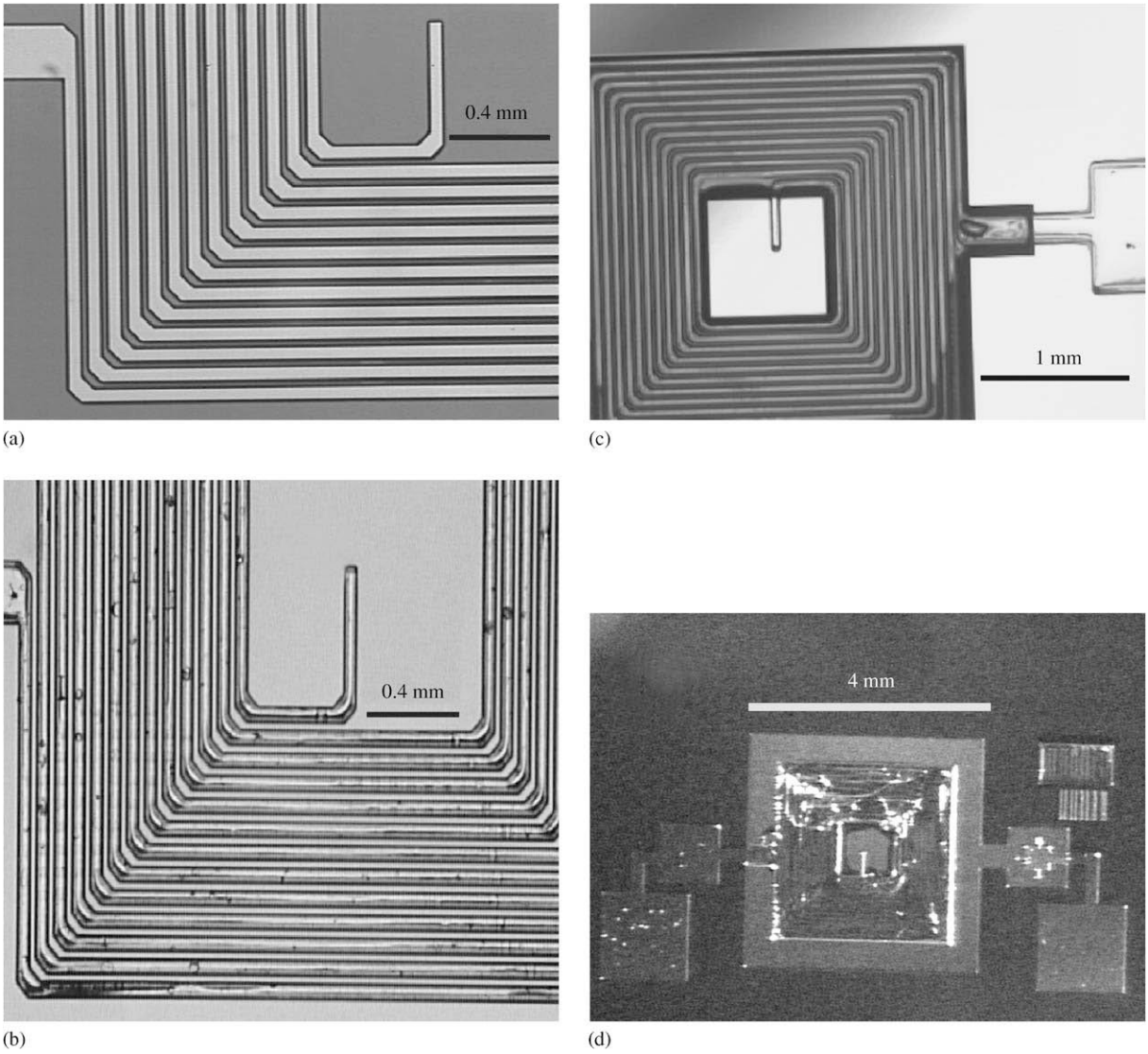

Fig. 2. Micrographs of the microelectromagnetic structure at different process steps. (a) After definition of the resist mould for the copper wires (corresponding to Fig. 1(c)). (b) After electroplating of copper wires (corresponding to Fig. 1(d)). (c) After deposition of the dielectric layer (corresponding to Fig. 1(e)). (d) The finalized structure (corresponding to Fig. 1(g)).

tune it to our needs. Fig. 3 illustrates the resist procedure that has been used throughout.

In Fig. 1(a) a 50 nm dry silicon oxide is grown on both sides of a 350 μm thick double polished (100) 4″ silicon wafer. This is followed by the growth of a 100 nm low-stress low-pressure chemical vapour deposition (LPCVD) silicon nitride on both sides. These layers serve as electrical insulation between the copper wires that will be fabricated on the wafer at a later stage and the silicon wafer.

In Fig. 1(b) a microfluidic channel is defined. First the channel is defined in photoresist using UV-lithography. Then the nitride and oxide are etched away in the resist openings using reactive ion etching (RIE) and hydrofluoric acid,

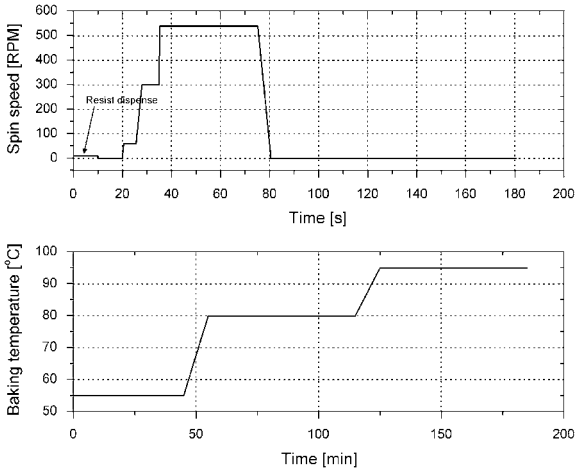

Fig. 3. Procedure for patterning of thick AZ4562 photoresist (Hoechst). The top graph shows the spinning recipe used on a Karl Süss RC-8 spinner with the Gyrset option. The bottom graph shows the oven baking recipe for the resist. After the last high-temperature step, the oven was turned off. After edge bead removal, the resist is exposed using an EV-alignment system in hard contact mode.

respectively. A 150 μm deep channel is then etched into the backside of the silicon wafer using deep reactive ion etching (DRIE). After resist removal and etch of the remaining oxide and nitride using the same techniques as before, a pyrex wafer is anodically bonded to the backside of the wafer.

In Fig. 1(c) a photoresist mould for electroplating copper wires is created. First a seed layer for the electroplating process is deposited on the wafer by e-beam evaporation; the layer consists of 30 nm Ti, 300 nm Cu, and 30 nm of Ti. A 25 μm thick layer of photoresist is spun onto the wafer. Using UV-lithography the photoresist is patterned to define the mould for electroplating. In order to remove resist residue that will be present in the bottom of the resist openings the top titanium layer is etched away in the openings using hydrofluoric acid immediately before electroplating. The resulting structure is shown in Fig. 2a.

In Fig. 1(d) 25 μm high copper wires are electroplated into the resist mould. We use a commercially available plating bath (UBAC ER, Enthone, www.enthone.com). One micrometer of nickel is electroplated on top of the copper wires using a sulphamate nickel plating bath [22], and finally an 80 nm thick gold layer is deposited on top of the nickel layer using ion-exchange plating (ORMEX, Engelhard). The latter two metal layers serve to prevent oxidation of the copper wire that otherwise might cause poor electrical contact to the magnetic yoke. The resist is removed, and a selective etching sequence is applied to remove the seed layer. Ti is etched in hydrofluoric acid, and Cu is etched in a solution of 50 g ammoniumpersulfate per litre of water. The resulting structure is shown in Fig. 2b.

In Fig. 1(e) a dielectric layer is created to encapsulate the copper wires using photoresist. A layer of photoresist, 25 μm in thickness is spun onto the wafer and it is patterned using UV-lithography. The resist is hard baked at approximately 130 °C for 10 min using slow ramping of the temperature. Notice in Fig. 2(c) how the dielectric layer does not cover part of the copper wire in the center of the copper coil. This is the electrical connection between the copper wire and the magnetic yoke.

In Fig. 1(f) a resist mould for electroplating of the soft magnetic yoke is defined. A seed layer for electroplating similar to the one used in Fig. 1(c) is deposited on top of the structures. A 25 μm thick layer of photoresist is spun onto the wafer, and it is patterned using UV-lithography to define the mould for electroplating. The top Ti layer is etched in hydrofluoric acid to remove the resist residue in the resist openings.

In Fig. 1(g) the soft magnetic yoke, 25 μm in thickness, is electroplated into the resist mould. Upon resist removal the selective etching sequence of Fig. 1(d) is applied to remove the seed layer.

Fig. 2(d) shows an overview of the final electromagnet including bond pads.

In Figs. 1(e) and 1(f) photoresist layers are spun on while tall structures are already on the wafer. Using the resist recipe of Fig. 3, the initial slow spinning ensures that a thick resist layer deposits all over the wafer (~100 μm). The final high spin speed thins the resist to the desired thickness. In areas without any underlying structures the thickness will be 25 μm thick. On top of underlying structures the thickness will be ~10–12 μm. Since the resist layer is continuous, there will be areas close to the structures where the resist thickness is

~30–40 μm. Therefore it has been necessary to enhance the exposure dose with 50% for these layers. Since the structures defined in Figs. 1(e) and 1(f) are large and thus have low aspect ratios, the resulting overexposure of some parts is not critical.

Both nickel and PermAlloy have been used as soft magnetic yoke. We used the same nickel bath as for Fig. 1d. We used a pulsed reversal plating sequence for the PermAlloy films. The PermAlloy electrolyte [22] was not running at optimal condition and exhibited large internal tensile stress, which caused the electroplated films to delaminate. While delaminating is acceptable to some extent in conventional fabrication schemes it is essential in this fabrication scheme that good electrical contacts exist between the spiral coil, the magnetic yoke, and the rightmost bond pad in Fig. 2(d).

Since the electroplated nickel has a much lower or no internal stress and thus gives better yield, we have chosen to apply this material also although it is magnetically inferior to PermAlloy.

3. Characterization of the fabricated microelectromagnets

We have measured the impedance of the fabricated electromagnets as a function of frequency. This impedance characteristic has been used to extract the values of the inductance, resistance and parasitic capacitance of the fabricated systems.

The impedance has been measured inside an electromagnetically shielded probe station using an HP 4194 Impedance Analyser connected to the bond pads.

Fig. 4 shows the real and imaginary part of the measured impedance. The values of L, R, and C have been extracted by fitting the impedance characteristic of the equivalent circuit (insert on Fig. 4) to the measured characteristic.

Only the low-frequency part of the data has been used in the fitting procedure, since the simple equivalent circuit fails to describe the impedance at higher frequencies. The extracted values of L, R, and C are shown in an insert on Fig. 4.

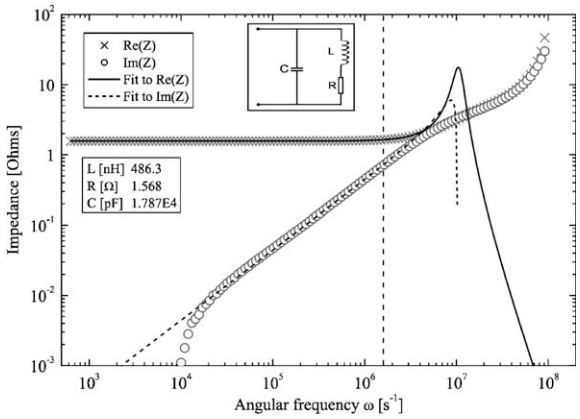

Fig. 4. The measured impedance, Z, of a fabricated microelectromagnet shown as a function of angular frequency. An insert shows the extracted values of L, R, and C of the equivalent circuit (the other insert). Only the measurements to the left of the dashed vertical line (placed at the frequency 250 kHz) are used when extracting L, R, and C. For low frequencies the imaginary part of the measured impedance is so small that it cannot be accurately measured with the current set-up. This is the reason for the discrepancy between the measured and the modelled imaginary part of the impedance at very low frequencies.

There are several reasons for the breakdown of the simple equivalent circuit. The equivalent circuit is a lumped model of a distributed electrical network but also physical effects invalidate the approximation that the circuit consists of ideal components. These effects include: hysteretic losses [23], eddy currents in the magnetic material [23], substrate losses [24,25], skin depth effects [25], and eddy currents in the copper coil [25]. Using the magnetic yoke as a current conductor increases the hysteretic losses and the eddy currents in the magnetic material, which are both high-frequency effects.

It is observed that the microelectromagnet behaves ideally for frequencies below 250 kHz, and thus it is useful for applications operating at and below this frequency.

We have found that for microelectromagnets without magnetic yokes the simple equivalent circuit is sufficient to describe the impedance for frequencies below 1 MHz and thus we conclude that it is the physical effects related to the magnetic yoke that limit the operating frequency. Since we are using these electromagnets as DC- or

low-frequency field generators rather than electrical components, we are only interested in the low-frequency behavior. For high-frequency applications one should seek to suppress the effects described above to achieve good high-frequency characteristics. This is discussed in Ref. [12].

We have fabricated spiral coils with various geometries and various magnetic yokes. From the geometries a theoretical inductance in the absence of a magnetic yoke can be calculated using the monomial formula of Mohan et al. [24]. The fabricated geometries and the calculated inductances are summarized in Table 1.

According to Hurley and Duffy [26] the addition of a magnetic yoke is expected to enhance the inductance with a factor between 1 and 2 that depends only on the thickness and relative magnetic permeability of the yoke. Fig. 5 shows measured inductances for several systems plotted against the theoretical values of the inductances if no magnetic yokes were present. It is seen that for air, which means that there is no magnetic yoke, the measured inductance deviates approximately 2% from the theoretically expected inductance. When a 25 μm thick magnetic yoke of nickel or PermAlloy is added to the system, the inductance is enhanced by 30% and 63%, respectively. Since the thickness of the magnetic yokes is the same it is expected that the enhancement should be largest when a PermAlloy magnetic yoke is applied, since PermAlloy has a larger magnetic permeability than nickel. It is also seen that the enhancement factor is constant for several geometries, which is also expected.

Since the forces generated in magnetic bead manipulation are proportional to the gradient of the magnetic field energy, which is proportional to the coil current squared, the safe upper coil current limit is important. Experimentally we find that all designs can carry 1.5 A without degradation; increasing the current significantly above this level leads to an irreversible increase of the series resistance of the systems, possibly due to degradation of the contact between the Cu coil and the magnetic yoke current return path. However, with a current of 1.0 A through all three electromagnets of design B, water was observed to boil in the microfluidic channel. Therefore the limiting factor for biochemical applications will most likely be the on-chip heat generation. For most bio-chemical applications a reasonable limit on the temperature inside the microfluidic channel is ~37 °C, and the practical upper coil current limit is thus expected to be in the range of 400–500 mA depending on the fluid flow rate and how well the chip is thermally

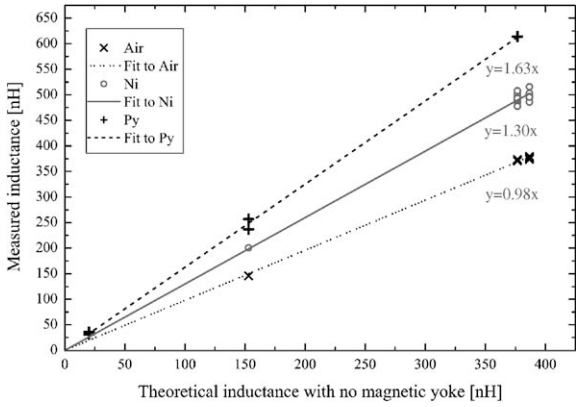

Fig. 5. Measured inductances with different magnetic yokes vs. the theoretically calculated inductances of the geometries without magnetic yoke. Air, Ni, and Py means that the magnetic yokes are made of air (no yoke), nickel, and PermAlloy, respectively.

Table 1
Summary of the geometries of the fabricated microelectromagnets

Design	Total coil width (μm)	Coil wire width c (μm)	Coil wire height (μm)	Coil wire spacing (μm)	Number of turns(·)	Theoretical inductance (nH)
A	3000	50	25	30	12	386.7
B	3000	60	25	20	12	376.7
C	1200	20	25	12	12	152.9
D	600	20	25	12	6	20.2

connected to the surroundings. Since the electrical resistance is unchanged if the total coil width, coil wire width, and coil wire spacing are scaled with the same number and the coil height remains the same, the on-chip joule heating is the same also for smaller and larger systems. For the smaller systems, however, the heat will be generated in a smaller area, and therefore the heating of the sample might be more severe. On the other hand silicon is a very good heat conductor (the thermal conductivity of silicon is approximately two orders of magnitude larger than that of pyrex), and the heat will therefore quickly dissipate to other areas of the chip, and to the surroundings, if the chip is properly thermally clamped.

We have calculated the expected magnetic performance at a coil current of 500 mA numerically. For the calculation we have used FEMLAB® with a cylindrical approximation to the square electromagnet [27]. The calculated expected values of the maximum magnetic field strengths and magnetic field gradients within the microfluidic channel (150 μm above the microelectromagnet) are reported in Table 2.

The magnetic force from a magnetic field on a magnetically unsaturated magnetic particle is given by [28]:

$$\mathbf{F}_{\text{magn}} = \frac{1}{\mu_0}\chi_{\text{m}} V_{\text{bead}}(\mathbf{B}\cdot\nabla)\mathbf{B}, \tag{1}$$

where μ_0 is the permeability of free space, χ_{m} is the measured magnetic volume susceptibility of the particle, V_{bead} is the volume of a magnetic bead, and $\mathbf{B}$ is the magnetic flux density from the electromagnet. The maximum value of $|(\mathbf{B}\cdot\nabla)\mathbf{B}|$ is also given in Table 2.

Table 2
Calculated performance of the fabricated systems with Ni yoke at a coil current of 0.5 A

Design	Maximum magnetic field (mT)	Maximum magnetic field gradient (T/m)	Maximum value of $\lvert(\mathbf{B}\cdot\nabla)\mathbf{B}\rvert$ (T^2/m)
A	5.3	13	0.066
B	5.3	13	0.066
C	10	42	0.42
D	6.4	47	0.30

For a magnetic bead (MyOne®, Dynal Biotech [14]) with a diameter of 1.05 μm and a magnetic susceptibility of approximately 1.5, the data in Table 2 corresponds to forces in the range of 40–300 fN.

Due to their very small radius the inertial force on magnetic beads will be negligible compared to the fluid drag on the beads, and thus the fluid drag will ensure that the beads always move with an equilibrium velocity, such that the fluid drag force cancels the magnetic (and gravitational) force(s). The downward velocity of the beads due to the magnetic force will be [29]:

$$v_{\downarrow} = \frac{\mathbf{F}_{\text{magn},\downarrow}}{3\pi D\eta}, \tag{2}$$

where only the downward component of the magnetic force is considered, D is the diameter of the magnetic bead, and η is the viscosity of the fluid (in this case water). For a magnetic force of 40 fN Eq. (2) gives a downward velocity of approximately 4 μm/s, which should be compared to the average linear velocity of the fluid. In the experiment described in the next section the average linear velocity is 110 μm/s. Microfluidic channels are generally much longer than their depth (for the experiment in the next section the channel is 100 times longer than it is deep). Simulations [30] indicate that this is sufficient for bead capture.

4. Magnetic bead separation

We have fabricated chips with three microelectromagnets integrated with a microfluidic channel. Magnetic bead separation has been performed using these systems. Fig. 6 shows an overview (a) and a cross-section (b) of the entire system complete with fluid access holes drilled through the Pyrex wafer.

Fig. 7 shows excerpts from a series of micrographs recording magnetic separation. The spiral coils are of design B. This system was chosen over the smaller, theoretically more efficient systems, because of the higher fabrication yield. The lower fabrication yield of the smaller systems is due to the less than optimal resist process. The soft

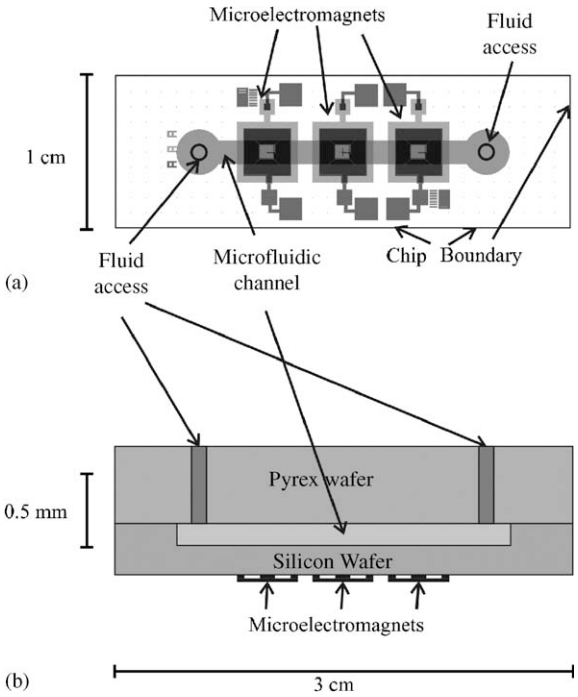

Fig. 6. The complete microsystem. (a) Overview of the microsystem showing the position of the electromagnets and the microfluidic channel. (b) Cross-section of the microsystem showing the wafers, microfluidic channel, and the microelectromagnets. Note that the horizontal scale at the bottom applies to both (a) and (b).

magnetic yoke is electroplated nickel. The current through each of the electromagnets is 360 mA.The microfluidic channel is 0.15 mm deep, 1.5 mm wide, and 14 mm long. Using the same calculation method as before we have estimated that inside the microfluidic channel, the maximum magnetic field is 4.5 mT, the maximum field gradient is 10 T/m, and the maximum value of $|(\mathbf{B}\cdot\nabla)\mathbf{B}|$ is 0.05 T^2/m. These values are found near the edge of the center of the electromagnet.

An aqueous solution containing 76×10^3 magnetic beads per mL of water is pumped through the microfluidic channel using a syringe pump with a volumetric flow rate of 2 μL/min. The magnetic beads are of the type MyOne from Dynal Biotech [15].

With the solution flowing in the channel the current is turned on at $t = 0$ (refer to Fig. 7). After 5 min the first sign of a brighter line consisting of magnetic beads can be seen. After 10 min this line

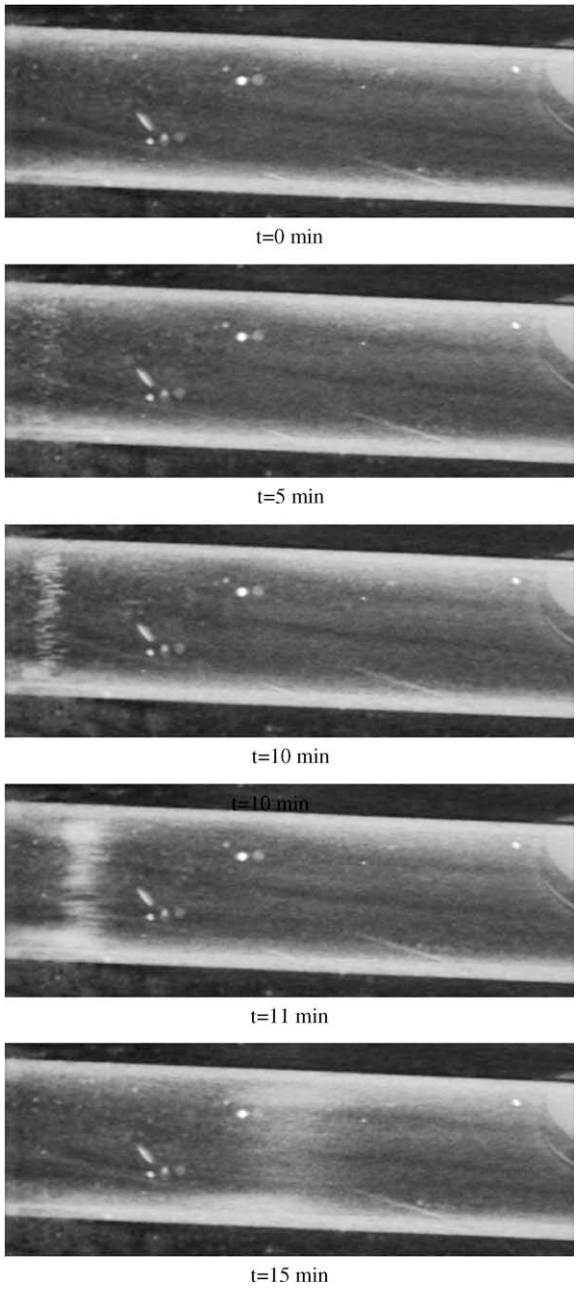

Fig. 7. Capture and release of magnetic beads in a 1.5 mm wide microfluidic channel. A solution of water and magnetic beads flows in the channel. $t = 0$: the current is turned on in the electromagnets at the other side of the wafer. $t = 5$ min: The first sign of captured magnetic beads. $t = 10$ min: clear evidence of bead capture. The current is turned off after 10 min and 19 s. $t = 11$ min: the beads are released. $t = 15$ min: The beads flow out of the channel and the collected beads are redispersed.

is clearly seen as a sharp line. After 10 min and 19 s the current is turned off. After 11 min it is seen that the line of magnetic beads has moved and also it is slightly blurred. After 15 min the line of magnetic beads is heavily blurred and it has clearly moved along the channel.

Fig. 7 demonstrates the ability to capture and subsequently release magnetic beads. According to Choi et al. [10] these are the only requirements necessary to be able to apply magnetic bead separation in biochemical analysis and processing.

We have not been able to measure the bead capture efficiency directly. However, simulations [30] indicate that the bead capture efficiency under these conditions is approximately 89%. Also the bead capture efficiency can be tuned to a desired value by tuning the volumetric flow rate in the channel and the current in the electromagnets.

5. Conclusion

We have demonstrated a simple fabrication scheme for microelectromagnets made from semi-encapsulated planar spiral coils.

The fabricated electromagnets have been shown to behave in good agreement with current theory and to be suitable for applications operating below 250 kHz.

By integrating the microelectromagnets and microfluidic channels on the same silicon wafer, we have improved the efficiency of a magnetic separation system, and we have demonstrated the ability to separate magnetic beads from a fluid, which is useful in biochemical applications and for lab-on-a-chip systems.

References

[1] A. Rida, V. Fernandez, M.A.M. Gijs, Appl. Phys. Lett. 83 (2003) 2396.
[2] T. Deng, G.M. Whitesides, M. Radakrishnan, G. Zabow, M. Prentiss, Appl. Phys. Lett. 78 (2001) 1775.
[3] K.S. Ryu, K. Shaikh, C. Liu, Proc. microTAS 2003 (2003) 635.
[4] R. Rong, J-W. Choi, C.H. Ahn, Proc. microTAS 2003 (2003) 335.
[5] J-W. Choi, T.M. Liakopoulos, C.H. Ahn, Biosens. Bioelectron. 16 (2001) 409.
[6] M. Tondra, M. Granger, R. Fuerst, M. Porter, C. Nordman, J. Taylor, S. Akou, IEEE Trans. Magn. 37 (2001) 2621.
[7] C.H. Ahn, M.G. Allen, W. Trimmer, Y.N. Jun, S. Erramilli, J. Microelectromech. Syst. 5 (1996) 151.
[8] T. Deng, M. Prentiss, G.M. Whitesides, Appl. Phys. Lett. 80 (2002) 461.
[9] J-W. Choi, C.H. Ahn, S. Bhansali, T.H. Henderson, Sensor. Actuat. B-Chem. 68 (2000) 34.
[10] J-W. Choi, K.W. Oh, A. Han, N. Okulan, C.A. Wijayawardhana, C. Lannes, S. Bhansali, K.T. Schlueter, W.R. Heineman, H.B. Halsall, J.H. Nevin, A.J. Helmicki, H.T. Henderson, C.H. Ahn, Biomed. Microdevices 3 (2001) 191.
[11] R. Rong, J-W. Choi, C.H. Ahn, Proc. IEEE MEMS 2003 (2003) 530.
[12] J.N. Burghartz, Int. J. RF and Microwave CAE 8 (1998) 422.
[13] D.J. Sadler, W. Zhang, H.J. Kim, S.H. Han, C.H. Ahn, IEEE Trans. Magn. 33 (1997) 3319.
[14] D.J. Sadler, S. Gupta, C.H. Ahn, IEEE Trans. Magn. 37 (2001) 2897.
[15] www.dynabead.com.
[16] S. Roth, L. Dellmann, G-A. Racine, N.F. de Rooij, J. Micromech. Microeng. 9 (1999) 105.
[17] J. Gobet, F. Cardot, J. Bergqvist, F. Rudolf, J. Micromech. Microeng. 3 (1993) 123.
[18] M. Brunet, T. O'Donnell, J. O'Brien, P. McCloskey, and Ó Mathuna, J. Micromech. Microeng. 12 (1993) 444.
[19] J. O'Brien, P.J. Hughes, M. Brunet, B. O'Neill, J. Alderman, B. Lane, A. O'Riordan, C. O'Driscoll, J. Micromech. Microeng. 11 (2001) 353.
[20] E. Lennon, F. Ayela, J. Micromech. Microeng. 12 (2002) 122.
[21] J. Rehder, micromachined loudspeaker for hearing instrument application, Ph.D. Thesis Technical University of Denmark, MIC—Department of Micro and Nanotechnology, April 2002.
[22] P.T. Tang, fabrication of micro components by electrochemical deposition, Ph.D. Thesis Technical University of Denmark, Department of Manufacturing Engineering and Management, March 1998.
[23] R.C. O'Handley, Modern magnetic materials — Principles and applications, Wiley, New York, ISBN 0-471-15566-7, 2000, pp. 338–345.
[24] S.S. Mohan, M.M. Hershenson, S.P. Boyd, T.H. Lee, IEEE J. Solid-St. Circ. 34 (1999) 1419.
[25] C.R. Neagu, H.V. Jansen, A. Smith, J.G.E. Gardeniers, M.C. Elwenspoek, Sensor. Actuat. A-Phys. 62 (1997) 599.
[26] G.H. Hurley, M.C. Duffy, IEEE Trans. Magn. 33 (1997) 2282.
[27] M. Shafique, M.F. Hansen, Proc. Nordic Matlab Con (2003) 209.
[28] A. Engel, R. Friedrichs, Am. J. Phys. 70 (2002) 428.
[29] K.C. Warnke, IEEE Trans. Magn. 39 (2003) 1771.
[30] K. Smistrup, O. Hansen, H. Bruus, M.F. Hansen, J. Magn. Magn. Mater. 293 (2005) 597.

Available online at www.sciencedirect.com
SCIENCE DIRECT®
ELSEVIER
Journal of Magnetism and Magnetic Materials 293 (2005) 597–604
Journal of magnetism and magnetic materials
www.elsevier.com/locate/jmmm

Magnetic separation in microfluidic systems using microfabricated electromagnets—experiments and simulations

Kristian Smistrup*, Ole Hansen, Henrik Bruus, Mikkel F. Hansen

MIC—Department of Micro and Nanotechnology, Technical University of Denmark, DTU - Building 345 East, DK-2800 Kongens Lyngby, Denmark

Available online 7 March 2005

Abstract

We present experiments and simulations of magnetic separation of magnetic beads in a microfluidic channel. The separation is obtained by microfabricated electromagnets. The results of our simulations using FEMLAB and Mathematica are compared with experimental results obtained using our own microfabricated systems.

Keywords: Microsystems; Magnetic separation; Computational fluid dynamics; Magnetophoresis; FEMLAB software; Microfluidics; Simulation; Electromagnet; Microelectromagnet; Nanotechnology; Channel flow

1. Introduction

Manipulation of superparamagnetic nanoparticles encapsulated in polymer beads (magnetic beads) is a well-known technique in biochemical analysis and processing [1,2]. In magnetic separation biochemically functionalized magnetic beads are separated from a solution using magnetic forces. Recently, microsystems offering the same functionality have been reported [3–5]. Microsystems capable of magnetic separation are ideal for inclusion in Lab-on-a-chip systems. The vision of Lab-on-a-chip systems is to have entire biochemical laboratories on a single chip. The advantages of such Lab-on-a-chip systems are that they can handle minute sample volumes (e.g. micro or nanolitres), they are highly portable, and they are potentially inexpensive and thus disposable [6,7].

We present numerical simulations of the movements of such magnetic beads in microfluidic systems and compare with experiments.

2. Design and fabrication

The design of our microsystem is shown in Fig. 1. Each microsystem contains three microelectromagnets, each consisting of a copper coil semi-encapsulated in a dielectric layer and a nickel soft magnetic yoke on top of that.

*Corresponding author. Tel.: +45 4525 5753; fax: +45 4588 7762.
E-mail address: krs@mic.dtu.dk (K. Smistrup).

0304-8853/$ - see front matter © 2005 Elsevier B.V. All rights reserved.
doi:10.1016/j.jmmm.2005.01.079

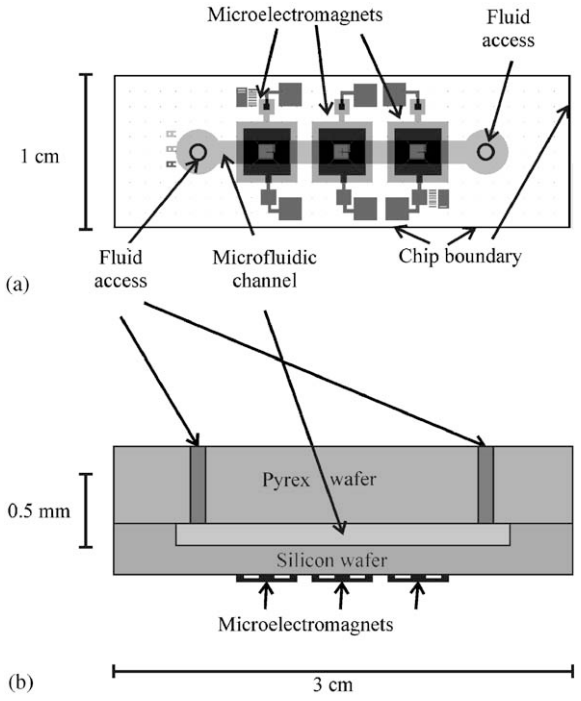

Fig. 1. Overview of the microsystem design. (a) Top-view of the fabricated chip. The microelectromagnets are planar spiral copper coils with 12 turns. The coils are semi-encapsulated in a soft magnetic yoke made from nickel. (b) The microsystem seen from the side. The horizontal scale bar at the bottom applies to both (a) and (b).

We have fabricated electromagnets by use of standard cleanroom technology. Fig. 2 summarizes the fabrication process. For more details see Ref. [8]. The electromagnets that we have used for the experimental part of this paper have the following design parameters: number of turns 12; coil wire height 25 μm, width 60 μm, and spacing 20 μm; electromagnet width 4 mm, and yoke thickness 25 μm; fluid channel depth 150 μm, length 14 mm, and width 1.5 mm.

3. Magnetostatic theory

The magnetic induction $\mathbf{B}$ is calculated using magnetostatics formulae,

$$\mathbf{B} = \nabla \times \mathbf{A} = \mu_0 \mu_r \mathbf{H}, \tag{1}$$

$$\nabla \times \mathbf{H} = \mathbf{J}^f, \tag{2}$$

where $\mathbf{H}$ is the magnetic field, $\mathbf{A}$ is the magnetic vector potential, μ_0 is the permeability of vacuum, μ_r is the relative permeability of the material, and $\mathbf{J}^f$ is the free current density. These equations can be combined to yield

$$\nabla \times ((\mu_0 \mu_r)^{-1}(\nabla \times \mathbf{A})) = \mathbf{J}^f. \tag{3}$$

To simplify the simulations we study circular electromagnets, and thus the magnetostatic problem is reduced from 3D to 2D. This still allows for qualitative comparison with the square magnets of the experiments as discussed by Shafique et al. [9].

We apply cylindrical coordinates (r, θ, z) with $r = 0$ at the centre of the electromagnet. All free currents are thus in the azimuthal direction $\mathbf{J}^f = J^f(r, z)\hat{\mathbf{e}}_\theta$ which is consistent with a magnetic vector potential $\mathbf{A} = A_\theta(r, z)\hat{\mathbf{e}}_\theta$.

To bring Eq. (3) into a form suitable for the software, FEMLAB®, we introduce the function $u(r, z)$ given by

$$u(r, z) = \frac{A_\theta(r, z)}{r}. \tag{4}$$

Using this, the only non-zero component of Eq. (3) is

$$-\frac{\partial}{\partial r}\left(r(\mu_0\mu_r)^{-1}\frac{\partial u}{\partial r} + 2(\mu_0\mu)^{-1}u\right) - \frac{\partial}{\partial z}\left(r(\mu_0\mu_r)^{-1}\frac{\partial u}{\partial z}\right) = J_\theta^f, \tag{5}$$

which is the canonical form that FEMLAB® solves in its "Magnetostatics–Azimuthal currents" mode of its Electromagnetics Module [10]. In terms of $u(r, z)$ the components of the magnetic induction become:

$$\mathbf{B} = (B_r, B_\theta, B_z) = \left(-r\frac{\partial u}{\partial z}, 0, r\frac{\partial u}{\partial r} + 2u\right). \tag{6}$$

Nickel is a ferromagnetic material, and thus μ_r is not a constant. However, since nickel is a soft magnetic material and thus almost hysteresis-free, we use the approximate empirical Fröhlich–Kennelly relation $\mathbf{M} = M_s\mathbf{H}/(C + |\mathbf{H}|)$ for hysteresis-free magnetization to describe the material [11].

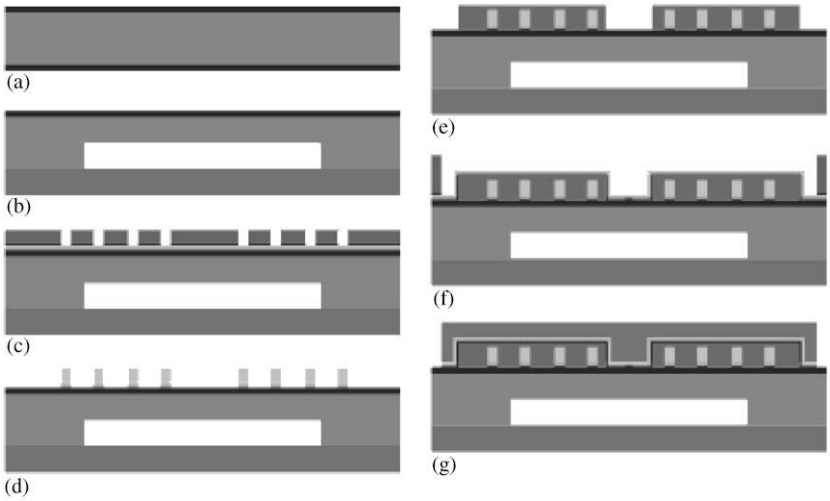

Fig. 2. Process flow for the fabrication of a micromachined magnetic bead separator. (a) A double polished silicon wafer is oxidized (50 nm) and 100 nm silicon nitride is grown. (b) The microfluidic channel (150 μm deep) is etched using deep reactive ion etching (DRIE), and a pyrex lid is attached by anodic bonding. (c) A seed layer is deposited, and a 25 μm layer of photoresist (AZ4562 from Hoechst is used throughout) is spun onto the wafer and patterned using UV-lithography. (d) The copper wire is electroplated into the resist mould followed by resist and seed layer removal. (e) A patterned layer of hard-baked photoresist forms the dielectric layer. (f) A seed layer is deposited and a new photoresist mould is defined. (g) A 25 μm nickel magnetic yoke is electroplated into the resist openings. Finally the resist and seed layer are removed.

The relative permeability $\mu_r(\mathbf{H})$ thus becomes

$$\mu_r(\mathbf{H}) = 1 + \frac{M_s}{C + |\mathbf{H}|}, \tag{7}$$

where M_s is the saturation magnetization of the material, and C is an experimentally determined parameter.

In order to solve Eq. (5) in FEMLAB®, it is necessary to express μ_r as a function of $\mathbf{B}$ (or actually as a function of u and its partial derivatives) rather than $\mathbf{H}$ in order to use it in Eq. (5). By setting $|\mathbf{H}| = |\mathbf{B}|/\mu_0\mu_r$ in Eq. (7), μ_r is found as the positive root of a second order polynomial, which to first order in $|\mathbf{B}|$ is

$$\mu_r(|\mathbf{B}|) = 1 + \frac{M_s}{C} - \frac{M_s}{C(C + M_s)} \frac{|\mathbf{B}|}{\mu_0} + O(|\mathbf{B}|^2). \tag{8}$$

It is seen that $\mu_r(|\mathbf{B}|)$ is constant until the magnetic field inside the magnetic material approaches the saturation magnetization (assuming $M_s \gg C$).

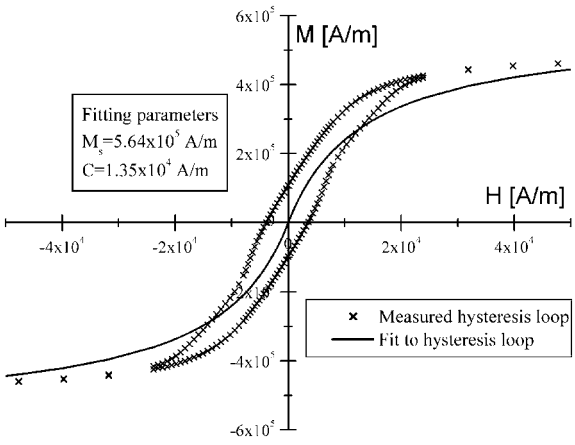

Fig. 3. **M** vs. **H** loop of an electroplated nickel film. The measured saturation magnetization is 4.84×10^5 A/m. The line is the fitted Fröhlich–Kennelly relation described in the text.

Fig. 3 features the measured hysteresis loop of one of our electroplated nickel thin films together with a fit based on Eq. (7). We have focused on a good fit for the low-field part of the hysteresis loop, which is why we have allowed for a saturation magnetization in the fit, which is

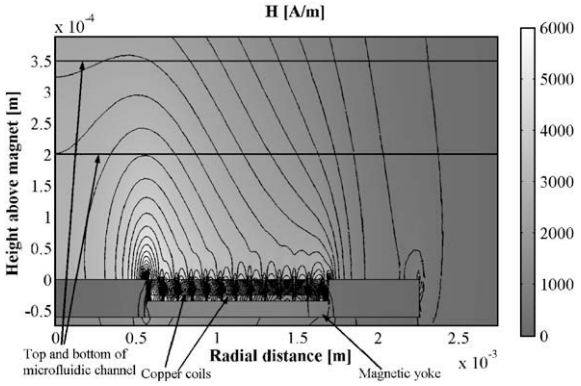

Fig. 4. Contour plot of the magnitude of the calculated **H**-field. The current in the copper coil is 360 mA. Also shown is the position of the microfluidic channel relative to the electromagnet. The magnetic beads will be attracted to regions where the magnetic field is large.

different from the nickel saturation magnetization of 4.84×10^5 A/m.

We have used the electromagnetics module of FEMLAB® 2.3 to solve Eqs. (4) through (7) with the parameters of the electroplated nickel thin film. In order to keep the magnetic reluctance of the entire system constant, all length scales have been scaled in order to have the same area in the circular geometry as in the original square geometry [9]. This yields a scaling factor of $(4/\pi)^{1/2}$. The free current density has been scaled with the inverse factor to ensure that the total current is unchanged.

Fig. 4 shows the result of such a calculation. Note that the magnetic beads will be attracted to areas in the microfluidic channel with large magnetic field and thus the attraction will be perpendicular to the contours of Fig. 4 (since these are also contours of $|\mathbf{H}|^2$). The fact that $|\mathbf{H}|$ inside the magnetic yoke does not exceed 2000 A/m, means that μ_r is everywhere within 80% of the constant $1 + M_s/C$ in Eq. (8).

4. Magnetic force on a magnetic bead

First, the magnetic force on a magnetic bead is calculated from the calculated magnetic field. The general expression for the magnetic force on a magnetizable object is given by [12]

$$\mathbf{F}_{\text{mag}} = \mu_0 \int_V (\mathbf{M} \cdot \nabla)\mathbf{H}_a \, \mathrm{d}^3 r, \tag{9}$$

where the integral is taken over the volume of the magnetizable object, and $\mathbf{H}_a$ is the magnetic field in the absence of the magnetizable object.

For a spherical bead in a homogeneous magnetizing field, the magnetization **M** inside the bead is given by [13]

$$\mathbf{M} = \chi_m \mathbf{H}_a = \frac{\chi_i}{1 + N\chi_i}\mathbf{H}_a = 3\,\frac{\mu_r - 1}{\mu_r + 2}\mathbf{H}_a, \tag{10}$$

where χ_i is the intrinsic susceptibility of the magnetic bead material, χ_m is the measured susceptibility of a single magnetic bead including demagnetization effects, and $\mu_r = 1 + \chi_i$ is the relative permeability of the magnetic bead material. It has been assumed that the sphere is surrounded by a medium with $\chi \approx 0$. The last equality follows from the fact that the demagnetization factor of a sphere is $N = \frac{1}{3}$. At this point it is not necessary to assume that χ is constant; however, this assumption simplifies the following equations substantially, and is justified for the fields inside the microfluidic channel in our case. Inserting this into Eq. (9) and taking the magnetizable object to be a magnetic bead yields:

$$\begin{aligned}\mathbf{F}_{\text{mag}} &= \mu_0 3\,\frac{\mu_r - 1}{\mu_r + 2}\int_{\text{Bead}} (\mathbf{H}_a \cdot \nabla)\mathbf{H}_a \, \mathrm{d}^3 r \\ &\approx 2\pi R^3 \mu_0\,\frac{\mu_r - 1}{\mu_r + 2}\,\nabla(|\mathbf{H}_a|^2) \\ &= \frac{1}{2}\mu_0 V_{\text{bead}} \chi_m \nabla(|\mathbf{H}_a|^2).\end{aligned} \tag{11}$$

The approximation is that the integrand is constant over the volume V_{bead} of a magnetic bead with radius R, and it has been used that $\mathbf{H}_a$ is curl-free, since there are no free currents outside the copper coils. This result is consistent with the effective dipole approximation reported by Jones [14], but it has been found through different means.

5. Dynamics and microfluidic theory

Low Reynolds numbers and hence laminar flows generally characterize fluid flows in

microfluidic systems. For example in our system and for the used flow rates the Reynolds number is approximately 10^{-2}, and thus all inertial terms in the Navier–Stokes equation can be discarded. Since we are considering stationary incompressible flow in straight channels with no net body force on the fluid, the Navier–Stokes equation reduces to:

$$\left(\frac{\partial^2}{\partial y^2}+\frac{\partial^2}{\partial z^2}\right)v_x(y,z)=-\frac{\Delta p}{\eta L}, \tag{12}$$

where Δp is the pressure drop across the length L of the microfluidic channel, η is the viscosity of the fluid, and $v_x(y,z)$ is the longitudinal velocity in the channel. Using the usual no-slip boundary conditions on the walls $(y,z)\in[0,y_0]\times[0,z_0]$ the solution to Eq. (12) can be written as

$$v_x(y,z)=v_{\text{avr}}\frac{\phi(y,z)}{\langle\phi\rangle}, \tag{13}$$

$$\phi(y,z)=\sum_{n=0}^{\infty}f_n(z)\sin(k_n y),\quad k_n=(2n+1)\frac{\pi}{y_0}, \tag{14}$$

$$f_n(z)=\frac{-1}{(2n+1)^3}\left(\cosh(k_n z)-\tanh\left(k_n\frac{z_0}{2}\right)\sinh(k_n z)-1\right), \tag{15}$$

$$\langle\phi\rangle=\frac{1}{y_0 z_0}\int_0^{z_0}\int_0^{y_0}\phi(y,z)\,\mathrm{d}y\,\mathrm{d}z, \tag{16}$$

where v_{avr} is the average flow velocity in the channel given by $v_{\text{avr}}=Q/y_0z_0$ where Q is the volumetric flow rate. In experimental microfluidics the flow rate is often the adjustable parameter rather than the pressure difference, and the solution is expressed in terms of Q. For the numerical calculations, the sum in Eq. (14) was truncated at $n=100$.

We take the fluid drag on a magnetic bead to be the Stokes drag:

$$\mathbf{F}_{\text{fluid}}=6\pi R\eta(\mathbf{v}_{\text{fluid}}-\mathbf{v}), \tag{17}$$

where η is the viscosity of the fluid, and $\mathbf{v}_{\text{fluid}}$ and $\mathbf{v}$ are the velocity vectors of the fluid and bead, respectively.

Finally gravity is included through a buoyancy term:

$$\mathbf{F}_{\text{grav}}=\tfrac{4}{3}\pi R^3(\rho_{\text{fluid}}-\rho)g\hat{\mathbf{z}}, \tag{18}$$

where the ρ_{fluid} and ρ are the densities of the fluid and bead, respectively.

At this point we have accounted for all the forces that affect a magnetic bead in the fluid, and thus Newton's second law yields:

$$\rho\,\frac{4}{3}\,\pi R^3\,\frac{\mathrm{d}\mathbf{v}}{\mathrm{d}t}=\mathbf{F}_{\text{mag}}(\mathbf{r})+\mathbf{F}_{\text{grav}}(\mathbf{r})+\mathbf{F}_{\text{fluid}}(\mathbf{r},\mathbf{v}). \tag{19}$$

At a given bead position all forces can be considered constant except for $\mathbf{F}_{\text{fluid}}$ that depends on $\mathbf{v}$, and that yields a differential equation for $\mathbf{v}$ with a solution that has a constant term (the equilibrium velocity) and a decaying exponential function with a time constant τ given by:

$$\tau=\frac{2R^2\rho}{9\eta}\approx 10^{-7}\ \text{s}. \tag{20}$$

This shows that the bead reaches its equilibrium velocity, where all forces cancel, instantaneously compared to other time scales in the simulation, e.g. capture times, and thus it is justifiable to use the equilibrium velocity for calculations of the bead flows [15]. Hence we neglect the inertial term of Eq. (19), and obtain

$$\mathbf{v}=\frac{\mathrm{d}\mathbf{r}}{\mathrm{d}t}=\mathbf{v}_{\text{fluid}}(\mathbf{r})+\frac{1}{6\pi R\eta}(\mathbf{F}_{\text{mag}}(\mathbf{r})+\mathbf{F}_{\text{grav}}(\mathbf{r})). \tag{21}$$

Eq. (21) constitutes three coupled, first-order, ordinary differential equations of motion for the bead.

From the equations of motion it is seen that the largest magnetic forces appear in regions with the largest gradients in $|\mathbf{H}|^2$. Once caught by the magnetic gradient force, the particles are brought towards the local magnetic field maximum. Hence, we expect a high capture efficiency near such points, i.e. near edges and corners of magnetic structures.

6. Simulations

For the simulations we have used the parameters of the bead type MyOne® from Dynal Biotech [2], which are approximately: $2R = 1.05\,\mu m$, $\rho = 1.8 \times 10^3\,kg/m^3$, and $\mu_r = 2.5$. Also, the permeability of the magnetic beads can be assumed constant, since the applied fields do not saturate the beads. The fluid is water with $\rho = 1.0 \times 10^3\,kg/m^3$ and $\eta = 8.90 \times 10^{-4}\,Pa\,s$.

We have solved Eq. (21) using the numerical solver NDSolve of Mathematica® for many different initial positions of the magnetic beads. We have assumed that whenever a bead hits the bottom of the microfluidic channel, it sticks without any possibility of further motion.

Fig. 5 shows the result of a calculation where 10,000 magnetic beads have been released into the microfluidic channel from the left at equally spaced points. The flow rate is $1\,\mu L/min$. From Fig. 5(a) it is noticed that many beads settle near the entrance of the channel. This is due to the low velocity of beads that are released very close to the bottom of the microfluidic channel so that gravity will have a large effect over short distances. However, since the fluid velocity near the bottom of the channel is small, the bead in-flux is also small there. In other words, the in-flux of magnetic beads is low for $z \approx 0$, whereas the in-flux is large for $z \approx z_0/2$. This is reflected in Fig. 5(b) that shows the bead settling probability density across the microfluidic channel. Each of the settling points from Fig. 5(a) has been scaled with the fluid velocity at the entry point of the bead, since the in-flux of magnetic beads at an entry point is proportional to the fluid velocity at that entry point, if the bead concentration in the fluid is constant. Since the in-flux of magnetic beads in the part of the channel entrance (near the bottom of the channel) that would lead to settling points in the beginning of the channel is low, the settling probability density is not as high in the left part of the channel as might be expected from Fig. 5(a). It is Fig. 5(b) rather than Fig. 5(a) that one would expect to observe experimentally.

The most important feature of Fig. 5 is that the beads clearly tend to settle near the inner pole piece edges of the electromagnets, i.e., where the magnetic field is largest according to Fig. 4. This means that an experimentally observed bead-settling pattern would be expected to concentrate in these areas.

Fig. 6 shows a magnetic capture diagram of the entrance of the microfluidic channel, and it shows where beads with different initial positions settle in the microfluidic channel. It is seen how beads released near the sides or bottom of the microfluidic channel are more easily captured in the channel, since the fluid velocity at the release point is small, and thus both gravity and magnetic force will be large compared to the fluid drag. Fig. 6 also allows us to calculate the bead capture efficiency for the microsystem. It is simply the summed probabilities for bead entrance at all the different

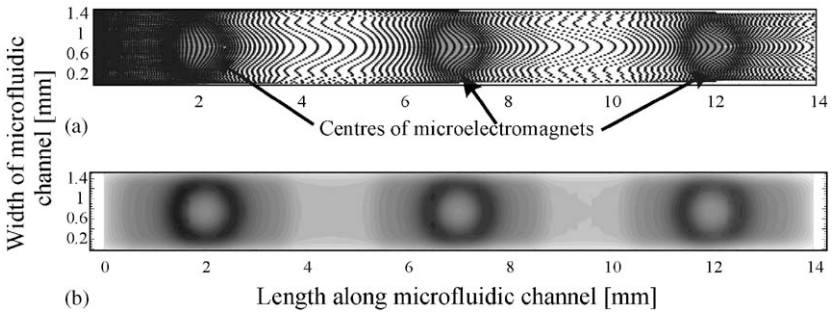

Fig. 5. Calculation of the trajectories of 10,000 magnetic beads, whose initial positions were equally spaced across the left entrance of the microfluidic channel. Each cross in the figure corresponds to a point, where a magnetic bead has settled. In (b) the settling points have been transformed into a settling probability density. The dark parts of the plot correspond to places with high settling probability density.

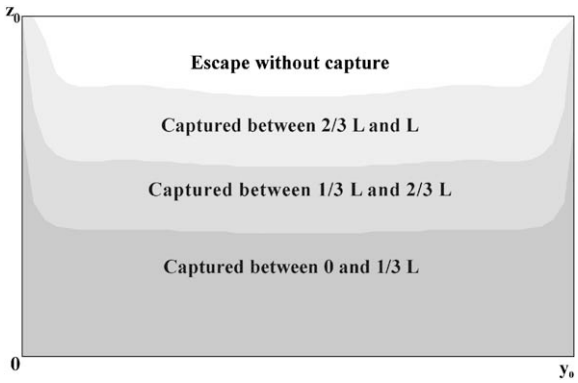

Fig. 6. The plot shows the fluid and bead entrance of the microfluidic channel, which has been divided into four areas corresponding to the position where a bead that started in that phase settled in the microfluidic channel, or if the bead escaped capture. L is the length of the microfluidic channel.

points in the entrance of the microfluidic channel that correspond to caught beads. In this case the capture efficiency is ~89%.

7. Experiments

We have performed bead capture experiments using the described microfabricated system. While it is difficult to measure bead capture efficiencies and almost impossible to study bead trajectories when the dimensions of the microfluidic channel are large compared to the bead diameter, the bead-settling pattern is more easily observed. In the experiments we have used bead concentrations that are large enough to capture a significant number of magnetic beads, but still low enough that interactions between the magnetic beads in the solution are negligible.

Fig. 7 shows the bead-settling pattern of such an experiment. The picture is taken after 20 min, and it is seen how the beads have settled near the edges of the inner pole region of the square microelectromagnet. Beads captured along the edges are vaguely seen, but most beads have settled near the corners of the square electromagnet. As the simulations have been carried out for cylindrical electromagnets, the bead accumulation near corners is not predicted. However, the magnetic field is expected to be even more concentrated near the

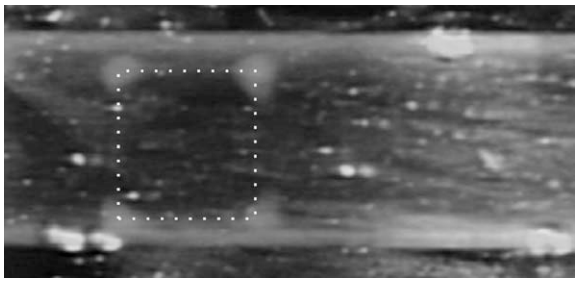

Fig. 7. Micrograph of captured beads on top of one microelectromagnet. The dotted square marks the inner pole of the electromagnet and has a side length of 1 mm. The magnetic beads are seen as the bright areas along the edge and close to the corners of the inner pole region of the electromagnets.

corners of the electromagnet, so when beads approach the bottom of the microfluidic channels, they will experience a horizontal force towards the corners. Also in the simulations the beads were supposed to stick, when they hit the bottom. Experimentally they might move along the bottom of the microfluidic channel, giving rise to the very high density of captured magnetic beads at the corners.

8. Conclusion

We have presented a simulation scheme for the movement and capture efficiency of magnetic beads in a microfluidic channel. Furthermore we have shown that the results of the simulations are in qualitative agreement with experimental data.

In the simulation scheme, we have neglected the effect of hydrodynamic and magnetic interactions between magnetic beads, and interactions between beads and channel walls. These effects are discussed in Ref. [16]. Also the movement of magnetic beads after they first hit the channel bottom has been neglected.

In Ref. [15] another simulation scheme is presented, where the local concentration of magnetic beads in the fluid is treated as a continuous function, and the behaviour of the local bead concentration as a function of time is discussed. In that scheme it is also found that the beads move towards regions with large magnetic field, so there is a qualitative agreement between that simulation

scheme and the one presented here, where the movement of single magnetic beads are considered.

References

[1] J.H.P. Watson, J. Appl. Phys. 44 (1973) 4209.
[2] Dynal BioTech, www.dynabead.com.
[3] C.H. Ahn, M.G. Allen, W. Trimmer, et al., J. Microelectromech. Syst. 5 (1996) 151.
[4] J.W. Choi, T.M. Liakopoulos, C.H. Ahn, Biosens. Bioelectron. 16 (2001) 409.
[5] T. Deng, M. Prentiss, G.M. Whitesides, Appl. Phys. Lett. 80 (2002) 461.
[6] J. Knight, Nature 418 (2002) 474.
[7] B.H. Weigl, R.L. Bardell, C.R. Cabrera, Adv. Drug Del. Rev. 55 (2003) 349.
[8] K. Smistrup, O. Hansen, P.T. Tang, et al., Lab-on-a-Chip, submitted.
[9] M. Shafique and M.F. Hansen, Proceedings of the Nordic Matlab Conference, 2003, p. 209.
[10] Documentation manual for FEMLAB® 2.3, www.femlab.com.
[11] D. Jiles, Introduction to Magnetism and Magnetic Materials, second ed., Chapman & Hall, ISBN 0-412-79860-3, 1998, pp. 115–117.
[12] A. Engel, R. Friedrichs, Am. J. Phys. 70 (2002) 428.
[13] R.C. O'Handley, Modern Magnetic Materials—Principles and Applications, Wiley, New York, ISBN 0-471-15566-7, 2000, pp. 38–47.
[14] T.B. Jones, Electromechanics of Particles, Cambridge University Press, ISBN 0-521-43196-4, 1995.
[15] K.C. Warnke, IEEE Trans. Magn. 39 (2003) 1771.
[16] C. Mikkelsen, M.F. Hansen, H. Bruus, J. Magn. Magn. Mater. (2005), this issue.

JOURNAL OF APPLIED PHYSICS **99**, 08P102 (2006)

Microfluidic magnetic separator using an array of soft magnetic elements

Kristian Smistrup,[a] Torsten Lund-Olesen, and Mikkel F. Hansen
MIC—Department of Micro and Nanotechnology, Technical University of Denmark, Building 345 East, DK-2800 Kongens Lyngby, Denmark

Peter T. Tang
Department of Manufacturing Engineering and Management, Technical University of Denmark, Building 424, DK-2800 Kongens Lyngby, Denmark

(Presented on 2 November 2005; published online 17 April 2006)

We present the design, fabrication, characterization, and demonstration of a new passive magnetic bead separator. The device operates in an effective state when magnetized by an external magnetic field of only 50 mT, which is available from a tabletop electromagnet. We demonstrate the complete capture of 1.0 μm fluorescent magnetic beads from a 7.5 μL sample volume traveling at an average linear fluid velocity of 5 mm/s. © *2006 American Institute of Physics*. [DOI: 10.1063/1.2159418]

I. INTRODUCTION

Recently several magnetic bead separators in microfluidic formats have been reported in the literature. Most use active on-chip microelectromagnets,[1–6] while others use passive designs where on-chip soft magnetic structures are magnetized by external magnetic fields.[7–9] While designs using on-chip electromagnets generally produce small magnetic fields in the microfluidic channels, the passive designs generally provide larger fields and gradients in the channel.

We present a microsystem with a passive magnetic separator featuring an array of electroplated long soft magnetic elements facing the microfluidic channel. Capture of fluorescent magnetic beads is demonstrated using fluorescence microscopy.

II. MICROSYSTEM FABRICATION

Figure 1 shows a photograph of the entire chip. The microfluidic channel measures $1\times h\times w=13\ 500\times 80\times 200\ \mu m^3$ ($\approx 0.2\ \mu L$), and each of the permalloy magnetic elements measures $1\times h\times w=4400\times 50\times 150\ \mu m^3$. The elements are placed with a periodicity of 350 μm and a spacing to the channel of 20 μm. The long thin shape of the magnetic elements is chosen to minimize demagnetization effects and thus maximize fields and gradients.

Figure 2 summarizes the fabrication procedure. As Wu *et al.*,[10] we use Deep Reactive Ion Etched (DRIE) structures as electroplating molds, but we have developed the method substantially. In (a) and (b) of Fig. 2, a 9.5 μm thick layer of AZ4562 photoresist (Hoechst, NJ, USA) is patterned using UV lithography on a single polished Si (100) wafer. The photoresist pattern is used as an etch mask for a DRIE in (c) to create trenches for the electroplating mold as well as the microfluidic channels. In (d) the wafer is RCA cleaned, a 1 μm thick SiO_2 is grown on the wafer, and finally a seed layer of 5 nm Ti and 200 nm Au is E-beam evaporated onto the wafer.

The trenches designated for electroplated magnetic elements are all connected to the outer rim of the wafer by a network of conducting paths. The poor step coverage obtained by the metal E-beam evaporation ensures that little or no contact exists between the metal in the conducting network and the metal on top of the wafer. Short etches of Au are performed in Entreat 100 (Engelhard, NJ, USA) until no contact persists between the top and the bottom. A 2.5 μm thick protective Cu layer is electroplated in the bottom of the conducting network using the commercially available CuproStar LP-1 electrolyte (Enthone, CT, USA). Subsequently, the unprotected Au and Ti is etched away in Entreat 100 and 5% hydrofluoric acid, respectively. Finally, the Cu layer is removed in nitric acid.

At this point the wafer features the microfluidic channels and the conducting network. Permalloy ($Ni_{80}Fe_{20}$) is electroplated into the network, including the trenches for magnetic elements using a pulse-reversal plating electrolyte as described in Ref. 11. The resulting structure is shown in (e). In (f) a pyrex lid is bonded anodically to the top of the wafer, sealing the microfluidic channel. When the wafer is diced into chips, the conducting paths are cut away, leaving only the soft magnetic elements on the chip. Access to the microfluidic channel is gained by drilling holes in the pyrex wafer.

III. EXPERIMENTAL DETAIL

Magnetic hysteresis measurements on an entire microsystem and the magnetic beads were performed in a Lake-Shore 7407 vibrating sample magnetometer (VSM).

The bead capture experiments were carried out with FITC fluorescence labeled 1.0 μm magnetic beads (FCM 1052-2, Spherotec, IL, USA). A solution of 7×10^7 beads/mL H_2O was injected into the microfluidic channel using a syringe pump at a flow rate of 5 μL/min.

With the bead solution flowing in the channel pictures were taken starting at time $t=0$. At $t=10$ s a tabletop electromagnet supplying a homogeneous field perpendicular to the fluid channel was switched on at its maximum field of 50 mT. At $t=100$ s the field was switched off.

[a]Electronic mail: krs@mic.dtu.dk

Paper #3 Page 1 of 3

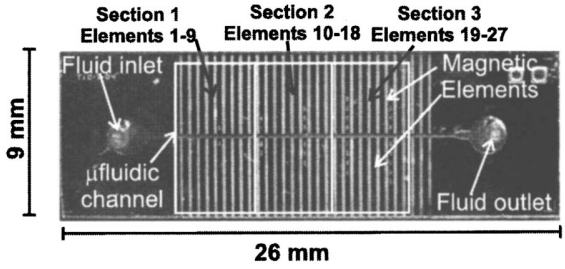

FIG. 1. Picture of the magnetic separation chip showing the position of the microfluidic channel and the passive soft magnetic elements. The external homogenous magnetic field is applied vertically in the plane of the paper.

The bead capture in the microfluidic channel was quantified at different times using the FITC fluorescence images taken every second with an exposure time of 0.9 s on a Leica MZ FL III microscope equipped with a Sony DFW-X710 CCD camera. Images were taken for each of the channel sections defined in Fig. 1 and the fluorescence signal from each section was quantified using MATHEMATICA as follows: First, the color micrographs were converted to gray scale by summing the RGB values pixel by pixel. Then the intensity values of all pixels having an intensity larger than a threshold value of 45 were summed to give the fluorescence signal of the specific section. This value was chosen by trial and error and is necessary to filter out the background noise from dark pixels.

IV. RESULTS AND DISCUSSION

Figure 3 shows the magnetic hysteresis curve of the microsystem. The saturation flux density of Permalloy ($Ni_{80}Fe_{20}$) is approximately 1 T. An applied field of $\mu_0 H \approx 20$ mT is sufficient to saturate the magnetic elements. The coercive field is $\mu_0 H_c \approx 0.5$ mT, and the remanence relative to saturation is $\approx 25\%$, ensuring that the beads are released when the external field is switched off.

Figure 4 shows the magnetic hysteresis curve of the beads. It is seen that the beads are saturated in a field of 250 mT and that the applied field of 50 mT brings the beads to 50% of their saturation value. Also, these beads show a

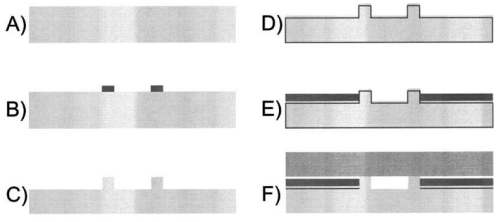

FIG. 2. Fabrication scheme (cross-section view). (a) shows the starting double polished Si wafer. In (b) a photoresist mask is applied using UV lithography. In (c) trenches for both the microfluidic channel and magnetic elements are etched. RCA-clean, oxide growth (1 μm, wet), and seed layer deposition (5/200 nm Ti/Au, E-beam evaporation) with intentionally low step coverage is performed in (d). The areas designated for magnetic elements are connected through conducting paths and isolated from the rest of the wafer. In (e) a thin layer of Cu is electroplated in these places, and the seed layer is removed on the rest of the wafer using the Cu layer as etch mask. After Cu-removal permalloy are electroplated into the conducting paths and magnetic elements. After seed layer and oxide removal a pyrex lid is bonded anodically to the wafer in (f).

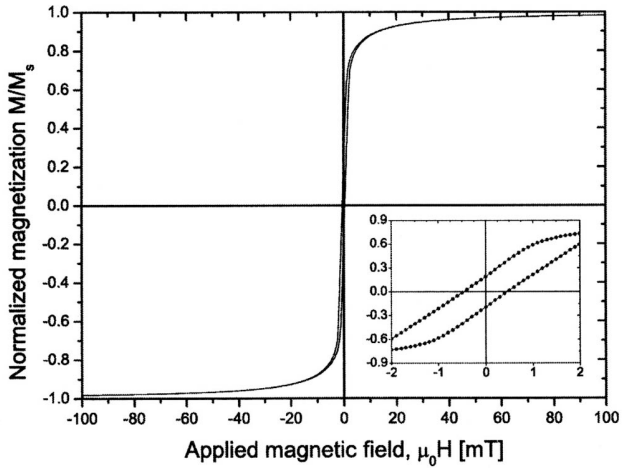

FIG. 3. Normalized magnetic hysteresis curve of the magnetic separation chip. The inset shows the low-field region.

considerable amount of hysteresis, which is unusual for magnetic beads that are normally considered to be ensembles of superparamagnetic particles.

The magnetic force, $\boldsymbol{F}$, on a magnetic bead is given by

$$\boldsymbol{F} = \mu_0 \int_{\text{Bead}} \{\boldsymbol{M}[\boldsymbol{H}_0(\boldsymbol{x})] \cdot \nabla\} \boldsymbol{H}_0(\boldsymbol{x}) \mathrm{d}v$$
$$\approx \mu_0 V_b \{\boldsymbol{M}[\boldsymbol{H}_0(\boldsymbol{x}_b)] \cdot \nabla\} \boldsymbol{H}_0(\boldsymbol{x}_b), \quad (1)$$

where μ_0 is the magnetic permeability of vacuum, $\boldsymbol{M}$ is the magnetization of the magnetic bead, and $\boldsymbol{H}_0$ is the magnetic field in the absence of a magnetic bead. V_b and $\boldsymbol{x}_b$ are the volume and position of the magnetic bead, respectively.[12]

Equation (1) shows that the magnetic force is proportional to the magnetic field gradient, which originates from the magnetic elements, since the applied field is homogeneous. The force is also proportional to the magnetization of the magnetic bead (assuming the approximation that the angle between the magnetization and the applied field does not change substantially when the field is increased.)

Earlier, we have seen that the soft magnetic elements are saturated by an external magnetic field of 50 mT, and that

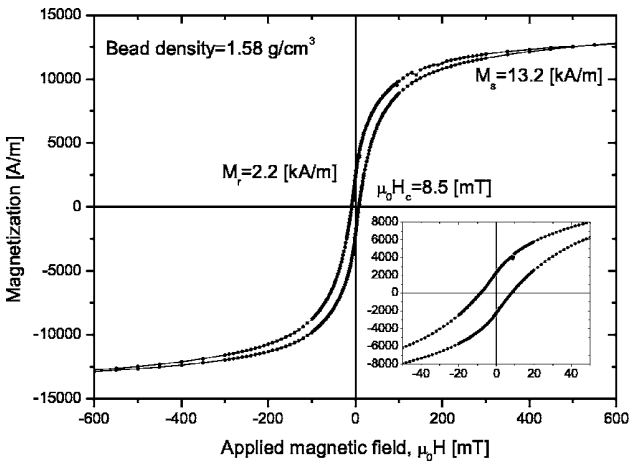

FIG. 4. Magnetic hysteresis curve for the 1.0 μm fluorescent magnetic beads (Spherotec FCM-1052-2). The inset shows the low-field region.

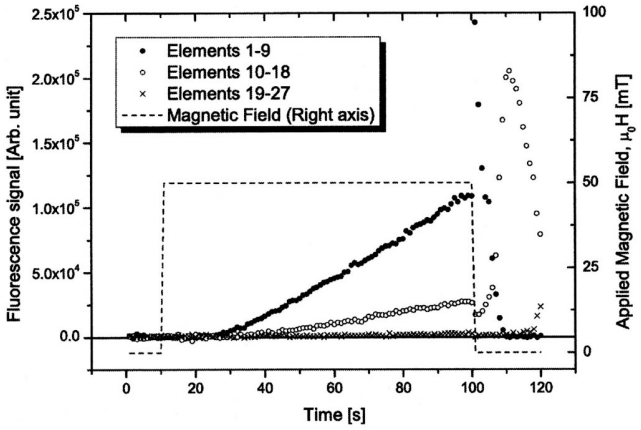

FIG. 5. The applied magnetic field and the measured fluorescent signal for the three sections of the microfluidic channel as a function of time.

the same field will bring a magnetic bead within 50% of its saturation magnetization. This means that increasing the applied field beyond 50 mT will not affect the gradient, but it will bring the magnetization of the beads closer to saturation. Together Figs. 3 and 4 show that using a larger applied field could ultimately give a less than twofold increase in the magnetic forces and bead capture efficiency in the microfluidic channel.

Figure 5 shows the quantified fluorescence signals for the three channel sections as a function of time. Most beads are captured on elements 1–9 (large signal rise), some are captured on elements 10–18 (smaller signal rise), and none are captured at elements 19–27 (zero signal rise). The fact that no significant fluorescence signal is observed from elements 19–27 while the magnet is on indicates that the amount of beads that are not captured in the first two sections is negligible and hence that we have complete bead capture. When the magnetic field is turned off at $t=100$ s, large peaks appear in the fluorescence signals from the three sections after which the signals return to the baseline, indicating that all beads have been released. This is seen most clearly for elements 1–9.

Compared to the design of Deng *et al.* with Ni post inside the fluidic channel,[7] our design has the advantage that the magnetic material is located outside the channel and that both an effective bead capture and release is achieved. Compared to Ichikawa *et al.*,[8] who use sputtered thin films, our magnetic elements are thicker and hence influence a larger region of space with a potentially better bead capture. Compared to the design of Rida and Gijs,[9] our system has more capture points, allowing for higher capture efficiency. As it is fabricated using Si MEMS technology, there is better control of dimensions allowing for smaller magnetic element to channel separation and potentially higher magnetic forces, and the process has a greater potential for integration with other functionalities and batch production.

We have demonstrated a new passive magnetic bead separator and demonstrated that it effectively captures magnetic beads from a bead solution traveling at an average linear velocity of 5 mm/s (5 μL/min) in the field supplied from a small tabletop electromagnet. At this flow rate, however, only two-thirds of the channel length participate in the capture, so the system is expected to be effective up to even higher flow rates. Furthermore, we have demonstrated that the beads can be released after capture. This makes the system reusable and suited for use in a portable lab-on-a-chip system.

ACKNOWLEDGMENTS

Danish Technological Institute and the Copenhagen Graduate School for Nanoscience and Nanotechnology (C:O:N:T) are acknowledged for financially supporting Kristian Smistrup's Ph.D. studies.

[1]K. Smistrup, O. Hansen, H. Bruus, and M. F. Hansen, J. Magn. Magn. Mater. **293**, 597 (2005).
[2]C. H. Ahn, M. G. Allen, W. Trimmer, Y.-N. Jun, and S. Erramilli, J. Microelectromech. Syst. **5**, 151 (1996).
[3]J.-W. Choi, K. W. Oh, A. Han, C. A. Wijayawardhana, C. Lannes, S. Bhansali, K. T. Schlueter, W. R. Heineman, H. B. Halsall, J. H. Nevin, *et al.*, Biomed. Microdevices **3**, 191 (2001).
[4]R. Rong, J.-W. Choi, and C. H. Ahn, in *Proceedings IEEE Sixteenth Annual International Conference on Micro Electro Mechanical Systems*, MEMS-03 Kyoto, Japan, January 19–23 (IEEE, New York, 2003), p. 530–533.
[5]M. Tondra, M. Granger, R. Fuerst, M. Porter, C. Nordman, J. Taylor, and S. Akou, IEEE Trans. Magn. **37**, 2621 (2001).
[6]Q. Ramadana, V. Samperb, D. Poenara, and C. Yub, J. Magn. Magn. Mater. **281**, 150 (2004).
[7]T. Deng, M. Prentiss, and G. M. Whitesides, Appl. Phys. Lett. **80**, 461 (2002).
[8]N. Ichikawa, Y. Katsuyama, Y. Nagasaki, and T. Ichiki, in *Proceedings of the 8th International Conference on Miniaturized Systems in Chemistry and Life Sciences (μTAS)*, 2004, Vol. 2, p. 384.
[9]A. Rida and M. A. M. Gijs, Anal. Chem. **76**, 6239 (2004).
[10]J. Wu, V. Quinn, and G. H. Bernstein, J. Micromech. Microeng. **14**, 576 (2004).
[11]P. T. Tang, in *Proceedings of SUR/FIN 2001*, Nashville, June 25–28, 2001.
[12]A. Engel and R. Friedrichs, Am. J. Phys. **70**, 428 (2002).

PAPER www.rsc.org/loc | Lab on a Chip

On-chip magnetic bead microarray using hydrodynamic focusing in a passive magnetic separator†

K. Smistrup,* B. G. Kjeldsen, J. L. Reimers, M. Dufva, J. Petersen and M. F. Hansen

Received 2nd August 2005, Accepted 13th September 2005
First published as an Advance Article on the web 4th October 2005
DOI: 10.1039/b510995g

Implementing DNA and protein microarrays into lab-on-a-chip systems can be problematic since these are sensitive to heat and strong chemicals. Here, we describe the functionalization of a microchannel with two types of magnetic beads using hydrodynamic focusing combined with a passive magnetic separator with arrays of soft magnetic elements. The soft magnetic elements placed on both sides of the channel are magnetized by a relatively weak applied external magnetic field (21 mT) and provide magnetic field gradients attracting magnetic beads. Flows with two differently functionalized magnetic beads and a separating barrier flow are introduced simultaneously at the two channel sides and the centre of the microfluidic channel, respectively. On-chip experiments with fluorescence labeled beads demonstrate that the two types of beads are captured at each of the channel sidewalls. On-chip hybridization experiments show that the microfluidic systems can be functionalized with two sets of beads carrying different probes that selectively recognize a single base pair mismatch in target DNA. By switching the places of the two types of beads it is shown that the microsystem can be cleaned and functionalized repeatedly with different beads with no cross-talk between experiments.

Introduction

A microarray of biomolecules is a powerful tool for DNA and protein diagnostics[1,2] since it allows highly parallel analyses of a sample in a single batch process. To enable complete lab-on-a-chip systems for diagnostics it is therefore desirable to integrate a microarray within a microfluidic channel.

A number of solutions have been suggested to put microarrays in microfluidic channels.[3–5] In these studies, the probe array is typically constructed by micro-contact printing in the channels[3,4] or by spotting the probes in the channels or on the channel lid before sealing the system.[5] Common for these methods is that the functionalization is carried out as a part of the microsystem fabrication. As the probes (DNA and proteins) are sensitive to, *e.g.*, temperature, this limits the processes the microsystem can be exposed to after the functionalization. Furthermore, as the probes are fixed the flexibility and potential for automated repeated operation of the system are reduced.

Micrometersized magnetic beads are commonly used for laboratory scale biochemical assays and separations and are commercially available with numerous different surface functionalizations.[6] Such beads are attracted to regions with large magnetic fields and can thus be manipulated by applying spatially varying magnetic fields. As most biological and chemical substances are non-magnetic, this manipulation is independent of the biological and chemical processes taking place in the microsystem. Thus, magnetic beads constitute a suitable dynamic template for a microarray within a microfluidic channel.

The manipulation of magnetic beads in lab-on-a-chip systems is a rapidly growing activity.[7] Two general approaches have been followed to capture and release magnetic beads in microfluidic systems. The first approach utilizes microelectromagnets in various forms integrated with microfluidic channels.[8–11] These active magnetic separators have the advantage of local addressability but suffer from complex fabrication procedures and limited field strengths. The second approach utilizes permanent magnets,[12,13] structures of a soft magnetic material magnetized by the external magnetic field from an electromagnet or a permanent magnet[14,15] or a mixture thereof.[16] These passive magnetic separators have the advantage of simpler fabrication schemes and that comparably large magnetic forces can be achieved but lack addressability.

With a few exceptions[12,16] the reported active and passive magnetic separators focus only on the separation of a single species of magnetic beads.

We present a new passive magnetic separator design consisting of permalloy elements adjacent to a microfluidic channel. When an external magnetic field is applied, the elements are magnetized and generate magnetic field gradients within the channel such that the magnetic beads are attracted to and captured at the channel sidewalls. We show that two types of magnetic beads can be selectively placed at either side of the channel with negligible cross-talk by use of hydrodynamic focusing. This enables the simultaneous exposure of a sample to two probes, which we demonstrate on the detection of a specific point mutation (insertion of a single base) in human DNA associated with the disorder β-thalassemia.

MIC—Department of Micro and Nanotechnology, Technical University of Denmark, Building 345east, DK-2800 Kongens Lyngby, Denmark. E-mail: krs@mic.dtu.dk; Tel: +45 4525 5753

† Electronic supplementary information (ESI) available: Fig. 3, 5 and 6 in colour. See DOI: 10.1039/b510995g.

Experimental

Microsystem design and fabrication

Fig. 1 shows the layout of the microsystem. It consists of a long, straight microfluidic channel with width × height × length = 100 μm × 120 μm × 13 mm corresponding to a volume of 0.16 μL. To facilitate hydrodynamic focusing the channel has three inlets, enumerated A, B and C. The channel has a single outlet, which is placed at the bottom to minimize beads getting stuck in the system due to gravitational settling. The magnetic elements with width × height × length = 50 μm × 40 μm × 4.9 mm are placed symmetrically with respect to the channel with a periodicity of 350 μm and an element to channel spacing of 50 μm.

The element geometry is based on finite element method calculations of the magnetic field and is chosen to maximize the attractive force towards the wall by minimizing demagnetization effects. The division of the magnetic material into several elements also minimizes rolling of captured magnetic beads along the channel wall and ensures that the beads are captured in a spot of well-defined shape and size.

For the fabrication of the microsystem etched structures in a silicon wafer are used as the electroplating mould. This principle was pioneered by Wu and Bernstein,[17] but the process presented below is significantly developed compared to their work. The fabrication procedure is schematically illustrated in Fig. 2. In (1), a 2.45 μm thick oxide is grown on a 100 mm double polished (100) silicon wafer. In (2) a 1.5 μm thick layer of AZ5214e photoresist (Hoechst, NJ, USA) is spun onto the wafer and patterned using UV-lithography. The photoresist is hard-baked in an oven at 120 °C for 25 minutes. The exposed oxide is etched by immersing the wafers in buffered hydrofluoric acid (BHF) for 10 minutes. In (3) the photoresist is stripped and a 9.5 μm thick layer of AZ4562 photoresist (Hoechst, NJ, USA) is spun onto the wafer and patterned using UV-lithography. The photoresist pattern is used as an etch mask in a 300 μm Deep Reactive Ion Etch (DRIE) that defines a through-hole to the wafer backside. (A) illustrates the top-view of the microchip; the oxide pattern is visible through the photoresist. In (4) a layer of aluminum is E-beam evaporated onto the backside of the wafer to serve as etch-stop for the through-hole etching. The photoresist is stripped, and the exposed oxide layer serves as a mask for a 120 μm DRIE of the channels and trenches. In (5) the oxide and aluminum is stripped, an RCA clean is performed and a

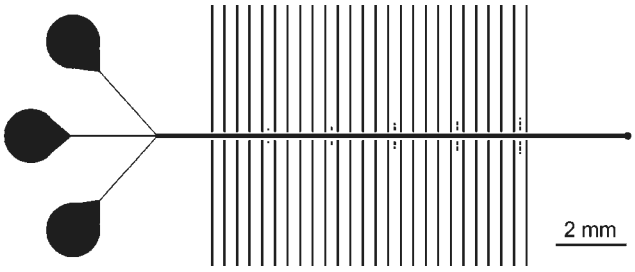

Fig. 1 Layout of the magnetic separation chip. The three inlets, A–C (top to bottom), and the array of soft magnetic elements are seen surrounding the microfluidic channel.

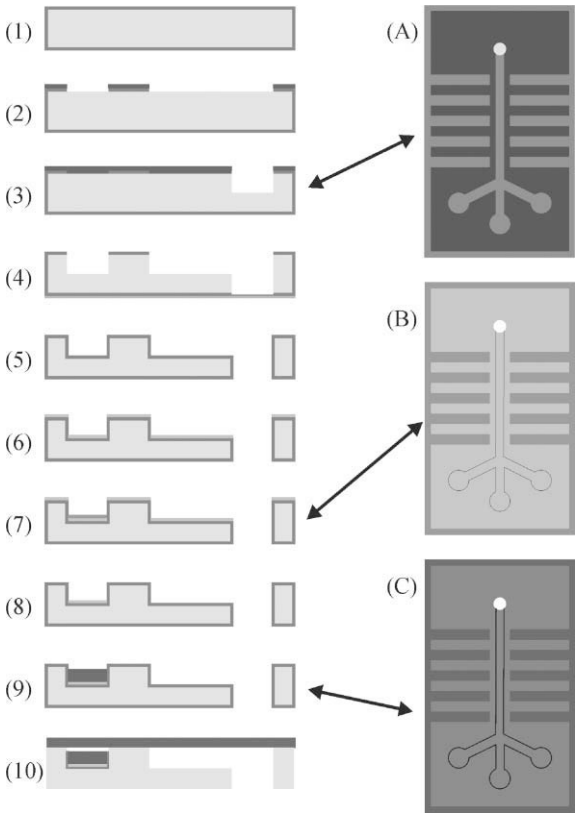

Fig. 2 Fabrication scheme for the passive magnetic separator shown in cross-section (left side) and top-view (right side). (1) 2.45 μm SiO_2 is grown on a double polished (100) Si wafer. (2) The oxide is patterned using UV-lithography and SiO_2 etch. (3) A second UV-lithography step is applied, and the resulting resist pattern is used as an etch mask for DRIE. (4) 1 μm protective Al layer is E-beam evaporated onto the backside of the wafer. The resist is stripped, and the underlying oxide pattern is used as a second etch mask for DRIE. (5) The SiO_2 and Al layers are removed, an RCA-clean is performed and 500 nm SiO_2 is grown. (6) A 5/200 nm Ti/Au seed layer is E-beam evaporated onto the wafer. (7) A protective Cu layer is selectively electroplated in trenches with electrical contact to the wafer edge. (8) The unprotected seed layer is etched. (9) The permalloy magnetic elements are electroplated. (10) A pyrex lid is anodically bonded to the silicon wafer.

500 nm thick oxide is grown on the wafer to make it electrically insulating. In (6) a metal seed layer of 5 nm titanium and 200 nm gold is E-beam evaporated onto the wafer.

As the DRIE process results in almost vertical sidewalls and the metal E-beam evaporation is designed to have poor step coverage, there is little or no electrical contact between the metal in the bottom of the etched structures and that on the top of the wafer. Short gold etches in Entreat 100 (Engelhard, NJ, USA) are performed followed by resistance measurements until no electrical contact persists between the top and bottom of the etched structures. As illustrated in (B) the trenches where the magnetic material is desired are electrically connected through conduction streets to the rim of the wafer, whereas the etched microfluidic channel is not. This it utilized to selectively electroplate a protective layer of 2.5 μm copper in the trenches as illustrated in (7) and (B). Then the unprotected metal in the channels and on the wafer top is etched away in Entreat 100 and hydrofluoric acid. Finally the copper is

removed in nitric acid and we are left with an oxide covered silicon wafer with gold only in the bottom of the trenches designated for the magnetic elements and the conducting streets. The resulting structure is shown in (8).

In (9), a 40 μm thick layer of permalloy is electroplated by use of a pulse-reversal plating bath.[18] The resulting structure is also shown in (C). In (10) the silicon oxide is removed in BHF, and a pyrex wafer is anodically bonded to the silicon wafer. After bonding the wafer is diced into chips and inlet holes are drilled using diamond drills. The conducting streets are removed in the dicing process.

Magnetic beads

MyOne™ Streptavidin Dynabeads® (0.1 mg mL^{-1}) were used for all experiments.[6] The beads are 1.05 μm in diameter and have a saturation magnetization of 336 A m^2 kg^{-1}, an initial mass susceptibility of 8.1 × 10^{-4} m^3 kg^{-1} and a density of 1.3 g cm^{-3}.[6,19] The beads were functionalized with biotinylated oligonucleotides (Table 1) according to the manufacturer's instructions.[6] Thus, FITC labeled beads were obtained by functionalizing beads with a DNA oligo having FITC in one end and biotin in the other end (Table 1). Beads for mutation analysis were functionalized with DNA that specifically capture Wild Type (WT) or a Mutant Type (MT) DNA (Table 1). The functionalized beads were suspended in TE-buffer solution (10 mM TRIS·HCl, 1 mM EDTA, 2.0 M NaCl) with a pH of 7.5 to a concentration of 10^8 beads mL^{-1}.

Operation of the microfluidic system

The fabricated microsystem was mounted in a polycarbonate holder providing O-ring sealed fluidic connections. The fluidic set-up is sketched schematically in Fig. 3.

During an experiment, a permanent magnet frame provides a homogeneous magnetic flux density of approximately 21 mT applied perpendicular to the channel. This magnetizes the magnetic elements and attracts beads introduced into the system to the channel sidewalls. The magnetic elements are placed symmetrically with respect to the channel and thus the transverse magnetic force on a bead in the centre of the channel is zero. The beads are so large that their diffusion on experimental time scales is negligible. Moreover, the fluid flow rates applied during the experiments are small enough to make the flow laminar at all times. This ensures that magnetic beads are captured at the sidewall, which is nearest to the point where they enter the microfluidic channel. Hence, no cross-talk between the beads of the two channel sides is expected. The beads are collected in spots near the ends of the magnetic elements.

Table 1 Nucleotide sequences

FITC	5′-Biotin-TGCCACGCTCATCGACAAGCTTGTC-Fluorescein-3′
WT	5′-Biotin-TTTTTTTTTTTTTTTTTTTT GGAGAA-GTCTGCC
MT	5′-Biotin-TTTTTTTTTTTTTTTTTTTT GAGAAG-GTCTGC C
WT Target	5′-Cy5-CAGGGCAGTAACGGCAGACTT CTCCTCAGGAGTCAGATGCAC

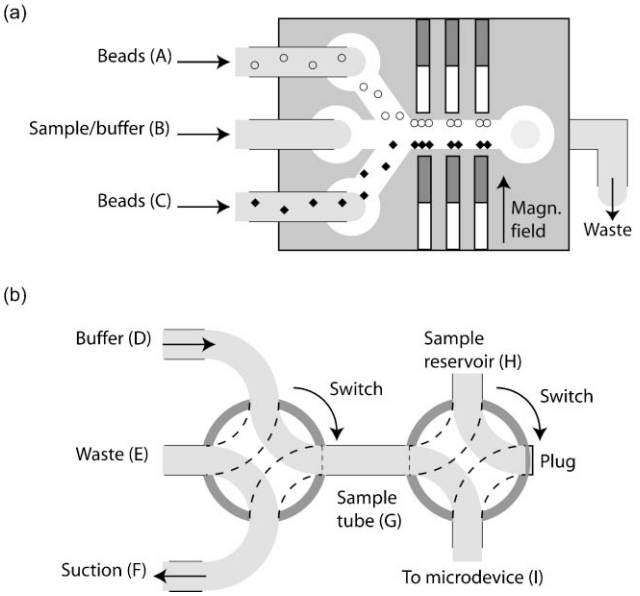

Fig. 3 (a) Schematic illustration of the microsystem and the fluid connections to the three inlets A–C. The two types of beads are applied through inlets A and C, respectively, and separated by a buffer flow applied through inlet B. The applied magnetic field and the magnetized magnetic elements with captured beads are indicated. (b) Illustration of system with two rotatable fluid switch valves used to collect and inject the well-defined volume of the sample tube, G, by a buffer flow from D.

Each of the three channel inlets (A to C in Fig. 3(a)) was connected to syringe pumps through a system of fluidic switches illustrated in Fig. 3(b). This system enables the introduction of both buffer stream and a well-defined sample volume through the same channel inlet and ensures reproducible experimental conditions. It works as follows: The syringe pump providing a buffer flow is on at all times. When the fluidic switch valves are in the position indicated by the dotted lines and suction is applied to port F, the sample is sucked from the sample reservoir H into the sample tube G, which has a volume defined by the length of the tubing between the two fluidic switches. When both switches are rotated 90° the contents of the sample tube G is now flushed into the system by the buffer flow. During experiments, great care was taken to avoid bubbles as these will flush out captured beads.

All micrographs and fluorescence micrographs were taken using a Leica MZ FL III microscope equipped with a Sony DFW-X710 CCD camera.

Functionalization of magnetic structures with beads

To demonstrate the ability to spatially localize differently functionalized beads on the two channel sides, FITC conjugated beads and non-conjugated beads were flushed simultaneously into the channel through inlet A and C, respectively, at 9 μL min^{-1} while a barrier flow of MilliQ water was flushed through inlet B at 12 μL min^{-1}. Control experiments were performed in which the FITC labeled and unlabelled beads were introduced through inlets C and A, respectively.

To functionalize the structure with MT and WT beads, MT and WT conjugated beads were simultaneously flushed through inlet A and C, respectively, at 9 μL min^{-1} while a barrier flow of MilliQ water was flushed at 12 μL min^{-1} through inlet B. After the functionalization, the flows through inlets A and C were stopped.

Hybridization and stringency wash

Microstructures functionalized with captured beads carrying WT and MT DNA probes were flushed with Cy5 labeled WT oligonucleotide target (100 nM diluted in 5 × SSC + 0.5%SDS) through inlet B. The flow was stopped and hybridization occurred for 1 h at 26 °C. Subsequently, the channel was washed using 0.1 × SSC, 0.5% SDS solution for 5 min at a flow rate of 20 μL min^{-1}. The fluorescence signal was detected using Cy5 filters at different points in time before and during the washing.

Microsystem cleaning

To clean the microfluidic channel after an experiment the magnetic field was removed and a flow of 0.1 × SSC, 0.5% SDS solution was applied at a high rate ($\approx$300 μL min^{-1}) for a few minutes.

Results and discussion

Magnetic characteristics of system

The long and thin shape of the magnetic elements suppresses demagnetization effects and ensures that they are easily magnetized along their long axis. Fig. 4 shows the normalized magnetic hysteresis curve for an entire system. It is seen that an applied field of approximately 20 mT is sufficient to magnetically saturate the elements and that the coercive field is about 0.5 mT. This has two important consequences. First, we can use small external magnets to magnetize the elements. This is important since it reduces cost and makes the system truly portable. Second, when the external magnetic field is removed the magnetic elements lose their magnetization, so the captured magnetic beads are released and can be collected, and the system can be reused.

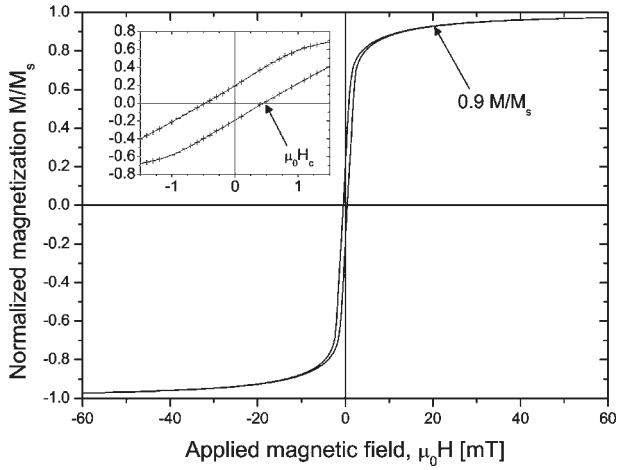

Fig. 4 Magnetic hysteresis loop for the entire microsystem. The inset shows the low-field region. The saturation flux density of the electroplated permalloy is about 1 T.

Spatial localization of differently functionalized beads

FITC labeled and unlabeled beads were introduced through inlet A and C, respectively, as described in the experimental section. Fig. 5 shows micrographs of (a) the captured beads and (b) the FITC fluorescence signal from the same area. The amounts of beads collected at the two channel sides are comparable. The fluorescent signal from the beads at the image top is eight-fold stronger than that from the bottom indicating that specific localization of beads can be obtained.

Subsequently, the microsystem was cleaned and FITC labeled and unlabeled beads were now introduced into inlet C and A, respectively, as described in the experimental section. This resulted in fluorescence from the beads at the image bottom while those at the top, that were previously fluorescent, showed no fluorescence (data not shown). This indicates that the cleaning procedure efficiently removes the beads from the channel and hence that there is negligible bead cross-talk from one experiment to the next.

Hybridization reactions within the microstructure

The microchannel was functionalized with equal amounts of MT beads at the top of the images and WT beads at the bottom as described in the experimental section (Fig. 6(a)). After hybridization with Cy5 labeled WT target but prior to the stringency wash equal fluorescent signal was observed from the two sides (Fig. 6(b)) indicating that equal amounts of probes were immobilized on the two sides of the channel. A steady decrease in signal from the MT mismatch hybrid (upper side, Fig. 6(c)–(d)) was observed after initiation of the stringency wash. The signal from the MT probe was reduced to background level after 5 min of washing while the perfect match signal (WT) remained essentially constant (Fig. 6). This

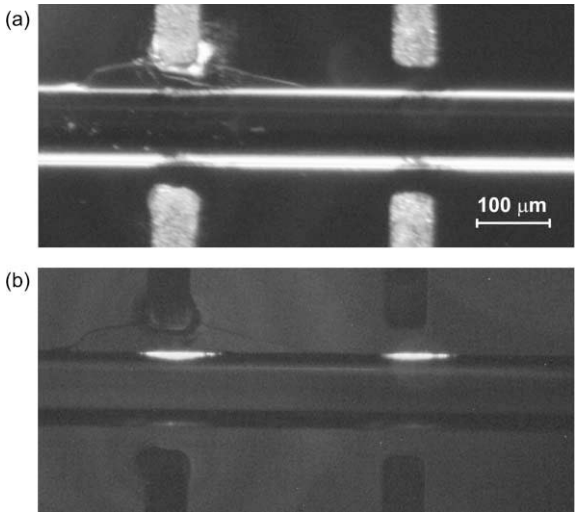

Fig. 5 Capture of FITC labeled beads and unlabeled beads in the microsystem. (a) Micrograph of channel section showing that beads are captured on both sides. (b) Fluorescence micrograph of same section showing only a fluorescence signal at the top indicating no bead cross-talk.

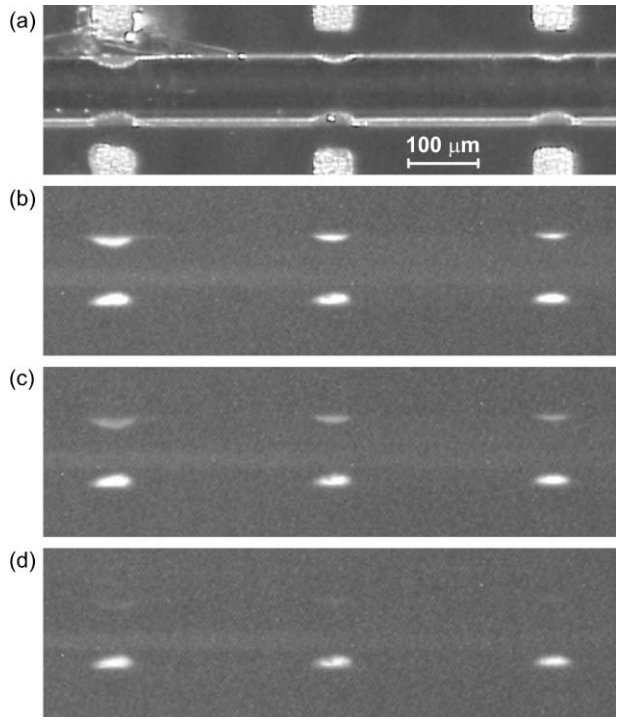

Fig. 6 SNP detection of WT target. The channel is functionalized with WT beads (image bottom) and MT beads (image top). (a) Micrograph showing that beads are captured on both sides of the channel. Cy5 fluorescence micrograph of the same channel section after (b) hybridization with Cy5 labeled WT target, (c) washing with 0.1 × SSC,0.5%SDS for approximately 2 min, (d) further washing for 2 min.

strongly indicates that specific removal of mismatch hybrids is possible. Quantified signals showed a ratio of 77 between perfect match and mismatch after washing for 10 min. A similar high ratio could also be observed by immobilization of probes with the same capture sequences to an agarose film using standard microarray technology[20] (data not shown).

After this experiment, the channel was cleaned as described in the experimental section and now functionalized with WT and MT beads at the image top and bottom, respectively. After hybridization and stringency wash, a signal of the same magnitude as above could be observed from the top part of the image while no signal was observed from the bottom (data not shown). This indicates that the *same* channel can conditionally be functionalized with different beads and that the beads can be released efficiently without cross-talk between different hybridization experiments.

Conclusions

We have designed and fabricated a new type of passive magnetic separator and demonstrated its capability to capture magnetic beads. Using hydrodynamic focusing, we have demonstrated the construction of dynamic arrays consisting of beads with two different surface functionalizations and that the cross-talk between the two types of beads is negligible. Finally, we have demonstrated that the constructed microarray can be used for single nucleotide polymorphism/point mutation detection with selectivity comparable to regular spotted DNA microarrays. The microsystem and the constructed microarray are generic and their usability is only limited by the surface functionalization of the magnetic beads.

Acknowledgements

K. Smistrup acknowledges the financial support for his PhD study from the Copenhagen Graduate School for Nanoscience and Nanotechnology and the Danish Technological Institute. Support from Aase and Ejnar Danielsen's foundation is gratefully acknowledged.

References

1 A. C. Syvanen, *Nat. Rev. Genet.*, 2001, **2**, 930–942.
2 M. Dufva and C.B.V. Christensen, *Expert Review Proteomics*, 2005, **2**, 41–48.
3 H. Andersson, C. Jönsson, C. Moberg and G. Stemme, *Electrophoresis*, 2001, **22**, 3876–3882.
4 Y. Wang, B. Vaidya, H. D. Farquar, W. Stryjewski, R. P. Hammer, R. L. McCarley and S. A. Soper, *Anal. Chem.*, 2003, **75**, 1130–1140.
5 Y. Liu and C. B. Rauch, *Anal. Biochem.*, 2003, **317**, 76–84.
6 Dynal biotechnology, Norway, *www.dynalbiotech.com*.
7 M. A. M. Gijs, *Microfluid Nanofluid*, 2004, **1**, 22–40.
8 C. H. Ahn, M. G. Allen, W. Trimmer, Y.-N. Jun and S. Erramilli, *J. Microelectromech. Syst.*, 1996, **5**, 151–158.
9 J.-W. Choi, C. H. Ahn, S. B. Bhansali and H. T. Henderson, *Sens. Actuators, B*, 2000, **68**, 34–39.
10 J.-W. Choi, T. M. Liakopoulos and C. H. Ahn, *Biosens. Bioelectron.*, 2001, **16**, 409–416.
11 K. Smistrup, P. T. Tang, O. Hansen and M. F. Hansen, *J. Magn. Magn. Mater.*, 2005, doi: 10.1016/j.jmmm.2005.05.031.
12 Z. H. Fan, S. Mangru, R. Granzow, P. Heaney, W. Ho, Q. Dong and R. Kumar, *Anal. Chem.*, 1999, **71**, 4851–4859.
13 M. A. Hayes, N. A. Polson, A. N. Phayre and A. A. Garcia, *Anal. Chem.*, 2001, **73**, 5896–5902.
14 T. Deng, M. Prentiss and G. M. Whitesides, *Appl. Phys. Lett.*, 2002, **80**, 461–463.
15 E. Mirowski, J. Moreland, S. E. Russek and M. Donahue, *Appl. Phys. Lett.*, 2004, **84**, 1786–1788.
16 B. B. Yellen and G. Friedman, *Langmuir*, 2004, **20**, 2553–2559.
17 J. Wu and G. H. Bernstein, *J. Vac. Sci. Technol., B*, 2004, **22**, 611–618.
18 P. T. Tang, Pulse Reversal Plating of Nickel and Nickel Alloys for MEMS, *Procedings of SUR/FIN 2001*, Nashville, June 25–28, 2001.
19 G. Fonnum, C. Johansson, A. Molteberg, S. Mørup and E. Aksnes, *J. Magn. Magn. Mater.*, 2005, **293**, 41–47.
20 M. Dufva, S. Petronis, L. Bjerremann Jensen, C. Krag and C. B. V. Christensen, *Biotechniques*, 2004, **37**, 286–296.

SELECTIVE MAGNETIC BEAD CAPTURE USING AN ADRESSABLE ON-CHIP ELECTROMAGNET ARRAY

Kristian Smistrup[1*], Ole Hansen[1], Peter T. Tang[2], and Mikkel F. Hansen[1]
[1]MIC - Department of Micro and Nanotechnology, Technical University of Denmark, Building 345 East, DK-2800 Kongens Lyngby, Denmark, *krs@mic.dtu.dk
[2] Department of Manufacturing Engineering and Management, Technical University of Denmark, DK-2800 Kongens Lyngby, Denmark

Keywords: Magnetic Separation, Immunoassay, Magnetic Microbeads, MEMS, Adressable.

1. Introduction

Magnetic separation is a well-known technique in macroscopic systems [1] and in recent years technologies for magnetic separation in microfluidic systems have emerged. Furthermore, the principle of magnetic separation, i.e., manipulation of biochemically functionalised magnetic beads, has been used in microsystems for several different applications such as magnetic tweezers, magnetic mixing and extraction of DNA or antigens from a suspension [2-5].

In this work we demonstrate the principle of a new application of magnetic bead capture. Magnetically identical beads are selectively captured at and released from different sites in a microfluidic channel using an addressable array of electromagnets. Thus, placing differently functionalized beads on each of the addressable spots of the array it is in principle possible to carry out several assays simultaneously.

2. Design and fabrication

The design of our microsystem is shown in Fig. 1. Each microsystem contains three microelectromagnets, each consisting of a square spiral copper coil semi-encapsulated in a dielectric layer and a soft magnetic yoke on top of that. The soft magnetic yoke is also used as a return path for the electrical current. Both nickel and permalloy has been used as magnetic material for the yoke. A microfluidic channel is etched into the opposite side of the wafer. The microsystems are fabricated using standard cleanroom technology. Fig. 2 summarizes the fabrication process. For more details see [6].

3. Theory

In microfluidic systems three forces generally affect magnetic beads; magnetic force $\mathbf{F}_{mag}$, gravitational force (buoyancy) $\mathbf{F}_{grav}$, and the fluid drag $\mathbf{F}_{fluid}$. Furthermore, the Reynolds number for the fluid flow is small such that the Navier-Stokes equation reduces to a Poisson equation in the absence of a net body force on the fluid, and the fluid drag on the magnetic beads can be described by the Stokes drag. Due to the small radius R_{bead} of the magnetic beads $\mathbf{F}_{fluid}$ ($\propto R_{bead}$) will dominate over the inertial term ($\propto R_{bead}^3$) in the equation of motion. Therefore the inertial term can be discarded, and the equation of motion reduces to a first order differential equation for the bead position $\mathbf{r}_{bead}$

$$\mathbf{v}_{bead} = \frac{\partial \mathbf{r}_{bead}}{\partial t} = \mathbf{v}_{fluid}\left(\mathbf{r}_{bead}\right) + \frac{1}{6\pi\eta R_{bead}}\left(\mathbf{F}_{mag}\left(\mathbf{r}_{bead}\right) + \mathbf{F}_{grav}\right) \quad (1)$$

$$\mathbf{F}_{mag}\left(\mathbf{r}_{bead}\right) = \tfrac{1}{2}\mu_0 V_{bead}\chi_m \nabla\left(\left|\mathbf{H}\left(\mathbf{r}_{bead}\right)\right|^2\right) \quad (2)$$

where η is the viscosity of the fluid, μ_0 is the magnetic permeability of vacuum, χ_m is the measured magnetic susceptibility of the magnetic beads, and V_{bead} is the volume of a magnetic bead. The buoyancy of the fluid is included in $\mathbf{F}_{grav}$.

If hydrodynamic interactions are neglected, and the microfluidic channel is straight and has rectangular cross-section, the velocity profile of the fluid $\mathbf{v}_{fluid}$ can be found analytically as a series

expansion. Using this and by calculating the magnetic field **H** using FEMLAB® (neglecting magnetic interactions between beads), we have simulated the flow of magnetic beads in our microfluidic channels. [7] We have used this to determine the optimum experimental parameters, volumetric flow rate and current in the electromagnets.

4. Results and discussion

Figure 3 shows the fabricated microsystem mounted in a housing with optical access as well as electrical and fluidic connections. This system has been placed under an optical microscope, and it has been observed how the beads settle in the microfluidic channel.

In Fig. 4 we show micrographs of the microfluidic channel at different times. With a solution of water and 76×10^3 μL^{-1} magnetic beads (MyOne®, Dynal, Norway, $2R_{Bead}$ = 1.05 μm, $\chi_m \approx 1.5$) flowing in the microfluidic channel from the left at a volumetric flow rate of 1 μL/min, a current of 0.5 A was fed to the rightmost electromagnet at t = 0 min. After 15 min. it is seen that magnetic beads have settled on top of the rightmost electromagnet. At t = 15 min. the current in the leftmost electromagnet was also set to 0.5 A. After 30 minutes it is seen that beads have now settled on both electromagnets, but the amount of beads on the rightmost electromagnet has not changed significantly since t = 15 min. The aforementioned simulations show that all beads should be captured on the leftmost microelectromagnet with this flow rate and current. At t = 30 minutes the rightmost electromagnet is turned off. After 35 min. it is seen that all beads have been released from the rightmost electromagnet, while no beads have apparently left the leftmost electromagnets. This shows that it is possible to selectively capture and release magnetic beads at the two different microelectromagnets in the microfluidic channel.

With this simple experiment we have demonstrated that it is in principle possible to create a microfluidic system containing an array of differently functionalized sites within a microfluidic channel, and since the functionalization of the sites is limited only by the chemistry that can be applied on the surface of magnetic beads, it is possible to create an addressable array of functionalities within the microfluidic system by having individually addressable electromagnets.

As an example of a potential application of this technique, we describe simultaneous magnetic separation of two species of antigens. If one set (set-1) of magnetic beads are coated with one kind of antibody, and another set (set-2) is coated with a different antibody, set-1 can be placed at the rightmost electromagnet, and set-2 can be placed at the leftmost electromagnet by selective bead capture. When a suspension containing a number of different antigens is sent through the microfluidic channel, the target antigen of set-1 will be caught on the rightmost electromagnet, and the (different) target antigen of set-2 will be captured on the leftmost electromagnet. Afterwards the two sets can be sequentially released and collected into different test tubes.

References

[1] J. Watson, *J. Appl. Phys.* **44**, 4209-4213, (1973)
[2] C-H. Chiou, Z-F. Tseng, G-B. Lee, *Proc. MEMS 2004*, 613-616
[3] R. Rong, J-W. Choi, and C. H. Ahn, *Proc. μTAS 2003*, 335-338
[4] T. Deng, M. Prentiss, and G. M. Whitesides, *Appl. Phys. Lett.* **80**, 461-463 (2002)
[5] J-W Choi, T. F. Liakopoulos, C. H. Ahn, *Biosensors & Bioelectronics* **16**, 409-416 (2001)
[6] K. Smistrup, O. Hansen, P. T. Tang, and M. F. Hansen, "Microelectromagnet for magnetic manipulation in microfluidic systems", *IEEE – Nanoscale Devices and Systems Integration, Miami, USA 2004,* submitted to *J. Micromech. Microeng.*
[7] K. Smistrup, O. Hansen, H. Bruus, and M. F. Hansen, "Magnetic separation in microfluidic systems using microfabricated electromagnets – experiments and simulation", *Scientific and Clinical Applications of Magnetic Carriers, Lyon, France 2004*, submitted to *J. Magn. Magn. Mat.*

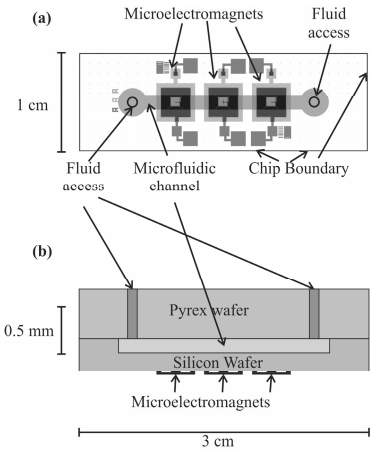

Figure 1. Overview (a) and cross-section (b) of the microfluidic system design. The electromagnets have the following parameters: Number of turns 12; coil wire height 25 μm, width 60 μm, and spacing 20 μm; electromagnet width 4 mm, and yoke thickness 25 μm; fluid channel depth 150 μm, length 14 mm, and width 1.5 mm. Notice that the scale at the bottom applies to both (a) and (b).

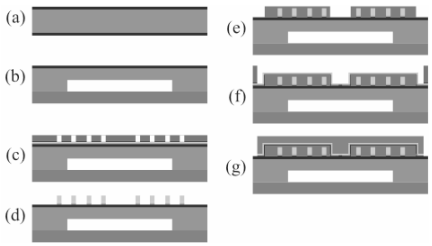

Figure 2. Fabrication process for the microfluidic system. In (a) SiO_2 and Si_3N_4 is deposited on a double polished Si wafer. In (b) the microfluidic channel is defined using DRIE and sealed with a pyrex wafer using anodic bonding. In (c) and (d) the Cu coil is defined by electroplating using thick photoresist as a mould. In (e) a dielectric layer of hard-baked photoresist is defined. In (f) and (g) the magnetic yoke (Ni or NiFe) is defined by electroplating using a thick photoresist mould.

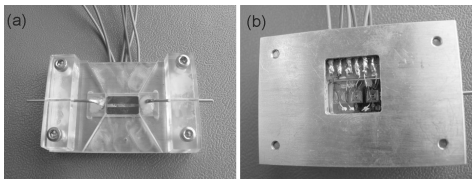

Figure 3. Photographs of the fabricated microsystem complete with fluid and electrical connections. (a) shows the channel side, and (b) shows the electromagnet side. The mounted system is 4 by 6 centimeters.

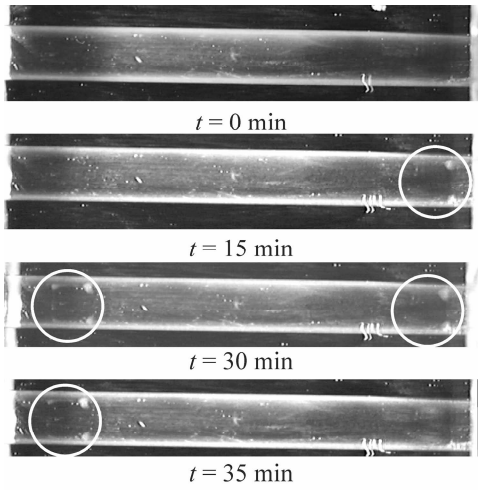

Figure 4. Demonstration of selective bead capture and release in the microfluidic system. The encircled gray dots in the microfluidic channel is the reflection of the ferrite content of the magnetic beads. The beads settle above the corners of the square inner pole piece of the electromagnets. After 15 min. beads have been captured on the rightmost electromagnet. After 30 min. beads have been captured on both the leftmost and the rightmost electromagnet. After 35 min. the beads have been released from the rightmost electromagnet, but is still present on the leftmost electromagnet. The width of the microfluidic channel is 1.5 mm.

Available online at www.sciencedirect.com
ScienceDirect
Journal of Magnetism and Magnetic Materials 311 (2007) 409–415
Journal of magnetism and magnetic materials
www.elsevier.com/locate/jmmm

Towards a programmable magnetic bead microarray in a microfluidic channel

Kristian Smistrup, Henrik Bruus, Mikkel F. Hansen*

MIC—Department of Micro and Nanotechnology, Technical University of Denmark, DTU, Building 345 East, DK-2800 Kongens Lyngby, Denmark

Available online 19 December 2006

Abstract

A new hybrid magnetic bead separator that combines an external magnetic field with 175 μm thick current lines buried in the back side of a silicon wafer is presented. A microfluidic channel was etched into the front side of the wafer. The large cross-section of the current lines makes it possible to use larger currents and obtain forces of longer range than from thin current lines at a given power limit. Guiding of magnetic beads in the hybrid magnetic separator and the construction of a programmable microarray of magnetic beads in the microfluidic channel by hydrodynamic focusing is presented.

Keywords: Magnetic microsystems; Magnetic separation; Magnetic bead; Programmability; Microarray; Lab on a chip

1. Introduction

Magnetic manipulation of magnetic beads in microfluidic channels is receiving growing attention in the literature due to its high potential for use in bioanalysis in lab-on-a-chip systems [1,2]. Recently, several reports have appeared on the creation of arrays of magnetic beads in microfluidic channels [3–5]. Conventional microarrays in lab-on-a-chip systems are usually constructed by micro-contact printing during the fabrication process. While this process allow for many array spots, these arrays are static and single-use. When the array is constructed from differently functionalized magnetic beads addressed to specific capture sites, a dynamic array is achieved that is potentially reusable. This makes the system fabrication and use more flexible as several assays can be performed in the same portable microsystem simply by changing the functionalization of the beads [5]. For example, a medical doctor may be able to acquire beads functionalized with antibodies for a new strand of the flu, and with the microsystem and a microscope, she can perform assays testing for the new strand as well as older ones on the patient sample while the patient is still in the office. With conventional methods, a new system would have to be made as the spotting takes place during the fabrication. Bead manipulation has been carried out using active systems with on-chip electromagnets [6–9], passive systems where on-chip magnetic structures are magnetized by an external magnetic field [5], and hybrid systems where on-chip current lines work in combination with an applied external magnetic field [10–12]. Large magnetic forces are achievable in the passive systems, but these lack addressability of the individual capture sites. The systems with active electromagnetic structures are addressable but the forces are typically small and short-range. Furthermore, the large currents needed to achieve sufficient forces for capturing beads typically lead to hot spots, which may interfere with the biology in the channels.

Here, we present and demonstrate a new design, shown in Fig. 1, for creating arrays of magnetic beads in a microfluidic channel. The design is based on on-chip current lines combined with an external magnetic field and hydrodynamic focusing of a stream of beads. The 175 μm thick current lines are buried in the back side of a silicon wafer in which the fluidic channel is etched into the front side. This is different from previous reports in the literature where the current lines are structured in a 0.1–0.3 μm thick film at or near the channel bottom [10–13]. Due to the larger cross-section of the buried

*Corresponding author. Tel.: +45 4525 6338; fax: +45 4588 7762.
E-mail address: mfh@mic.dtu.dk (M.F. Hansen).

0304-8853/$ - see front matter © 2006 Elsevier B.V. All rights reserved.
doi:10.1016/j.jmmm.2006.10.1190

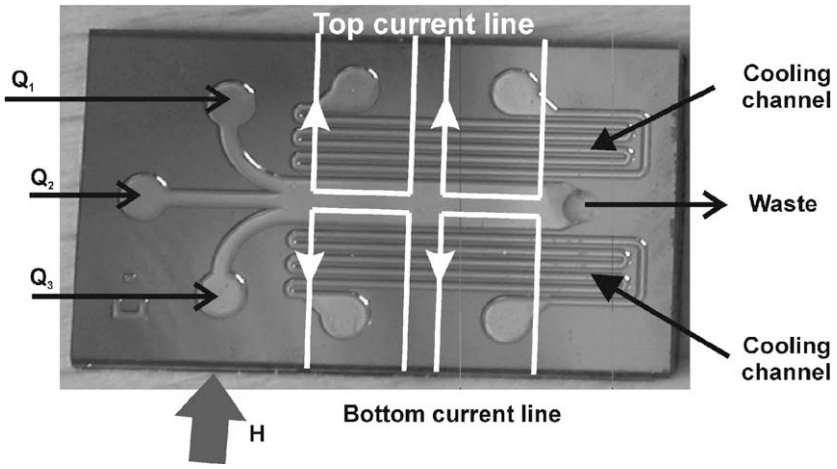

Fig. 1. Top view of channel side of microsystem. The channel has three inlets 1, 2, and 3 with flow rates Q_1, Q_2, and Q_3, respectively. The channel has length × width × depth = $8500 \times 1500 \times 100\,\mu m^3$. The outlet is through the bottom of the wafer. Cu current lines with $t \times w = 175 \times 20\,\mu m^2$ are buried in the back side of the wafer at the positions indicated by the white lines. An external magnetic field is applied across the chip as indicated. Also included on the chip is a set of channels for cooling by heat-exchange with a coolant.

current lines, they can sustain a larger current at a given power limit. Moreover, heat is efficiently dispersed due to the high thermal conductance of the silicon wafer, which can also contain microfluidic channels for a coolant. We show that the resulting magnetic forces are of longer range than when the current lines are fabricated in thin films on the channel bottom and demonstrate the construction of arrays of different types of magnetic beads within a microfluidic channel by this approach.

2. Theory and microsystem design

The magnetic force, $\mathbf{F}_{mag}$, on a bead is

$$\mathbf{F}_{mag} \cong \mu_0 V_{bead}(\mathbf{M}_{bead} \cdot \nabla)\mathbf{H}_0, \quad (1)$$

where μ_0 is the permeability of free space, V_{bead} the volume of a bead, $\mathbf{M}_{bead}$ the magnetization of the magnetic bead calculated at the bead center, and $\mathbf{H}_0$ the applied magnetic field present in the absence of the bead calculated at the centre of the bead. The force on a bead in a non-magnetic medium is directed towards field maxima. To maximize this force, the bead must be magnetically saturated, and the gradient of the magnetic field must be as large as possible.

Below, we assume that the bead magnetization is saturated along the external magnetic field, and thus we only consider the magnitude of the field gradient. We consider the field and current line geometry sketched in Fig. 1. This configuration allows for both attractive and repulsive forces near the current lines. When the current is applied in the indicated positive direction, the magnetic field from the current line adds to the external field and creates a local field maximum over the line to which the beads are attracted. A current applied in the opposite direction leads to a repulsive force.

The power, P, dissipated in a current line is $P = I^2R$, where I is the current, and $R = \rho L(tw)^{-1}$ is the resistance of the wire, where ρ is the material resistivity, L is the length of the wire, t is the thickness, and w is the width of the wire. Using the definitions of P and R, we obtain $I = (Pwt)^{1/2}(\rho L)^{-1/2}$. We now consider the magnitude of the magnetic field above the middle of a current line. Denoting the distance from the channel bottom to the bead r and the distance from the top of the current line to the channel bottom r_0, the magnitude of the magnetic field is approximately $H(r) \approx I[\{2\pi(r + r_0) + 2t + 2w\}]^{-1}$ (Ampére's law). Inserting I and taking the gradient, we find

$$\left|\nabla H(r)\right| \approx \frac{C\sqrt{t}}{(2\pi(r + r_0) + 2t + 2w)^2} \quad (2)$$

with $C = 2\pi(Pw)^{1/2}(\rho L)^{-1/2}$. For a fixed power and geometry ($w = 20\,\mu m$), we now compare a system with $t_1 = 0.3\,\mu m$ and $r_{0,1} = 1\,\mu m$ representing a thin film current line at the bottom of a channel with one with $t_2 = 175\,\mu m$ and $r_{0,2} = 50\,\mu m$ representing a thick current line of the present study. The simple approximation in Eq. (2) predicts that the ratio of the field gradient due to the thick current line to that due to the thin current line is $(t_2/t_1)^{1/2}[\{2\pi(r + r_{0,1}) + 2t_1 + 2w\}/\{2\pi(r + r_{0,2}) + 2t_2 + 2w\}]^2$. At the channel bottom ($r = 0$) and top ($r = 100\,\mu m$), respectively, it predicts the ratios 0.1 and 6. The ratio is larger than 1 for r larger than 19 μm. A numerical calculation by the method outlined below yields the ratios 0.4 and 10 at the bottom and top of the channel, respectively, and that the ratio is greater than 1 for r larger than 15 μm in reasonable agreement with the approximate model. Hence, a significantly larger force is achievable at the channel bottom by use of the thin current lines, but this force is of shorter range and acts locally. A thick current line can provide strong field gradients of longer range than the thin current lines and thus seems to be a better choice for the capture of magnetic beads in typical microfluidic channels.

The choice of geometry in the present work was based on simulations and fabrication limitations. Each current line

sketched in Fig. 1 has a cross section of $t \times w = 175 \times 20\,\mu m^2$ and it is placed at a spacing of 50 μm to the channel of length × width × depth $= 8500 \times 1500 \times 100\,\mu m^3$. The current lines were placed in pairs of two with a centre-to-centre spacing of 750 μm.

We find the magnetic field $\mathbf{H} = \mu_0^{-1}\nabla \times \mathbf{A}$ using the finite element method in Comsol Multiphysics 3.2a and solve the differential equation

$$\mu_0^{-1}\nabla \times \nabla \times (A_z\hat{\mathbf{z}}) = J_z\hat{\mathbf{z}},$$

where J_z is the current density in the z-direction, and A_z is the z-component of the magnetic vector potential, $\mathbf{A}$. The outline of the simulation geometry is sketched in Fig. 2. The shown (left) boundary has the condition $\mathbf{n} \times \mathbf{H} = \mathbf{0}$, where $\mathbf{n}$ is a boundary normal vector, since the magnetic field must be perpendicular to this boundary due to symmetry. The other boundaries are far away, and subject to the condition $A_z = \mu_0 H_0 y$, where y is the vertical coordinate and H_0 is the magnetic field applied in the horizontal direction.

We now compare the magnetic force on a MyOne magnetic bead to the buoyancy force. The beads have the diameter $d_{bead} = 1.05$ μm, the mass density $\rho_{bead} = 1.7\,g/cm^3$, the saturation magnetization $M_s = 39950\,A/m$, and the initial susceptibility $\chi_0 = 1.377$ (SI) [14]. With these numbers, the downwards buoyancy force is $F_{buoy} = V_{bead}(\rho_{bead} - \rho_{water})g = 4.2 \times 10^{-15}\,N$, where g is the gravitational acceleration. The magnetic force is found from Eq. (1) with $|\mathbf{M}_{bead}| = M_s L(3\chi_0|\mathbf{H}|/M_s)$, where L is the Langevin function. Fig. 2 shows the magnitude of the magnetic force field on a MyOne magnetic bead calculated in an external magnetic field of 50 kA/m with a current of 2 A through the current line. The arrows show the direction of the force field, the greyscale chart and the contour lines show the base 10 logarithm of the magnetic force divided by the buoyancy force. For example, within the 2.0 contour, the magnetic force is more than 100 times the buoyancy force. The situation below the current line is equivalent to reversing the current showing that a repulsive force can be obtained.

3. Experimental

3.1. Microsystem fabrication

The microsystem was fabricated using cleanroom technology. The labels below refer to Fig. 3, which schematically illustrates a cross-section of a chip during fabrication. (a) A 2.45 μm thick oxide is grown on a double-polished 350 μm thick Si wafer. (b) The fluid channels are defined in the oxide on the front side using

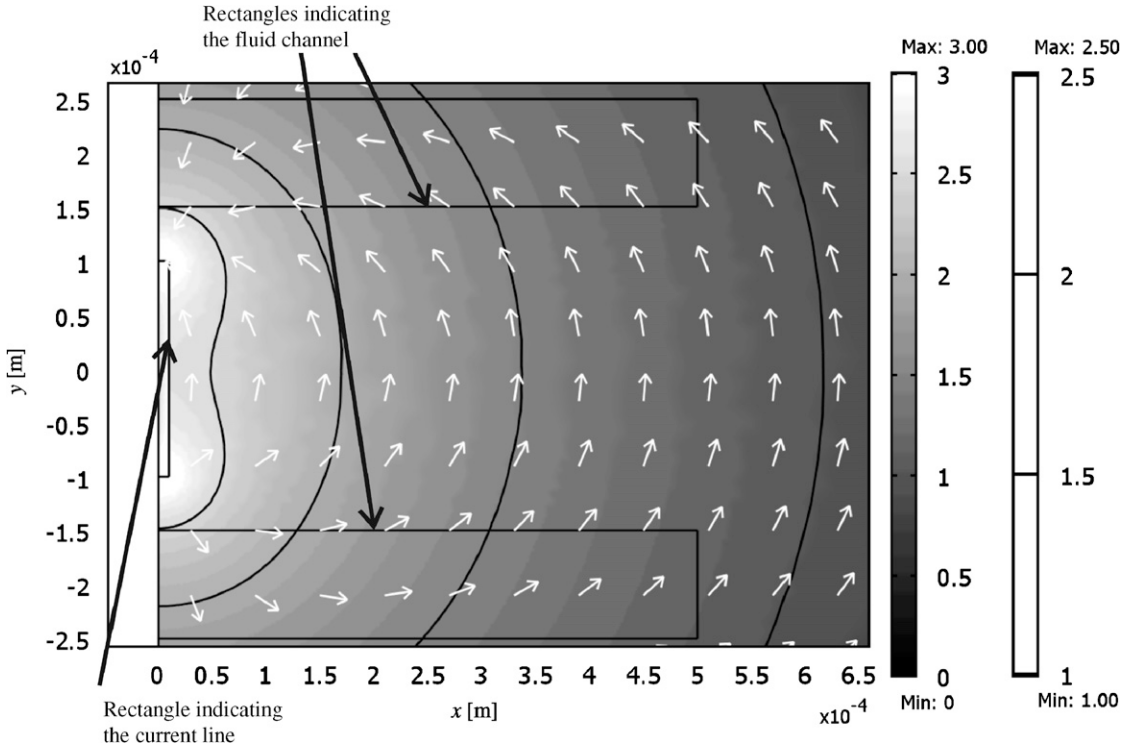

Fig. 2. Result of finite element calculation of the magnetic force field on a MyOne magnetic bead near a current line carrying a current of 2 A in an external field of 50 kA/m applied in the horizontal direction. The outlines of the current line and the channel are indicated in black. The channel is shown both above and below the current line. The force field above corresponds to the situation where the external field and the field from the current line couples constructively. That below corresponds to a situation, where the current is reversed, and repulsive forces are generated. Due to symmetry, only half of the geometry is considered. The arrows show the direction of the magnetic force. The gray scale and contour plots show the base 10 logarithm of the magnetic force over the buoyancy force on the scales shown to the right of the graph.

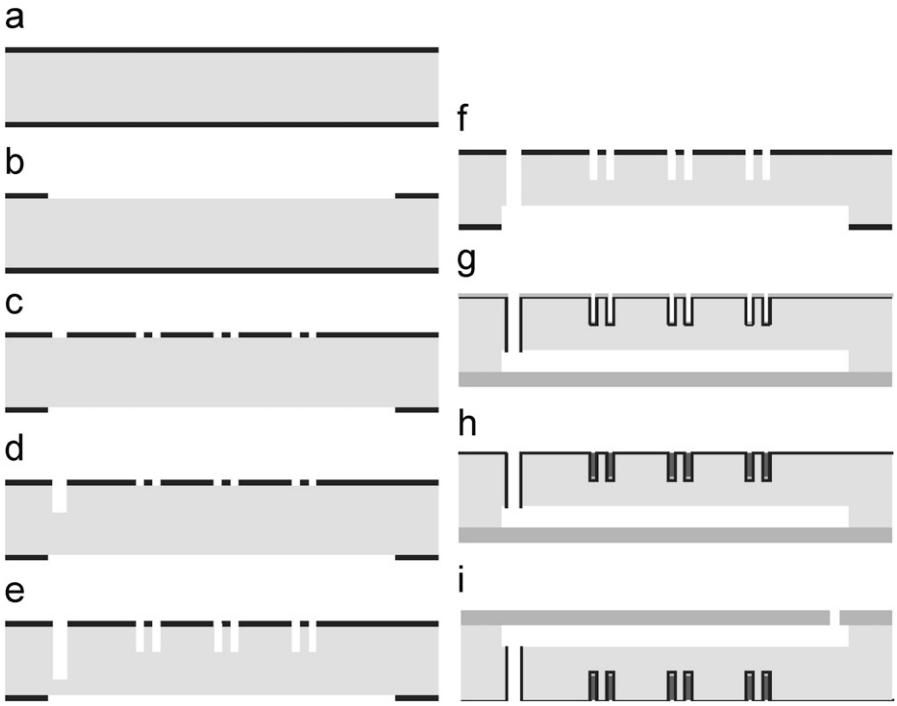

Fig. 3. Schematic illustration of a chip cross-section during the cleanroom fabrication described in the text.

photolithography and oxide etch in buffered HF. (c) The current lines and the through-hole for the fluid outlet are defined in the oxide on the back side. (d) Using a third photoresist mask, the through-hole is etched using deep reactive ion etching (DRIE) to a depth of approximately 130 μm. (e) After resist strip, the trenches for the current lines are etched using DRIE to a depth of 200 μm using the oxide as a mask. (f) The fluidic channels are etched to a depth of 100 μm using DRIE. During the etching, the wafer is temporarily bonded to a handle wafer as the through-hole is etched all the way through the wafer. (g) An RCA-clean is performed, a 1.2 μm thick oxide is grown, the oxide is removed on the fluid side, a pyrex wafer is bonded anodically to the fluid side, and a seed layer of 5/200 nm Ti/Au is deposited using e-beam evaporation on the current line side. E-beam evaporation gives poor step coverage and thus poor or no electrical contact between the Au on top of the wafer and that in the bottom of the trenches. (h) A series of short Au etches are performed using Entreat (Engelhard, NJ, USA) until the resistance between the top and bottom of the wafer back side with the current lines is larger than 250 kΩ. Then, a 2.5 μm thick Cu layer is electroplated in the bottom of the trenches using a CuproStar LP-1 electrolyte (Enthone, CT, USA). The mask is designed such that all trenches for the current lines are connected to the rim of the wafer. Using the Cu as etch mask, the remaining uncovered Au is removed in an Au etch. Then Cu is electroplated to a total thickness of 175 μm using the same electrolyte as before. (i) Fluid inlets are drilled through the pyrex wafer using a diamond drill.

3.2. Experimental setup

For the experiments, the chips were mounted in a chip-holder with O-ring sealed fluidic connections. Electrical contact to the current lines was established by soldering. The currents and the numbering of the inlets and liquid flows refer to Fig. 1. The bead solution was infused through inlet 2 and the buffer solution (milli-Q water) was infused through inlets 1 and 3 by use of three syringe pumps. Electrical currents I_{top} and I_{bottom} could be applied to the top and bottom current lines, respectively. Pictures were taken using a Leica MZ FL III microscope equipped with a Sony DFW-X710 CCD camera and FITC fluorescence filters. A homogeneous magnetic field of 50 kA/m was supplied by permanent magnets mounted in a soft iron frame.

3.3. Bead guiding experiments

Eight micron FITC-fluorescent magnetic beads (FCM-8052-2, Spherotech, Inc.) were used for the demonstration of bead focusing and guiding experiments. The solution supplied from the manufacturer was diluted with milliQ water to 20 μg/mL. The bead solution was infused at $Q_2 = 2\,\mu\text{L/min}$ (buffer: $Q_1 = Q_3 = 0$). A current of $I_{\text{top}} = I_{\text{bottom}} = 2\,\text{A}$ was applied to the current lines. Pictures were taken with a FITC-filter, and an exposure time of 9 s.

3.4. Magnetic bead microarray experiments

First, the bead capturing capability of the system was tested with 2 A through all current lines and 1 μm magnetic

bead solution with 20 μg/mL (MyOne, Invitrogen) flowing at $Q_2 = 2\,\mu L/min$ and no buffer flows ($Q_1 = Q_3 = 0$). Then, the capability to create arrays of different types of beads was demonstrated. Two types of beads were used for these experiments: 1 μm non-fluorescent magnetic beads (MyOne, Invitrogen) and 1 μm FITC-fluorescent magnetic beads (FCM-1052-2, Spherotech). All bead solutions were diluted with milliQ water to 20 μg/mL. The procedure was as follows: (1a) With $I_{bottom} = 2.5$ A and $I_{top} = 0$, MyOne bead solution was infused at $Q_2 = 10\,\mu L/min$ for 2 min (buffer: $Q_1 = 10$ and $Q_3 = 0\,\mu L/min$), such that the bead solution is hydrodynamically focused at the side of the channel at the bottom of Fig. 1. (1b) The flow rates were then lowered to $Q_2 = 0.7\,\mu L/min$ and $Q_1 = 1.5\,\mu L/min$ for 15 min to facilitate the capture of the hydrodynamically focused magnetic beads at the bottom current lines. (1c) The non-fluorescent MyOne beads remaining in the inlet tubes were then flushed out and through the channel by buffer at $Q_2 = 3$ and $Q_1 = 3\,\mu L/min$ for 5 min. (2a) Currents of $I_{bottom} = I_{top} = 2.5$ A were applied and the fluorescent Spherotec bead solution was infused at $Q_2 = 3\,\mu L/min$ for 5 min (buffer: $Q_3 = 3\,\mu L/min$ and $Q_1 = 0$), such that the bead solution was now hydrodynamically focused at the side of the channel at the top of Fig. 1. (2b) Again, the flow rates were lowered to $Q_2 = 0.7\,\mu L/min$ and $Q_3 = 1.5\,\mu L/min$ for 15 min. Micrographs were recorded with and without FITC-fluorescence filters to demonstrate the successful construction of the bead array.

4. Results and discussion

4.1. Bead guiding experiments

Fig. 4 shows fluorescence micrographs taken with long exposure time during the capture of 8 μm fluorescent magnetic beads. In the figure, the trajectories of individual beads are traced during the exposure. It is clearly seen that the beads are guided towards the current lines. Close to the current lines, the beads slow down and finally settle at the bottom of the channel. This demonstrates the bead focusing due to the current lines and that the system is able to capture 8 μm magnetic beads.

4.2. Magnetic bead microarray experiments

First, we present the demonstration of the bead capturing capability of the system. Fig. 5(a) shows a micrograph after 1 μm MyOne magnetic beads have been introduced into the entire channel. It is clearly seen that the beads are captured at the top of the current lines in the channel, whereas essentially no beads are present elsewhere in the channel. This shows the ability of the system to capture 1 μm magnetic beads and illustrates the attraction of the beads towards the current lines. Moreover, it should be noted that the beads are evenly distributed along each current line. This makes the surface of the bead agglomerates large and hence more available for biochemical reactions. In the greyscale micrographs in Figs. 5(a) and (b) not only the captured beads are visible, but also some spurious dots. The latter are either dust from the drilling process or freely flowing beads, neither of which show up on a fluorescence micrograph, such as Fig. 5(c).

Now, we turn to the demonstration of the construction of a magnetic bead microarray. Experiments in which 1 μm fluorescent and non-fluorescent magnetic beads were placed at the top and bottom of the images of the channel were carried out as described in the experimental section. Figs. 5(b) and (c) show a normal micrograph and a fluorescence micrograph, respectively, of the same section of the microfluidic channel. In the normal micrograph, two lines of beads are situated on top of the current lines

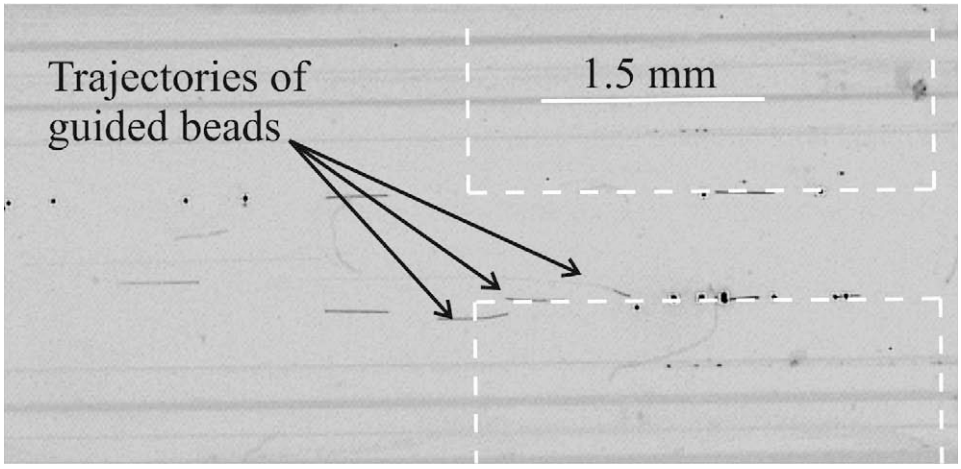

Fig. 4. Fluorescence micrograph illustrating magnetic beads being guided towards current lines and captured. The original image has been converted to grayscale, inverted, and some color/sharpness adjustments have been made. The long exposure time allows tracking of individual 8 μm beads in the microfluidic channel. The darker the bead trajectory, the slower the bead moves. The white dotted lines indicate the position of the current lines on the backside of the wafer.

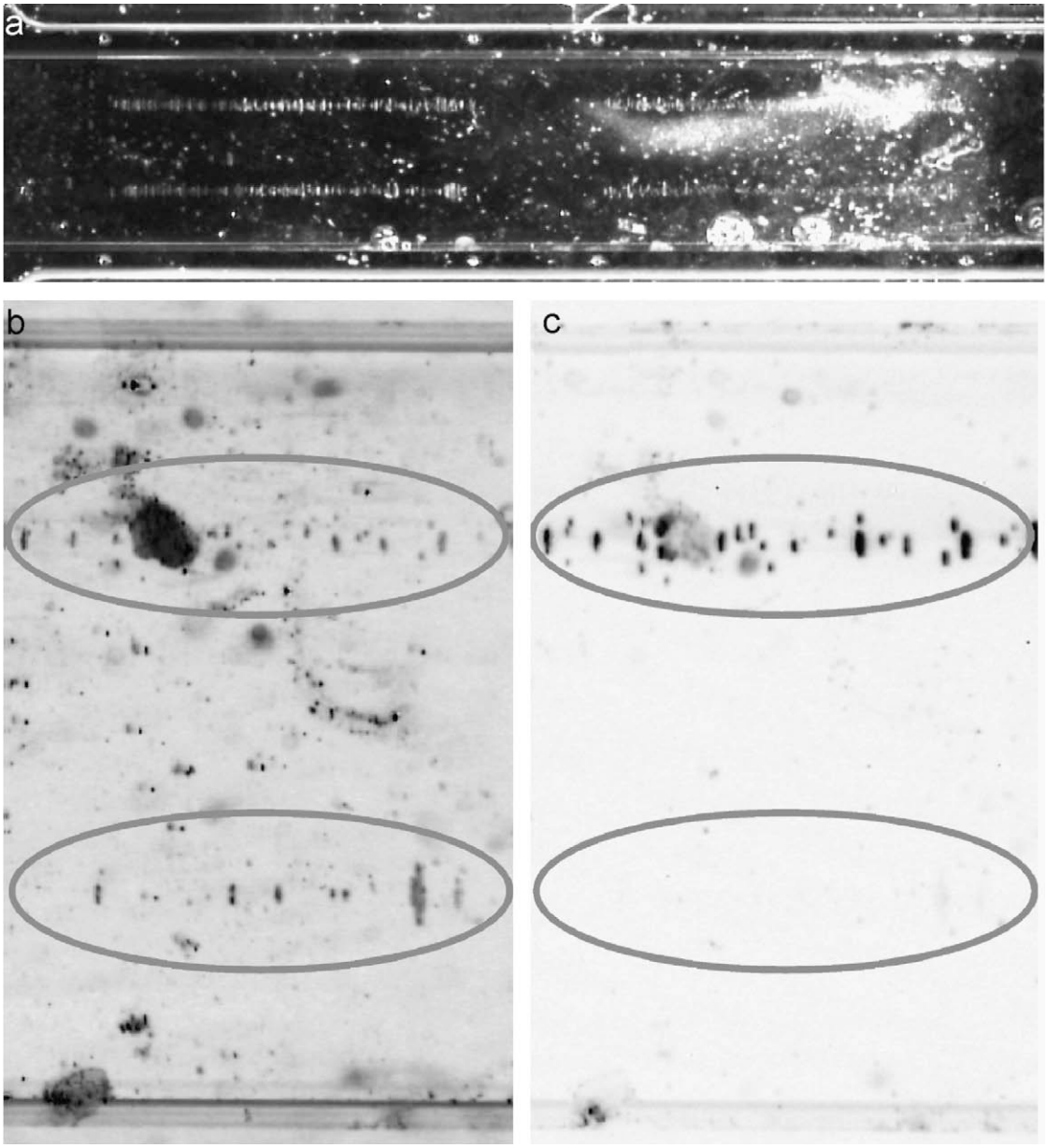

Fig. 5. (a) Micrograph of MyOne beads captured on all four current lines. In (b) and (c) fluorescent and non-fluorescent magnetic beads are captured at the top and bottom current lines as described in the text. The close-ups in (b) and (c) show a micrograph and a fluorescence micrograph of the same section of the channel, respectively. The colors have been inverted in both (b) and (c). Both types of beads are seen in (b), whereas in (c) only the fluorescent beads are observed. The width of the microfluidic channel in all images is 1.5 mm.

(encircled), whereas in the fluorescence micrograph only one line of beads is observable (encircled). This shows that it is possible to selectively place beads at each of the current lines with no cross-talk by combining hydrodynamic focusing of the beads and the guiding of each current line.

During the experiments, it was noted that beads were not only captured at the first current line but also at the current line further down the channel. Bead trajectory simulations, performed using the methods described by Smistrup et al. [15], indicated that all beads should be captured at a single current line. This difference is most likely due to the fact that the holding force (the force opposing the liquid flow) on the beads along the channel direction is weak such that they tend to roll along with the liquid flow. Furthermore, the simulations only deal with the capture of a single bead and the influence of beads that are already captured is neglected. Finally, the syringe pump introduces a slightly pulsating flow, which tends to tear captured beads loose. Air bubbles in the fluidic setup can also cause pulsations in the fluid pressure. These facts make it difficult to create arrays of beads at sites along the length of the channel, which are at the same position along the width of the channel.

We have previously reported on other designs of array systems [4,5]. The hybrid system of the present paper is clearly superior to the active system presented in Ref. [4];

the hybrid system has the same addressability, more capture sites, create larger magnetic forces, and it is easier to fabricate. Compared to the passive system in Ref. [5], the hybrid system has the potential for more capture sites, the beads are spread out along the channel bottom instead of being captured on the channel sidewall, it is addressable, but it creates smaller magnetic forces. Here the magnetic forces have not been measured, but they have been calculated in Comsol Multiphysics for all three systems.

5. Conclusion

We have demonstrated a new design of a hybrid magnetic separator where thick current lines are fabricated in trenches etched into the back side of a silicon wafer and a fluidic channel is etched into the front side. Simple theoretical considerations show that this procedure significantly increases the range of the magnetic force compared to thin current lines. Hence, by this approach the range of the magnetic force of hybrid magnetic separators is extended to length scales that are relevant for lab-on-a-chip applications. The integration of the current lines into the silicon wafer, which is a good heat conductor, makes it possible to efficiently disperse the generated heat and channels for a coolant are also easily integrated.

We have demonstrated the use of the new hybrid magnetic separator design for guiding and capturing magnetic beads as well as for the selective placement of two different types of magnetic beads at the bottom of a microfluidic channel in a hybrid magnetic separator by use of hydrodynamic focusing. This is the prerequisite for creating an array of different types of magnetic beads at the bottom of the channel and the method is expandable to more than two types of beads.

Acknowledgments

K. Smistrup acknowledges support from C:O:N:T and the Danish Technological Institute.

References

[1] M.A.M. Gijs, Microfluid. Nanofluid. 1 (2004) 22.
[2] N. Pamme, Lab Chip 6 (2006) 24.
[3] B.B. Yellen, G. Friedman, Lab Chip 20 (2004) 2553.
[4] K. Smistrup, O. Hansen, P.T. Tang, et al., in: Proceedings of the MicroTAS 2004, Malmö, Sweden 1 (2004) 509.
[5] K. Smistrup, B.G. Kjeldsen, J.L. Reimers, et al., Lab Chip 5 (2005) 1315.
[6] J.W. Choi, T.M. Liakopoulos, C.H. Ahn, Biosens. Bioelec. 16 (2001) 409.
[7] R. Rong, J.W. Choi, C.H. Ahn, in: Proceeding of the MEMS 2003, Kyoto, Japan, IEEE, Piscataway, NJ, 2003, p. 530.
[8] C.S. Lee, H. Lee, R.M. Westervelt, Appl. Phys. Lett. 79 (2001) 3308.
[9] K. Smistrup, P.T. Tang, O. Hansen, et al., J. Magn. Magn. Mater. 300 (2006) 418.
[10] M. Tondra, M. Granger, R. Fuerst, et al., IEEE Trans. Magn. 37 (2001) 2621.
[11] A. Rida, V. Fernandez, M.A.M. Gijs, Appl. Phys. Lett. 83 (2003) 2396.
[12] T. Deng, G.M. Whitesides, M. Radhakrishnan, et al., Appl. Phys. Lett. 78 (2001) 1775.
[13] A. Ramadan, V. Samper, D. Poenar, et al., J. Magn. Magn. Mater. 281 (2004) 150.
[14] G. Fonnum, C. Johansson, A. Molteberg, et al., J. Magn. Magn. Mater. 293 (2005) 41.
[15] K. Smistrup, O. Hansen, H. Bruus, et al., J. Magn. Magn. Mater. 293 (2006) 597.

Microfluid Nanofluid (2008) 4:565–573
DOI 10.1007/s10404-007-0213-0

RESEARCH PAPER

Theoretical analysis of a new, efficient microfluidic magnetic bead separator based on magnetic structures on multiple length scales

Kristian Smistrup · Minqiang Bu · Anders Wolff · Henrik Bruus · Mikkel Fougt Hansen

Received: 7 May 2007 / Accepted: 30 July 2007 / Published online: 22 August 2007

Abstract We present a theoretical analysis of a new design for microfluidic magnetic bead separation. It combines an external array of mm-sized permanent magnets with magnetization directions alternating between up and down with μm-sized soft magnetic structures integrated in the bottom of the separation channel. The concept is studied analytically for simple representative geometries and by numerical simulation of an experimentally realistic system geometry. The array of permanent magnets provides long-range magnetic forces that attract the beads to the channel bottom, while the soft magnetic elements provide strong local retaining forces that prevent captured beads from being torn loose by the fluid drag. The addition of the soft magnetic elements increases the maximum retaining force by two orders of magnitude. The design is scalable and provides an efficient and simple solution to the capture of large amounts of magnetic beads on a microsystem platform.

Keywords Lab-on-a-chip system · High gradient magnetic separation · Magnetic beads · Bioseparation

1 Introduction

Microscopic surface-functionalized magnetic beads have been used for bioseparation in biochemical laboratories for a number of years (Safarik 1999; Safarik and Safarikova 2004). Recently, their use for bioseparation in microfluidic systems or so-called lab-on-a-chip systems has received growing interest (Verpoorte 2003; Gijs 2004; Pamme 2006).

The simplest and most prominent class of microsystems for magnetic bead separation relies on the combination of microstructures of a soft magnetic material and an externally applied magnetic field (Rida and Gijs 2004; Deng et al. 2002; Do et al. 2004; Furlani and Sahoo 2006; Furlani 2006; Smistrup et al. 2005; Lund-Olesen et al. 2007). The basic principle is that the external field magnetizes the beads and the soft magnetic structures. The latter thereby provide local magnetic field gradients that lead to the capture of the magnetic beads. This is reminiscent of the high gradient magnetic separators (HGMSs) used for large scale magnetic separation, which comprise a separation column filled with a steel wool matrix in a large external magnetic field (Watson 1973; Svoboda 2001). However, a significant difference to large scale HGMSs is that in most microsystems the magnetic material is located outside the separation channel and thus not in direct contact with the fluid sample. The magnetic forces due to microscopic magnetic structures are inherently short-ranged. One solution to overcome this limitation has been to integrate systems for magnetic separation with microfluidic mixer structures that force the beads closer to the magnetic structures resulting in substantial improvements of the capture efficiency (Lund-Olesen et al. 2007).

For some applications, magnetic beads are premixed with a dilute sample with a volume on the order of milliliter. As the separation time is limited by the diffusion of the biochemical species to the surface of the beads, a substantial number of beads has to be used to maintain a

K. Smistrup · M. Bu · A. Wolff · H. Bruus · M. F. Hansen (✉)
MIC, Department of Micro and Nanotechnology,
Technical University of Denmark, Building 345 East,
2800 Kongens Lyngby, Denmark
e-mail: mfh@mic.dtu.dk

separation time on the order of minutes. Thus, we are faced with the challenge of constructing microsystems that efficiently capture substantial amounts of beads introduced at a high volume flow rate.

In this work, we present a new "multiple length scale" solution, sketched in Fig. 1, that combines an external array of mm-sized permanent magnets outside the system with microfabricated μm-sized soft magnetic elements placed very close to the bottom of the fluid channel. The basic concept is that the permanent magnet array provides long range magnetic forces attracting the beads to the channel bottom where the soft magnetic elements are situated. The soft magnetic elements are magnetized by the permanent magnets and provide strong local forces that retain the beads at the channel bottom.

First, we illustrate that an array of permanent magnets with alternating magnetization directions provides much stronger forces attracting the beads to the channel bottom than a single large permanent magnet. We show that the optimum lateral magnet dimension is roughly twice the distance from the top face of the magnet to the channel top.

Next, we demonstrate the concept of "multiple length scale" design and its force scaling for a simplified analytical model shown in Fig. 2.

Finally, we present a detailed numerical finite element analysis of the effect for a specific geometry chosen with experimentally realistic parameters (Fig. 1). In this geometry, long permanent magnets parallel to the horizontal *z*-axis (out-of-plane in Fig. 1) are placed next to each other 0.5 mm below the bottom of the fluid channel. Their cross-section in the vertical *xy*-plane is 2×2 mm^2 (the large length scale), and their magnetization directions alternate between the positive and negative *y*-direction. Soft magnetic elements with a cross-section in the vertical *xy*-plane of 200×5 μm^2 (the small length scale) are microfabricated on top of a 0.5 mm thick wafer placed on top of the permanent magnets. We label variables related to the permanent magnet and the magnetic elements with "pm" and "me", respectively. For our numerical analysis, we have chosen the soft magnetic material to have properties similar to permalloy. The soft magnetic elements are covered by 5 μm material that constitutes the planar bottom of the microchannel. The walls of the channel can then be constructed on top of the planarized channel bottom and a lid can be bonded onto the chip. The channel can have an arbitrary width in the *z*-direction. The material for the channel bottom and the channel walls could be the photodefinable epoxy resin, SU-8.

Both the simplified analytical studies and the finite element analysis show that substantial magnetic capturing and retaining forces can be obtained in a microchannel. The permanent magnet array provides a strong force attracting beads towards the channel bottom that varies only little over the height of the microfluidic channel. The soft magnetic elements enhance the retaining force acting on the beads by up to two orders of magnitude. This simple design provides the means to efficiently capture large amounts of magnetic beads in fluid channels capable of large fluid volume flows.

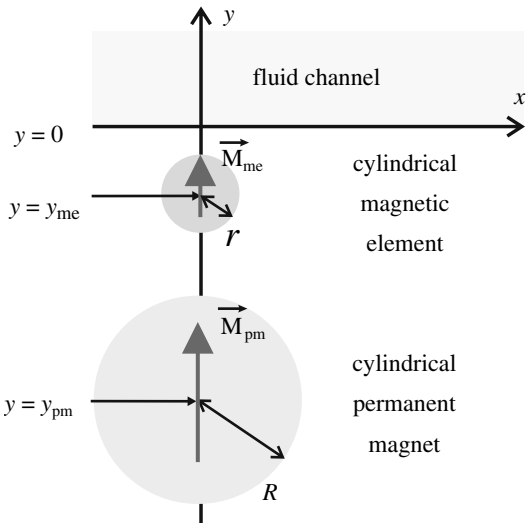

Fig. 2 Schematic of the simple analytical model with two parallel magnetic cylinders placed along the *z*-axis. The fluid channel is along the *x*-axis. The forces are calculated on the *y*-axis only. The large disk with radius *R* is the permanent magnet with the remanent magnetization M_{pm} in the positive *y*-direction. The smaller disk with radius *r* is the magnetic element with the saturated magnetization M_{me} in the positive *y*-direction

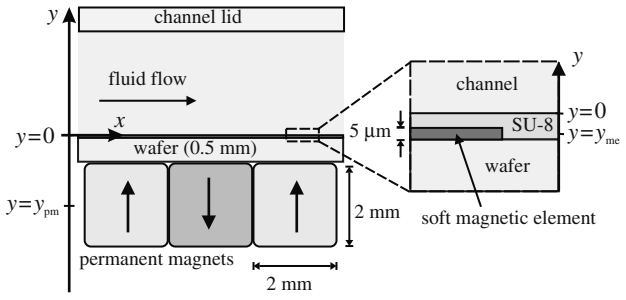

Fig. 1 Schematic illustration of the cross-section geometry of the system. Permanent magnets with alternating magnetizations are integrated in the chip holder and provide long range magnetic forces attracting magnetic beads to the channel bottom ($y = 0$). The zoom-in shows part of a soft magnetic element integrated in the chip. To create a smooth channel bottom and to separate the elements from the fluid, the elements are covered by a planarization layer (e.g., SU-8) with a thickness of 5 μm. The magnetic elements provide short range magnetic forces that aid in the bead capture and prevent beads from rolling along the channel bottom

2 Theory

2.1 Magnetostatics and magnetic forces

We choose to write the magnetic flux density as

$$\mathbf{B} = \mu\mathbf{H} + \mu_0\mathbf{M}_0, \tag{1}$$

where μ is the field-dependent magnetic permeability, μ_0 is the permeability of free space, $\mathbf{H}$ is the magnetic field intensity and $\mathbf{M}_0$ is a permanent, field-independent magnetization. In the absence of free electrical currents, the magnetic scalar potential ϕ can be introduced, such that $\mathbf{H} = -\nabla\phi$. Further, using that $\nabla \cdot \mathbf{B} = 0$, we obtain

$$\nabla \cdot (-\mu\nabla\phi + \mu_0\mathbf{M}_0) = 0. \tag{2}$$

This is the differential equation used for determining the $\mathbf{H}$-field in the finite element analysis below.

The force on a magnetic bead is given by (Engel and Friedrichs 2002)

$$\mathbf{F} = \mu_0 \int_V (\mathbf{M} \cdot \nabla)\mathbf{H}\mathrm{d}V, \tag{3}$$

where $\mathbf{M}$ is the field-dependent bead magnetization. Note, that $\mathbf{H}$ in Eq. (3) is the magnetic field intensity in the absence of the bead. In our case the external field is so strong that the bead magnetization can be considered equal to its saturation value M_b. Assuming a small variation of the integrand over the bead, we write

$$\mathbf{F} \simeq V_\mathrm{b} M_\mathrm{b} \mathbf{G}, \tag{4}$$

where V_b is the bead volume and $\mathbf{G}$ [T/m] is the magnetic field gradient in the direction of $\mathbf{H}$ given by

$$\mathbf{G} = \mu_0(\mathbf{e}_H \cdot \nabla)\mathbf{H}, \tag{5}$$

where $\mathbf{e}_H \equiv \mathbf{H}/H$. Thus, the magnetic force on a bead equals the saturation bead magnetic moment, $V_\mathrm{b}M_\mathrm{b}$, multiplied by $\mathbf{G}$, which we will refer to as the effective magnetic field gradient. The latter is independent of the bead type, and therefore we choose it as the measure we report in the numerical section.

In the discussion it will be illustrative to relate the calculated effective magnetic field gradients to bead velocities. As a numerical example, we have chosen MyOne magnetic beads (Invitrogen, CA, USA) with diameter $d_\mathrm{b} = 1.05$ μm, which are commonly used for magnetic bioseparation. The bead saturation magnetization is $M_\mathrm{b} = 40$ kA/m (Fonnum et al. 2005) and the fluid is chosen to be water with a viscosity of $\eta = 1.0$ mPa s. Balancing the magnetic force [Eq. (4)] with the fluid drag force ($\mathbf{F}_\mathrm{d} = -3\pi\eta d_\mathrm{b}\mathbf{v}_\mathrm{b}$) yields the magnetophoretic bead velocity

$$\mathbf{v}_\mathrm{b} = \mu_\mathrm{mb}\mathbf{G}, \tag{6}$$

where μ_mb is the magnetic mobility given by

$$\mu_\mathrm{mb} \equiv \frac{M_\mathrm{b} d_\mathrm{b}^2}{18\eta} = 2.5 \times 10^{-6}\,\frac{\mathrm{m}^2}{\mathrm{Ts}}. \tag{7}$$

This conversion factor makes it easy to relate the calculated effective magnetic field gradients to bead velocities.

2.2 Force considerations for a single permanent magnet

First, we consider the force obtained using a single permanent magnet. For the simplicity of the arguments, we only consider the axial field from a homogeneously axially magnetized cylindrical magnet of diameter $2R$, length L and magnetization M_pm. Using a standard solenoid representation of the magnetized cylinder, this field becomes

$$H(y) = \frac{M_\mathrm{pm}}{2}\left(\frac{L + y - y_0}{\sqrt{(L + y - y_0)^2 + R^2}} - \frac{y - y_0}{\sqrt{(y - y_0)^2 + R^2}}\right). \tag{8}$$

Here, the channel bottom is placed at $y = 0$ and the top face of the permanent magnet is at $y = y_0$. To simplify the expressions and to obtain an upper limit of the magnetic force, we consider below an infinitely long cylinder ($L = \infty$). In this limit, Eq. (8) becomes

$$H(y) = \frac{M_\mathrm{pm}}{2}\left(1 - \frac{y - y_0}{\sqrt{(y - y_0)^2 + R^2}}\right). \tag{9}$$

It can easily be shown that the effective magnetic field gradient along the axis of the magnet is

$$G_y(y) = -\frac{\mu_0 M_\mathrm{pm}}{2}\frac{R^2}{\left[R^2 + (y - y_0)^2\right]^{3/2}}. \tag{10}$$

The numerically largest value of G_y is obtained at the top face of the magnet, $G_y(y_0) = -\mu_0 M_\mathrm{pm}/2R$, and G_y has dropped to half of this value when y–$y_0 = [2^{2/3} - 1]^{1/2}R \approx 0.8R$. Thus, the maximum force scales as R^{-1} and the range of the magnetic field gradient and force is about half of the lateral dimension of the magnet. Therefore, the optimum lateral dimension of the magnet is roughly twice the distance from the top face of the magnet to the top of the fluid channel.

For $y_0 = -0.5$ mm and a typical Nd-Fe-B magnet with $\mu_0 M_\mathrm{pm} = 1.2$ T and diameter $2R = 10$ mm, one finds $G_y(0) = -1.2 \times 10^2$ T/m for the infinitely long magnet and

$G_y(0) = -3.2 \times 10^1$ T/m for a 2 mm long magnet. The corresponding MyOne bead velocities obtained using Eq. (6) are –0.3 and –0.08 mm/s, respectively. For a smaller magnet with the more optimal lateral dimension $2R = 2$ mm, this value increases to $G_y(0) \simeq -4.3 \times 10^2$ T/m (infinitely long magnet) and $G_y(0) \simeq -4.0 \times 10^2$ T/m (2 mm long magnet), respectively. Hence, for a magnet with a realistic thickness the force attracting the beads to the channel bottom can be enhanced by an order of magnitude by going from a cm-sized magnet to an optimized mm-sized magnet.

These arguments clearly show the advantage of using smaller magnets. Note, that if several magnets are arranged with the magnetization directions in the same direction they correspond to a single larger magnet. An array of magnets with alternating magnetization directions with dimensions comparable to half the distance to the top of the microfluidic channel will ensure that the magnetic field and the magnetic field gradient are localized and concentrated in the channel.

2.3 Scaling of forces in a simple analytical model

To illustrate the basic principle of further enhancing the magnetic forces by including soft magnetic elements at the bottom of the channel and the scaling of the forces, we calculate the magnetic forces on a bead due to a permanent magnet and a magnetic element separately for the simple 2D two-body model sketched in Fig. 2. Both the permanent magnet and the magnetic element are shaped as infinitely long cylinders parallel to the z-axis (out-of-plane). The channel bottom is at $y = 0$ and the centers of the permanent magnet and soft magnetic element are placed at $y = y_{\mathrm{pm}}$ and $y = y_{\mathrm{me}}$, respectively. For simplicity we consider only the magnetic field intensity on the y-axis. With this choice of geometry, the magnetic field and the magnetic field gradient are parallel to the y-axis and we write $\mathbf{H} = H(y)\mathbf{e}_y$. We assume that both the permanent magnet and the magnetic element are homogeneously magnetized with magnetizations M_{pm} and M_{me}, respectively, and that the magnetic element is magnetically saturated. In this case, the 2D dipole fields H_{pm} and H_{me} from the permanent magnet and the magnetic element on the y-axis can be obtained by solving Laplace's equation for the magnetic scalar potential in cylindrical coordinates [see, e.g., (Watson 1973)] and are

$$H_{\mathrm{pm}}(y) = \alpha_1 \frac{R^2 M_{\mathrm{pm}}}{(y - y_{\mathrm{pm}})^2}, \tag{11}$$

$$H_{\mathrm{me}}(y) = \alpha_1 \frac{r^2 M_{\mathrm{me}}}{(y - y_{\mathrm{me}})^2}, \tag{12}$$

where the radii r and R are defined in Fig. 2 and α_1 is a constant. The magnetic forces on a bead due to the permanent magnet and the magnetic element are obtained from Eqs. (4) and (5) as

$$F_{\mathrm{pm}}(y) = \alpha_2 \frac{R^2 M_{\mathrm{pm}}}{(y - y_{\mathrm{pm}})^3}, \tag{13}$$

$$F_{\mathrm{me}}(y) = \alpha_2 \frac{r^2 M_{\mathrm{me}}}{(y - y_{\mathrm{me}})^3}, \tag{14}$$

where α_2 is a new constant. Thus, the ratio of the two forces becomes

$$\frac{F_{\mathrm{me}}(y)}{F_{\mathrm{pm}}(y)} = \left(\frac{r}{R}\right)^2 \left(\frac{M_{\mathrm{me}}}{M_{\mathrm{pm}}}\right) \left(\frac{y - y_{\mathrm{pm}}}{y - y_{\mathrm{me}}}\right)^3. \tag{15}$$

Typical parameters for microsystems are $r \simeq 5$ μm and $R \simeq 1$ mm, yielding $r/R \simeq 5 \times 10^{-3}$, and $M_{\mathrm{me}} \simeq M_{\mathrm{pm}}$. If the permanent magnet is placed on the back side of a 0.5 mm thick wafer on which the magnetic element and the fluid channel are fabricated on the front side, typical values are $y_{\mathrm{pm}} \simeq -1.5$ mm and $y_{\mathrm{me}} \simeq -10$ μm, i.e., $y_{\mathrm{me}}/y_{\mathrm{pm}} \simeq 7 \times 10^{-3}$. At the channel bottom, $y = 0$, these parameters yield the ratio of forces

$$\frac{F_{\mathrm{me}}(0)}{F_{\mathrm{pm}}(0)} \simeq 84. \tag{16}$$

Moreover, it is found that $F_{\mathrm{me}}(y)/F_{\mathrm{pm}}(y) \simeq 1$ when $y \simeq 35$ μm. Thus, the element strongly enhances the magnetic force on the beads in the vicinity of the magnetic element.

3 Finite element analysis

In this section, we calculate the magnetic force on beads in a microchannel for the realistic geometry of Fig. 1. This geometry can be represented by the model geometry reduced by symmetry arguments, which is illustrated in Fig. 3a that we solve numerically using the finite element method. We investigate the sensitivity of our calculations of the magnetic force to the gap $2g_{\mathrm{pm}}$ between the permanent magnets in the permanent magnet array and the radius of curvature ρ_{pm} of the edges of the permanent magnets as these parameters are important for the convergence and accuracy of the calculations.

In Sect. 4, we calculate the effect of adding the soft magnetic elements at different positions relative to the permanent magnet.

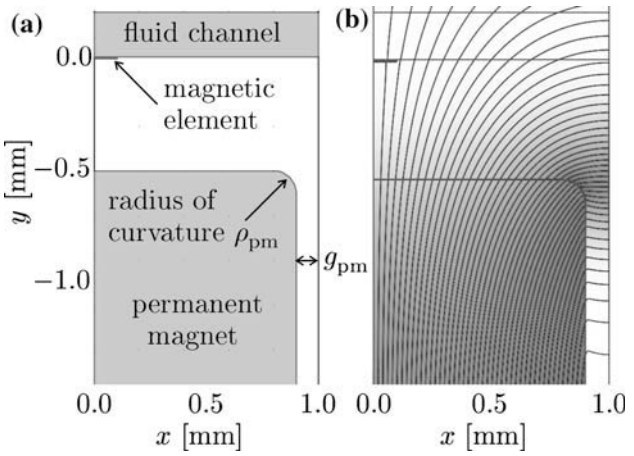

Fig. 3 **a** Zoom-in of the model geometry. The figure shows half of one of the permanent magnets, the position of the fluid channel, and the position of a soft magnetic element. The magnetic element has a height of 5 μm, a total width of 200 μm and is placed with its top 5 μm below the bottom of the channel. The total calculation domain extends from y = –100 to 100 mm. The solution ϕ is symmetric and antisymmetric around the vertical boundaries at x = 0 and 1 mm, respectively. The gap $2g_{pm}$ between adjacent permanent magnets and the radius of curvature ρ_{pm} of the permanent magnet edges are defined. **b** Example of calculated field lines for the magnetic flux density. Near the corner of the magnet, the flux density attains its maximum value of about 1.3 T. In the fluid channel it attains values in the range 0.2–0.4 T with the lowest value at the top of the channel

Prior to the numerical investigations of the specific geometry below, the finite element analysis was validated against known analytical results for a simple geometry.

3.1 Geometry and boundary conditions

Figure 3a shows the geometry and calculation domain of our model. The boundary conditions used in conjunction with Eq. (2) are implemented in Comsol Multiphysics 3.3 as

$$\hat{\mathrm{n}} \cdot \nabla\phi = 0, \quad x = 0\,\mathrm{mm}, \tag{17}$$

$$\phi = 0, \quad x = 1\,\mathrm{mm}, \tag{18}$$

$$\hat{\mathrm{n}} \cdot \nabla\phi = 0, \quad y = 100\,\mathrm{mm}, \tag{19}$$

$$\hat{\mathrm{n}} \cdot \nabla\phi = 0, \quad y = -100\,\mathrm{mm}, \tag{20}$$

where $\hat{\mathrm{n}}$ denotes the outward normal vector of the boundary.

Conditions (17), (19) and (20) cause field lines to be parallel to the corresponding boundaries, while condition (18) causes the field lines to be perpendicular to the x = 1 mm boundary. These conditions correspond to H_x being antisymmetric around x = 0 mm and symmetric around x = 1 mm, while H_y is symmetric around x = 0 mm and antisymmetric around x = 1 mm. Likewise, G_x is antisymmetric around both x = 0 and 1 mm, whereas G_y is symmetric around both x = 0 and 1 mm.

Hence, the simulation domain corresponds to half the width of one permanent magnet in an infinite 1D array of permanent magnets along the x-axis with magnetization directions alternating between the positive and negative y-direction as sketched in Fig. 1.

The magnetization of the permanent magnet was set to the constant value $\mathbf{M}_0 = M_{pm}\mathbf{e}_y$. We chose $\mu_0 M_{pm}$ = 1.2 T, which is a typical value for Nd-Fe-B magnets. The permeability of the soft magnetic material was set to

$$\mu = \mu_0\left[1 + \frac{M_{me}}{H}\tanh\left(\frac{\chi_0 H}{M_{me}}\right)\right], \tag{21}$$

with χ_0 = 1,000 and $\mu_0 M_{me}$ = 1.25 T to emulate the magnetization curve of permalloy. This expression for the permeability shows the correct behavior in the limits $H \to 0$ and $H \to \pm\infty$ and is one of several possible choices for approximating the magnetization curve of a soft magnetic material. The magnetization behavior is largely dominated by demagnetization effects and is thus insensitive to the detailed shape of the intrinsic magnetization curve of the soft magnetic material.

In the model shown in Fig. 3a, we have introduced both the gap g_{pm} from the edge of the permanent magnet to the symmetry axis at x = 1 mm and the curvature of radius ρ_{pm} of the edge of the magnet. These features will always be present in a real system. Moreover, the introduction of the gap and curvature substantially improves convergence of the calculations and reduces the numerical uncertainty. This is due to the fact that the magnetic potential diverges near the corners of two adjacent permanent magnets with opposite magnetization placed next to each other and that the finite element solver does not handle divergences well. Introduction of a curvature of the corner also reduces the need for mesh resolution near the corner. The effects of different gaps and radii of curvature of the edges of the permanent magnets are investigated in Sect. 3.2.

3.2 Investigation of magnet gap and edge curvature

Figure 3b shows an example of magnetic flux density field lines calculated for the geometry in Fig. 3a by solving Eq. (2) with boundary conditions (17)–(20). The calculation was carried out in Comsol Multiphysics 3.3 using third order elements. The standard mesh was set up as "Normal mesh" except that the "Element growth rate" was set to 1.2, and "Resolution of narrow regions" was set to 3, and the "Maximum element size" was set to 10 μm in the fluid channel subdomain, where we wish to measure **G**.

We aim to find values of g_{pm} and ρ_{pm} for the permanent magnet edge that allow for a maximum deviation of G of 1% in the microchannel relative to a reference geometry. We cannot use an analytic solution as reference geometry, since no such solution exists. Therefore, we use as reference the geometry that has the smallest possible gap and/or the smallest possible radius of curvature. The geometries used for reference are defined in the caption of Fig. 4. Figure 4 shows the results of this investigation. Each magnet had a fixed height of 2 mm and a total width of $2 \times (1\text{ mm} - g_{pm})$. Note that the reference values of the magnet gap g_{pm} and the radius of curvature ρ_{pm} of the edge of the permanent magnet are both much smaller than the distance between the permanent magnets and to the fluid channel. In Fig. 4 we estimate the numerical error in our calculations. The mesh was refined once more than the mesh used for calculations, and the graph shows the normalized magnitude of the change in the result as a function of position. It is observed that a deviation in the calculation of **G** smaller than 1% relative to the refined mesh can be obtained with the standard mesh, $g_{pm} = 0.03$ mm and $\rho_{pm} = 0.1$ mm. This deviation was measured 20 μm above the channel bottom. We will also be reporting **G** at the channel bottom, so for completeness, we report that the maximum change in **G** due to refining the mesh is approximately 10% at the channel bottom (data not shown). As we shall see, the effect we are investigating gives order-of-magnitude changes, so an error of 10% or less is negligible in this context.

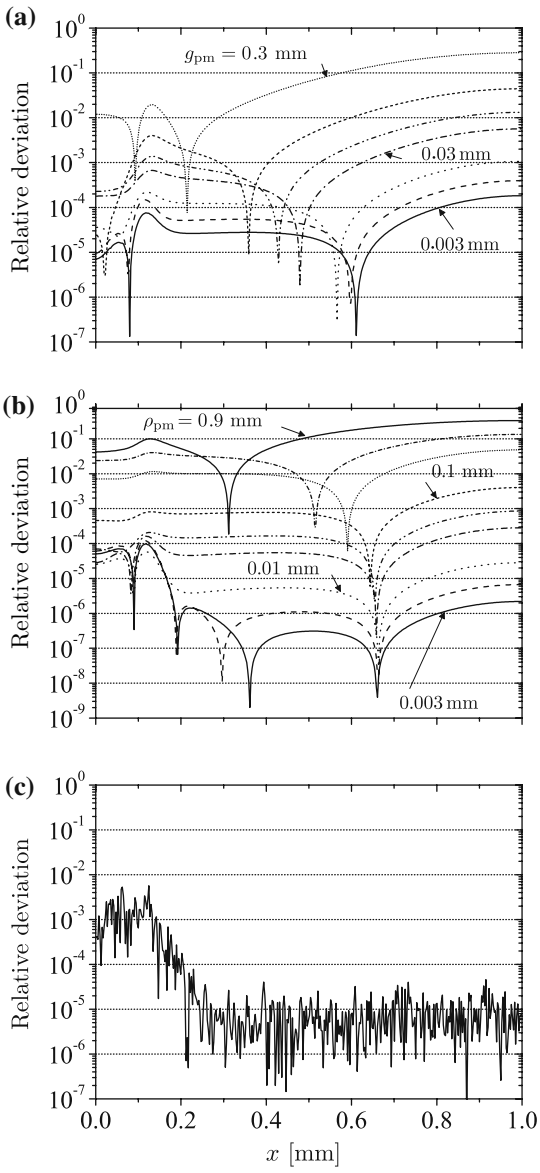

Fig. 4 Results of the numerical investigation of the magnet gap and edge curvature of the permanent magnet. All results were calculated at $y = 20$ μm. **a** Relative deviation, $|G_y(g_{pm})/G_y(g_{pm}^{(0)})-1|$ with $g_{pm}^{(0)} = 0.001$ mm, calculated for the magnet gaps $g_{pm} = 0.3, 0.1, 0.05, 0.03, 0.01, 0.005, 0.003$ mm and a radius of curvature of $\rho_{pm} = 0.1$ mm. **b** Relative deviation, $|G_y(\rho_{pm})/G_y(\rho_{pm}^{(0)})-1|$ with $\rho_{pm}^{(0)} = 0.001$ mm, calculated for the radii $\rho_{pm} = 0.9, 0.5, 0.3, 0.1, 0.05, 0.03, 0.01, 0.005, 0.003$ mm and a gap of $g_{pm} = 0.03$ mm. **c** Relative change in G_y when the standard mesh is refined one time. The calculation was performed for a gap of $g_{pm} = 0.03$ mm and a radius of curvature of $\rho_{pm} = 0.1$ mm

4 Results and discussion

We have performed a finite element analysis of the infinite array of permanent magnets with magnetization directions alternating between the positive and negative y-direction represented by the calculation geometry in Fig. 3a. The permanent magnet array was set up as described in Sect. 3 with $\rho_{pm} = 0.1$ mm and $g_{pm} = 0.03$ mm. Thus, a permanent magnet is placed in the simulation domain with its horizontal center at $x = 0$ mm and its edge at $x = 0.97$ mm, i.e., $x = 1$ mm corresponds to the middle of the gap between adjacent permanent magnets with opposite magnetization orientations. Figure 5 shows the variation of G_y and G_x calculated at the indicated distances above the channel bottom without soft magnetic elements and with soft magnetic elements at the indicated positions.

4.1 Magnetic force without soft magnetic elements

We first discuss the results when no soft magnetic elements are present. For this case, the effective magnetic field gradient can be seen as the thick, dashed lines in Fig. 5. The effective magnetic field gradient in the y-direction, Fig. 5a, attains values that are essentially independent of the height above the channel bottom as all studied y-values are small compared to the dimensions of a magnet. The values of G_y are symmetric around $x = 0$ and negative for all x. The values are numerically largest ($G_y \simeq -$

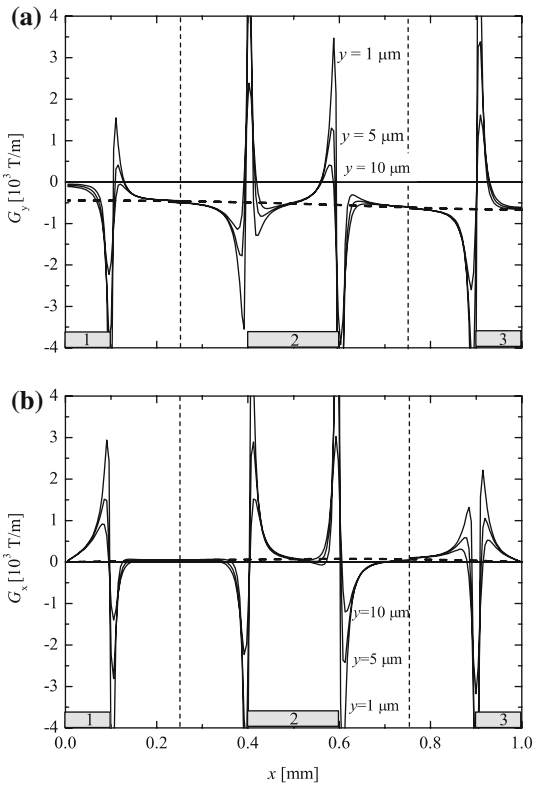

Fig. 5 Results of the numerical calculation for the geometry in Fig. 3a representing an infinite array of magnets. An upwards magnetized permanent magnet with g_{pm} = 0.03 mm and ρ_{pm} = 0.1 mm is placed in the simulation domain with its center at (x,y) = (0 mm,–1.51 mm). **a** and **b** show G_y and G_x, respectively, at the distances y = 1, 5 and 10 μm above the channel bottom calculated without magnetic elements (*dashed lines*) and with magnetic elements (*full lines*). The calculations with magnetic elements were carried out separately for three different element positions indicated by the *grey bars* at the x-axes. The magnetic elements are 5 μm thick, 200 μm wide (in total) and placed with their top 5 μm below the channel bottom

6.5×10^2 T/m) near the corner of a magnet ($x \simeq 1$ mm). Above the center of a magnet (x = 0 mm), the value of G_y reduces slightly to $G_y \simeq -4.5 \times 10^2$ T/m. Using Eq. (6), these numbers correspond to MyOne magnetophoretic bead velocities of –1.6 and –1.1 mm/s, respectively. Note that the values correspond well to that resulting from the simplified analytical treatment in Sect. 2.2.

The values of G_x due to the permanent magnets are positive for the x-values shown in Fig. 5b, but attain much smaller numerical values (not discernible in the figure) ranging from the maximum value $G_x \simeq 0.8 \times 10^2$ T/m ($v_b \simeq 0.2$ mm/s) near $x \simeq 0.6$ mm to 0 T/m for x = 0 and 1 mm. G_x is antisymmetric around x = 0 mm and therefore attains negative values for $-1 < x < 0$ mm.

Thus, the permanent magnet array provides a strong force attracting the beads towards the bottom of the channel. However, the force in the x-direction is weak in comparison and attracts the beads towards the gap between the permanent magnets. Due to the weak forces in the x-direction, the beads may tend to be torn loose by the fluid drag and roll along the channel bottom when a fluid flow is applied.

4.2 Magnetic force with soft magnetic elements

We now discuss the effect of the presence of soft magnetic elements. The solid lines in Fig. 5 show the effect of elements placed at the three different positions indicated by the grey boxes labeled 1–3 at the x-axes. Separate calculations were carried out for each of the studied element positions. It is seen that the contribution to **G** from an element decreases rapidly with the distance from the element in the x-direction and is negligible outside the dashed vertical lines in the figure. We have therefore chosen to plot each contribution only between the indicated vertical dashed lines.

From Fig. 5a, it is seen that the effect of the elements on G_y is to superpose a number of spikes near the corners of the magnetic elements on top of the slowly varying contribution from the permanent magnet. The magnitude of the spikes in G_y is highest near $x \simeq 0.5$ mm and attains numerical values up to 1.5×10^4 T/m at y = 1 μm. Note, that G_y is symmetric around both x = 0 and 1 mm. Beads close to the channel bottom will be strongly attracted to the channel bottom near the negative spikes and repulsed from channel bottom near the positions where the positive spikes lead to $G_y > 0$. The effect of the soft magnetic elements on the capture of beads further up in the channel is less clear. An inspection of the areas of the positive and negative peaks due to the magnetic elements using the symmetry of G_y yields that the average effect of elements on the force in the y-direction is negligible. Thus, as the beads are traveling in the upper region of the channel, the effect of the soft magnetic elements is to perturb the bead trajectories up and down around the "average" trajectory due to the permanent magnets. When the "average" position of the beads gets below a certain height, the beads are rapidly pulled to the bottom of the channel and kept there by the soft magnetic elements.

In the x-direction, the elements lead to spikes in G_x with magnitudes up to 1.5×10^4 T/m at y = 1 μm. The force in the x-direction attracts beads to regions, where a positive spike is followed by a negative spike (e.g., x = 0.6 mm), and repulses them from regions, where a negative spike is followed by a positive spike (e.g., x = 0.4 mm). The maximum values of G_x keeping the beads fixed at the attractive regions now have a magnitude with the magnetic elements in the range $0.2–1.5 \times 10^4$ T/m compared to less than 0.8×10^2 T/m without the magnetic elements. The

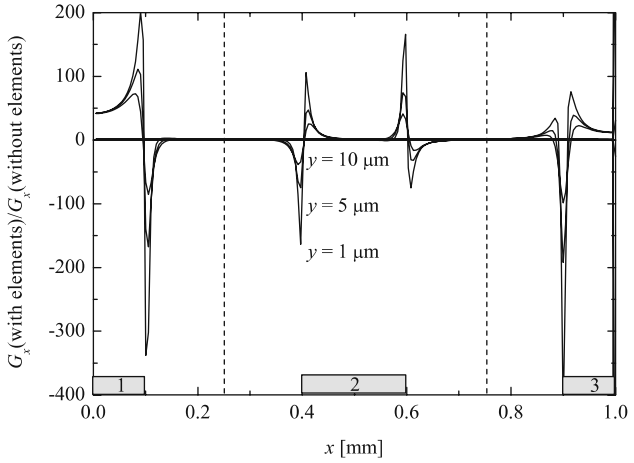

Fig. 6 Values of G_x calculated with soft magnetic elements relative to those calculated without soft magnetic elements at the distances y = 1, 5 and 10 μm above the channel bottom

corresponding maximum MyOne bead magnetophoretic velocities with and without magnetic elements are 5–37 and 0.2 mm/s, respectively. Thus, the relative effect of the magnetic elements is much more pronounced in the x-direction.

Figure 6 shows the values of G_x calculated with soft magnetic elements relative to those calculated without soft magnetic elements. It is seen that G_x increases with a factor of up to 400 due to the soft magnetic elements depending on the position of the element. This 100-fold increase implies that assemblies of captured magnetic beads are much more robust against being torn loose or rolling along the channel bottom with the fluid flow in the channel.

5 Conclusions

We have theoretically and numerically investigated a new design of a magnetic bead separator combining mm-sized permanent magnets with μm-sized soft magnetic elements by analytical calculations for simplified models and a finite element analysis for a realistic microsystem geometry. The two analyses yield effects on the same order of magnitude.

The permanent magnet array provides significant magnetic forces, extending over a length scale of about half the lateral magnet dimension, that effectively attract the magnetic beads to the bottom of the channel. This force exceeds that from a single larger permanent magnet by an order of magnitude. The magnetic force retaining the beads at the channel bottom due to the permanent magnet array, however, is comparatively weak leaving the beads susceptible to being torn loose or to rolling when a fluid is flowing in the channel. The soft magnetic elements, integrated with the microchannel and magnetized by the field from the permanent magnets, however, provide a further increase of the maximum retaining force on the magnetic beads by two orders of magnitude. These very strong local magnetic forces substantially reduce the effect of a fluid flow on the stability of the bead assemblies and facilitate the robust capture of more magnetic beads at a given fluid flow rate.

The permanent magnets can be integrated into the chip holder and the soft magnetic elements are relatively simple to integrate in fabrication schemes. The advantage of the "multiple length scale" design over designs incorporating magnetic structures under or adjacent to the microchannel in a homogeneous applied field (Furlani and Sahoo 2006; Furlani 2006; Smistrup et al. 2005; Lund-Olesen et al. 2007) is the long range (tuned to the distance to the top of the microfluidic channel) and the significantly higher strength of the capturing forces along the channel height. Compared to designs with magnetic structures adjacent to the microchannel (Smistrup et al. 2005; Lund-Olesen et al. 2007), a potential further advantage is the scalability of the channel width and the capacity for capturing large amounts of beads. Thus, the present design can be utilized for applications where a large number of magnetic beads is to be separated from a fluid at a high flow rate.

Acknowledgments K. Smistrup acknowledges support from Copenhagen School of Nanotechnology (C:O:N:T) and the Danish Technological Institute. M. Bu acknowledges support from EU FP6 STREP project OPTOLABCARD (contract no 016727).

References

Safarik I (1999) Use of magnetic techniques for the isolation of cells. J Chromatogr B: Biomed Sci Appl 722(1–2):33–53
Safarik I, Safarikova M (2004) Magnetic techniques for the isolation and purification of proteins and peptides. Biomagn Res Technol 2:7
Verpoorte E (2003) Beads and chips: new recipes for analysis. Lab Chip 3:60N–68N
Gijs MAM (2004) Magnetic bead handling on-chip: new opportunities for analytical applications. Microfluid Nanofluid 1:22–40
Pamme N (2006) Magnetism and microfluidics. Lab Chip 6:24–38
Rida A, Gijs MAM (2004) Manipulation of self-assembled structures of magnetic beads for microfluidic mixing and assaying. Anal Chem 76(21):6239–6246
Deng T, Prentiss M, Whitesides GM (2002) Manipulation of magnetic microbeads in suspension using micromagnetic systems fabricated with soft lithography. Appl Phys Lett 80:461–463
Do J, Choi J-W, Ahn CH (2004) Low-Cost magnetic interdigitated array on a plastic wafer. IEEE Trans Magn 40:3009–3011
Furlani EP, Sahoo Y (2006) Analytical model for the magnetic field and force in a magnetophoretic microsystem. J Phys D: Appl Phys 39(9):1724–1732
Furlani EP (2006) Analysis of particle transport in a magnetophoretic microsystem. J Appl Phys 99(2):024912
Smistrup K, Kjeldsen BG, Reimers JL, Dufva M, Petersen J, Hansen MF (2005) On-chip magnetic bead microarray using

hydrodynamic focusing in a passive magnetic separator. Lab Chip 5(11):1315–1319

Lund-Olesen T, Bruus H, Hansen MF (2007) Quantitative Characterization of Magnetic Separators: Comparison of Systems with and without Integrated Microfluidic Mixers. Biomed Microdevices 9:195–205

Watson JHP (1973) Magnetic filtration. J Appl Phys 44(9):4209–4213

Svoboda J (2001) A realistic description of the process of high-gradient magnetic separation. Miner Eng 14(11):1493–1503

Engel A, Friedrichs R (2002) On the electromagnetic force on a polarizable body. Am J Phys 70:428

Fonnum G, Johansson C, Molteberg A, Mørup S, Aksnes E (2005) Characterization of Dynabeads by magnetization measurements and Mössbauer spectroscopy. J Magn Magn Mat 293:41–47

PHYSICS OF FLUIDS **19**, 063101 (2007)

A magnetically actuated ball valve applicable for small-scale fluid flows

Kristian Smistrup
Division of Engineering and Applied Sciences, Harvard University, Cambridge, Massachusetts 02138 and MIC, Department of Micro and Nanotechnology, Technical University of Denmark, Building 345 East, DK-2800 Kongens Lyngby, Denmark

Howard A. Stone[a)]
Division of Engineering and Applied Sciences, Harvard University, Cambridge, Massachusetts 02138

(Received 4 September 2006; accepted 9 January 2007; published online 27 June 2007)

We present three possible designs for magnetically actuated ball valves that can be scaled down to nanometer length scales. Analytical expressions are presented for the hydraulic resistance of the ball valve as a function of geometric parameters and the state of the valve, and we also present analytical expressions for the hydrodynamic force on the magnetic bead that functions as the ball in the valve. We verify these expressions numerically and calculate the magnetic forces that can be exerted on the magnetic bead using the proposed structures. Finally, for typical parameters we show that these structures will be able to withstand a back pressure between 3 and 30 kPa regardless of the size of the bead/ball. © *2007 American Institute of Physics*. [DOI: 10.1063/1.2717690]

I. INTRODUCTION

The spectrum of research and development activities that are impacted by microfluidic devices continues to grow at a rapid pace.[1,2] One significant reason for the growth is the ability to control fluid flow and chemical composition at the scale of tens and hundreds of microns. Future developments will likely occur in many areas of biology, chemistry, and engineering, such as fields requiring increased precision or control, and where scaling down to smaller (e.g., nanoscales) brings additional advantages. The opportunity to control fluid flows without the need of external mechanical linkages provides one pathway for innovation.

Lab on a chip systems are being developed for use in chemical analysis, synthesis, identification, and delivery.[3,4] In many of these systems it is problematic to make small valves. This difficulty will only be accentuated as designs are scaled down. As one illustration, in recent years systems have been proposed for timed drug delivery.[5,6] For example, a diabetes patient needs to take doses of insulin at given time intervals. Imagine a system with 10^5 small compartments filled with insulin. If each of these compartments could be opened or closed by a magnetic valve, it would be possible to do timed delivery to the patient by integrating a small chip into the patients body. Of course, there are other routes to timed drug delivery.

Conventional valves in microsystems are commonly used for fluid handling and in micropumps. They can be divided into two main classes: Passive valves that basically function as fluid rectifiers blocking the flow in one direction, but not the other, and active valves, where some form of actuation is used to open or close the valve. Pneumatic, thermopneumatic, electrostatic, piezoelectric, or electromagnetic actuation is commonly used.[7–9] Almost all of these designs are fabricated using silicon micromachining and MEMS technology, and almost all of them involve a silicon or rubber-like diaphragm or a silicon-based cantilever. In general these valve designs can withstand pressures of a few kPa. Also, a few (passive) ball valve designs exist.[10,11]

In addition, a few polymer valve designs have been demonstrated. Simple twist valves were used with soft lithography,[12] and a PDMS soft-lithography design of an active pneumatic valve was demonstrated.[13] Other active and passive valve designs include a polymer plug moving inside a glass microfluidic system.[14–16] These designs have proven effective at pressures greater than 30 MPa.[16]

The above active valve types do not scale down easily, as the designs require relatively large structures for actuation, and/or moving parts. A nanoscale cantilever based design was presented recently.[17] To the best of the authors' knowledge the only experimentally realized nanoscale valve design is a chemically actuated molecular valve.[18]

In this paper we propose an active valve arrangement using a magnetic bead or particle, which is actuated magnetically, and is suitable for the regulation of small-scale fluid flows. The necessary magnetic forces are created by passive elements of soft magnetic material that create strong magnetic field gradients, when they are magnetized by an external magnetic field. Magnetic beads and particles are available with a range of magnetic properties and sizes ranging from 10 μm down to 5 nm.[19] We believe that our design is realizable in both PDMS and silicon, and can be scaled down to the nanoscale. We calculate analytically using a lubrication approach (and verify numerically) the flow in our valve arrangement. Furthermore, we present scaling arguments and demonstrate numerically that the proposed geometry will produce sufficient magnetic force to operate the valves at reasonable pressures and flow rates. At these length scales Brownian motion plays an important role. We do not include Brownian motion directly in the following, but at the end we discuss the possible influence of this random motion on the results.

[a)]Electronic mail: has@deas.harvard.edu

Paper #8 Page 1 of 9

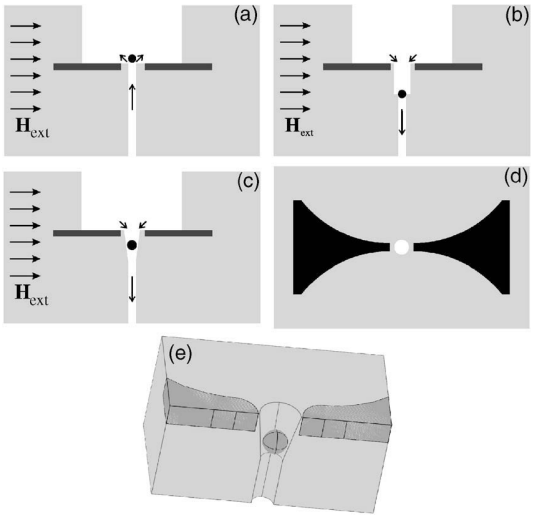

FIG. 1. (a)–(c) Cross sections of the three proposed geometries for magnetically actuated ball valves. The dark gray "plates" are slabs of soft magnetic material. The lighter gray is the silicon or PMDS structure that defines the microfluidic network. The solid black circle is the magnetic bead or particle. The arrows indicate the expected direction of the fluid flow and the external magnetic field, $\mathbf{H}_{ext}$. (a) In this configuration the magnetic field is constantly on, and thus the magnetic bead blocks the outlet of a channel. (b) An alternative configuration, where the magnetic field is initially off, but the fluid pressure holds the bead in the fluid inlet which is thus blocked. Turning on the magnetic field lifts the bead out of the inlet. (c) Same principle as (b), but the design has tapering sidewalls. This makes it easier to control the bead position, but it may be harder to fabricate than (b). (d) The magnetic structure viewed from above as well as the position of the fluid channel. It is seen how only the fluid channel has cylindrical symmetry. (e) 3D image of a spherical bead in the opening of the tapering tube. The dark gray is the magnetic material, the light gray is the silicon/PDMS, and the spherical object is the bead.

Figure 1 shows the proposed geometries for small-scale externally actuated valves. In all the designs the small fluid channel has a circular cross section, whereas the large channel or reservoir can have any shape; generalization to other shapes is, of course, possible. Figures 1(a) and 1(b) both have a small channel with straight sidewalls. In Fig. 1(a) the bead is envisioned to be smaller than the channel opening, and thus fluid flow is regulated (but not blocked totally) by controlling the position of the bead. The design of Fig. 1(a) also works well if the bead is larger than the channel opening, but in that case one might choose the design of Fig. 1(b), where the fluid pressure forces the bead to block the flow. By applying a magnetic force the valve can be opened. The structure in Fig. 1(c) has tapering sidewalls, and thus the bead will block the flow at some position in the tapering channel. This design has the advantage that the bead is forced into the opening by the fluid pressure, and also the bead diameter is less critical.

The thin magnetic slabs are shown from above in Fig. 1(d) and from the side in Figs. 1(a)–1(c) and Fig. 1(e). For this type of external magnetic actuation we imagine that the slabs are composed of a soft magnetic material, e.g., permalloy or CoNiFe. When these materials are magnetized by an external magnetic field, strong magnetic fields and field gradients are created in the vicinity of the gap (fluid inlet/outlet). These fields exert a force on the bead, which pulls the bead out of or into the fluid inlet/outlet, and so regulates fluid flow.

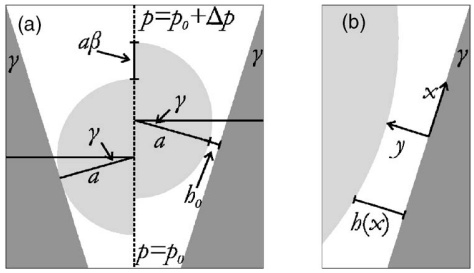

FIG. 2. (a) The calculation geometry for the tapered tube configuration of Fig. 1(c). A bead with radius a is inserted into a tapering tube. There is cylindrical symmetry around the dashed line. The situation where the bead is resting in the tube is shown on the left-hand side of the dashed line, and in this situation there can be no flow. On the right-hand side of the dashed line is shown the bead lifted a distance βa from the resting situation, and in this case, there is fluid flow. The inclination angle of the tube is γ, and the pressure drop across the sphere is Δp. (b) Definition of the coordinate system used. $h(x=0)=h_0=a\beta \sin \gamma$.

II. THEORY

In this section, we set up the general equations for calculations of the fluid flow in the narrow gaps around the magnetic bead. We will show in detail how the problem in Fig. 1(c) is solved, and we will give the final results for the other configurations. We will also give a scaling argument for the magnetic force that shows that it is indeed possible to create sufficient force to manipulate the bead for regulation of the flow.

A. Analytical solution for the tapered tube

Figure 2 introduces the flow geometry for the tapered tube version of the valve. Two geometric parameters characterize the valve configuration: (i) β is the vertical displacement of the sphere center from a (no flow) resting position against the channel walls, and (ii) γ is the inclination angle of the taper. We study the flow problem in the lubrication limit, where the gap between the tube wall and the bead has minimum size, $h_0=a\beta \sin \gamma$, and where the gap is narrow, i.e., $h_0 \ll a$. The geometry is rotationally symmetric around the dashed line in Fig. 2(a), but since $h_0 \ll a$, the coordinate system can be viewed locally as Cartesian, so we use the Cartesian coordinate system indicated in Fig. 2(b).

In the lubrication limit, everything is determined by the flow in the narrow gap, where we can approximate the shape of the spherical bead by a parabolic shape and obtain

$$h(x) = h_0\left(1 + \frac{x^2}{2h_0 a} + \mathcal{O}\left(\frac{x^4}{h_0 a^3}\right)\right). \tag{1}$$

This shape function establishes the characteristic length scale, $x_0=\sqrt{2h_0 a}$. Since everything is determined by the flow in the gap, only the part, $|x| < x_0$, matters, and thus $h(x) = h_0\left(1+\frac{x^2}{2h_0 a}\right)$ will suffice as an approximation to the shape.

With these opening statements the derivation of the flow, $\mathbf{u}=u(x,y)\hat{\mathbf{e}}_x+v(x,y)\hat{\mathbf{e}}_y$, and pressure distribution, $p(x,y)$, follows the usual path of lubrication analysis, where we consider the lubrication equations[20,21]

$$\frac{\partial p}{\partial x}=\eta\frac{\partial^2 u}{\partial y^2}, \tag{2a}$$

$$\frac{\partial p}{\partial y}=0, \tag{2b}$$

$$\frac{\partial u}{\partial x}+\frac{\partial v}{\partial y}=0. \tag{2c}$$

Equation (2b) states that the pressure does not depend on y, and therefore Eq. (2a) can be integrated to give

$$u(x,y)=\frac{1}{2\eta}\frac{\partial p}{\partial x}y(h(x)-y), \tag{3}$$

where no-slip boundary conditions have been imposed at $y=0$ and $y=h(x)$.

In order to find the pressure gradient, we integrate over a cross section of the fluid domain to obtain the total flow rate Q at any x,

$$Q=2\pi a\sin\gamma\int_0^{h(x)}u(x,y)dy=\frac{\pi a\sin\gamma}{6\eta}\frac{\partial p}{\partial x}h^3(x). \tag{4}$$

Continuity requires that Q must be independent of x, so Eq. (4) relates the flow rate, the position, and the pressure gradient in a unique way. The total flow rate is determined by integrating Eq. (4),

$$\Delta p=\frac{6\eta Q}{\pi a\sin\gamma}\int_{-\infty}^{\infty}(h(x))^{-3}dx=\frac{9\eta Q\csc\gamma}{2\sqrt{2ah_0^5}}, \tag{5}$$

where Δp is the pressure drop across the sphere.

Combining Eqs. (3)–(5) thus determines the flow and pressure fields, while the hydrodynamic resistance is

$$\frac{\eta Q}{a^3\Delta p}=\frac{4}{9\sqrt{2}}\beta^{5/2}(\sin\gamma)^{7/2}, \tag{6}$$

which depends on the two geometric parameters β and γ.

To obtain the hydrodynamic force on the sphere, we note that in the lubrication limit the force is dominated by the pressure force.[20] Thus we obtain the hydrodynamic force in the opposite direction of the pressure gradient,

$$F^h=\pi(a\cos\gamma)^2\Delta p. \tag{7}$$

Note that if we consider the force and flow rate specified, then, for a given inclination angle γ, the position β of the sphere is determined.

B. Straight channel geometry

Figure 3 defines the calculation geometry for the flow calculations for Figs. 1(a) and 1(b). Again there are two geometric parameters, (i) the difference εa between the radius of the feed channel and the sphere radius, and (ii) the vertical displacement βa of the bead. If $\varepsilon>0$, we have Fig. 1(a) and when $\varepsilon<0$, we have Fig. 1(b).

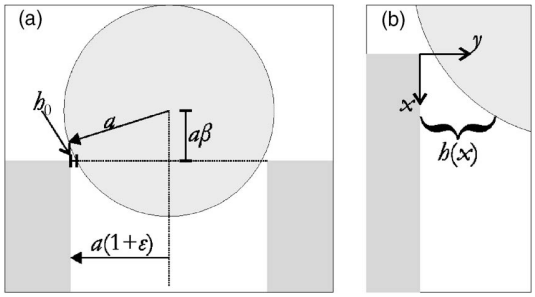

FIG. 3. (a) Definition of variables for the geometry where the channel is straight, i.e., Figs. 1(a) and 1(b). A bead with radius a is positioned at the opening of a tube (marked by the dark gray) with radius $a(1+\varepsilon)$. If $\varepsilon>0$, we have the situation in Fig. 1(a) and if $\varepsilon<0$, we have the situation in Fig. 1(b). $\varepsilon<0$ is shown here. The vertical distance between the center of the bead and the opening of the tube is $a\beta$. The pressure drop across the sphere is Δp. (b) Definition of the coordinate system.

In both cases, a little geometry gives us the height as $h(x)=a(\varepsilon+\beta^2/2)+\beta x+x^2/(2a)$, which can be rewritten as

$$h(x)=h_0\left(1+\frac{2\beta}{\sqrt{\beta^2+2\varepsilon}}\frac{x}{\sqrt{2ah_0}}+\frac{x^2}{2ah_0}\right), \tag{8}$$

where $h_0=h(0)=a(\varepsilon+\beta^2/2)$ is the minimum height in the gap, and a, ε, and β were defined in Fig. 3. We notice that for $\varepsilon<0$, we must require that $\beta>\beta_{\min}\equiv\sqrt{-2\varepsilon}$.

Following the steps of Eqs. (3)–(5), we arrive at

$$\Delta p=\frac{6\eta Q}{\pi a}\int_0^{\infty}(h(x))^{-3}dx, \tag{9}$$

which immediately gives

$$\frac{\eta Q}{a^3\Delta p}=\frac{\pi(\pm\varepsilon)^{5/2}}{48}(\lambda^2\pm 2)^{5/2}\times\left[\int_0^{\infty}\left(1+\frac{2\lambda}{\sqrt{\lambda^2\pm 2}}s+s^2\right)^{-3}ds\right]^{-1}, \tag{10}$$

where $\lambda=\beta(\pm\varepsilon)^{-1/2}$, and the plus signs are used, if $\varepsilon>0$, and the minus signs are used for $\varepsilon<0$. The force on the bead is $F^h=\pi a^2\Delta p$, if $\varepsilon>0$ and $F^h=\pi a^2(1+\varepsilon)^2\Delta p$ otherwise.

Since the requirement $\beta>\beta_{\min}$ ensures that the integrand is always real, the integral in Eq. (10) is easily evaluated numerically, and a closed form expression can also be given, but this form is messy and does not convey any new information.

Finally, we show how this result behaves in different limits,

$$\frac{\eta Q}{a^3\Delta p}=\frac{5}{48}\pi\beta^5,\quad \varepsilon=0, \tag{11a}$$

$$\frac{\eta Q}{a^3\Delta p}=\frac{4}{9}\sqrt{2}\varepsilon^{5/2},\quad \varepsilon>0,\beta\to 0, \tag{11b}$$

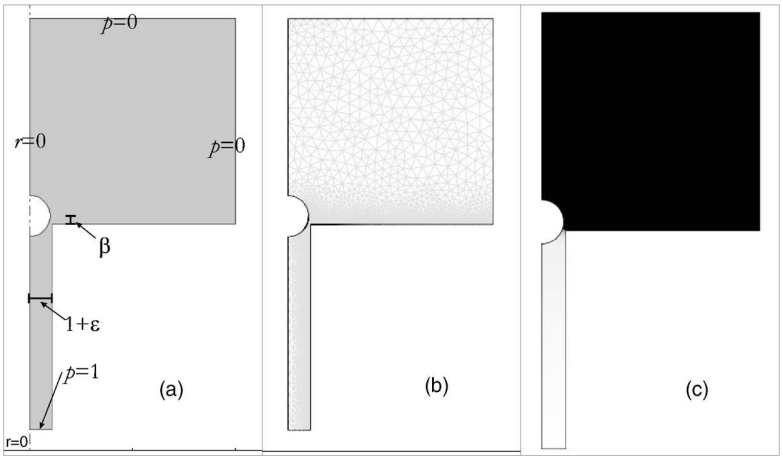

FIG. 4. Example of a Comsol Multiphysics calculation. (a) The calculation geometry with all lengths scaled by the sphere radius. The magnetic bead is treated as a stationary sphere with no-slip boundary conditions on the surface. The boundary conditions for the dimensionless pressure distribution and fluid flow are shown on the figure; if the boundary condition is not explicitly shown, no-slip conditions have been imposed. The dimensionless geometric parameters ε and β are defined. (b) An example of the mesh used for the numerical calculation. The mesh is very fine in the gap region, where most of the interesting fluid dynamics take place. (c) An example of a numerical result for small values of $\beta > |\varepsilon|$. The gray scale surface plot shows the pressure field, where since the change from black to white occurs abruptly across the gap region; the entire pressure drop occurs over the narrow gap.

$$\frac{\eta Q}{a^3 \Delta p} = \frac{\pi}{3}\beta_{\min}^3(\beta - \beta_{\min})^2, \quad \varepsilon < 0, \beta \to \beta_{\min}. \tag{11c}$$

C. Magnetic force scaling law

The magnetic force on a magnetic particle is[22]

$$\mathbf{F}^{\text{mag}} = \mu_0 \int_{V_{\text{bead}}} (\mathbf{M} \cdot \nabla)\mathbf{H}_{\text{ext}} dv, \tag{12}$$

where μ_0 is the magnetic permeability of free space, $\mathbf{M}$ is the magnetization of the bead, $\mathbf{H}_{\text{ext}}$ is the magnetic field that would be present, if the bead were not, and V_{bead} is the volume of the bead.

The magnetization of the bead is limited by the saturation magnetization of the bead, $M_{s,\text{bead}}$, and since an applied homogenous field will not contribute to the force, only the field disturbance caused by the magnetic slabs [shown in Fig. 1(d)] will contribute to the gradient. This disturbance is limited by the saturation magnetization of the soft magnetic material, $M_{s,\text{slab}}$. The characteristic length scale of the magnetic gradient outside the gap is set by a combination of the thickness of the two magnetic slabs and the distance between their tips. In order to achieve the largest gradients this distance should be as small as possible, and therefore it should also scale with the bead diameter, and so the length scale for the magnetic field gradient is the bead diameter. Combined, these statements say that for a sufficiently large applied magnetic field, the force that pulls the particle towards the gap between the magnetic plates is approximately

$$F^{\text{mag}} = \mathcal{O}\left(\frac{4}{3}\pi a^3 \mu_0 M_{s,\text{bead}} \frac{M_{s,\text{slab}}}{2a}\right) = \mathcal{O}(2a^2 \mu_0 M_{s,\text{bead}} M_{s,\text{slab}}). \tag{13}$$

For a MyOne[23] magnetic bead from Invitrogen ($2a = 1.05$ μm, $M_{s,\text{bead}} \approx 40$ kA/m) and permalloy (Py) magnetic slabs ($M_{s,\text{Py}} \approx 8.8 \cdot 10^5$ A/m) this force is approximately 24 nN.

If we compare Eqs. (7) and (13), we obtain an estimate for the maximum applied pressure for a given flow configuration,

$$\Delta p_{\max} = \mathcal{O}\left(\frac{2}{\pi \cos^2 \gamma} \mu_0 M_{s,\text{bead}} M_{s,\text{slab}}\right), \tag{14}$$

which is independent of the diameter of the particle and is approximately 30 kPa=0.3 bar for a small angle (γ; Fig. 2) and the aforementioned parameters.

III. NUMERICAL APPROACH AND RESULTS

We have performed numerical calculations for the fluid flow [for the configurations in Figs. 1(a) and 1(b)] and magnetic field distribution [for the configuration in Fig. 1(d)] using Comsol Multiphysics 3.2a. The calculations allow us to explore configurations beyond the narrow gap limit considered in Sec. II.

A. Numerical methods for the fluid motion

The calculations for the fluid flow were performed in a two-dimensional cylindrical coordinate system (r,z) with rotational symmetry around the z axis. Figure 4 shows the calculation geometry, an example of a mesh, and an example of the result from this kind of calculation.

Since we expect this valve arrangement to be applied on the microscale, and since the fluid dynamics is dominated by the small gap between the bead and the outlet of the tube, we neglect the inertial term in the Navier-Stokes equations, and thus we only solve the Stokes equations combined with the continuity equation. We lose no generality by using dimensionless variables, so in the calculations we have the dimen-

sionless position, $\tilde{\mathbf{x}}=\mathbf{x}/a$, where a is the bead radius, fluid velocity, $\tilde{\mathbf{u}}=\mathbf{u}\eta/(a\Delta p)$, and pressure, $\tilde{p}=(p-p_0)/\Delta p$, where Δp is the applied pressure drop and p_0 is the ambient pressure.

For completeness we note that the meshes were set up by choosing the "Finer" mesh setting under Mesh Parameters, except that the "Resolution of narrow regions" parameter was set to 3, and the "Maximum element size" and the "Element growth rate" was set to 10^{-4} and 1.007, respectively, at the corner of the cylindrical tube closest to the bead. Figure 4(b) shows an example of such a mesh.

A sample result of this type of calculation is shown in Fig. 4(c). The dimensionless pressure field is shown as a gray scale surface plot. The white regions have high pressure, $\tilde{p}\approx 1$ and the black regions have low pressure, $\tilde{p}\approx 0$. It is observed that the entire pressure drop happens across the small gap between the bead and the end of the cylindrical tube.

We have extracted the total flow rate from the results using Comsol Multiphysics' built-in postprocessing integration routine. The flow rate is obtained by integrating $Q=\int 2\pi r v_z dr$ along the boundary where $p=1$. The force on the bead is calculated by integration of the total stress tensor over the surface of the bead.

B. Numerical method for the magnetic force calculations

The magnetic calculations were performed using the Electromagnetics module in Comsol Multiphysics. We are considering a situation without currents, and thus the **H** field is curl free and can be written as the gradient of a scalar potential, $\mathbf{H}=-\nabla\psi$. The potential can be found as the solution to $\nabla\cdot\mathbf{B}=-\nabla\cdot(\mu_0\mu_r(|\mathbf{H}|)\nabla\psi)=0$, where **B** is the magnetic flux density, μ_0 is the permeability of free space, and $\mu_r(|\mathbf{H}|)$ is the relative permeability that depends on the magnitude of the **H** field. In general μ_r is a nonlinear hysteretic tensor, but in these calculations, it is treated as a nonhysteretic scalar that depends on $|\mathbf{H}|$.

Figure 5 shows the geometry. The shape of the magnetic slab has not been optimized, but for illustration purposes we have chosen a shape that concentrates the magnetic field in the gap near the bead. Symmetry has been used at $y=0$, and antisymmetry in the magnetic potential has been used at $x=0$, so that the entire geometric structure of the magnetic field is obtained by including the mirror images at $x=0$ and $y=0$. The boundary conditions are specified in the figure. It is also shown how the geometry depends on the dimensionless horizontal distance between the bead and the magnetic slab, ε, the dimensionless height of the bead center above the slab center, β, and the dimensionless difference between the slab thickness and the bead radius, δ. A change in ε corresponds to a translation of the magnetic slab, the geometry of the slab remains constant.

We treat both pieces of magnetic material as nonlinear and have used the relation $\mathbf{M}=M_s\tanh\left(\frac{\chi_0|\mathbf{H}|}{M_s}\right)\frac{\mathbf{H}}{|\mathbf{H}|}$, such that $\mu_r(|\mathbf{H}|)=1+\frac{M_s}{|\mathbf{H}|}\tanh\left(\frac{\chi_0|\mathbf{H}|}{M_s}\right)$, where **M** is the magnetization field, M_s is the saturation magnetization, and χ_0 is the initial susceptibility of the material. For the bead, we have used

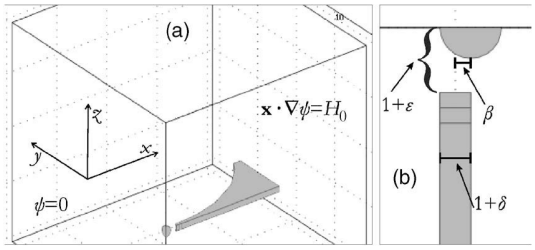

FIG. 5. Definitions of the geometry and boundary conditions for the magnetic calculations. (a) The three-dimensional calculation geometry. The gray region is the magnetic slab, and the bead is the quarter sphere. The coordinate system is defined on the figure, and the origin is chosen such that the center of the bead is at (0,0,0), when $\beta=0$. The magnetic slab has length (x direction) 20 and maximum width (y direction) 10. The calculation domain is $40\times 40\times 40$. On the boundary where $x=x_{\max}$, the boundary condition is the applied homogenous magnetic field H_0, and at $x=0$, we have $\psi=0$. On all other boundaries, the flux of the magnetic field is $\mathbf{n}\cdot\nabla\psi=0$. Symmetry considerations have been used, such that only one quarter of the entire magnetic structure (see Fig. 1) is included in the calculation domain. (b) A close-up of the region near the bead in the plane $y=0$. It has been rotated 90° relative to (a). The geometric parameters ε, β, and δ are defined.

typical values $\chi_0=1.485$ and $M_s=39950$ A/m,[23] and for the magnetic material, we have used the approximate parameters of electroplated permalloy, $\chi_0=1000$, and $M_s=8.8\cdot 10^5$ A/m. For these calculations, we have used $H_0=50$ kA/m, which is easily generated by a table top electromagnet and has proven to be sufficient to saturate the bead as well as the magnetic slab.

The standard mesh was created choosing the "Normal mesh" under Comsol's mesh parameters and setting the mesh on boundaries on the surface of the bead to have "Maximum element size" 0.2 and "Element growth rate" 1.1. These steps gave a mesh with approximately 24 000 elements. The fine mesh (used for the mesh investigation below) was produced by refining the standard mesh. This step resulted in a mesh with approximately 90 000 elements.

We calculated the magnetic force on the bead by integration of the Maxwell stress tensor. We used the built-in Comsol Multiphysics Electromagnetics module routine[24] to obtain the magnetic force by surface integration of[22]

$$\mathbf{F}=\int_{\partial\Omega}\mathbf{n}\cdot\left(\mathbf{BH}-\frac{1}{2}\mu_0\mathbf{I}|\mathbf{H}|^2\right)dS, \tag{15}$$

where **I** is the unit tensor, and $\partial\Omega$ is the outside surface of the quarter bead that is included in the calculation geometry. On the surfaces lying inside the bead, which are on the calculation domain boundaries, we did not use the built-in routine, but instead we used a postprocessing integration routine.

In the numerics we calculate the dimensional force using Eq. (15), and then we multiply by four to account for the whole sphere, and finally we normalize the force by the expected magnetic force given by Eq. (13).

C. Numerical results for the fluid flow

We now characterize the response of the fluid flow to changes in the geometric parameters ε, which is the dimensionless difference between the channel radius and the bead

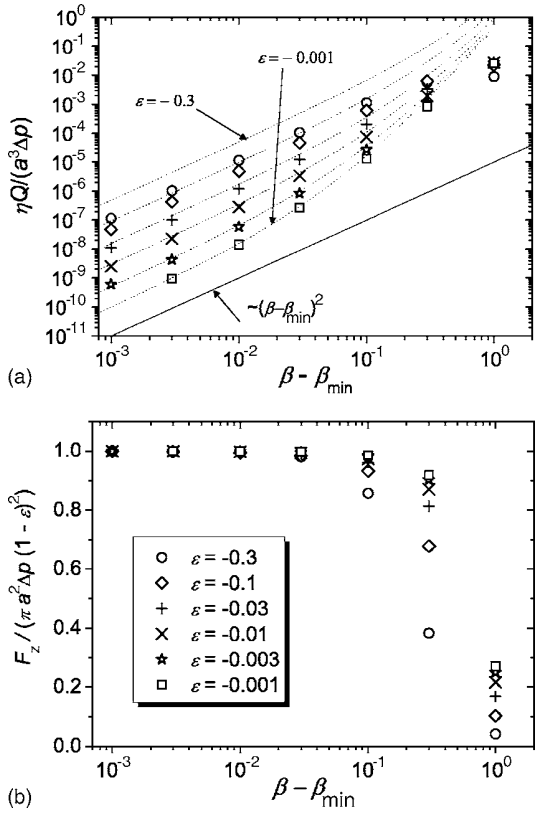

FIG. 6. Numerical results for the straight tube in the case where $\varepsilon<0$. (a) The hydrodynamic resistances for different values of ε as a function of β. The dotted lines are the analytical results given by Eq. (10). (b) The fluid force in the z direction on the magnetic bead for the same values of ε as a function of β. The legend in (b) also applies to (a).

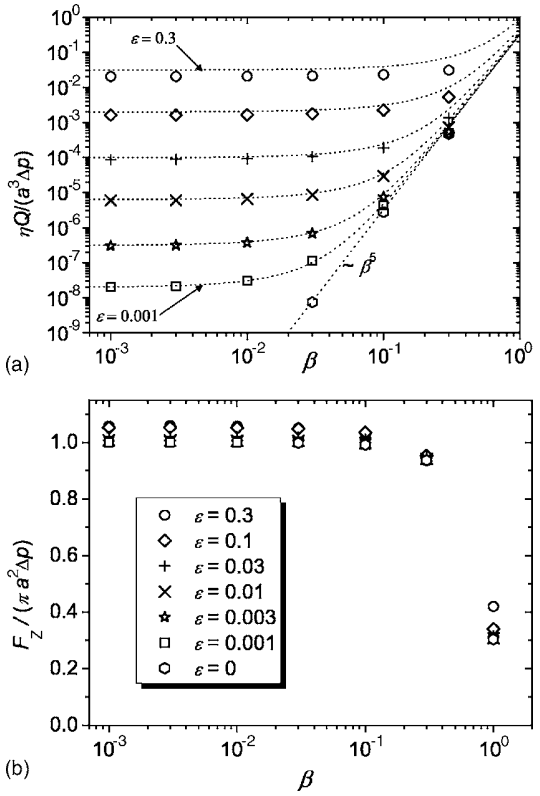

FIG. 7. Numerical results for the straight tube in the case where $\varepsilon\geq 0$. (a) The hydrodynamic resistances for different values of ε as a function of β. The dotted lines are the analytical results given by Eq. (10). (b) The fluid force in the z direction on the magnetic bead for the same values of ε as a function of β. The legend in (b) also applies to (a).

radius, and β, which is the dimensionless height of the center of the bead above the channel outlet. Figure 6 shows the results of calculations, where $\varepsilon<0$. In the theory section we showed that in this case there is a lower limit on β, $\beta>\beta_{\min}=\sqrt{-2\varepsilon}$, such that the bead is always above the outlet of the cylindrical tube. Therefore the plots are made relative to $\beta_{\min}$.

First we consider the hydrodynamic resistance, which is reported in Fig. 6(a). The symbols are the numerical data, and the dotted lines are the analytical result given by Eq. (10). It is seen that the analytical and numerical results agree well for small values of β and $|\varepsilon|$; for example, for $\varepsilon=-0.01$ the analytical result is in good agreement with the numerical calculation for $\beta-\beta_{\min}\lesssim 0.1$.

For larger values of $|\varepsilon|$ the analytic expressions overestimate the flow rate by a factor of approximately 10 or more. For $\varepsilon=-0.3$, Eq. (8) fails to describe the conditions in the gap correctly, since $1-0.3=0.7\approx\sin(45°)$, and thus the gap on top of the channel between the bead and the opening of the channel at $x<0$ (refer to Fig. 3) dominates over the gap between the bead and the channel walls, and the gap on top of the channel is not treated by our calculations.

For $\beta-\beta_{\min}\gtrsim 0.3$, the analytic result completely fails to describe the numerical data. This result is simply because the bead is now so far removed from the outlet that the hydrodynamic resistance is no longer dominated by the presence of the bead, and without a narrow gap, the lubrication analysis is no longer valid.

For $|\varepsilon|\lesssim 0.1$ and $\beta\lesssim 0.1$, the lubrication analysis is in very good agreement with the numerical data, and it is seen that $\eta Q/(a^3\Delta p)\propto(\beta-\beta_{\min})^2$ as $\beta\to\beta_{\min}$. This agrees with the result from the theory section.

We next consider the total fluid force on the bead and report the results in Fig. 6(b) relative to the analytically calculated force. The analytical result agrees very well for $\beta\lesssim 0.1$. This shows that the entire pressure drop is indeed across the gap, and that the pressure force dominates over the viscous force as expected.

Now we treat the case $\varepsilon\geq 0$. The hydrodynamic resistance is given in Fig. 7(a). The markers are the numerical data, and the dotted lines are the analytical result given by Eq. (10). Again, the analytical and numerical results agree well for all data except where $\varepsilon=0.3$. When the gap becomes large, the hydrodynamic resistance of the cylindrical tube becomes increasingly important, and thus lubrication analysis will overestimate the flow rate. When ε is finite and β is small, we see that the hydrodynamic resistance goes towards a constant as expected from the theory section. This is due to the fact that when β is much smaller than ε, then the geometry of the gap is dominated by ε rather than β. For $\varepsilon=0$, and for values of β, where the geometry of the gap is dominated by β rather than ε, $\eta Q/(a^3\Delta p)\propto\beta^5$.

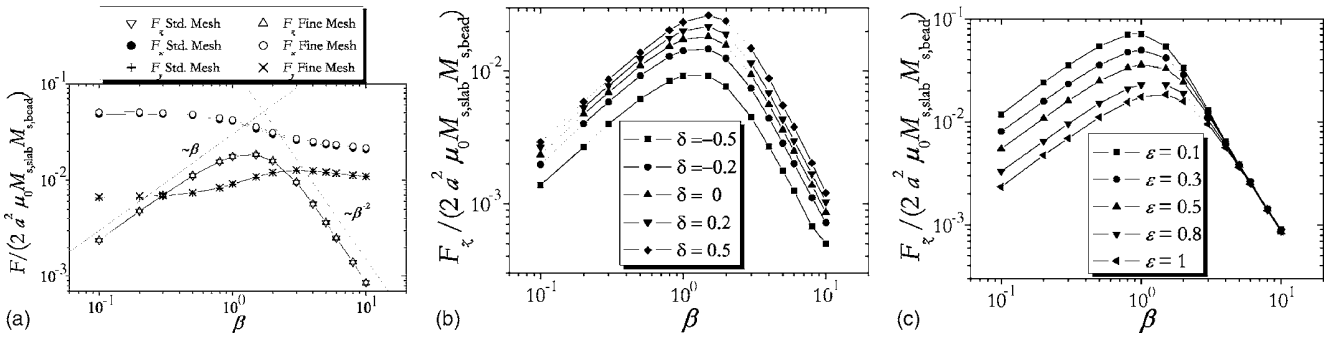

FIG. 8. Numerically calculated magnetic forces (absolute values) for various values of the parameters. All forces have been normalized by the value expected in Eq. (13). The force calculations have been done for the magnetic geometry shown in Fig. 5 and Fig. 1(d), and any of the fluidic designs Figs. 1(a)–1(c) can be applied. (a) Magnetic force calculations with the standard mesh and a further refined mesh. $\varepsilon=1$ and $\delta=0$. It is indicated how the force changes with β. (b) The force in the z direction as a function of β for different values of δ; $\varepsilon=1$. (c) The force in the z direction as a function of β for different values of ε; $\delta=0$.

Finally, we report the results for the forces in units of the analytical lubrication result in Fig. 7(b). For $\beta \lesssim 0.1$, and $\varepsilon \lesssim 0.1$ the numerical and analytical data agree very well. The discrepancy in the data for larger values of ε is caused by the substantial fluid flow present even for $\beta=0$, which causes a significant viscous force.

D. Numerical results for the magnetic force

We calculate the obtainable magnetic forces by variations of the geometric parameters ε, β, and δ in Fig. 8. We compare force calculations with the standard mesh to calculations with the fine mesh in Fig. 8(a) and find that the standard mesh is sufficient for these calculations. The forces in the x and y directions are not really meaningful, since both include an unbalanced magnetic pressure that would still be present in all directions if the bead was moved a little in either direction.

We investigate the influence on the magnetic force in the z direction of the thickness of the magnetic slab, described by δ, in Fig. 8(b). We find that it is preferable to have a thick magnetic slab. However, there must be an upper limit where a thicker magnetic slab does not contribute with any more force. This limit is most likely related to ε. It is outside the scope of this paper to determine this limit.

Finally, we present the forces in the z direction for different values of the distance between the magnetic slabs, which is determined by ε in Fig. 8(c). We find that the width of the gap, ε, has little influence on the force outside the gap, i.e., when $\beta>1$. However, when the bead approaches the gap, it is seen that it is best to have a small gap (ε should be small).

From Fig. 8 we see that we cannot generate the force given by Eq. (13), but we can get close to one tenth of this force. In addition, Fig. 8(b) shows that more force could be gained by increasing δ further, and also a more powerful applied magnetic field might increase the force. In Fig. 8 we found good design rules for design of the magnetic slabs; they should be thick, probably at least twice the diameter of the bead, and the gap between the magnetic slabs should be as small as possible.

IV. DISCUSSION AND OUTLOOK

In this paper, we have proposed a new design for a magnetically actuated valve that, in principle, may be reasonable for designs on the nanoscale, since control of the valve position is done externally. We have developed analytical expressions for the fluid forces and fluid flow through the valve at different conditions, and we have verified the results numerically. In addition, we have determined how the magnetic force depends on the same parameters, and from the results of the numerical calculations we have found design rules for optimum choices of the width of the gap, ε, and the thickness of the magnetic slabs, δ.

With the designs we have modelled here and typical material parameters, we have shown that it is possible to reach a force which is approximately one tenth of what we would expect from the scaling argument in Eq. (13), and thus referring to Eq. (14), we find that it is possible to withstand back pressures of approximately 3 kPa. With further improvements it should be possible to get close to the 3 kPa mentioned in Eq. (14).

The design in Fig. 1(a), where $\varepsilon>0$, has the property that if you have a tightly fitting tube with $|\varepsilon| \ll 1$, it is possible to have a change in hydrodynamic resistance over several orders of magnitude. The alternative design in Fig. 1(b) facilitates complete fluid blocking, and also the fluid forces can be reduced by choosing a more negative ε. However, the fitting and closing properties of the valve will then be diminished. The design in Fig. 1(c) clearly has the best properties for positioning the bead in the middle of the channel and flow blocking. The bead will automatically be guided into the opening of the tapering tube. Also, most commercially available magnetic beads have a considerable size distribution. Bead size distribution may be a problem with the two other designs, especially, if $|\varepsilon| \ll 1$ is desired, but the design in Fig. 1(c) overcomes this problem due to the tapering sidewalls. This design, however, poses a greater challenge in terms of microfabrication.

In all the calculations, we have assumed that the bead stays in the center of the fluid channel or between the magnetic slabs. Experimentally this may not be the case. The

bead may have a tendency to go to the side allowing for a larger fluid flow. This consideration favors the use of the design in Fig. 1(c), which will diminish this potential problem.

As the characteristic length scale (the bead radius) is reduced, the fluid-blocking efficiency for all the designs is limited by Brownian motion, which will cause the bead to oscillate around the closing position. Again, if the bead is away from the center the result will be greater flow than expected from the calculations. The quantitative influence of Brownian motion on the results shown here is a subject of active investigation. However, it is straightforward to estimate a bead radius, where the valve design breaks down completely when Brownian motion dominates over the magnetic force (which is equal to the maximum pressure force that can be applied). We simply compare thermal energy to the energy/work required to move a bead a distance of one bead radius against the magnetic force [Eq. (13)],

$$\frac{E^{\text{thermal}}}{E^{\text{mag}}} = \frac{kT}{2\mu_0 M_{s,\text{bead}} M_{s,\text{slab}} a^3}, \tag{16}$$

which at room temperature and for a 0.5 μm radius Invitrogen MyOne bead considered above is $\approx 4 \cdot 10^{-8}$, showing that Brownian motion is unimportant at this bead size. However, this ratio becomes unity as the bead radius is reduced to 4 nm (assuming that all other material properties are the same. In reality the bead saturation magnetization will most likely increase by approximately one order of magnitude).

The above scaling argument shows that the valve will not break down due to Brownian motion, as long as the bead/particle radius is more than approximately 10–20 nm. However, since we require that the fluid flow is completely dominated by the flow in the gap, we must require that the gap height is at least a few nanometers. Otherwise the assumption of a continuum fluid breaks down, and our calculations no longer apply. If we further assume that the bead diameter should be at least ten times the gap for the lubrication approximation to hold, then the bead must have a diameter of at least 40 nm. Such bead diameters are well above the limit where the valve breaks down due to Brownian motion.

In all microsystems and even more in nanosystems, stiction and van der Waals forces play an important role, and should definitely be considered, when one wants to fabricate valves on the nanoscale. This applies for any valve design on this length scale. However, recently there has been substantial progress towards coatings that are nonstick on the nanoscale (see, for example, Ref. 25). Comparing the numerical values given in Ref. 25 to Eq. (13) shows that the magnetic force should be sufficient to overcome stiction for beads with diameters of 5 and 20 μm.

Finally, we note that we have demonstrated a valve design with magnetic forces that will withstand fluid pressures of 3 kPa and that further optimization of the shape of the magnetic elements should increase this number. Also, magnetic particles with higher saturation magnetizations exist, and if those were used, higher forces and pressures could be reached. It is not unreasonable to expect an improvement by a factor of 5–10 on that account. We have argued that the continuum assumption breaks down before the valve is affected by Brownian motion. But still Brownian motion may play an important role in the performance of all of the valve designs but especially the one in Fig. 1(a). Stiction may be a problem, and it will most likely be the limiting factor for downscaling. As further progress is made with nonstick coatings, it will most likely be possible to fabricate magnetically actuated ball valves utilizing beads with diameters in the range of hundreds of nanometers or less.

ACKNOWLEDGMENTS

The Danish Technological Institute and the Copenhagen Graduate School for Nanoscience and Nanotechnology (C.O.N.T.) are acknowledged for financially supporting K.S.'s Ph.D. studies. We thank the Harvard NSEC for partial support of this research and Benny Davidovitch for helpful conversations.

[1] T. M. Squires and S. R. Quake, "Microfluidics: Fluid physics at the nanoliter scale," Rev. Mod. Phys. **77**, 977 (2005).
[2] H. A. Stone, A. D. Stroock, and A. Ajdari, "Engineering flows in small devices: Microfluidics toward a lab-on-a-chip," Annu. Rev. Fluid Mech. **36**, 381 (2004).
[3] *Microsystem Engineering of Lab-on-a-Chip Devices*, edited by O. Geschke, H. Klank, and P. Telleman (Wiley-VCH, Weinheim, 2004).
[4] J. Knight, "Honey, I shrunk the lab," Nature (London) **418**, 474 (2005).
[5] B. G. Stubbe, S. C. De Smedt, and J. Demeester, "Programmed polymeric devices for pulsed drug delivery," Pharm. Res. **21**, 1732 (2004).
[6] A. Grayson, R. Shawgo, A. Johnson, N. Flynn, Y. Li, M. Cima, and R. Langer, "A biomems review: Mems technology for physiologically integrated devices," Proc. IEEE **92**, 6 (2004).
[7] P. Gravesen, J. Branebjerg, and O. S. Jensen, "Microfluidics: A review," J. Micromech. Microeng. **3**, 168 (1993).
[8] P. K. Yuen, L. J. Kricka, and P. Wilding, "Semi-disposable microvalves for use with microfabricated devices or microchips," J. Micromech. Microeng. **10**, 401 (2000).
[9] D. J. Laser and J. G. Santiago, "A review of micropumps," J. Micromech. Microeng. **14**, R35 (2004).
[10] D. Accoto, M. Carrozza, and P. Dario, "Modelling of micropumps using unimorph piezoelectric actuator and ball valves," J. Micromech. Microeng. **10**, 277 (2000).
[11] M. Carrozza, N. Croce, B. Magnani, and P. Dario, "A piezoelectric-driven stereolithography-fabricated micropump," J. Micromech. Microeng. **5**, 177 (1995).
[12] D. B. Weibel, M. Kruithof, S. Potenta, S. K. Sia, A. Lee, and G. M. Whitesides, "Torque-actuated valves for microfluidics," Anal. Chem. **77**, 4726 (2005).
[13] J. M. K. Ng, I. Gitlin, A. D. Stroock, and G. M. Whitesides, "Components for integrated poly(dimethylsiloxane) microfluidic systems," Electrophoresis **23**, 3461 (2002).
[14] B. J. Kirby, D. S. Reichmuth, R. F. Renzi, T. J. Shepodd, and B. J. Wiedenman, "Microfluidic routing of aqueous and organic flows at high pressures: fabrication and characterization of integrated polymer microvalve elements," Lab Chip **5**, 184 (2005).
[15] B. J. Kirby, T. J. Shepodd, and E. F. Hasselbrink, "Voltage-addressable on/off microvalves for high-pressure microchip separations," J. Chromatogr., A **979** 147 (2002).
[16] E. F. J. Hasselbrink, T. J. Shepodd, and J. E. Rehm, "High-pressure microfluidic control in lab-on-a-chip devices using mobile polymer monoliths," Anal. Chem. **74**, 4913 (2002).
[17] S. D. Solares, M. Blanco, and W. A. Goddard III, "Design of a nanomechanical fluid control valve based on functionalized silicon cantilevers: Coupling molecular mechanics with classical engineering design," Nanotechnology **15**, 1405 (2004).
[18] T. D. Nguyen, H.-R. Tseng, P. C. Celestre, A. H. Flood, Y. Liu, J. F. Stoddart, and J. I. Zink, "A reversible molecular valve," Proc. Natl. Acad. Sci. U.S.A. **102**, 10029 (2005).

[19] See www.magneticmicrosphere.com for suppliers of magnetic beads and particles.
[20] H. A. Stone, "On lubrication flows in geometries with zero local curvature," Chem. Eng. Sci. **60**, 4838 (2005).
[21] G. K. Batchelor, *An Introduction to Fluid Dynamics* (Cambridge University Press, Cambridge, 1967).
[22] A. Engel and R. Friedrichs, "On the electromagnetic force on a polarizable body," Am. J. Phys. **70**, 428 (2002).
[23] G. Fonnum, C. Johansson, A. Molteberg, S. Mørup, and E. Aksnes, "Characterization of dynabeads by magnetization measurements and mössbauer spectroscopy," J. Magn. Magn. Mater. **293**, 41 (2005).
[24] Comsol support and Comsol Multiphysics documentation, www.comsol.com
[25] K. Gjerde, J. Kjelstrup-Hansen, C. H. Clausen, K. B. K. Teo, W. I. Milne, H Rubahn, and P. Boggild, "Carbon nanotube forests: A nonstick workbench for nanomanipulation," Nanotechnology **17**, 4917 (2006).

Pulse Reversal Permalloy Plating Process for MEMS Applications

K. Smistrup[a], P. T. Tang[b], and P. Møller[b]
[a] MIC – Department of Micro and Nanotechnology
[b] Department of Manufacturing Engineering and Management (IPL)
Technical University or Denmark, DK-2800 Kgs. Lyngby, Denmark

Nickel-iron, and especially Permalloy, plating has been known and used for more than 40 years, but there are still several problems related to stability and maintenance that should be resolved. This paper presents a saccharine-free pulse reversal plating Permalloy electrolyte, which gives low-stress deposits. We demonstrate selected MEMS applications of the electrolyte. The use of the strong complexing agent 5-sulfosalicylic acid allows for a photometric determination of the Fe^{3+}-level in the bath and eliminate precipitates. This makes the electrolyte suitable as a Permalloy plating process used on an irregular basis.

Introduction

Electroplating of nickel-iron alloys has been known for many years. IBM filed some of the first patents aiming at deposition of soft magnetic films around 1970 (1, 2). At that time the preferred plating bath for electrodeposition of nickel-iron alloys, and particularly the $Ni_{80}Fe_{20}$ or Permalloy, consisted of simple mixtures of the sulfate or chloride salts of nickel and iron. The typical bath would furthermore contain boric acid as a pH buffer and a few organic additives such as lauryl sulfate (wetting agent) and saccharin (stress reducer). Especially when chloride salts are used, the internal stresses in the deposits are very high and must be reduced using efficient stress reducing additives. Unfortunately, the use of the so-called sulfur containing additives results in small amounts of sulfur being co-deposited (up to a few percent). Even a small sulfur content will influence the corrosion resistance (3), as well as both the mechanical and the magnetic properties, in a negative way.

In order to reduce the internal stress, or to avoid the use of sulfur containing stress reducing additives, some authors have reported Permalloy plating processes based on sulphamate rather than sulfate (and chloride) (4).

The mechanism of nickel-iron alloy plating belong to the so-called anomalous type (5) which means that the iron is plated preferentially although it is not the most noble metal of the two. The degree of anomalous deposition depends on bath temperature (5) but also on pH and the use of pH-buffers (6). A bath without pH-buffer is less anomalous in behavior as compared to a bath with 0.4 M of boric acid (6). According to the literature (5), but also the experience obtained within the present work, simple sulfate or chloride based Permalloy baths, should be operated in a pH range from 3 to 5. Much below 3 the current efficiency will drop to unacceptable values, see also (6), and above 5 the formation of Fe^{3+}-based precipitates will slowly destroy the electrolyte. Adding a suitable complexing agent for Fe^{3+} postpones the formation of ferric compounds. Venkatasetty (7) reports that the addition of citrate (to an otherwise simple sulfate bath) will increase the

period in which good deposits can be obtained from a few hours to more than 25 hours. Depending on the complexing agent, it may also have the effect that the iron to "total metal" concentration ratio can be increased from 2 percent to 4 percent or more – while still depositing the desired Permalloy composition. As most baths use pure nickel anodes, having a relatively high iron concentration in the bath will make the bath easier to operate and less susceptible to small concentration changes.

Electroplated Permalloy has several applications in MEMS technology. Permalloy is widely used when some form of magnetic actuation is required, such as magnetically actuated valves or flux guides in electromagnet applications (see for example (8-12)). In recent years magnetic manipulation in microfluidic systems has emerged as a promising technology for bio-separation in lab-on-a-chip systems. A receptor molecule (DNA, RNA, proteins, cells, antigens etc.) is bound on the surfaces on magnetic beads or particles. These beads or particles are attracted to regions of large magnetic field, and thus if they are suspended in a solution containing target molecules for the receptor molecules, the target molecules can be separated from the solution by application of a spatially varying magnetic field. Both active systems with on-chip electromagnets and passive systems with on-chip soft magnetic structures have been realized using electroplated Permalloy (see (13, 14) and references therein). The microsystems described in refs. (13-15) are all fabricated using the electrolyte presented in this paper.

One key requirement for a MEMS-compatible deposit is that it should have relatively low internal stress. Many MEMS-structures contain thin beams or membranes that will not react well to stress, and in other cases thick films are needed, and a large internal stress might make such films peel off.

The permalloy plating bath we present here has been used to plate 150 μm thick bars with widths of 50 μm and lengths of 4.5 mm without any peel off. We have not measured the stress of deposits made with this bath, but in (16) a similar pulse reversal plating bath for CoNiFe is presented, where the stress is measured to be approximately 70-80 Mpa, which is relatively low.

Experimental Methods

TABLE I. Recipe for the Permalloy electrolyte. The pH-value was adjusted to 3.0 using sodium hydroxide. The bath was operated at 35 °C.

Compound	Formula	Concentration (M)
Nickel sulfate	$NiSO_4 \cdot 6\ H_2O$	0.2000
Nickel chloride	$NiCl_2 \cdot 6\ H_2O$	0.2000
Iron Sulfate	$FeSO_4 \cdot 7\ H_2O$	0.0293
Boric acid	H_3BO_3	0.5000
5-sulfosalicylic acid	$HO_3S{\cdot}C_6H_3OH{\cdot}COOH$	0.0350
Naphthalene tri-sulfonic acid (sodium salt)	$(NaO_3S)_3C_{10}H_8$	0.0070

The main stability problem associated with alloy plating baths containing iron, is the oxidation of Fe^{2+} to Fe^{3+} and the following formation of strong hydroxide complexes (see TABLE II) leading to precipitation of $Fe(OH)_3$. The complexing agent 5-sulfosalicylic acid, is one of very few candidates for a compound forming complexes with Fe^{3+} that are stronger than the hydroxides. In TABLE II the formation constants of oxalate, which is usually regarded as a strong complexing agent for Fe^{3+}, is clearly weaker than 5-sulfosalicylic acid.

TABLE II: Cumulative formation constants for metal complexes with hydroxide, 5-sulfosalicylic acid and oxalate (17).

Metal ion	Ligand	log K_1	log K_2	log K_3
Fe^{2+}	OH^-	5.56	9.77	9.67
Fe^{3+}	OH^-	11.87	21.17	29.67
Ni^{2+}	OH^-	4.97	8.55	11.33
Fe^{2+}	$HO_3S{\cdot}C_6H_3OH{\cdot}COOH$	5.90		
Fe^{3+}	$HO_3S{\cdot}C_6H_3OH{\cdot}COOH$	14.64	25.18	32.12
Ni^{2+}	$HO_3S{\cdot}C_6H_3OH{\cdot}COOH$	6.42	10.24	
Fe^{2+}	$C_2O_4^{2-}$	2.9	4.52	5.22
Fe^{3+}	$C_2O_4^{2-}$	9.4	16.2	20.2
Ni^{2+}	$C_2O_4^{2-}$	5.3	7.64	~8.5

The use of 5-sulfosalicylic acid, and a few other related compounds, in iron alloy plating baths was patented in 1978 (18). Besides the capabilities as complexing agent, other advantages of 5-sulfosalicylic acid include a very strong red color (absorbance at 480 nm) of the complexes with Fe^{3+} and that 5-sulfosalicylic aced is a stable molecule which is not destroyed in the electrolyte and does not seem to cause co-deposit of sulfur or carbon.

Initially 2 liters of bath were mixed using the recipe of TABLE I. During the mixing process the spectrophotometric data for each of the components were measured (see figure 1) in the range 350 nm to 1100 nm using a Shimadzu UV mini 1240 Spectrophotometer. The mixed bath was split into two 1-litre bottles. One was used as the plating bath, and the other was used for reference.

These two baths were used to study of the development of the electrolyte over time. Once a week for eight weeks, Permalloy was electroplated onto a 3×3 cm^2 copper plate for 30 minutes using pulse reversal plating with the cathodic pulse being 60 ms of 4 A/dm^2 and the anodic pulse being 20 ms of 6 A/dm^2 corresponding to an average current density of 1.5 A/dm^2. Absorbance, as well as pH, was recorded in the plating bath before and after each deposition. At the same time similar data were also measured for the reference bath. pH was measured using an Accumet model 15 pH-meter using a Radiometer pHC2001 electrode.

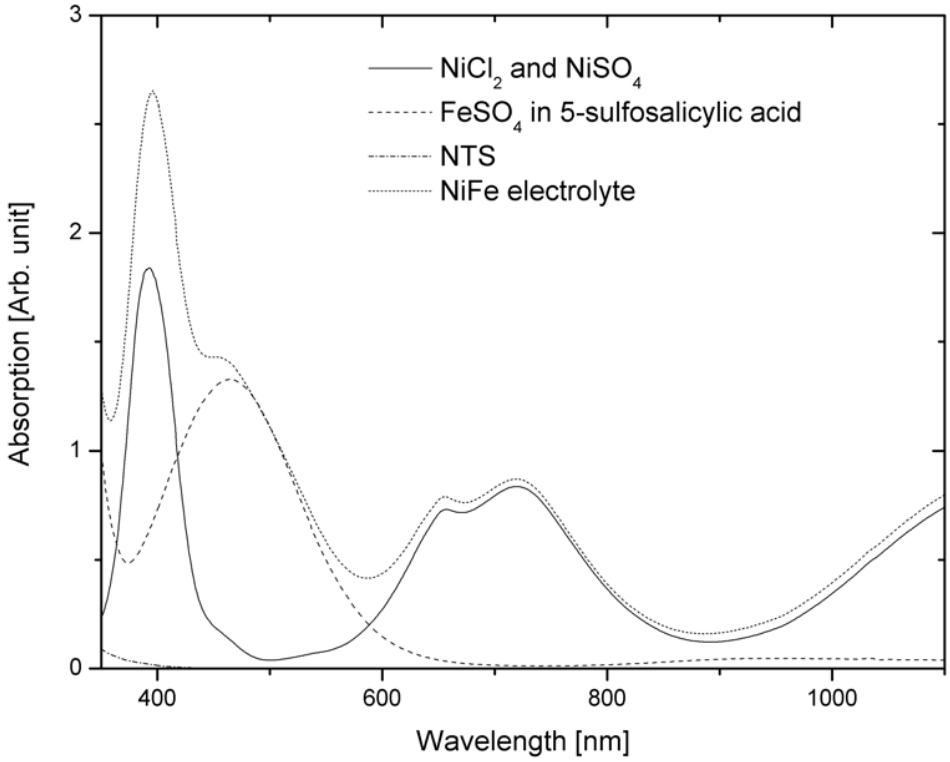

Figure 1: Spectrophotometric data for the components of the Permalloy electrolyte. The data for the individual components add up to give the data for the finished electrolyte.

Two other baths were mixed to establish the connection between spectrophotometric data and the concentration of Fe^{3+} and Fe^{2+} ions in solution. 800 ml of bath was mixed using the recipe of TABLE I without the iron sulfate. This was split into two 400 ml portions, and 0.0293 M $FeSO_4$ was added to one portion, and 0.01465 M $Fe_2(SO_4)_3$ was added to the other, such that the amount of Fe ions was the same in the two solutions. This gave two baths; one containing Fe^{2+} ions only – the regular bath, and one containing Fe^{3+} ions only. These two baths were mixed in various ratios to determine the absorbance at 480 nm as a function of Fe^{3+}-content.

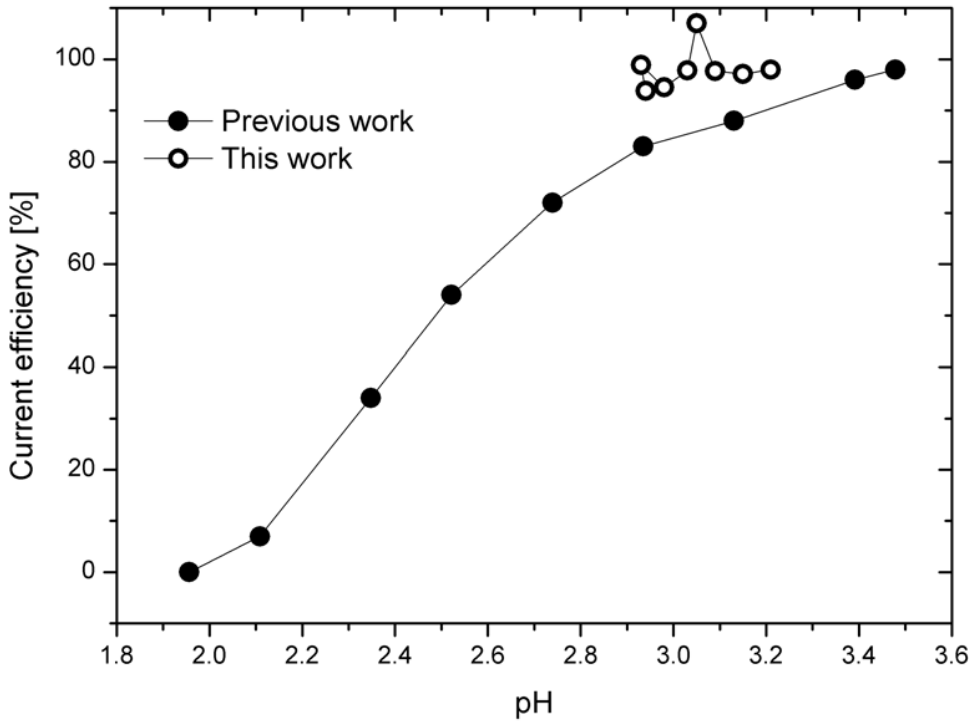

Figure 2: Current efficiency as a function of pH. Results from this work are compared to previous work (19) using almost identical electrolytes.

The current efficiency was established by weighing the samples before and after the electroplating using a Sartorius BP61 scale with a maximum precision of ±0.1 mg. The Fe (and Ni) content in the deposits was determined semi-quantitatively with standardless energy dispersive X-Ray spectrometry (EDX, Oxford Scientific) in a JEOL Scanning electron microscope (SEM, JSM-5900).

Results and Discussion

Korsbæk and Rubæk previously developed the current recipe for the Permalloy electroplating bath in collaboration with Hansen and Tang (19). They established the relation between pH of the bath and current efficiency (see Figure 2). These results are compared to results obtained during the present investigation. There is a relatively good correlation between the old results and the new ones. The only differences between the experiments are a higher chloride content in the new bath (called “This work” in Figure 2) and that in this work we did not compensate for a known inaccuracy in the pulse plating rectifier (TCD research, double cathode WinCAPP) when operating at small currents.

In ref. (15) we report the magnetic properties and fabrication scheme of a magnetic separation system that was fabricated using the present electrolyte.

The spectrophotometric data for the different bath components were measured on the individual components and in an unused electrolyte with the composition presented in TABLE I. It is seen in figure 1 how the curves for the individual components add up to

give the total curve for the bath. Also, it is seen that the Fe sulfate has a distinct peak at 480 nm, whereas Ni have several peaks at 393, 657 and 720 nm (see Figure 1). This means that we can distinguish the Fe peak from the nickel peaks, and thus we can monitor the development of the different components.

We have monitored the development of the spectrophotometric data over time. Figure 3 displays our findings. It is seen that the Fe peak grows rapidly. Within 25 days it has grown to a state, where it completely dominates the entire spectrum. It is well-known that Fe^{2+} and Fe^{3+} absorb at the same wavelength, but Fe^{3+} absorbs much more strongly than Fe^{2+}. Therefore the rise in the peak is interpreted as a sign that some of the Fe^{2+} ions have been oxidized to Fe^{3+}. Also, we see that the Fe peak at 480 nm is reduced after plating. This means that some of the Fe^{3+} ions are removed (deposited or more likely reduced to Fe^{2+}) during the plating process.

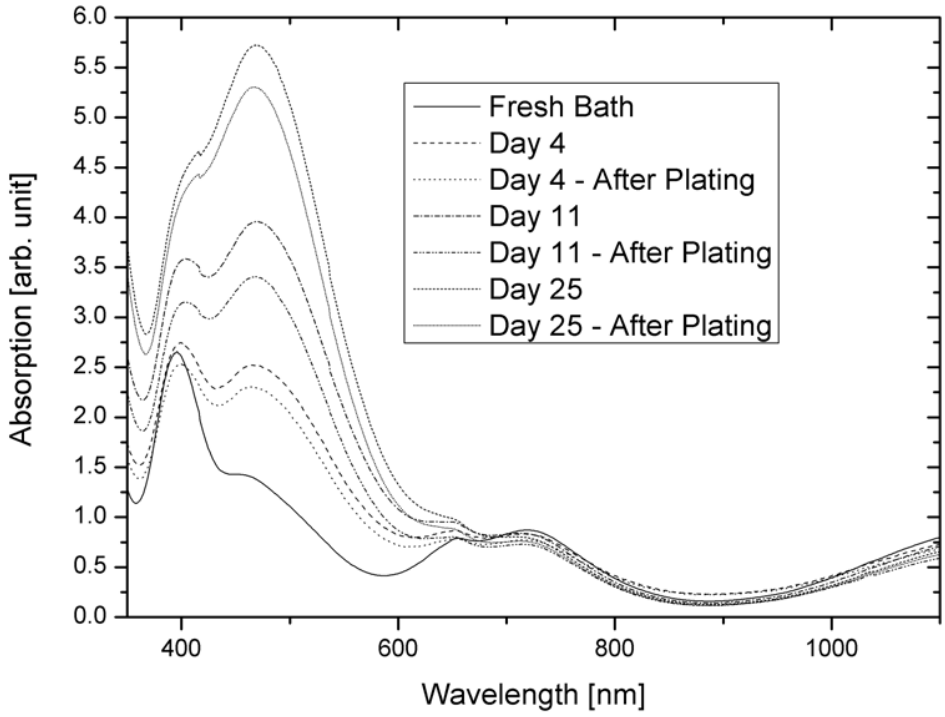

Figure 3: Development in the spectrophotometric data over time. The graph also shows how the spectrophotometric data change during electroplating.

In Figure 4 the data for the absorption at 480 nm and the pH-value of the plating bath before and after plating are compared with data for an unused reference bath. We see that the absorption grows steadily and that the plating bath grows slightly faster than the reference bath. This may be due to the fact that the plating bath was exposed more to air than the reference bath. It is also seen that the plating process consistently causes the absorption to drop – at least temporarily – which indicates that Fe^{3+} ions are reduced to Fe^{2+} ions during plating.

We also learn from Figure 4 that pH rises substantially during electrodeposition such that pH is enhanced just after plating, but during the time before the next experiment (around one week) pH drops back to a value that is only a little higher than before the

previous experiment. On the other hand pH in the reference bath is consistently falling, even if the total change is small.

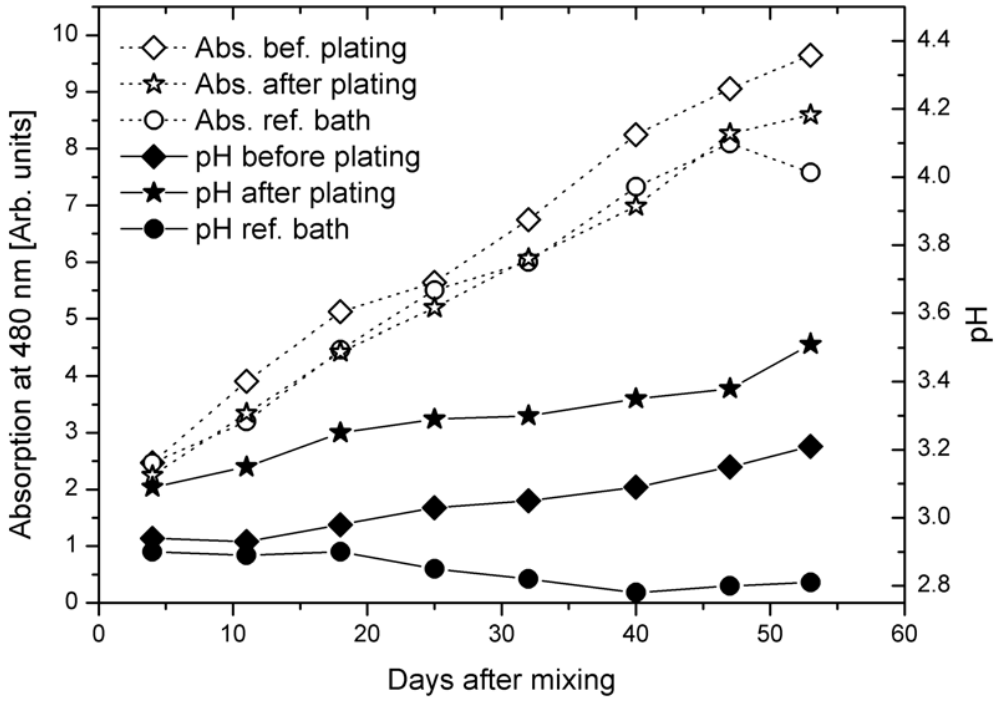

Figure 4: Development of the characteristic spectrophotometric peak at 480 nm (left axis) and pH (right axis) as function of time. Data is shown before and after plating as well as for the unused reference bath. A total of 8 plating experiments were conducted.

During the electrodeposition, although pulse reversal plating is applied and thus makes many reactions possible, the dominating or resulting electrochemical reactions are:

$$2\,H^+ + 2\,e^- \rightarrow H_2\,(g), \qquad [1]$$

$$Fe^{3+} + e^- \rightarrow Fe^{2+}, \qquad [2]$$

$$Fe^{2+} + 2\,e^- \rightarrow Fe, \qquad [3]$$

$$Ni^{2+} + 2\,e^- \rightarrow Ni. \qquad [4]$$

Reactions [1] and [2] are directly responsible for the current efficiency being in the range from 94-98% (see Figure 2), whereas reactions [3] and [4] are the ones leading to the actual deposit.

After electrodeposition, when the solution is resting in a closed PE bottle, the following reaction is anticipated:

$$4\,Fe^{2+} + O_2 + 4\,H^+ \rightarrow 4\,Fe^{3+} + 2\,H_2O. \qquad [5]$$

Following this oxidation, we expect a protolysation-like process to take place. The exact role of 5-sulfosalicylic acid and the complexes formed during and after electrodeposition, as compared to the protolysation reactions when water is acting as a ligand (see reactions [6] and [7] below), is somewhat unclear.

$$Fe(H_2O)_6^{3+} \rightarrow Fe(H_2O)_5(OH)^{2+} + H^+, \quad K_1=9.0\cdot10^{-4}\ (20), \qquad [6]$$

$$Fe(H_2O)_5(OH)^{2+} \rightarrow Fe(H_2O)_4(OH)_2^{+} + H^+, \quad K_2=5.5\cdot10^{-4}\ (20). \qquad [7]$$

Reaction [2] explains why the absorption at 480 nm decreases during electroplating, since it predicts that the Fe^{3+} content of the bath decreases during electroplating. The reaction in [5] explains why we see the general rise in absorption at that wavelength and thus Fe^{3+} content over time. There is not enough 5-sulfosalicylic acid in the bath to form complexes with all the metal ions, but it will most likely form complexes with all Fe^{3+} ions. Therefore complexes between Fe^{2+} and Ni^{2+} with water, OH^-, and Cl^- will also be present and protolysis may occur with these complexes as well. This combined with reactions [6] and [7] explains why we see a general decrease in pH in the reference bath. We expect that reaction [1] is the cause of the general increase in pH for the plating bath.

Just after the electroplating, pH has risen to a level that is substantially above the level before plating. We expect that this be due to the reaction [2], since the Fe^{3+} has to be released from the complexes formed in reactions like [6] and [7] which will release OH^- that will quickly recombine with H^+, and thus pH rises. Complexes formed with Ni^{2+} and Fe^{2+} and 5-sulfosalicylic acid as well as the other bath ingredients may also contribute to this pH rise, when the complexes are dissociated during electroplating.

In order to quantify the rise in absorption at 480 nm and relate it to the concentration of Fe^{3+} ions in the solution, we measured the absorption at different known concentrations of Fe^{3+} and Fe^{2+}. The results are displayed in Figure 5. We have made a linear fit based on the first three data points. Another fit is made based on the last 4 data points. It is not uncommon for the absorption to 'fall off' at high absorption values due to screening.

The standard curve in Figure 5 allow us to calculate the concentration of Fe^{3+} ions in the bath, and by measuring the mass and chemical composition of the deposits, we are able to calculate the amount of remaining Fe^{2+} ions in the bath.

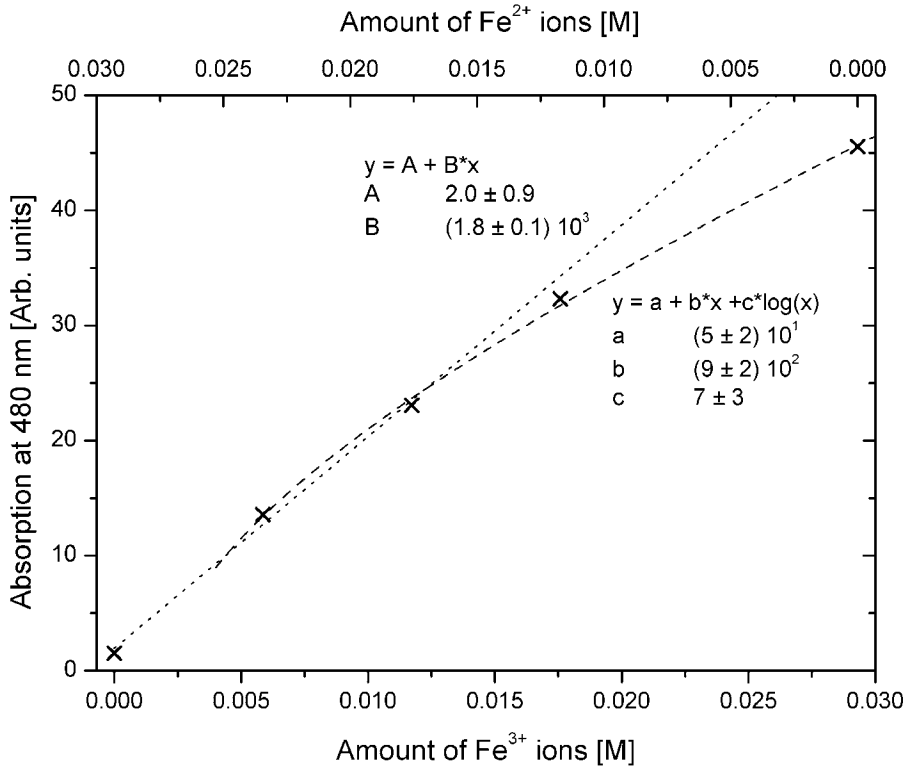

Figure 5: Absorption at 480 nm as a function of Fe^{3+} (and Fe^{2+}) concentration. For concentrations below 0.01 M a linear fit is used. In the fits 'y' denotes the absorption, and 'x' denotes the amount of Fe^{3+} ions. Suitable units are assumed on 'A', 'B', 'a', 'b', and 'c'.

These data are collected in Figure 6. Over the course of eight weeks and 8 experiments, over 20 % of the originally available Fe^{2+} ions have disappeared due to deposition or oxidation.

In Figure 7 the amount of Fe^{2+} in the bath is related to the percentage of iron in the deposited alloy. Although there is an obvious relation between these quantities, and the iron content of the alloy certainly decreases with the calculated Fe^{2+} concentration in the bath, the uncertainty in the linear fit (mainly due to uncertainties related to the EDX measurements) is too large make any real predictions of the exact alloy composition.

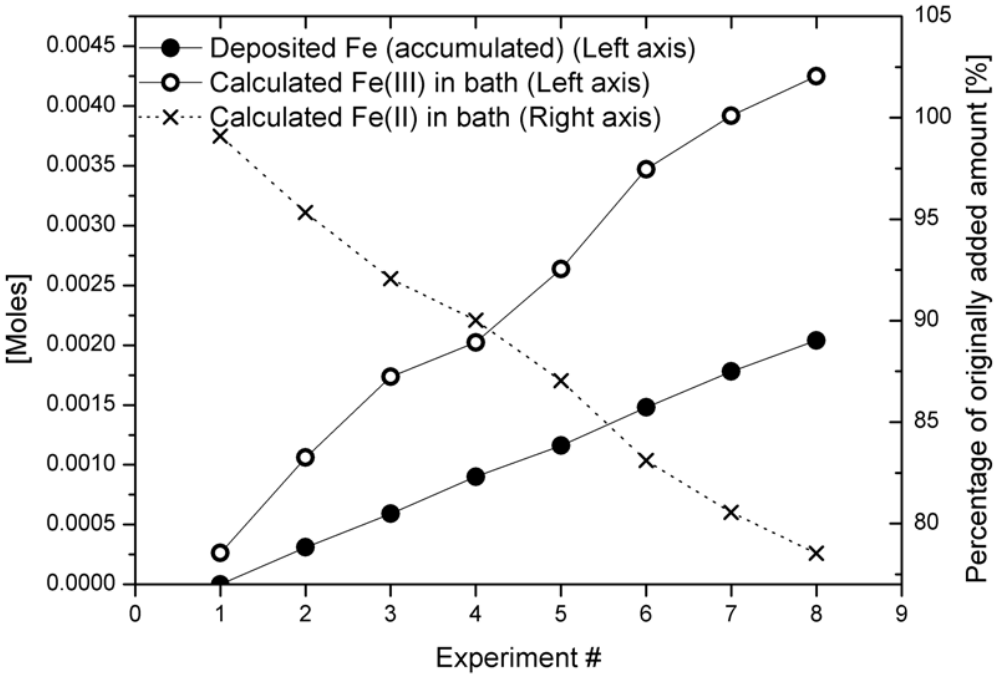

Figure 6: Development of Fe content in the bath. Spectrophotometric measurements of Fe^{3+}, deposit weight and composition allows for calculations of the remaining amount of Fe^{2+} in the bath.

Conclusion

A reliable and stable Permalloy plating bath is presented, which is suitable for MEMS applications due to low internal stress, good magnetic properties and long term bath stability – even without using nitrogen purging or other means to remove oxygen dissolved in the electrolyte. The bath is especially well suited in situations, where the bath is only used every once in a while, such that continuous bath replenishment is not feasible.

We have demonstrated a way to monitor the amount of available Fe^{2+} ions in the bath, allowing for simple bath maintenance by regular addition of iron (sulfate or chloride) and pH adjustments (diluted hydrochloric or sulfuric acid). When operating our 25 l version of the bath, we have found that it is helpful to electroplate for a few hours on a dummy wafer before electroplating on real samples. This reactivates the anode, and as we have seen some of the Fe^{3+} ions will be reduced to Fe^{2+}. With typical use the bath will then be able to last for more than 1 year.

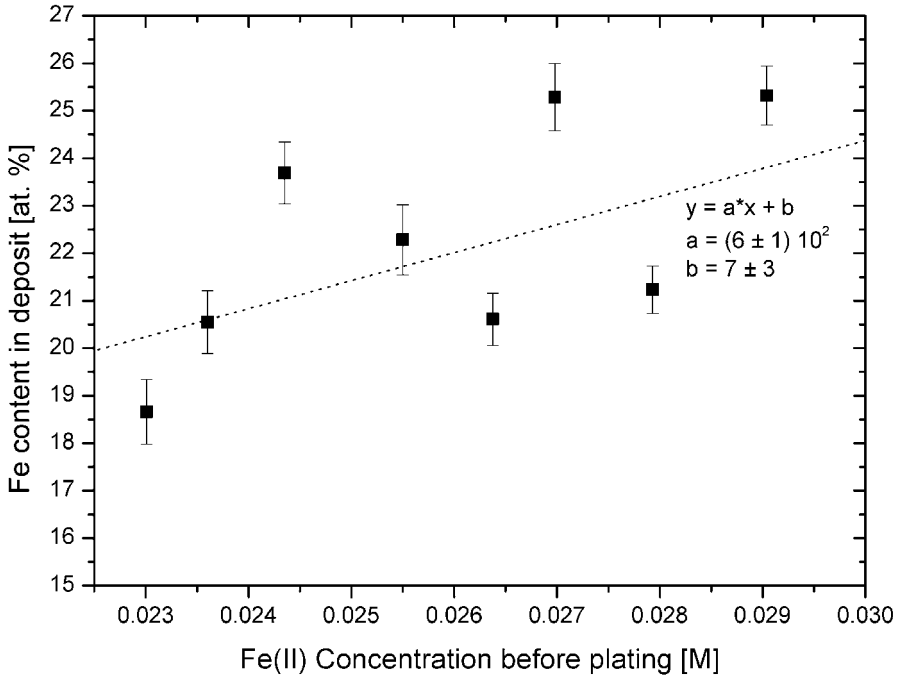

Figure 7: Fe content in deposits as a function of Fe^{2+} concentration in the bath. When the amount of deposited metal is known, the concentration of Fe^{3+} ions is computed from the standard curve in Figure 5, and when we know the initial amount of Fe ions, we can calculate the amount of available Fe^{2+} ions. In the included fit 'x' denotes the Fe(II) concentration before plating, and 'y' denotes the iron content in the deposit. Suitable units on 'a' and 'b' are implied.

Acknowledgments

Kristian Smistrup acknowledges support from Copenhagen School of Nano-technology (C:O:N:T), and Danish Technological Institute.

References

1. J.V. Powers & L.T. Romankiw, US 3,652,442, March 28 (1972)
2. E.E. Castellani, J.V. Powers & L.T. Romankiw, US 4,102,756, Juli 25 (1978)
3. T. Osaka *et al.*, "Influence of Crystalline Structure and Sulfur Inclusion on Corrosion Properties of Electrodeposited CoNiFe Soft Magnetic Films", J. Electrochem. Soc., Vol. 146, No. 6, pp. 2092-2096 (1999)
4. A.F. Bogenschütz & U. Georg, "Galvanische Legierungsabscheidung and Analytik" (in German), Eugen G. Leuze Verlag, Saulgau (1982)
5. A. Brenner, "Electrodeposition of Alloys", Academic Press, New York (1963)
6. J. Horkans, "Effect of Plating Parameters on Electrodeposited NiFe", J. Electrochem. Soc. Vol. 128, No. 1, pp. 44-49 (1981)

7. H.V. Venkatasetty, “Electrodepostion of Thin Magnetic Permalloy Films”, J. Electrochem. Soc., Vol. 117, No. 3, pp. 403-407 (1970)
8. D.J. Sadler, T.M. Liakopoulos & C.H. Ahn, “A Universal Electromagnetic Microactuator Using Magnetic Interconnection Concepts”, J. Microelectromech. Syst. Vol. 9, No. 4, pp. 460-468 (2000)
9. M. Ruan, J. Shen & C.B. Wheeler, “Latching microelectromagnetic relays”, Sensors & Actuators A, Vol. 91 pp. 346-350 (2001)
10. C. Liu, T. Tsao, Y-C Tai, T-S Leu, C-M Ho, W-L Tang & D. Miu, “Out-of-plane Permalloy Magnetic Actuators for Delta-Wing Control”, Proc. IEEE Micro Electro Mechanical Systems 1995 pp. 7-12 (1995)
11. E.J. O’Sullivan *et al.*, ”Integrated, variable reluctance magnetic micromotor”, IBM J. Res. Dev. Vol. 42, No. 5, pp. 681-691 (1998)
12. C. Liu, “Development of surface micromachined magnetic actuators using electroplated permalloy”, Mechatronics Vol. 8, pp. 613-633 (1998)
13. K. Smistrup, P.T. Tang, O. Hansen & M.F. Hansen, ”Microelectromagnet for magnetic manipulation in lab-on-a-chip systems”, J. Magn. Magn. Mat. Vol. 300, pp. 418-426 (2006)
14. K. Smistrup, B.G. Kjeldsen, J.L. Reimers, M. Dufva, J. Petersen & M.F. Hansen, ”On-chip magnetic bead microarray using hydrodynamic focusing in a passive magnetic bead separator”, Lab Chip, Vol. 5, pp. 1315-1319 (2005)
15. K. Smistrup, T. Lund-Olesen & M.F. Hansen, ”Microfluidic magnetic separator using an array of soft magnetic elements”, J. Appl. Phys. Vol. 99, No. 8 (2006)
16. J.G. Speight, “Lange’s Handbook of Chemistry”, McGraw-Hill, New York (2005)
17. F.E. Rasmussen, J.T. Ravnkilde, P.T. Tang, O. Hansen, & S. Bouwstra, ”Electroplating and characterization of cobalt-nickel-iron and nickel-iron for magnetic micro-system applications”, Sensors & Actuators A, Vol. 92 pp. 242-248 (2001)
18. R.J. Lash, “Electroplating Iron Group Metal Alloys”, US 4,129,482 patent, Dec. 12 (1978)
19. K. Korsbæk & R. Rubæk, ”Udvikling og karakterisering af magnetiske legeringer til mikromekaniske komponenter” (in Danish), master thesis at IPL, Technical University of Denmark (2004)
20. P. Kofstad, “Uorganisk kjemi” (in Norwegian), H. Aschehoug & Co., Lund (1979)